THE UNIVERSITY *of* EDINBURGH

Mapping small-scale tropical forest disturbances using SAR and optical satellite imagery

Chiara Aquino

Thesis submitted in fulfilment of
the requirements for the degree of
Doctor of Philosophy
to the University of Edinburgh
2022

Declaration

I declare that this thesis has been composed solely by myself and that it has not been submitted, either in whole or in part, in any previous application for a degree. Except where otherwise acknowledged, the work presented is entirely my own.

Chiara Aquino

September 2022

Abstract

Climate change is the greatest crisis that humanity has ever faced, threatening water supplies, food security, species and ecosystems worldwide. The tropical forest biome serves a fundamental regulatory function in the climate system, by absorbing 34% of carbon dioxide from the atmosphere every year. Moreover, tropical forests are unique biodiversity hotspots and provide an essential source of livelihood and socio-cultural identity to local communities. Their integrity is fundamental to the stability of the global climate and to the well-being of the populations that depend on them. Over the last 20 years, pressure from the extractive industries and an increasing global demand for commodities have accelerated the decline of tropical forest cover, with devastating implications for global warming, biodiversity loss and human health. In this scenario, understanding and monitoring spatio-temporal patterns of forest loss has become a complementary tool to national conservation policies to prevent further deforestation. Satellite remote sensing has emerged as the most viable system for estimating changes in forest cover at large spatial scales and in remote regions. In the last decade, thanks to the free availability of high-resolution satellite imagery, yearly maps of forest loss and forest monitoring alert systems have become operational at the national and global scale. Nevertheless, the magnitude and extent of small-scale disturbances, such as those caused by selective logging and understory fires, remain largely uncertain. In the Brazilian Amazon, it is estimated that forest degradation (as caused by selective logging, forest fragmentation, edge effects, forest fire and drought) has surpassed the rate of deforestation, contributing to 73% of the overall above ground biomass (AGB) loss in this region. It is likely that the same trend is true for other tropical areas, setting forest degradation as high priority

for forest conservation policies. On the other hand, a lack of reliable ground-truth data on AGB change, together with the limitations of satellite imagery in typically cloudy and densely forested regions, poses significant challenges to reliably mapping forest degradation in the tropics.

In this thesis, I use a novel biomass change dataset comprising eight 1-ha permanent sample plots that I established in logging concessions in Peru and Gabon as part of the Forest Degradation Experiment (FODEX). The plots were carefully inventoried by hand and Terrestrial Laser Scanning before and after selected number of trees were removed, giving different percentages of biomass loss values (5-30% AGB loss ha^{-1}). My aim is to use all the available remote sensing imagery, both optical and radar, to find the most accurate methodology and sensor characteristics to detect selective logging in the field sites, with the intent of extending the results over larger spatial scales, for regional and national assessment.

In Chapter 3, I focus on optical remote sensing and perform a comparative study of six multispectral satellite sensors ranging between 0.3 - 30 m in spatial resolution, namely WorldView-3, SkySat, SPOT-7, PlanetScope, Sentinel-2 and Landsat 8. For each sensor, I retrieve before/after logging differences in band reflectance, Normalized Difference Vegetation Index (NDVI) and texture parameters to find the best combination of sensor and remote sensing metrics to detect low-intensity logging over the field plots in Peru. The strength of the relationships between the change in these values and field-measured biomass loss (ΔAGB) is analysed using linear regression models. It is found that texture measures correlate more with ΔAGB than simple spectral parameters; moreover, the strongest correlations are achieved for those sensors with spatial resolutions in the intermediate range (1.5 - 10 m), while using a moving square window ranging between 9 - 14 m in length. Maps predicting ΔAGB show very promising results using a texture parameter from the infrared band of 3 m resolution PlanetScope (R^2 = 0.97).

Persistent cloud cover over large areas of the tropics often prevents optical remote sensing monitoring of vegetation on a continuous basis. Synthetic Aperture Radar (SAR) data from the C-band Sentinel-1 mission provides cloud-free imagery on a 6 or 12-day repeat cycle at 10 m spatial resolution, offering the opportunity to monitor forest disturbances in a timely and accurate manner. In Chapter 4, I use a novel change detection method based on the cumulative sums (CuSum) of Sentinel-1 time-series to map low intensity forest disturbances in Peru and Gabon. Using the maximum of the CuSum distribution, I develop a single change metrics to retrieve location, time and magnitude of the disturbance events. The CuSum algorithm is calibrated using 1239 ha of very high resolution (25 cm) UAV LiDAR measurements of canopy height loss collected by the FODEX project over the field plots and the surrounding forest concessions. A comparison of the CuSum results with the LiDAR reference map yields a 78% success rate for the study site in Gabon and 65% success rate for the study site in Peru, for disturbances as small as 0.01 ha and for canopy height losses as fine as 10 m. In addition to other forest monitoring systems, the methodology outlined in this thesis has the potential of retrieving the magnitude of the disturbance events. A correlation between the CuSum change metric and AGB is found with R^2 = 0.95, and R^2 = 0.83 for canopy height loss. Low intensity disturbances captured by the CuSum method are largely undetected by state-of-the-art forest monitoring system such as the Global Forest Watch product and the RADD Alert system. While lacking near real-time monitoring capabilities, the CuSum algorithm can be adopted for building yearly maps of forest loss, providing more accurate figures of forest degradation for long-term monitoring purposes.

In Chapter 5, the method presented in Chapter 4 is employed for extending the analysis beyond the test sites, retrieving forest disturbance maps at the national scale. An image processing workflow is developed in Python to produce maps containing information on location, day of the year and biomass loss (in % ha^{-1}) in Peru and Gabon for the year

2020. The maps are compared with current large-scale products reporting deforestation and/or degradation in humid tropical forests.

Overall, the methods presented in this thesis refine the ability of both optical and radar satellite data to retrieve small-scale disturbances in dense tropical forests. The conclusions of the analysis support the usage of free-of-charge satellite data: free access to PlanetScope imagery is granted by Norway's International Climate & Forests Initiative, while the Copernicus Open Access Hub provides free and open access to Sentinel-1 data. Therefore, all methods are available to the public, with the aim of fostering citizen science to monitor the state of tropical forests.

Lay Summary

Tropical forests are disappearing at a staggering rate across the globe. Much of these forests are cleared and replaced for production of commodities including palm oil, soil and beef. The destruction of tropical forests releases a large amount of carbon dioxide to the atmosphere. In fact, deforestation is the second largest human contributor to climate change after the burning of fossil fuels. Thanks to the large-scale coverage and frequent revisit times, satellite remote sensing is used as the standard method for monitoring forests at the global scale. On the other hand, forest degradation, which is primarily caused by selective logging and fires, is challenging to detect and thus poorly understood. Forest degradation is thought to be widespread in the tropics and often precedes outright deforestation. Hence, stopping degradation may prevent further clearing of natural forests. The aim of this thesis is to improve detection of small-scale disturbances in tropical forests and develop new methods for estimating losses in forest biomass. In order to do so, I calibrate satellite imagery using unique measurements of forest degradation collected before and after selective logging, in forest concessions located in the Peruvian Amazon and in Gabon. First, I use optical data from six satellite sensors at increasing resolution, to find the best combination of sensor and parameter for detecting degradation in a study area in Peru. The results show that degradation is detected best using a texture measure derived from PlanetScope data at 3 m resolution. Unfortunately, persistent cloud cover in some parts of the tropics limits image availability and does not always guarantee continuous forest monitoring. Synthetic Aperture Radar (SAR) can offer a solution to this problem as it penetrates through clouds and interacts with the structural elements of the forests, in a way that scales with tree above ground biomass (AGB). Free and high-resolution SAR data is provided every 6 or 12 days by

the Sentinel-1 mission, thus offering the opportunity to monitor forest disturbances in a timely and accurate manner. In this thesis, I use the cumulative sums (CuSum) of Sentinel-1 time series to retrieve information on location, time and magnitude of the disturbance events. The results show that disturbances as small as 0.01 ha in size can be detected with a 78% success rate in Gabon and 65% success rate in Peru, when compared to high-resolution data of canopy height loss collected with aerial LiDAR. A statistical relationship is found between field-measured AGB and CuSum metrics, which allows to produce maps of biomass loss of the study areas. Based on these findings, I scale up the results to produce forest disturbance maps for Peru and Gabon for the study year 2020. As a result, I find that in 2020 Gabon lost 0.17% of its primary forests, more than double the figures reported by other maps derived from satellite optical data. These findings suggest that forest loss rates may be generally underestimated, while there is a critical need to develop better maps, which include estimates of small-scale degradation. The methods described in this thesis can be adapted to produce similar maps for other regions and periods of time, and can be adopted as a tool for widespread measuring of forest degradation.

Acknowledgements

I would like to thank Prof. Edward Mitchard for offering me the opportunity to undertake this research, for providing his guidance and for always giving me positive and kind encouragement. I also thank the European Research Council which funded my research through a Starting Grant awarded to Prof. Edward Mitchard. I would like to thank all the colleagues, postdoctoral and PhD students, of the Mitchard research group, with whom I had the pleasure to share this journey, and who supported me in so many ways. In particular, I would like to thank Dr. Iain McNicol for teaching me everything I know about forest inventory; Harry Carstairs, with whom I exchanged so much of this research, including knowledge, advice, support, but especially fieldwork adventures; Dr. Charlotte Wheeler, for her research insights and friendship; Dr. Keiko Nomura, for introducing me to the wonders of Google Earth Engine. I would also like to thank my second supervisor at UCL, Prof. Mat Disney, for carefully reviewing and offering significant advice on the third chapter of this thesis, and Dr. Andrew Burt, for participating to our fieldwork campaigns and collecting critical TLS data.

I am particularly grateful to the people that I met during my fieldwork in Peru and Gabon, without whom this research would not have been possible. In Peru, my deep gratitude goes to La Comunidad Nativa de Bélgica for opening the doors of their community and for making me feel like at home. I would like to thank Sylvia Mayta, who went a long way in helping us with fieldwork logistics, and in general I thank all the staff at the NGO AIDER for offering resources and support. I thank Beisit Luz Puma Vilca and the field assistants from Cuzco for their crucial work in making this research go ahead despite the challenges of the Covid-19 pandemic. From Bélgica, a particular thanks go to Don Arturo Aspajo López, Don Leoncio Aspajo Lopez and Don Luis López Chapiama for

assisting me during the forest inventory and teaching me about their forests. In Gabon, I would like to thank Anaick Modinga Dikongo and Creck Dassi for their precious work and dedication, but also for the conversations and fun moments that we shared. I thank the village of Ivindo and the staff at Rougier Gabon, in particular Joseph Amelim Boukandja, Evanillho Téodoro Muaño Bondjale and Armel Guipieri, for welcoming me at the site and for offering me their kind support.

This PhD would have not been the same without Margherita Scazza and Caterina Mogno, who have been colleagues, friends and my Italian family in Edinburgh, and with whom I shared so much of the joys and the struggles of this experience. I feel that we have done this together, and this journey will always be associated with you two in my memory. Also thanks to Francesca Taglini for her continuous presence, her comforting friendship and wise academic advice when I needed it the most. I would like to give special thanks to my friends in Edinburgh, in particular Andrzej, Claire and Isabella, and my friends and family in Italy for their emotional support. Lastly, my sincere gratitude goes to my partner Mijael, who encouraged me with immense patience and kindness through the critical moments of the last year, and who always believed in my ability to complete this journey.

Abbreviations

AGB	Above Ground Biomass
BGB	Below Ground Biomass
BGRN	Blue, Green, Red, Near-infrared
CHM	Canopy Height Model
CuSum	Cumulative Sum
DBH	Diameter at Breast Height
GEDI	Global Ecosystem Dynamics Investigation
GFW	Global Forest Watch
GFC	Global Forest Change
ESA	European Space Agency
Ha	Hectare
IPCC	International Panel on Climate Change
LiDAR	Light Detection and Ranging
NDVI	Normalized Difference Vegetation Index
NIR	Near-infrared
PSP	Permanent Sample Plot
Pg C	Petagram of Carbon
RADD	Radar for Detecting Deforestation
RGB	Red, Green, Blue
RMSE	Root Mean Square Error
SAR	Synthetic Aperture Radar
TLS	Terrestrial Laser Scanning

TMF	Tropical Moist Forest
UAV	Unoccupied Aerial Vehicle
USGS	United States Geological Survey
VH	Vertical transmission; Horizontal reception
VV	Vertical transmission; Vertical reception

Contents

Figures and Tables

Figures

Tables

Chapter 1

Introduction

1.1 Thesis context

1.1.1 Tropical forests in a warming climate

Tropical forests are the largest of the forest biomes, and the most biologically diverse ecosystems on Earth (FAO, 2020; Douglas, 2018). They are a source of livelihoods and cultural identity for traditional and indigenous populations, while providing food, water, medicine and fuelwood to millions of people across the tropics (Lewis, 2006; Vira et al., 2015). At a larger scale, tropical forests play a pivotal role in the carbon cycle by removing from the atmosphere $\approx$40 petagrams of carbon every year (Pg C yr^{-1}) (Beer et al., 2010) while also releasing a similar amount through respiration (Mitchard, 2018). However, since the start of the 21st century, increasing pressures from global markets and a growing demand for agricultural and wood commodities have accelerated the decline in tropical forest cover (Pendrill et al., 2019b,a; Curtis et al., 2018). Tropical regions experience the highest rates of deforestation globally: from 2000 to 2012, 102 Mha of tropical rainforests were lost, corresponding to 5% of total tropical forest area (for a definition of >25% canopy cover), surpassing forest recovery rates by 4.5 times (Figure 1.1) (Hansen et al., 2013). In 2019, the Intergovernmental Panel on Climate Change (IPCC) released a special report on climate and land, emphasising the critical role of tropical forests in the global cycles of water, energy and carbon (IPCC, 2019). At the local scale, tropical deforestation has been linked to biodiversity loss (Giam, 2017),

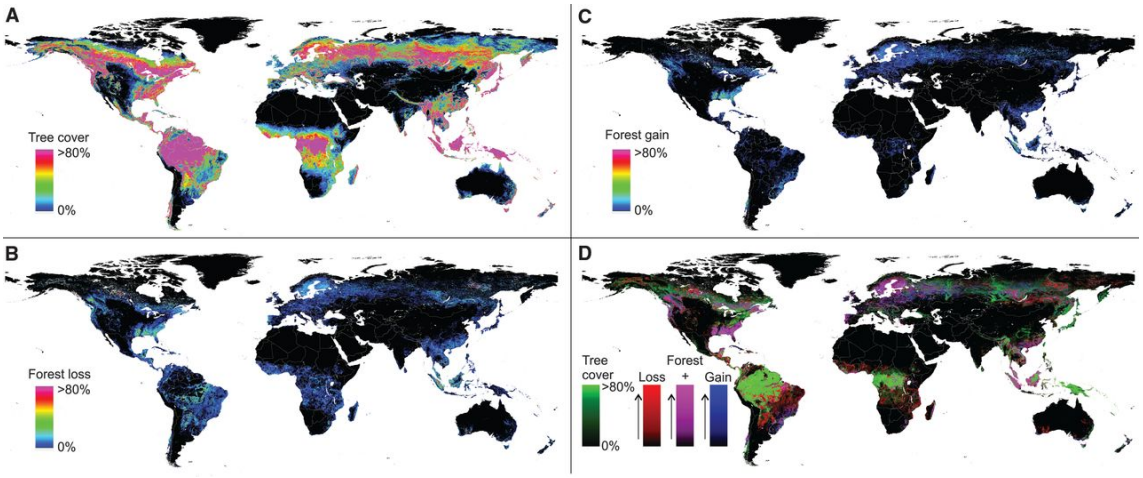

Figure 1.1: (A) Tree cover, (B) forest loss, (C) forest gain and (D) color composite of tree cover (green), forest loss (red), forest gain (blue) and loss + gain (magenta) for the period 2000-2012. Taken from Figure 1 in Hansen et al. (2013)

increasing air temperatures (Almeida et al., 2017; Marengo et al., 2018; Duveiller et al., 2018; Zeppetello et al., 2020) and changes in precipitation patterns (Leite-Filho et al., 2019). Higher temperatures and reduced rainfalls can alter the resilience of trees to a warming climate, triggering a positive feedback loop that enhances forest dieback and limits the ability of forests to sequester carbon dioxide (Zemp et al., 2017; Mitchard, 2018). After fossil fuel combustion, land-use change from tropical forest degradation and deforestation is the second largest source of anthropogenic greenhouse gas emissions to the atmosphere (van der Werf et al., 2009; Houghton and Nassikas, 2017). If fossil fuel extraction and deforestation continue, a rise in temperatures and regional droughts will greatly amplify the effects of global warming on ecosystems, societies and people across the tropics, which are already vulnerable to the effects of climate change (Zeppetello et al., 2020; IPCC, 2022). Atmospheric modelling studies have suggested that tropical forests are carbon neutral or carbon sinks, which implies that land-use emissions are approximately in balance with carbon uptakes by intact and regrowing forests (Pan et al., 2011; Schimel et al., 2015). Given all evidence on reducing reslience of the remaining

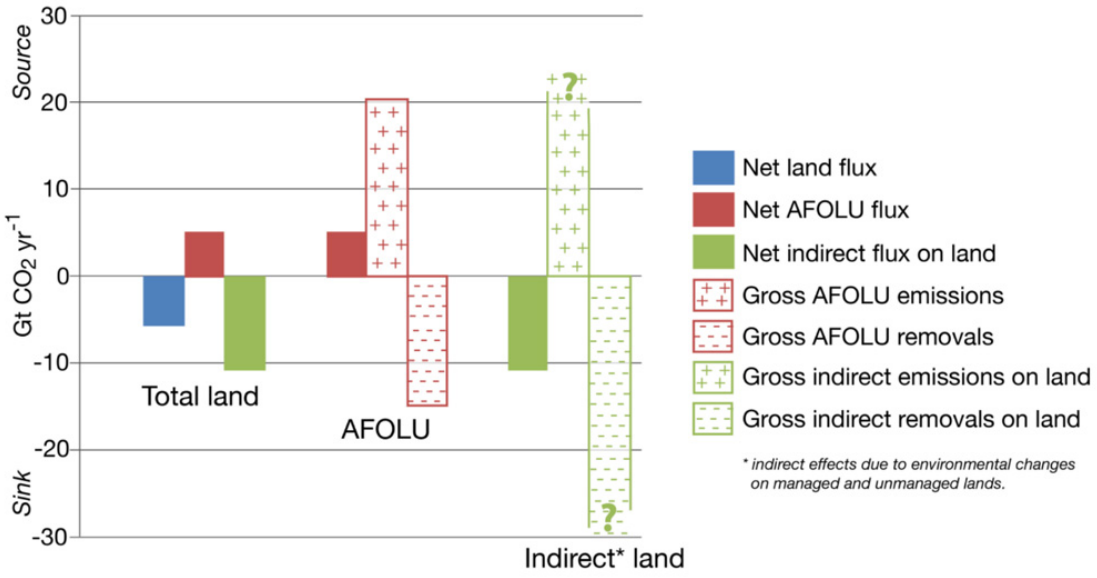

Figure 1.2: Net carbon emissions from the land (blue), human activity (agriculture, forestry and other land use, AFOLU; red) and 'indirect effects' of anthropogenic environmental change (e.g., climate change, increased atmospheric CO_2 concentration from forest degradation, nitrogen deposition) (green) for the period 2008-17. Taken from Figure 2.4 in IPCC (2019)

tropical forests in the face of climate change, and the current rates of deforestation, it is possible that tropical forests will reverse from being a carbon sink to a source of emissions. According to more recent studies, this has happened already in some years (Grace et al., 2014; Baccini et al., 2017; Gatti et al., 2021).

Contrary to deforestation, which occurs when a forest is converted to another land use, forest degradation results in the reduction of woody biomass or tree cover in areas that are still defined as 'forests' but that have experienced a significant loss of biological wealth (Joshi et al., 2015). According to the definition adopted by the United Nations Framework Convention on Climate Change (UNFCCC), a forest is an area of more than 0.05 - 1.0 hectares with a minimum canopy cover of 10–30%, and with the potential to reach a minimum tree height of 2-5 m at maturity (UNFCCC, 2002). The choice of parameters within these ranges varies by country, which makes the definitions of forest degradation and deforestation rather ambiguous: meaning a loss of canopy cover that would be deforestation in one country, could be degradation in another (Sasaki and Putz,

2009). The perception of what constitutes forest degradation also varies, independently of the forest definition (Ghazoul et al., 2015). In fact, carbon emissions from land-use and land-cover change, mainly driven by tropical deforestation and forest degradation, are the least certain major components of the global carbon cycle (Mitchard, 2018) (Figure 1.2). This is a consequence of many factors, including definitions, but more likely the use of different estimation methods and the difficulty of directly mapping the location of degradation (Harris et al., 2021). Most studies assessing the impacts of land-use change on tropical forest ecosystems have focused on deforestation, which is readily monitored with satellite imagery (Pearson et al., 2017). On the other hand, the rate and extent of forest degradation, which includes selective logging, understory fires and forest fragmentation, are challenging to detect and thus poorly understood (Gao et al., 2020). Forest degradation is typically measured by estimating changes in canopy cover, biomass, or annual productivity, as compared to intact and mature tree stems (de Andrade et al., 2017). Recent research has found that in the Brazilian Amazon and in the southern African woodlands forest degradation affects larger areas than deforestation, stressing the importance of including this type of disturbance in national monitoring and conservation efforts (McNicol et al., 2018; Matricardi et al., 2020; Qin et al., 2021; Beuchle et al., 2021). Since degradation often precedes deforestation, controlling the former may prevent the development of the latter (Joshi et al., 2015).

1.1.2 Measuring forest biomass

The main carbon pools in tropical forest ecosystems are the above ground biomass of trees (AGB), tree below ground biomass (BGB), and soil organic matter. AGB is normally the largest pool and is the one most directly impacted by deforestation and degradation, and the only one that can be estimated from space. Thus, it is a useful measure for quantifying changes in forest structure caused by deforestation or forest degradation (Brown and Nations, 1997). Scientific forest inventory plots are thought to provide the

most accurate data on the AGB of an area: these usually involve measuring the diameter at breast height (DBH), estimating tree height (directly or using a diameter-height model) and discerning the species of every tree with a DBH $>$ 10 cm (Brown and Nations, 1997; Phillips et al., 2001). AGB is then estimated from these measurements using either locally derived or standard allometric equations. Usually for tropical forests a pantropical equation is used, derived from 4004 destructively harvested trees from 58 sites (Chave et al., 2014):

$$\mathrm{AGB} = 0.0673 \times (\rho \times D^2 \times H)^{0.976} \tag{1.1}$$

where ρ (g cm^{-3}) is the wood specific gravity, D (cm) the trunk diameter at breast height and H (m) the tree height, either measured directly or inferred from a pantropical diameter-height model of the form:

$$H_{est} = a + a' \times E + b \times \ln(D) + c \times ln(D)^2 + \varepsilon \tag{1.2}$$

where a, a', b and c are coefficients derived from the best-fit model, E is a composite climatic index and ε is the error term, assumed to be normally distributed with zero mean and standard error σ (Chave et al., 2014).

Forest inventory plots will typically be biased towards more easily accessible regions and, due to time constrains, will only be able to sample a very small percentage of the total forest area (Rodríguez-Veiga et al., 2017). Despite the progress in AGB mapping and allometric models, uncertainties still remain important, especially for tropical forests (Mitchard et al., 2013a, 2014). The main sources of uncertainties in inventory-based estimates of AGB come from measurement and reporting errors, bias in the location of the sample plots and the choice of allometric functions (Hill et al., 2013). Assuming a regional height-diameter model (Eq. 1.2), the error term in the pantropical equation typically accounts for an uncertainty in AGB of $\pm$20-30% at a 1 ha plot level (Chave et al., 2004). When producing maps of AGB on a regional scale, it may be assumed that

with enough data points these errors would cancel out and averages could be calculated with better accuracy. This is not the case for AGB, since the main source of uncertainty is due to regional biases in the allometric equation, which do not reduce with averaging (Feldpausch et al., 2012).

1.1.3 Satellite remote sensing

Thanks to the large-scale coverage and the frequent revisit times, satellite imagery provides the ideal solution for scaling up AGB estimates from a network of ground plots to regional or country scales (Li et al., 2020). Different methodologies have been progressively developed to detect and map forest change, by using multi-spectral optical, Synthetic Aperture Radar (SAR) and/or Light Detection and Ranging (LiDAR) data. However, none of these sensors is able to measure AGB directly (Woodhouse et al., 2012). Instead, regression models are used to compare the remote sensing variable, such as vegetation indices, radar backscatter or canopy height, to AGB values measured on the ground (Rodríguez-Veiga et al., 2017).

Optical-based methods

Multispectral optical remote sensing data are abundant and relatively easy to obtain from various open data platforms, such as the Landsat time series, the Moderate Resolution Imaging Spectroradiometer (MODIS) or the Copernicus (EU funded) Sentinel-2 mission, operated by the European Space Agency (ESA). Numerous studies have demonstrated the ability of optical medium and high resolution satellite imagery to map changes in tropical forest cover (Margono et al., 2012; Potapov et al., 2012; Hansen et al., 2013; Souza et al., 2013; Achard et al., 2014; Wheeler et al., 2018; Puliti et al., 2021; Pacheco-Pascagaza et al., 2022). Unfortunately, all these methods are restricted to cloud-free conditions as they are based on optical sensors. This can be particularly problematic in tropical regions, where cloud-free imagery over forests is rare (Asner, 2001). Biomass

and leaf area are typically estimated using band-derived vegetation indices (Rodríguez-Veiga et al., 2016; Othman et al., 2018; Lin et al., 2021), but they tend to saturate at or soon after canopy closure, limiting their ability to provide useful data in closed-canopy forests (Huete et al., 1997).

SAR-based methods

The spatial resolution of radar data is limited by the altitude of the satellite and the length of the antenna. Therefore, the longer the antenna, the higher the image resolution. A Synthetic Aperture Radar (SAR) is a radar system mounted on an aircraft or spacecraft platform where the motion of the radar antenna along the flight path is used to reproduce (or *synthesise*) a long antenna with finer resolution. In essence, modern SAR systems allow to overcome the technical limitations of building very large antennas: the series of acquisitions at multiple locations along the flight track are combined to simulate a much larger antenna, allowing to measure objects at meter-scale resolutions (Figure 1.3). SAR has a major advantage compared to optical systems: it penetrates through clouds and is immune to many atmospheric effects (de Souza Mendes et al., 2019). Unlike optical sensors that only interact with the top of the canopy, SAR signal penetrates into the forest and has been related to forest structure and woody biomass (Woodhouse et al., 2012), up to a saturation threshold (Imhoff, 1995; Joshi et al., 2017). Because of its long wavelength (15.0 cm$\approx$30.0 cm), L-band SAR penetrates the forest canopy capturing backscattering from branches and trunks. In contrast, the shorter wavelength (3.8 cm$\approx$7.5 cm) of C-band SAR can only partially penetrate the crown thickness and mainly interacts with foliage and small branches (Le Toan et al., 1992) (Figure 1.4). Previous studies have used L-band SAR data to monitor land-use change and detect disturbances resulting specifically from degradation (Mitchard et al., 2011b; Ryan et al., 2012; Mitchard et al., 2013b). Despite its advantages, SAR sensors pose interpretation issues caused by intrinsic sensor noise (speckle) and the complicated physics involved in the backscatter process. Longer wavelength SAR imagery can be expensive and

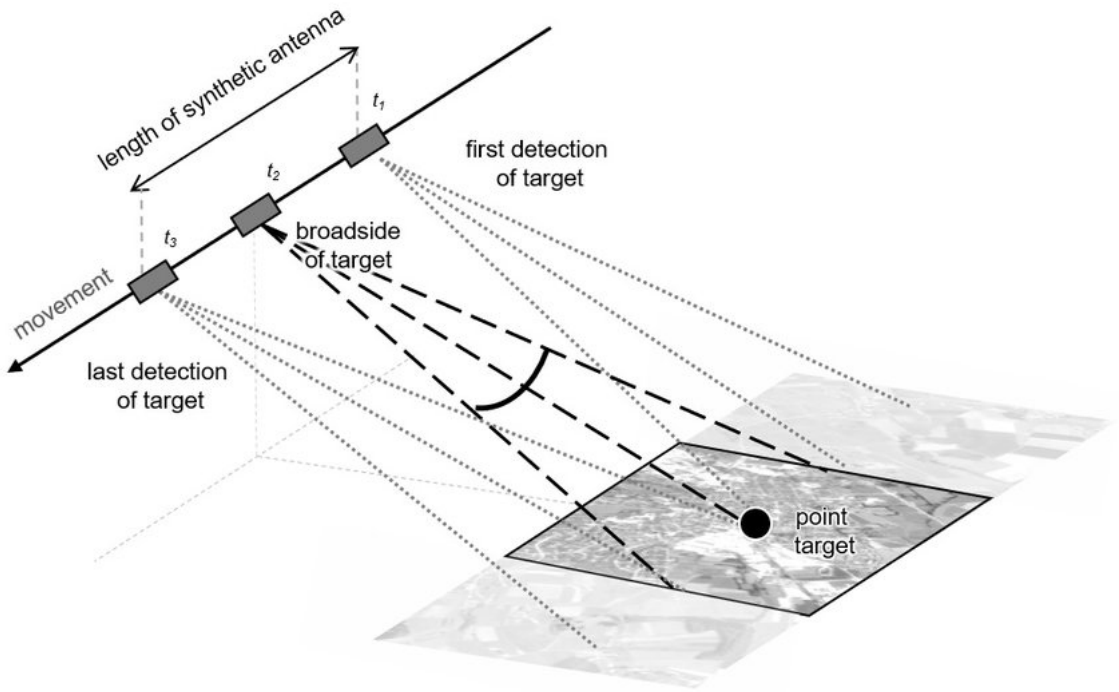

Figure 1.3: Principle of the Synthetic Aperture Radar (SAR). Taken from Figure 12 in Braun (2019)

available only for limited timeframes. However, recent studies have demonstrated that the short revisit times and the high spatial resolution of ESA's Sentinel-1 mission can overcome the limitations of C-band signal, successfully detecting tropical degradation (Reiche et al., 2018a,b; Bouvet et al., 2018b; Hirschmugl et al., 2020; Reiche et al., 2021; Ballère et al., 2021). These results, in addition to the upcoming launch of the P-Band (30.0 cm≈100 cm) BIOMASS mission in 2023, make the prospect of mapping forest disturbances through SAR data very promising (Quegan et al., 2019).

LiDAR-based methods

LiDAR detection is able to quantify vertical forest structure at the tree level and detect forest change, when repeat measurements are available (Dubayah et al., 2010; Meyer et al., 2013). Tree height and other LiDAR metrics have been used to measure forest biomass, without saturation at higher biomass values (Lefsky et al., 2005). Unfortunately,

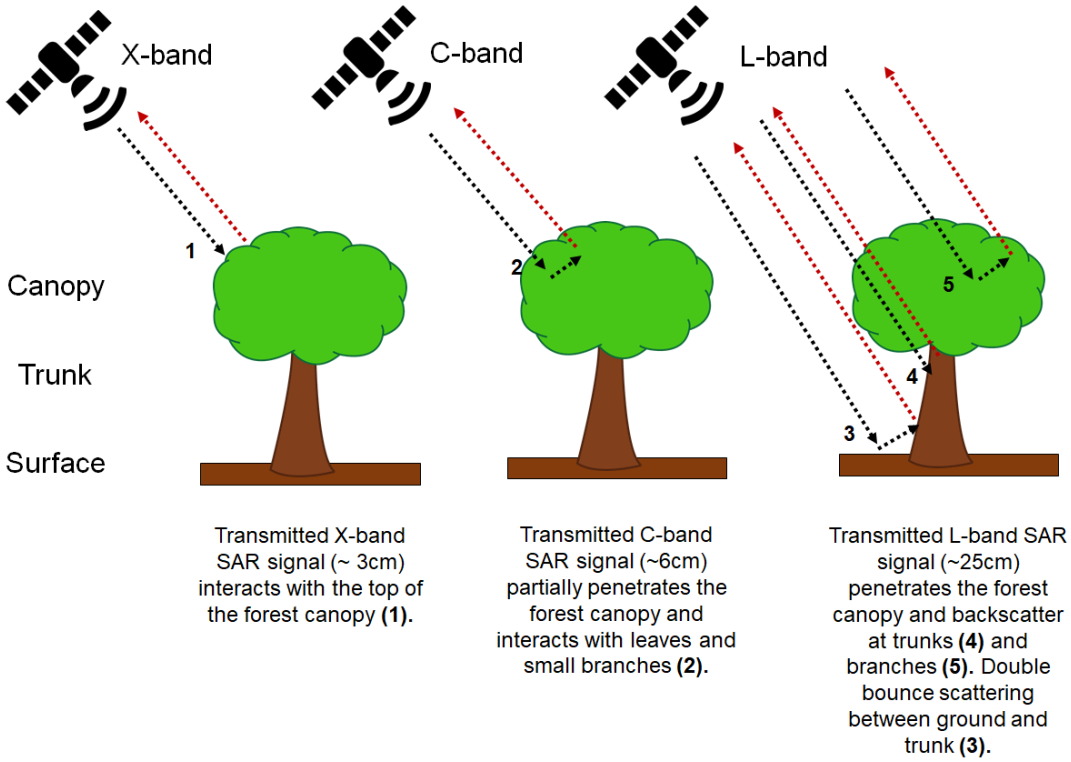

Figure 1.4: Basic interactions of X-band, C-band and L-band SAR remote sensing over tropical forest.

airborne LiDAR sensors are expensive, although they are very useful in combination with other remote sensing datasets (Saatchi et al., 2011; Baccini et al., 2012) and for calibration/validation purposes in absence of forest inventory ground data (Rodríguez-Veiga et al., 2017). The Global Ecosystem Dynamics Investigation (GEDI) mission, launched at the end of 2018, is a spaceborne LiDAR system designed to produce data on forest structure and AGB density (Hancock et al., 2019). It provides discrete 25 m footprints of vegetation structure, sparsely distributed over ≈4% of Earth's land surface over the four year mission (Dubayah et al., 2020). Very recently, GEDI has been deployed alone or in combination with optical/SAR data to produce biomass estimates at the regional and global scale (Silva et al., 2021; Dubayah et al., 2022; Francini et al., 2022) (Figure 1.5).

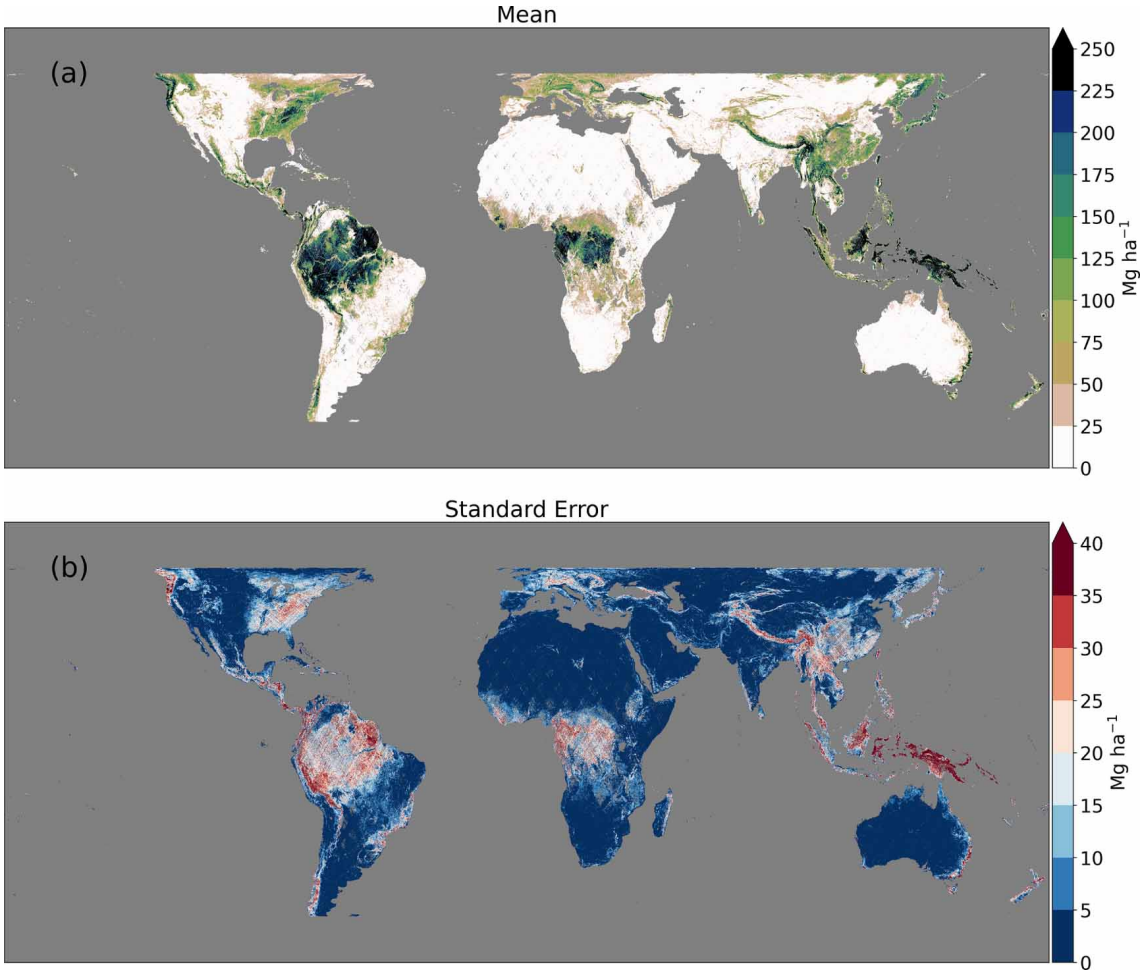

Figure 1.5: Maps of (a) mean above ground biomass density (AGBD) and (b) standard errors at 1 km resolution derived from 25 m GEDI footprints collected between April 2019 and August 2021. Taken from Figure 1 in Dubayah et al. (2022)

1.1.4 AGB change maps

Forest biomass maps have multiple sources of uncertainties that can be accumulated and propagated through modelling or mapping processes (Lu et al., 2016). First, when using field-measured AGB to calibrate the satellite observation, the error in the allometric equation propagates to the parametric function relating AGB to the remote sensing variable. Additionally, satellite measurements carry their own systematic errors, such as spatio-temporal decorrelations between data sources, geolocation errors and random

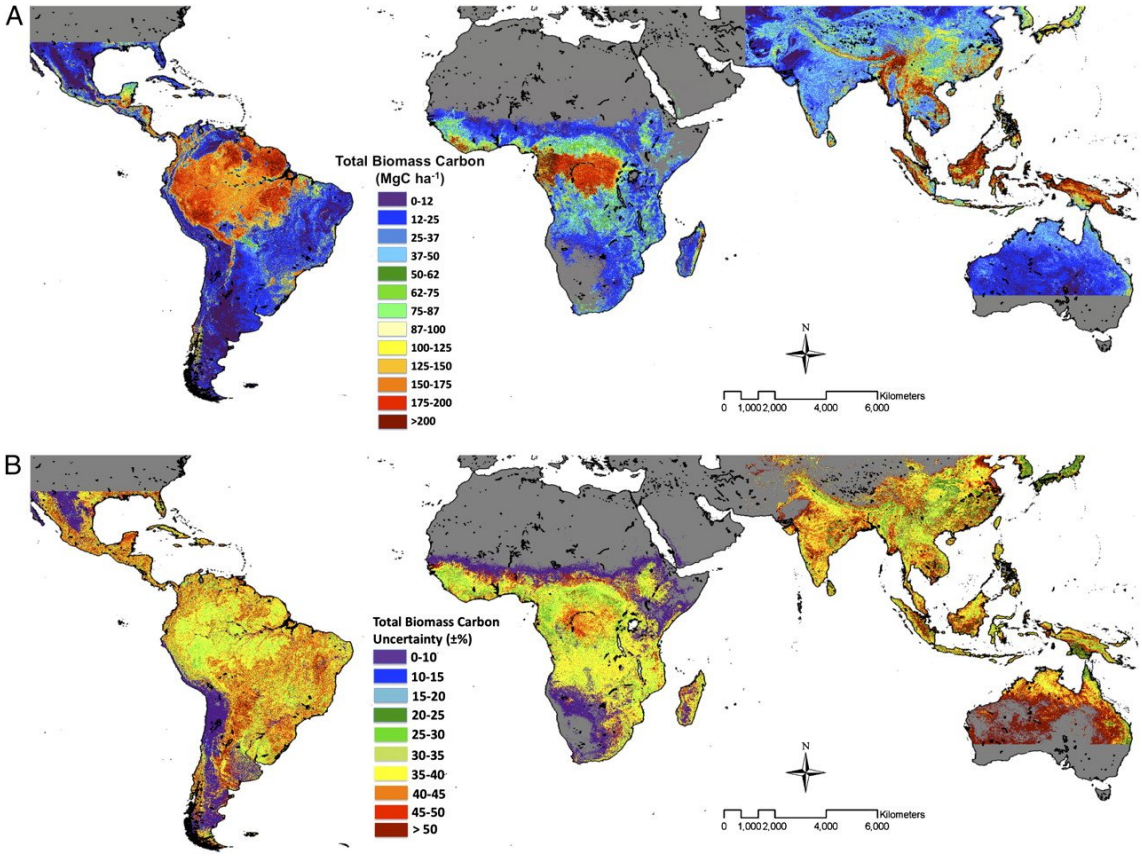

Figure 1.6: Benchmark map of (A) carbon stocks and (B) uncertainty. Carbon is estimated as 50% of total biomass (AGB + BGB). Taken from Figure 3 in Saatchi et al. (2011)

noise in the satellite imagery (Réjou-Méchain et al., 2019). These errors will not cancel with averaging and usually add another $\pm$10-20% on the AGB estimates (Hill et al., 2013). This is why AGB maps have large uncertainties, for example up to $\pm$50% on a 1 km pixel scale (Figure 1.5, Figure 1.6).

When creating maps of AGB change, one-time maps of AGB are produced and then differenced between two time points. Subtracting two such maps results in a product with a high, undetermined uncertainty. Maps of AGB change are rare and they are not usually validated by repeat measurements from ground points (McNicol et al., 2018). If the validation is performed by resampling standard inventory plots, the change in biomass is not significant enough to account for the degradation event, and thus it is hard to detect at coarser scales (Mitchard et al., 2013a; Réjou-Méchain et al., 2015). Although many

change detection algorithms have been developed to monitor forest dynamics, few can be used to estimate biomass change directly (Bollandsås et al., 2013; McRoberts et al., 2015; Amarnath et al., 2017; Poudel et al., 2018). This approach requires experimental data of forest biomass change, where the location, magnitude and timescale of the disturbance event are known with high accuracy.

1.2 Background to the thesis

The work presented in this thesis is part of the tropical Forest Degradation Experiment (FODEX), a 5-year ERC-funded project aiming at providing high quality data and novel methodologies for mapping forest degradation (McNicol et al., 2021a). In particular, FODEX established the first network of experimental biomass change plots across two distinct tropical ecosystems, located in logging concessions in Gabon and Peru. Within each plot, a subset of trees was removed through logging, giving different levels of forest degradation. Trees were measured before and after logging using standard forest inventory protocols (Phillips et al., 2001) (Figure 1.7). Additionally, high-resolution data was collected using a Terrestrial Laser Scanner (TLS) operated by collaborators from University College London, giving digital 3-D models of every tree in the plot. Another set of high quality data was retrieved by a LiDAR sensor mounted on a project-owned Unoccupied Aerial Vehicle (UAV) (Figure 1.8). High-resolution (240 points per m^2) aerial LiDAR data was collected over the forest concessions to retrieve accurate tree structure information in absence of TLS measurements. Tree reconstruction methods derived from LiDAR metrics allowed the development of canopy height models (CHM) at 25 cm spatial resolution (McNicol et al., 2021b), which were used to calibrate the satellite data and build AGB change maps at the regional and national scale. Using fused datasets (TLS, LiDAR, field inventory) and a multi-sensor approach (including both airborne and space-borne systems), this research aimed to develop new algorithms and methodologies to detect tropical forest degradation at the finest scale.

Figure 1.7: Forest inventory measurements in selectively logged plots in Gabon (left) and Peru (right). Image credit for Gabon: Harry Carstairs. Image credit for Peru: Beisit Luz Puma Vilca.

1.3 Data collection

The field data analysed in this thesis were collected by me and my FODEX colleagues over the course of four measurement campaigns, two for each study country. A timeline of the field campaigns is shown in Figure 1.9. In Peru, international travel bans following the spread of Covid-19 did not allow the collection of post-logging TLS data, and delayed the second part of the UAV LiDAR measurements to September 2021.

1.3.1 Forest inventory

The methods described in this section are based on the FODEX field inventory manual (McNicol, 2018), which follows RAINFOR protocols for establishing and measuring forest inventory plots (Phillips et al., 2001).

Figure 1.8: (Left) data collection with UAV LiDAR. (Right) example of a canopy gap following selective logging in one of the field plots in Gabon. Image credit: Harry Carstairs.

Plot location and setup

For each study site, four permanent sample plots were established on flat ground and in forested area that was homogeneous in terms of topography, soil type, vegetation structure and human activity (e.g., presence of logging). The plots were located between 20 to 300 m from the road and within 10 km of the UAV launch site. During the course of the project, the plots were expected to be logged to some degree, but not permanently cleared or modified for another land-use. The choice of the area was also determined by the presence of valuable tree species. The removed trees were destined to local construction projects or sold by the logging company for commercial purposes. After identifying a suitable location, the following steps were taken to delimit each plot:

(i) By choosing a compass bearing and measuring tape, the four corners of the plot were marked using 1 m rebar poles wrapped around the top in multi-coloured flagging tape. The start point, coded as “1.(0, 0)” in Figure 1.10, was located at the bottom-left, Southwest corner of the plot.

(ii) The plot edges were marked by placing rebar poles every 10 m along the X (North-South) and Y (East-West) axes. Yellow flagging tape was used for the X direction and orange flagging tape for the Y direction.

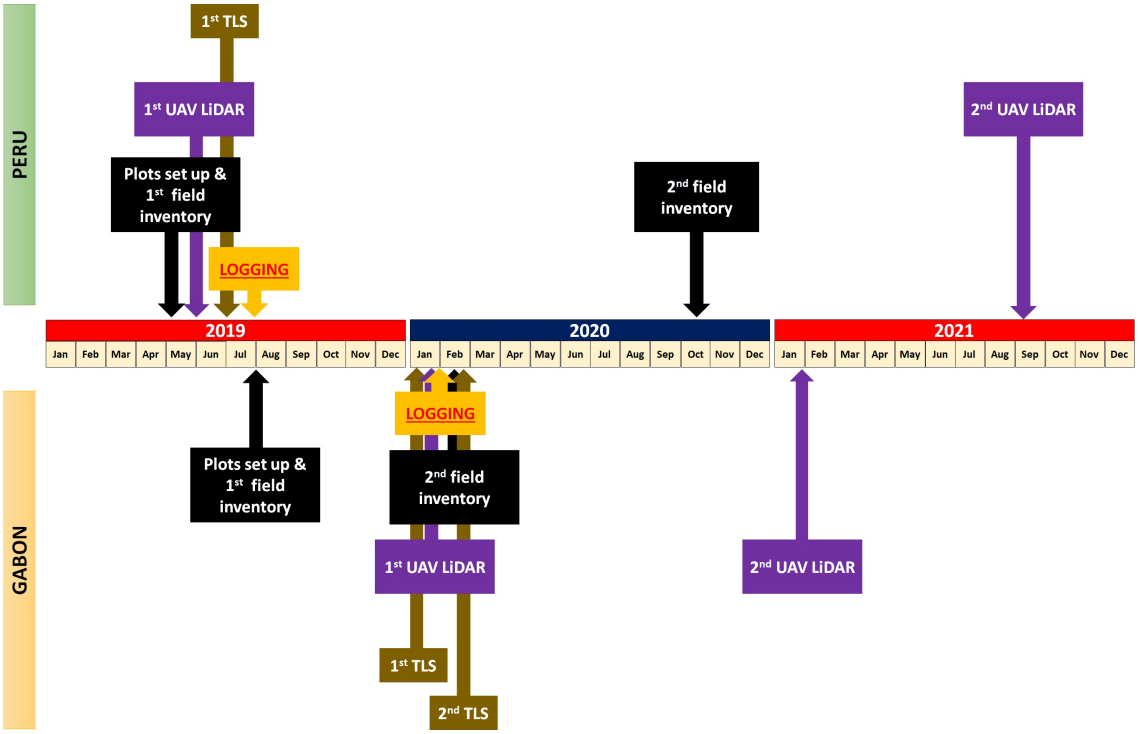

Figure 1.9: Timeline of the field measurement campaigns in Peru and Gabon.

(iii) Rebar (steel) poles wrapped in white flagging tape were placed every 10 x 10 m throughout the 1 ha plot to mark the location of the TLS captures, but they were also handy for internal orientation (Figure 1.10).

(iv) A handheld GPS was used to get an approximate location of each corner post, although its precision was limited by the presence of a thick forest canopy ($\approx$ 2 – 5 m).

(v) The plot data sheet was completed by including the GPS coordinates of the plot corners and the bearing (in degrees) of the (0,0) start point.

Once the plot was ready to be sampled, coloured 100 m strings were placed around the plot boundaries to help re-locate the plot at the start of each day's sampling. The strings also helped to determine which trees fell inside or outside of the plot. The forest inventory was carried out in subplots of 20 m x 20 m in size, so that no trees were missed. All trees with DBH $>$ 10 cm were tagged using aluminium tags and nails so they could be easily

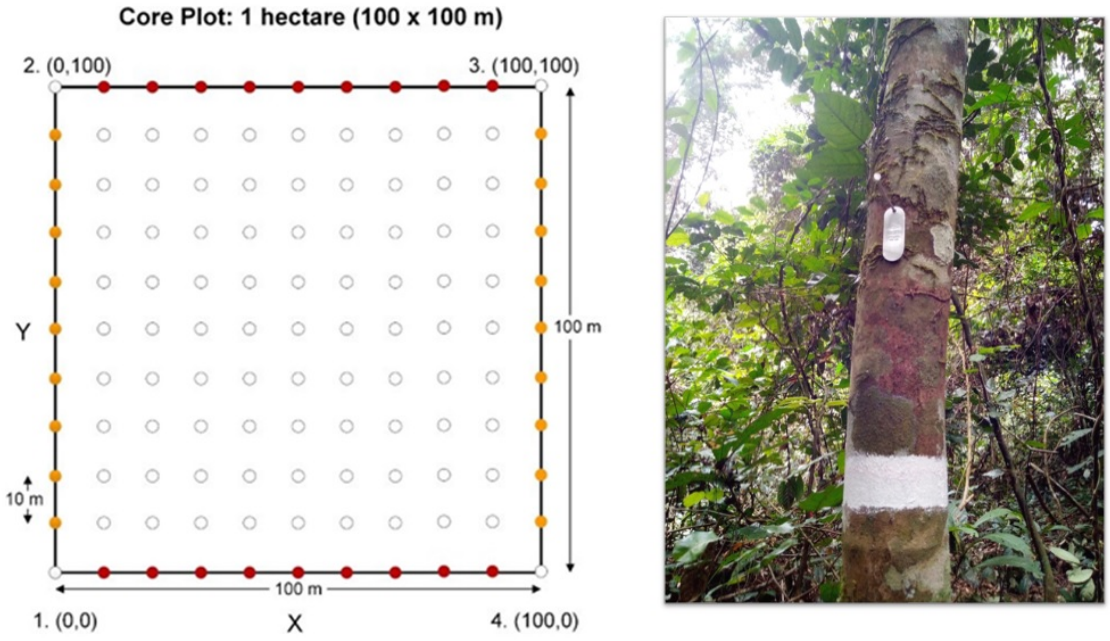

Figure 1.10: (Left) schematic of 1 hectare plot, showing the location of the boundary poles (coloured circles) and the TLS markers placed every 10 m x 10 m inside the plot (white circles). Taken from McNicol (2018). (Right) tree stem tagged and marked for remeasurement.

re-found. The point of measurement, or POM, is set at 1.3 m and clearly marked using white paint (Figure 1.10). DBH, local species and X and Y location relative to the start point were recorded on the data sheet for all the trees in the plot, along with damage classes, if necessary.

Plot re-inventory

Following the first measurement campaign, different proportions of forest biomass were removed by the logging contractor from each plot using selective logging methods. The post-logging field campaign focused on relocating the plots and re-measuring all the remaining trees. This included the census of the new recruits that reached critical DBH ($>$ 10 cm) in between the two field campaigns (Figure A.3). Particular care was taken to record all information that could aid assessing the logging damage, such as the direction of tree felling and the number of surrounding stems that were damaged or killed as a result of the logging operations (Figure A.2).

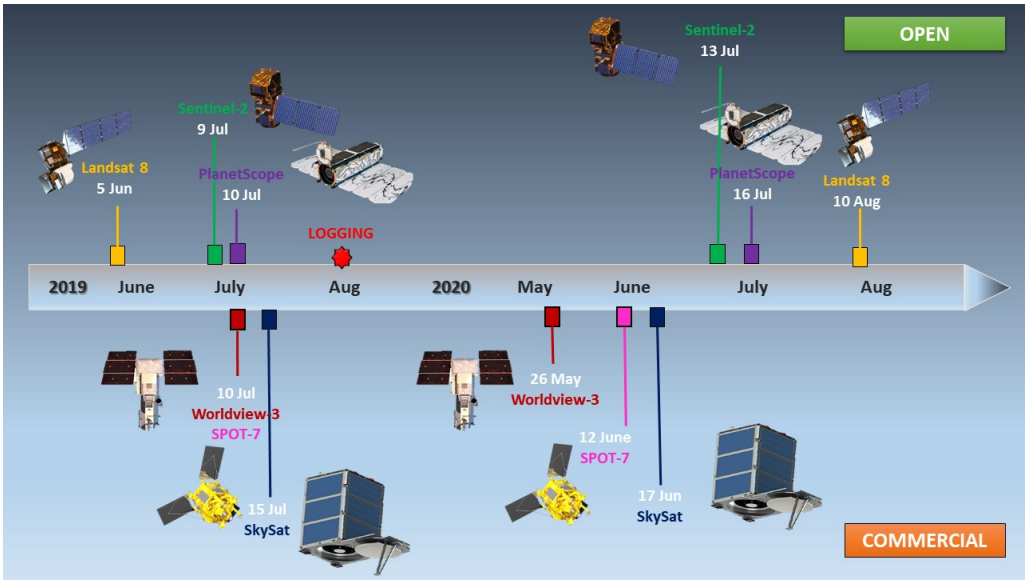

Figure 1.11: Acquisitions of optical satellite data over the field site in Peru before and after logging.

Region	Type	Acquisition	Provider	Sensor	Resolution
Peru	Optical	Commercial	Digital Globe	WorldView-3 *	0.3 m
Peru	Optical	Commercial	Planet Labs	SkySat	0.8 m
Peru	Optical	Commercial	Airbus	SPOT-7 *	1 m
Peru	Optical	Commercial **	Planet Labs	PlanetScope	3 m
Peru	Optical	Open	ESA	Sentinel-2	10 m
Peru	Optical	Open	USGS	Landsat 8	30 m
Peru, Gabon	SAR	Open	ESA	Sentinel-1	10 m

** Only collected on request.*
*** Non-commercial access through Planet's Education and Research Program (Planet Labs, 2021) or the NICFI Program (Norway, 2021).*

Table 1.1: List of satellite remote sensing data used in this study.

1.3.2 Satellite remote sensing data

Persistent cloud cover over the field site in Gabon did not allow the acquisition of good quality optical satellite imagery. In Peru, it was possible to collect free and commercial optical data from six multispectral sensors, with spatial resolutions in the range of 0.3 - 30 m (Figure 1.11). Very high resolution imagery, such as SkySat and WorldView-3, was specifically tasked by me over the field site. As for SAR imagery, C-band Sentinel-1 data were acquired free-of-charge over both study sites (Table 1.1).

1.4 Thesis objectives and key questions

The objective of this thesis is to link field measurements of selective logging to the satellite observations, to calibrate biomass change as observed in the satellite data with the physical change measured in the field. By knowing the exact magnitude and duration of the change, statistical relationships can be developed without the uncertainty due to the temporal decorrelation between disturbance events. The change detection methods will then be adopted to produce maps of AGB change at the regional and country scale. In particular, the thesis addresses the following research questions:

1. Can we detect small-scale forest disturbances in dense, multi-storied tropical forests using optical remote sensing data?
2. To overcome the limitations of optical imagery and improve detection accuracy, can we measure disturbances in high-biomass forest with Sentinel-1 C-band SAR data?
3. Can we generalise change detection methods from the local to the country scale, to derive accurate forest disturbance maps for monitoring AGB change?

The thesis comprises five chapters. Chapter 1 provides the background to the thesis and discusses the importance of the research in the context of climate change and current knowledge gaps. The next three chapters are designed as stand-alone publications: at the time of submission, one is undergoing peer-review (Chapter 2), one is published (Chapter 3) and another one is ready for submission (Chapter 4). Each chapter answers one of the three above mentioned research questions. Chapter 5 summarises the results and discusses the applications of the developed methodologies, as well as limitations and further research directions.

Chapter 2: Detecting tropical forest degradation using optical satellite data: an experiment in Peru show texture at 3 m gives best results

In the humid tropics, existing forest monitoring products are capable of detecting large-scale deforestation, but forest degradation due to selective logging and other small-scale disturbances is largely missed. The aim of this paper is to test the ability of six optical satellite sensors (0.3 – 30 m spatial resolutions) to detect selective logging in our field sites in Peru. In particular, I address the following questions:

- What is the best combination of optical sensor and remote sensing parameter to detect biomass change?
- How do optical sensors at different resolutions compare in their ability to detect biomass change?
- When using image texture as a change detection method, what are the optimum characteristics to detect forest degradation?

Chapter 3: Reliably mapping low-intensity forest disturbance using satellite radar data

Using optical data to monitor forest loss across the tropics can be severely limited by the lack of available cloud-free imagery. Continuous time series from the Sentinel-1 mission can offer a solution to this problem; however, new methodologies need to be developed to overcome the limitations of C-band SAR in high-biomass forests. In this paper, a cumulative sum (CuSum) change detection method is calibrated and tested for the first time on Sentinel-1 data, and using ground measurements of forest disturbance in two different tropical ecosystems. This paper advances the following hypotheses:

- Temporally dense and high-resolution data from C-band SAR can accurately map small-scale forest disturbances when using a CuSum change detection method.
- A single change metric can be developed from the CuSum algorithm providing information on location, timing and magnitude of the disturbance events.

- Compared to other forest monitoring products, the CuSum method maps small-scale forest disturbances with higher spatial accuracy.

Chapter 4: 2020 forest disturbance maps for Gabon and Peru at 10 m resolution

Despite recent advances in forest monitoring technology, there is a critical need for accurate maps showing selective logging and other small-scale forest disturbances at the country level. These products need to be free, open and reproducible to allow forest conservation plans to be reinforced by a variety of actors, including local communities and NGOs. Given this, the paper addresses the following questions:

- Is it possible to develop a processing workflow for Sentinel-1 data to scale up results from the local to the national scale, using free/open software and datasets?
- When small-scale disturbances are included, what is the total area of forest loss for Peru and Gabon?
- How do results compare with other available deforestation and degradation maps?

Chapter 2

Detecting Tropical Forest Degradation Using Optical Satellite Data: An Experiment in Peru Show Texture at 3 m Gives Best Results

C. Aquino[a], *E. T. A. Mitchard*[a], *I. M. McNicol*[a], *H. Carstairs*[a], *A. Burt*[b], *B. L. Puma Vilca*[c], *S. Mayta*[d] *and M. Disney*[b]

[a] *School of Geosciences, University of Edinburgh, Edinburgh, United Kingdom*

[b] *Department of Geography, University College London, London, United Kingdom*

[c] *Escuela Profesional de Biología, Universidad Nacional de San Antonio Abad del Cusco, Cusco, Perú*

[d] *Asociación para la Investigación y Desarrollo Integral, Lima, Perú*

Modified version of a paper submitted to *Remote Sensing in Ecology and Conservation* and currently undergoing peer-review, August 2022

This paper has undergone two rounds of peer-review at *Remote Sensing* during February-April 2022 and was rejected.

Author contribution: C.A. conducted the analysis and wrote the manuscript under the supervision of E.T.A.M.; C.A., I.M., H.C., A.B and B.P.V collected the field data; S.M., B.P.V and M.D. provided resources; E.T.A.M. obtained the funding. All authors reviewed the manuscript.

Abstract

Forest degradation is known to be widespread in the tropics, but is currently very poorly mapped, in part because there is little quantitative data on which satellite sensor characteristics and analysis methods are best at detecting it. To improve this, we used data from the Tropical Forest Degradation Experiment (FODEX) plots in the southern Peruvian Amazon, where different numbers of trees had been removed from four 1 ha forest plots, carefully inventoried by hand and Terrestrial Laser Scanning before and after the logging to give a range of biomass change (ΔAGB) values. We conducted a comparative study of six multispectral optical satellite sensors at 0.3 – 30 m spatial resolution, to find the best combination of sensor and remote sensing indicator for change detection. Spectral reflectance, the Normalized Difference Vegetation Index (NDVI) and texture parameters were extracted after radiometric calibration and image preprocessing. The strength of the relationships between the change in these values and field-measured ΔAGB (computed in % ha^{-1}) was analysed. The results demonstrate that: (a) texture measures correlates more with ΔAGB than simple spectral parameters; (b) the strongest correlations are achieved for those sensors with spatial resolutions in the intermediate range (1.5 - 10 m), with finer or coarser resolutions producing worse results, and (c) when texture is computed using a moving square window ranging between 9 - 14 m in length. Maps predicting ΔAGB showed very promising results using a NIR-derived texture parameter for 3 m resolution PlanetScope (R^2 = 0.97 and RMSE = 1.91 % ha^{-1}), followed by 1.5 m SPOT-7 (R^2 = 0.76 and RMSE = 5.06 % ha^{-1}) and 10 m Sentinel-2 (R^2 = 0.79 and RMSE = 4.77 % ha^{-1}). Texture models derived from 0.3 m WorldView-3 improved with increasing window size, with highest R^2 of 0.59 and RMSE = 6.65 % ha^{-1} for a window of 14 m in length. The degradation in our field plots is invisible to the 30 m resolution Landsat data. Our findings imply that, at least for lowland Peru, low-medium intensity disturbance can be detected best in optical wavelengths using a texture measure derived from 3 m PlanetScope data.

2.1 Introduction

Tropical forests play a complex and essential role in modulating the global climate system by removing carbon dioxide from the atmosphere through photosynthesis. They are home to a rich biodiversity and provide an essential source of livelihood and socio-cultural identity to local communities. However, pressures from extractive industries, commodity-driven agricultural expansion and fires are increasingly threatening the integrity of these forests (Austin et al., 2017; Gao et al., 2020). As a result of factors such as deforestation, forest degradation and climate change, the ability of tropical forests to sequester atmospheric carbon might be reduced or reversed in the near future (Gatti et al., 2021; Mitchard, 2018). Contrary to deforestation, which occurs when a forest has sufficient trees removed that it no longer meets the local definition of forest (Nabuurs et al., 2003), degradation is harder to define (Joshi et al., 2015). In general, forest degradation is considered to occur when humans cause partial deforestation, with more than 10–30% of forest cover remaining (Houghton, 2012). Half of tropical forest degradation is thought to be driven by selective logging, followed by fuelwood and charcoal production, fires and livestock grazing (Hosonuma et al., 2012). Studies aiming at quantifying the carbon emissions and extent of degradation show that it is diffuse across the tropics and affects land portions similar to, or even larger, than deforestation (Qin et al., 2021; Matricardi et al., 2020). Since degradation precedes deforestation, controlling the former may prevent the development of the latter (Joshi et al., 2015). Monitoring forest degradation while protecting existing old-growth, natural forests, has longer term climate and ecological benefits than planting new trees (Windisch et al., 2021; Duguma et al., 2020; Lewis et al., 2019; Moreno-Mateos et al., 2017; Matricardi et al., 2020), typically when forest lands are managed collectively (Sze et al., 2021; Gregorio et al., 2020; Rights and Resources Initiative, 2018; Santika et al., 2017; Chhatre and Agrawal, 2009) and the social drivers of deforestation are addressed (Fleischman et al., 2020). It is worth noting that the monitoring effort should not imply the commodification

of carbon stocks (Stephan, 2012; McAfee, 2012). An abundant literature has shown that market-based mechanisms reinforce exclusionary politics, such as the centralization of forest tenure and the exclusion of certain actors, practices, knowledge and claims to resources (Magessa et al., 2020; Plumb et al., 2012; Asiyanbi et al., 2017; Bayrak and Marafa, 2016; Bassey, 2015), which in turn exacerbates forest loss (Asiyanbi et al., 2017; Poudel et al., 2015). Addressing deforestation and forest degradation requires trade-offs between economic, ecological and social dimensions (Nielsen, 2014) and the recognition of the political and power dimensions behind the interventions; an aspect that carbon finance, with its unidimensional approach to forest management, tends to overlook, to the detriment of forests and forest-dependent communities (Johnson, 2021).

While it has been possible to map deforestation even with moderate resolution (30 – 250 m) satellite imagery (Hansen et al., 2013; Wheeler et al., 2018), disturbances at finer scales, as those caused by selective logging or other degradation processes, remain challenging to detect (Gao et al., 2020). High resolution optical data (e.g., WorldView-3) are cost prohibitive and are not always immediately available in all regions. On the other hand, Synthetic Aperture Radar (SAR) systems do not perform well in dense canopies due to biomass saturation effects (Lu, 2006). Airborne LiDAR has now gained widespread adoption in forestry applications because of its ability to produce 3D point clouds with centimeter accuracy (Mlambo et al., 2017; McNicol et al., 2021b; Kellner et al., 2019; Brede et al., 2019). However, LiDAR collection campaigns are very expensive and data availability is drastically limited in space and time (Filippelli et al., 2019).

In the last decade, the progressive release of remote sensing data that is both temporally dense and high-resolution ($\leq$10 m) has opened new frontiers for mapping and monitoring changes in forest cover in usually remote and inaccessible areas. The use of dense time series to detect forest disturbance events is particularly important in the tropics, as rapid vegetation turnover can remove the transient signs of the disturbance events rapidly (Shimizu et al., 2019), and cloud cover often masks images, meaning that many

attempts may be necessary before the trees are seen from space. Freely available, high-resolution optical multispectral imagery from the European Space Agency (ESA)'s Sentinel-2 mission and the monthly PlanetScope image mosaics - available across tropical forest areas only (Norway, 2021) - allow for unprecedented monitoring of forest loss at frequent time intervals and at minimum costs. While these satellite datasets are at a 3-4 m and 10 m resolution respectively, commercial satellite data at higher resolutions (up to 0.3 m) are available on request, and there remains a long archive of 30 m resolution Landsat imagery which, if suitable for mapping degradation, would open up a long and consistent record of forest disturbance. However, it is unclear which of these datasets, if any, is suitable for mapping forest degradation. Hence, there is an increasing necessity of matching satellite observations against ground truth data, showing the exact magnitude and location of forest loss and thus reducing the critical uncertainties in biomass change estimates (Hill et al., 2013).

The Normalized Difference Vegetation Index (NDVI) is one of the most widely used indices for estimating tree aboveground biomass (AGB). NDVI is computed from the ratio of the near-infrared (NIR) and red spectral bands. For healthy vegetation, the presence of chlorophyll pigments causes a strong absorption in the red band, while the internal leaf structure results in high reflectivity in the NIR. Therefore, healthy, dense canopy cover tends to have a high NDVI value, while degradation of ecosystem vegetation such that trunks, branches or the soil can be seen, or a decrease in the density of green vegetation, would result in lower NDVI (Somvanshi and Kumari, 2020; Othman et al., 2018). Unfortunately, NDVI saturates in regions of high forest biomass, partially due to the low 'penetrating' capability of the red band (Huete et al., 1997). As multiple layers of leaves are not entirely visible to the sensor, forests do not necessarily increase their canopy density as they become taller. In addition to this, biomass estimation methods based only on spectral information are complicated by the presence of canopy shadowing from large stands and the heterogeneity of forest stand structures (Sader et al.,

1989). Biomass estimation methods based on ratios and vegetation indices have proven to be more successful in temperate and boreal forests, where canopy cover is more sparse and there is less species diversity. In tropical and subtropical regions, with high biomass levels and multi-storied forest canopies, and where there is a greater diversity of tree species, vegetation indices have not been as effective at predicting forest biomass, generally with low or insignificant results (Nichol and Sarker, 2011; Lu, 2005).

If changes in direct reflectance, or vegetation indices, are unlikely to show subtle degradation, it is possible that changes in the texture of reflection or index patterns will show after disturbance. The texture of images has shown potential for overcoming the existing problems with biomass saturation (Eckert, 2012), both in optical and SAR images (Cutler et al., 2012; Nichol and Sarker, 2011; Kuplich et al., 2005; Luckman et al., 1997; Marceau et al., 1990), and thus it would follow that the same could be true for biomass change. Formally, texture analysis is an image processing technique that measures the variability in pixel intensity among neighboring pixels within a window of fixed size (Eckert, 2012). It contains information on the structural and geometric properties of forest canopies (De Grandi et al., 2009). However, most of the previous texture-based biomass estimation methods have used medium resolution images, such as the 30 m resolution Landsat TM data (Kelsey and Neff, 2014; Lu, 2005), with fewer studies employing higher resolutions datasets (Eckert, 2012; Nichol and Sarker, 2011). Texture metrics derived from finer spatial resolutions is expected to correlate better with field data, as the pixels will not mix several large canopies (which likely have diameters in the 10-30 m range) (Kuplich et al., 2005; Tuominen and Pekkarinen, 2005; Boyd and Danson, 2005; Puissant et al., 2005; Franklin et al., 2000). So far, texture-based biomass models have been developed to produce one-time maps of forest biomass (Kelsey and Neff, 2014; Eckert, 2012). In order to determine forest gains and losses, two such maps need to be subtracted from each other (Hansen et al., 2013; Margono et al., 2012). The uncertainty on the final product is computed from the propagation of the combined

uncertainties of the two static maps, which means that errors at the pixel level can be very large (Saatchi et al., 2011; Mitchard et al., 2013a). Considering that forest degradation is a dynamic process, one way to reduce these uncertainties might involve deriving a single regression model on the difference images (Bollandsås et al., 2013; McRoberts et al., 2015; Poudel et al., 2018). This approach requires experimental data of biomass change (ΔAGB) to derive the model, where the size and timeframe of the disturbance is precisely known.

This study makes use of field data of ΔAGB, collected in forest inventory plots where tree biomass loss has been determined through experimentally controlled logging of different intensities, and links it to the before/after logging differences in band reflectance, NDVI and texture for a variety of commercial and open optical multispectral data, at a range of resolutions (0.3 - 30 m). The overall aim of the study, therefore, is to ascertain the best combination of parameters and resolutions for detecting tropical forest degradation, evaluating the performance of both spectral and textural information. Local biomass change maps are then produced to give an indication of the prediction quality of the best performing models for potential use in forest research and monitoring applications.

2.2 Methods

2.2.1 Study Area

The South Eastern Peruvian Amazon, including the Madre de Dios region, has been identified by the Peruvian government as a tropical 'Capital of Biodiversity' (Law No. 26311: "Declaran Capital de la Biodiversidad del Perú al Departamento de Madre de Dios".). The area is threatened by deforestation and degradation following the paving of the tri-national interoceanic highway, opening up the area for development, and prolific illegal goldmining operations (Diringer et al., 2020). Our study area is located in the North Eastern part of Madre de Dios (11.02 °S, 69.72 °W), in the territory of the Indigenous

Bélgica Yine Community, which lies on the border between Peru and Brazil, on the right bank of the Acre River (Figure 2.1**a**). The Bélgica hold property and use rights over an area of 53,394 hectares, divided between agricultural use, timber extraction and forest conservation. In 2010, the Bélgica received certification from the Forest Stewardship Council (FSC) and contracted a logging company, MADERYJA, to carry out certified timber harvesting within their forest concession (Burga Cahuana, 2013). The study plots are located at 300 meters above sea level, in an area of planned logging operations. The dense forest canopy reaches heights of up to 40 meters and is very rich in tree species, for a total of 85 species in the surveyed area and an average stem density of about 650 trees ha^{-1}. The dominant vegetation type in this area is lowland tropical rainforest, characterised by a high turnover and tree mortality rates of 2.2% year^{-1} (Esquivel-Muelbert et al., 2020). The climate is warm, humid and seasonal. The dry season occurs from May to October and the rainy season from November to April. Data from the Tropical Rainfall Measuring Mission (TRMM 3B43) shows that the area receives a large amount of rain, with an average of 2915 mm year^{-1} for the decade 2009-2019 (Adler et al., 2003).

2.2.2 Field Data

Forest inventory data from four 1-ha plots was collected during May 2019, and again in October 2020, to measure biomass change resulting from selective logging in July 2019. To enhance the accuracy of the biomass estimates, we used Terrestrial Laser Scanning (TLS), providing digital three-dimensional models of every tree in the plot. We also collected UAV laser scanning (LiDAR) and multispectral optical data (< 10 cm spatial resolution) by flying two fixed-wing drones over the plots, part of the forest

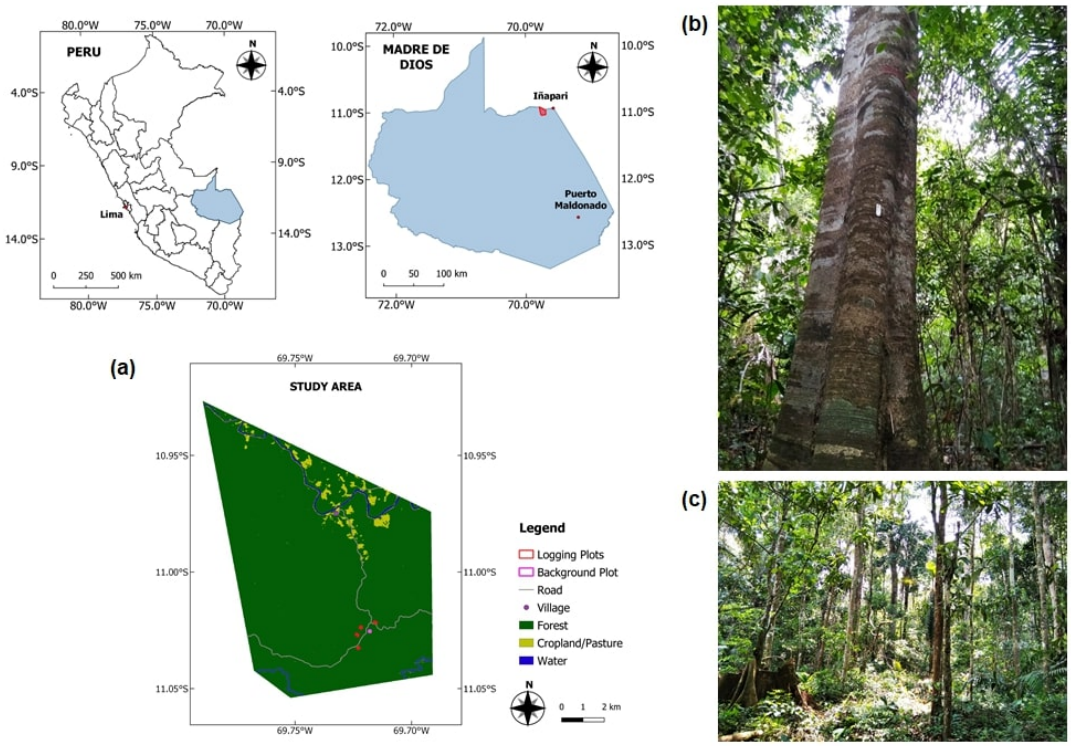

Figure 2.1: (**a**) Location and Land Cover Map of the study area, approximately 30 km west of the town of Iñapari, in the Madre de Dios Region of Peru. The Land Cover Map is a simple supervised classification produced by the authors using the Semi-Automatic Classification Plugin in QGIS and applying a Spectral Angle Mapping algorithm. The classification is derived from PlanetScope 3 m resolution data from July 2019. The images on the right hand side show an example of the forest in the study plot C1: (**b**) before and (**c**) after logging took place.

concession and the village area. Unfortunately, international travel bans following the spread of Covid-19 have not yet permitted the collection of post-logging TLS data, and delayed the second part of the UAV LiDAR measurements to September 2021 (data not available at the time of publication).

The 1-ha Permanent Sample Plots were established in the forest concession, along the road that connects Bélgica to Iñapari, following a West-East direction. The plots were located over flat ground, at a distance of maximum 300 m from the road, to facilitate the TLS operations and ensure accessibility from the UAV. The plots were designed to include loggable tree species that were of interest to the community, especially for their

use in building projects, and which were selected by community members during plot reconnaissance. Two of the plots were square, 100m x 100m, and two were rectangular plots of 145 m x 70 m, with orientations spanning 0-40° North. The locations of the plot corners were measured by a differential GPS and corrected using the coordinates of the integrated GNSS receiver of the TLS. We followed standard forest inventory protocols (Phillips et al., 2001) to collect information on Diameter at Breast Height (DBH), species, X and Y coordinates, damage and mortality classes for each stem in the plot with DBH > 10 cm. The average DBH recorded in our study area was 21 cm, with DBH values ranging between 10 - 158 cm. Each tree was visually assessed for damage and then categorised according to the percentage of its remaining biomass (25, 50, 75 or 90%) as compared to an intact stem. Wood density was derived from species information using a global wood density database (Chave et al., 2009). After the pre-logging measurements, Bélgica extracted a total of 24 trees, in different proportions in each plot, to simulate a range of degradation events. Figure 2.1**b** and 2.1**c** show an example of the forest before and after tree extraction in one of the plots. For the post-logging forest inventory, the direction of tree felling and the collateral damage caused by the logging operations was also noted.

To convert forest inventory metrics into AGB we used the pantropical allometric model from Chave *et al.* (Chave et al., 2014), using field-derived DBH (D) and wood density (ρ), and a regional environmental stress factor (E) with an average value of 0.068 across the four plots. The equation is in the following form:

$$\mathrm{AGB} = \exp[-1.803 - 0.976(E - \ln(\rho)) + 2.673\,\ln(D) - 0.0299 \times [\ln(D)]^2] \qquad (2.1)$$

Individual-tree biomass estimates from allometric equations are found to have large uncertainties associated with their values, with an error of about 50% of the mean (Chave et al., 2014). This error is even greater for large trees (DBH > 70 cm) (Gonzalez de Tanago et al., 2018), because of a bias towards small trees in allometric samples and

the greater variations in growth forms and biomass for large stems (Disney et al., 2018). On the other hand, it was found that AGB estimates from TLS measurements provide a better agreement with the reference data from destructive harvest experiments, with a mean tree-scale relative error of 3% (Burt et al., 2021). Considering that the logged trees in this study have an average DBH of 79 cm, and the number of extracted trees varies between 2 and 9 in each plot, we used TLS-derived AGB for the logged stems, yielding likely a more accurate measurement of biomass change.

TLS data were collected using a Riegl VZ-400 scanner, following the protocols outlined in Wilkes *et al.* (Wilkes et al., 2017). Each plot was subdivided in squares of 10 x 10 m and two scans were obtained at every grid intersection point. The point clouds of the logged trees were extracted using the treeseg package (Burt et al., 2019). Table B.1 contains a complete list of the logged trees, with information on height and crown width, as derived from the TLS point clouds. From the quantitative structural models (QSMs) (Calders et al., 2015; Raumonen et al., 2013), the AGB of each logged tree was derived by multiplying the model volume by wood density. Total AGB loss in each plot was then obtained by summing the TLS-derived AGB of the logged trees plus the change in AGB of the remaining trees as measured from the field surveys (Table 2.1). Unfortunately, processed TLS data volumes were not available for non-logged trees in the plots, so no comparison between allometric and TLS biomass values could be made for these trees. We expect that the much larger number of non-logged than logged trees in each plot, and their smaller average size, means that this difference is not important. On the other hand, if we use allometric equations for the logged trees, then the biomass removed per plot is overestimated by an amount ranging between 13% to 29%, as compared to the biomass change values derived from the TLS data (Table B.2).

Table 2.1: Aboveground Biomass (AGB) before and after logging and Aboveground Biomass Change (ΔAGB) figures of four 1-ha selectively logged plots, measured by field inventory and Terrestrial Laser Scanning (TLS). Standard errors are reported in parentheses.

Plot	AGB Before Logging [Mg ha^{-1}]	AGB After Logging [Mg ha^{-1}]	Number of Trees Logged	ΔAGB [Mg ha^{-1}]	ΔAGB [% ha^{-1}]
C1	295.6 (15.8)	245.9 (15.0)	9	49.7 (5.0)	16.8 (2.0)
C2	266.6 (13.4)	229.5 (12.2)	6	37.1 (3.2)	13.9 (1.4)
C3	270.7 (24.0)	189.7 (10.5)	7	81.0 (4.2)	29.9 (3.3)
C4	261.8 (17.7)	249.1 (15.3)	2	12.8 (1.0)	4.9 (0.5)

2.2.3 Satellite Data Acquisition and Pre-Processing

Commercial and open remote sensing data were collected over the field site before and after the logging event (Table 2.2). As part of the FODEX experiment, we tasked and collected Very High Resolution (VHR) and high resolution commercial satellite imagery from WorldView-3, Planet Skysat and SPOT-7. High and medium resolution data from PlanetScope, Sentinel-2 and Landsat 8 was also downloaded for the same period of time. To minimise seasonal effects, we aimed at collecting images that were captured in the same month of the year, and preferably at the same time of the field survey; however, the presence of cloud cover was a limiting factor, especially in the case of commercial acquisitions.

Launched on 13 August 2014, WorldView-3 is the highest spatial resolution optical satellite available for civilian applications. It is equipped with a panchromatic band (450 - 800 nm) at 0.31 m spatial resolution and can also provide eight multispectral bands in the visible and near-infrared (of which blue: 450 – 510 nm; green: 510 – 580 nm; red: 630 – 690 nm; near-infrared-1: 770 – 895 nm) at 1.24 m resolution and 8-band shortwave infrared (SWIR, 1195 - 2365 nm) imagery at 3.7 m resolution. The instrument swath width is of 13.1 km, allowing the acquisition of off-nadir images with an angle of up to 20 degrees, with a revisit time of 4.5 days.

Table 2.2: Summary of sensor specifications and data acquisitions used in this study.

Sensor	Acquisition	Resolution [m]	Revisit Time	Acquisition Date	Acquisition Time [UTC+0]	Sensor Viewing Angle [°]
WorldView-3 *	Commercial	0.31	4-5 days	10/07/2019	15:23:39	11.3
				26/05/2020	15:10:19	16.2
SkySat	Commercial	0.8	4-5 days	15/07/2019	15:23:07	9.9
				17/06/2020	14:55:53	27.8
SPOT-7 *	Commercial	1	1-3 days	10/07/2019	14:31:17	7.6
				12/06/2020	14:34:23	18.0
PlanetScope	Commercial **	3	Daily	10/07/2019	14:32:57	5.1
				16/07/2020	14:36:19	1.1
Sentinel-2	Open	10	5 days	09/07/2019	15:06:12	9.4
				28/07/2020	15:06:18	9.5
Landsat 8	Open	30	16 days	05/07/2019	14:45:37	0.0
				22/05/2020	14:45:17	0.0

* Only collected on request.

** Non-commercial access through Planet's Education and Research Program (Planet Labs, 2021) or the NICFI Program (Norway, 2021).

Two WorldView-3 images over the study area were tasked from the satellite data provider Digital Globe and acquired on 10 July 2019 and 26 May 2020. Only the panchromatic and blue, green, red and near-infrared (BGRN) bands were made available for this study. Imagery was delivered in product level LV2A, meaning that the data had been radiometrically corrected and geo-referenced to World Geodetic System (WGS) 1984 datum and the Universal Transverse Mercator (UTM) zone 19S projection. For each band, digital numbers were converted into top-of-atmosphere radiance using the absolute radiometric calibration factors and effective bandwidths available in the metadata files. The images were then normalised for solar spectral irradiance by conversion to top-of-atmosphere reflectance. The calibration steps described here were performed according to the formulas and procedures provided by DigitalGlobe (DigitalGlobe, 2016) and using the Geospatial Data Abstraction Library (GDAL, `http://www.gdal.org/`, version number 3.2.2) (Warmerdam, 2008) implemented in Python. To enhance the spatial details of the multispectral data, the panchromatic band was fused with the multispectral bands, using the pansharpening algorithm available in GDAL and choosing a cubic resampling method. This was preferred to ordering the pre-pansharpened product offered by Digital Globe, as it gave more control on the quality of the imagery. The resulting product, at 0.3 m resolution, was georeferenced using the QGIS software (version 3.10) by manually identifying and matching individual trees from the Canopy Height Model (CHM) of the study area, a LiDAR-derived product with a spatial resolution of 25 cm and a geometric accuracy of 1.8 cm (McNicol et al., 2021b). The pre-logging and post-logging georeferenced images were then aligned to match their extents.

The SkySat constellation, operated by Planet Lab, consists of a fleet of 21 commercial high-resolution microsatellites, equipped with optical and near-infrared imaging systems. The first satellite, SkySat-1, was launched on 21 November 2013. The SkySat constellation provide a panchromatic band (450 – 900 nm) with a resolution of 0.58 - 0.86 m and four multi-spectral bands (blue: 450 – 515 nm; green: 515 – 595 nm; red: 605 – 695

nm; near-infrared: 740 – 900 nm) with a resolution of 0.72 - 1.0 m. The system has a swath width of ∼6.5 km at nadir and revisits times of 4 - 5 days per satellite (Planet). Two SkySat imagery over the study area were tasked from Planet Labs and acquired on 15 July 2019 and 17 June 2020. The images were downloaded from the Planet Explorer platform (Planet Team, 2017) and acquired as an already orthorectified, pansharpened 4-band BGRN product at 0.81 m spatial resolution. To convert the digital numbers into top-of-atmosphere reflectance, each pixel value was multiplied by a radiometric scale factor and then corrected for solar spectral irradiance, as detailed in the technical sheet provided by Planet Labs (Planet). The calibrated products were then georeferenced using the processed WorldView-3 images. As for the WorldView-3 data, the pre-logging and post-logging images were aligned to match their extents.

The SPOT ("Satellite pour l'Observation de la Terre") series was developed within the French National Space Program and has been providing high-resolution, wide-area multispectral imagery since 1986. SPOT-7 was launched on 30 June 2014 and consists of four multispectral bands: blue (450 – 520 nm), green (530 – 590 nm), red (625 – 695 nm), and NIR (760 – 890 nm) at a spatial resolution of 6 m, and one panchromatic band (450 – 745 nm) at a spatial resolution of 1.5 m. SPOT-7 has revisits of 1 to 3 days and its imaging swath is 60 km at nadir. Two archived SPOT-7 imagery, captured on 10 July 2019 and 12 June 2020, were downloaded from the Airbus GeoStore Web Portal (`http://www.intelligence-airbusds.com`). Access to the imagery was possible through ESA's Third Party Mission scheme. The images were obtained in product level Ortho and in units of surface reflectance, which means that the data had been orthorectified and radiometrically corrected from sensor calibration and systematic atmospheric effects. The product was already pan-sharpened and it was delivered as a 4-band BGRN multispectral image at a spatial resolution of 1.5 m. The images matched the extent of the LiDAR layer, hence it was not necessary to apply a georeferencing procedure to

SPOT-7 data. The same results were found when comparing the other lower resolution images, which were inspected until it was possible to discern individual trees at the pixel level. In the latter case, clear references points (i.e. road and village) were used to test if the images aligned with each other.

First launched in 2016, the PlanetScope CubeSat constellation is operated by Planet Labs, with more than 180 individual nano-satellites named “Doves”, which capture the entire Earth’s surface at 3 m spatial resolution on a daily basis. PlanetScope imagery contains four spectral bands, i.e. blue (455 – 515 nm), green (500 – 590 nm), red (590 – 670 nm), and NIR (780 – 860 nm). Planet offers free monthly limited PlanetScope images to the scientific research community through the Education and Research Program (Planet Labs, 2021). Two images were acquired on 10 July 2019 and 16 July 2020 as an orthorectified, Level-3B analytic surface reflectance product, which has incorporated geometric and radiometric corrections, and is atmospherically corrected by Planet Labs using the 6S radiative transfer model with ancillary data from MODIS (Kotchenova et al., 2006; Planet).

The European Space Agency (ESA) Sentinel-2 mission supplies wide-swath (290 km), high-resolution, multi-spectral data, supporting land monitoring research; the imagery complements and enhances other missions, such as Landsat and SPOT. The Sentinel-2 constellation is made of two polar orbiting satellites, Sentinel-2A and Sentinel-2B, launched on 23 June 2015 and 7 March 2017, respectively. Each satellite carries onboard an optical imaging sensor MSI (Multi-Spectral Instrument) with the capabilities of recording reflected radiance in 13 spectral bands: four VNIR bands at 10 m spatial resolution, six red edge and SWIR bands at 20 m spatial resolution, and three atmospheric correction bands at 60 m spatial resolution. Each satellite has a revisit frequency of 10 days, while the combined constellation has a repetition cycle of 5 days. As a consequence, Sentinel-2 provides dense time series imagery, with data open to all. For this study, two-cloud free Sentinel-2 MSI granules acquired on 9 July 2019 and 28 July

2020 were downloaded from the Copernicus Data Hub (Copernicus, 2020) as Level-2A surface reflectance product. We used the bands available at 10 m, ie. blue (B2: 458 – 523 nm), green (B3: 543 – 578 nm), red (B4: 650 – 680 nm) and NIR (B8: 785 – 899 nm). Sentinel-2 Level 2A products provided by ESA are generated by the Sen2Cor processor (U Mueller-Wilm et al., 2017), already orthorectified as 100 x 100 km ortho-images in UTM/WGS84 projection and corrected for atmospheric effects.

The Landsat 8 satellite is part of the long-running Landsat joint mission of the United States Geological Survey (USGS) and NASA. It was launched on 11 February 2013 with the operational land imager (OLI) and the thermal infrared sensor (TIRS) onboard. The OLI collects measurements for nine spectral bands in the VNIR and SWIR at 30 m spatial resolution, including an infrared band for cirrus detection and a deep blue band for coastal monitoring. It also provides a single, panchromatic band at 15 m spatial resolution. The TIRS measures land surface temperature in two thermal infrared bands at 100 m spatial resolution. The system images the entire Earth's surface with a repeat cycle of 16 days and over a 185 km swath. Two Landsat 8 tiles from 5 June 2019 and 22 May 2020 were freely downloaded from the USGS Earth Explorer web (`https://glovis.usgs.gov/`) as a standard Level-2 surface reflectance product with the UTM/WGS84 projection. The data delivered by USGS is corrected for atmospheric effect using the Land Surface Reflectance Code (LaSRC) (Vermote et al., 2018). Only the BGRN bands are used in this study, i.e. blue (B2: 452 – 512 nm), green (B3: 533 – 590 nm), red (B4: 636 – 673 nm) and NIR (B5: 851 – 879 nm). Given the availability of the 10 m resolution Sentinel-2 imagery, the Landsat BGRN bands were not pansharpened using the 15 m panchromatic data Landsat also collects.

When performing multi-temporal analysis, image normalization is critical for ensuring homogeneity between two or more scenes captured under different atmospheric conditions or illumination geometries. This is achieved by altering the radiometric properties of the image series using the histogram of a reference image (Vicente-Serrano et al., 2008).

In this study, normalization is performed using the histogram matching function from the Python scikit-image package (van der Walt et al., 2014). For each sensor, the pre-logging image was chosen as the reference image and the histogram of this reference image was matched to the post-logging image. The same histogram matching technique was also used to correct for the presence of cloud shadow over plot C2 in the post-logging WorldView-3 image, after the latter was matched to the reference image. The pixel values of the shadow-covered region are recovered by matching the histogram of the shadow region to the histogram of the non-shadow area of the same land surface class (Sarabandi et al., 2004), which in this case is forested area (Figure 2.1**a**).

The image pre-processing pipeline is shown in Figure 2.2. In addition to the steps described in the diagram, PlanetScope, Sentinel-2 and Landsat 8 were resampled to a 1 m resolution using a Nearest Neighbour convolution, to allow for easy and direct comparison with the higher resolution data. This step was performed only after retrieving the texture parameters for each band.

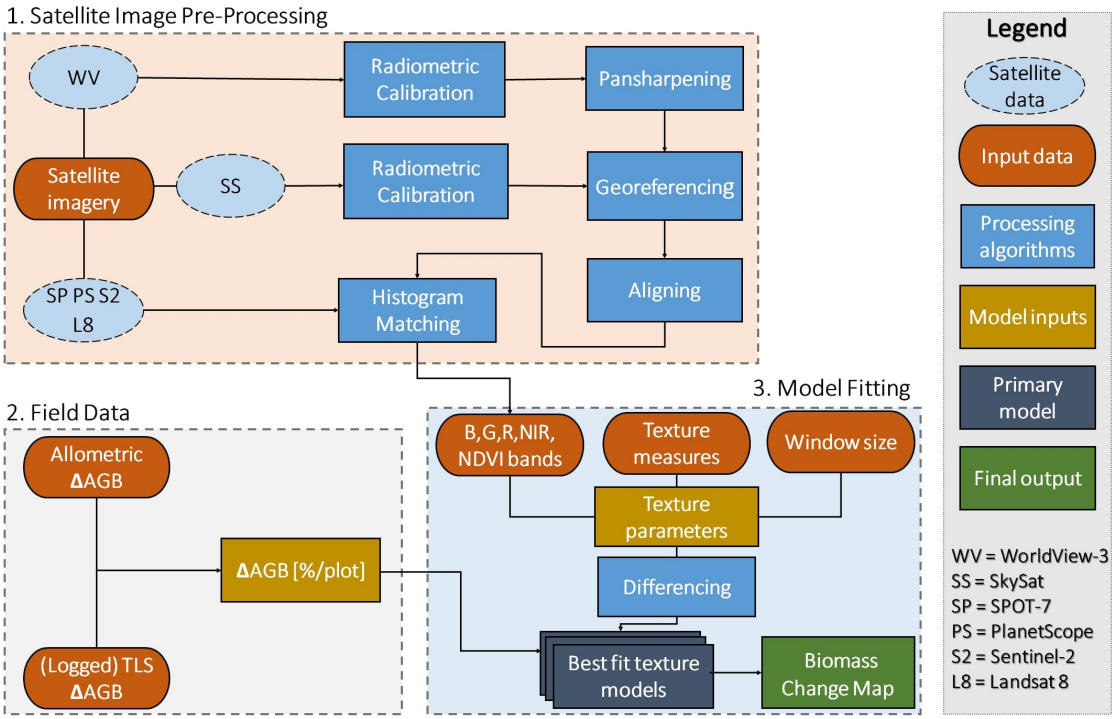

Figure 2.2: General methodology workflow used for producing biomass change maps over the study area using field-derived ΔAGB and remotely sensed data.

2.2.4 Simple Reflectance, NDVI and Texture Measures

After preprocessing, the resulting red and NIR bands were used for the calculation of the Normalized Difference Vegetation Index (NDVI):

$$\mathrm{NDVI} = \frac{\mathrm{NIR} - \mathrm{Red}}{\mathrm{NIR} + \mathrm{Red}} \tag{2.2}$$

The choice of this particular index was motivated by its widespread use in land-cover change detection and monitoring of vegetation dynamics (Townshend and Justice, 1986; Lyon et al., 1998), and the fact that it can be calculated from all the six satellite dataset types without the need of sensor-specific calibration constants, making it suitable for multi-sensor comparison. All the sensors had blue, green, red and NIR bands (BGRN), so these were also tested individually, and stacked into a raster with the NDVI band for subsequent analysis.

Identifying appropriate textures involves the selection of suitable texture measures, moving window sizes, and spectral bands from which to calculate it. In terms of texture measures, we based our selection on previous research predicting biomass values from optical satellite data (Eckert, 2012; Nichol and Sarker, 2011; Fuchs et al., 2009; Lu, 2005). Among the different techniques, local standard deviation was chosen as a promising method for detecting canopy loss. Figure 2.3 shows the Sentinel-2 NDVI time series of the degraded plot C1 as compared to the same signal from an intact area (a 1-ha plot located in the proximity of the study plots which did not experience any logging activity; see Figure 2.1**a**). A time series of the degraded plot derived from the NDVI mean (Figure 2.3**a**) does not show any significant variation immediately before and after logging, compared to the background signal. On the other hand, when using a textural metric, the standard deviation of the NDVI computed in a 3×3 pixel moving window, a signal peak is observed in correspondence of the logging event, that is not seen in the background signal (Figure 2.3**b**).

Texture gives an indication of local variance and is directly related to the resolution and size of the dominant feature. In this study, this corresponds to the size and spacing of the tree crowns. Low variance is expected in high resolution images where the pixel size is smaller than the tree crown size, though it will rise around the edge of such crowns, effectively acting as an edge detector. As pixel size increases to a scale that is comparable to the tree crown, local variance increases too, and this should especially apply to tropical forests, rich in tree species and with heterogeneous canopy structures (Nichol and Sarker, 2011). A small moving window amplifies the difference within the window frame, increasing image noise, but it retains a high spatial resolution. On the other hand, a large window may not extract the necessary information due to an excessive smoothing of the textural variations (Lu, 2005). Considering the large spread of resolutions in our dataset (0.3 - 30 m), we tested nine different sizes of moving windows (3×3, 5×5, 7×7, 9×9, 11×11, 15×15, 19×19, 25×25, 45×45, in pixels) using a texture metrics of standard deviation to check for variations within neighbouring pixels.

In summary, the following remotely sensed measures were used for this analysis, for each optical sensor:

- Spectral reflectances of each individual band (blue, red, green, NIR);
- Texture parameters of each individual band (blue, red, green, NIR) for 9 window sizes;
- NDVI (mean and texture for 9 window sizes).

To link the field biomass change with the satellite measurements, we extract the pre-logging and post-logging metric value for each remote sensing variable for all the pixels within the field plots. The difference pre- and post- logging was then calculated for each pixel, and then the mean difference calculated over the whole plot. For the texture parameters, the difference was squared first, and then the mean squared texture value of each plot was calculated. This ensures that the positive and negative values result-

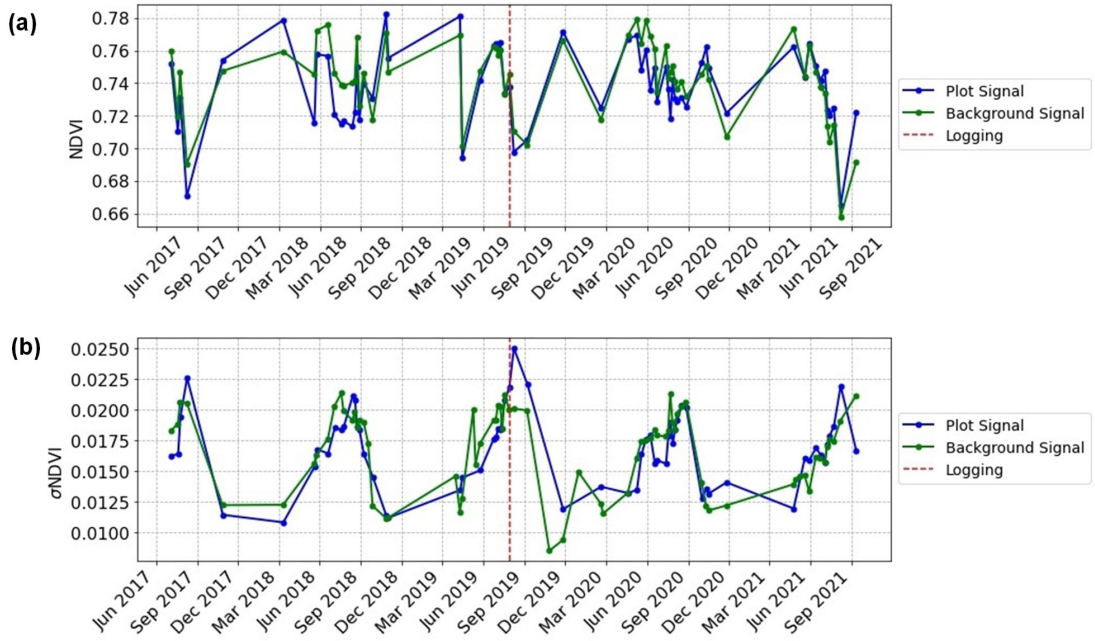

Figure 2.3: Sentinel-2 NDVI time series for the degraded plot C1 and background signal before and after the logging event, indicated by the dashed red line. The background signal is computed from a 1-ha undisturbed plot located in the study area. (**a**) NDVI mean and (**b**) NDVI texture for a 3×3 pixel moving window. The time series derived from texture shows a seasonal trend, with a peak in the dry season. An increase in standard deviation is observed in correspondence of the logging event.

ing from the differences between pre-logging and post-logging textures do not cancel out when taking the plot average, with the consequent loss of useful information. This squaring can be thought of as moving the difference from standard deviation to variance space.

2.2.5 Statistical Analysis

The relationship between field-measured biomass change and the difference of the remotely sensed variables per plot was analysed using linear regression, with the strength of the relationships assessed using Pearson's Correlation (r). ΔAGB (in units of % ha^{-1}) was used as a dependent variable and the computed remote sensing parameters were used as independent variables. The coefficient of determination (R^2), the p-value and

the Root Mean Square Error (RMSE) were used to evaluate the regression model performance. The regression equation from the best-fit models is in the form $y = mx + c$. Substituting x with the values of the remote sensing observations of the wider area will yield the ΔAGB values for building a biomass change map of the study region.

2.3 Results

A visual, multi-scale representation of some of the remotely sensed variables used in this analysis is illustrated in Figure 2.4, with the RGB images showing plot C1 before and after logging (Figure 2.4**a**). Figure 2.4**b** and Figure 2.4**c** show the difference in NDVI and in the texture of the NIR band before and after logging for the same plot.

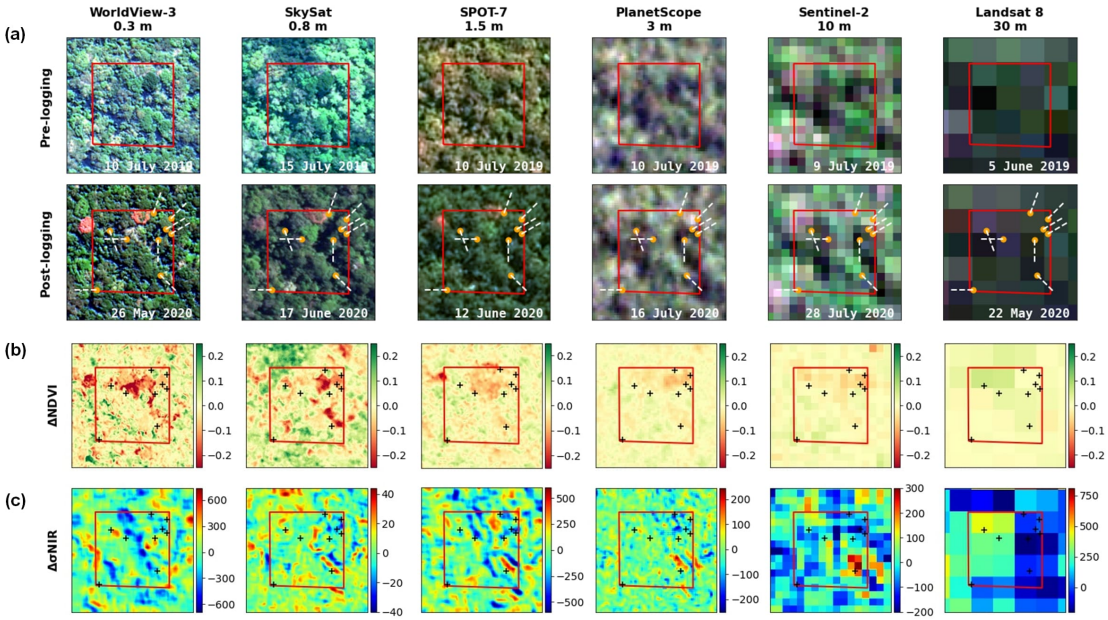

Figure 2.4: (**a**) Visual comparison of RGB imagery before and after logging at increasingly coarser resolutions for the plot C1. The post-logging images show the position of the harvested trees as orange dots and the direction of the felling as white dashed lines. (**b**) Difference in NDVI (ΔNDVI) and (**c**) in NIR texture (ΔσNIR) for the same plot. The window sizes used for each sensor correspond to those resulting from the best fit models (Table B.4).

2.3.1 Relationships between Spectral Reflectances/NDVI and Biomass Change

Linear regression models were calculated using biomass change as the dependent variable and all other parameters as the independent variables. The models include the four observations from the 1-ha change plots and one undisturbed plot (as determined from remote sensing observations and knowledge of the study area) and therefore used as a data point with zero biomass change. For the spectral parameters, the best fitting models are shown in Figure 2.5, with difference in simple NIR reflectance illustrated in Figure 2.5**a** and difference in NDVI shown in Figure 2.5**b**. All models show poor performance (with $R^2 < 0.50$). A full list of the models and corresponding statistics for the difference in spectral reflectance and biomass change, as well as ΔNDVI and biomass change, is available in Table B.3.

2.3.2 Relationships between Texture and Biomass Change

Table B.4 provides the complete list of all the generated models relating biomass change to the difference in textural parameters. It is important to note that the number of pixels in each window depends on the resolution of the dataset. The best-fitting model among all sensors is observed for PlanetScope, obtained from the texture parameter of the NIR band and for a window size of 3×3 pixels, corresponding to a physical square window of 9×9 m (R^2 = 0.97). The lowest performance for texture measurement is observed in SkySat, with the best performing model obtained by the texture of the NDVI and using a window size of 25×25 pixels, corresponding to a window of 20.2×20.2 m in size (R^2 = 0.51). The discrepancy in viewing angle between the pre-logging and post-logging image (Table 2.2) could explain the difference between SkySat and the other sensors. To illustrate how spectral and textural-based models compare, Figure 2.6 shows the best-fitting models for texture differences obtained from the NIR band (Figure 2.6**a**) and NDVI (Figure 2.6**b**).

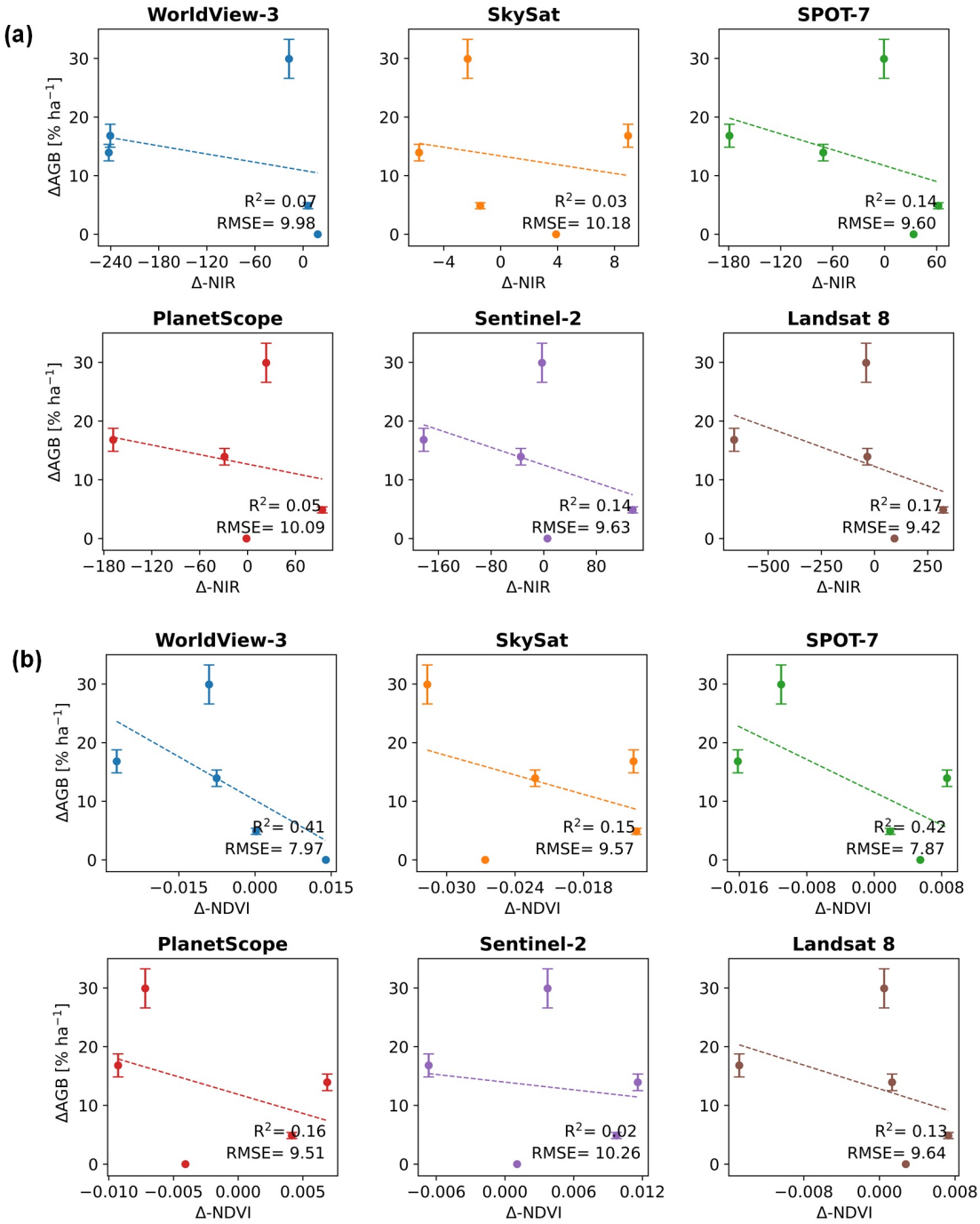

Figure 2.5: Multi-sensor comparison of regression models for (**a**) biomass loss and ΔNIR and (**b**) biomass loss and ΔNDVI.

A notable improvement in the ability to map degradation when using texture over direct changes in spectral data or NDVI is observed for all optical sensors (Figure 2.6**a**, Figure 2.5**a** and Figure 2.5**b**), in particular when using texture obtained from the NIR band. This pattern of improvement is illustrated in Figure 2.7, which compares the RMSE of three

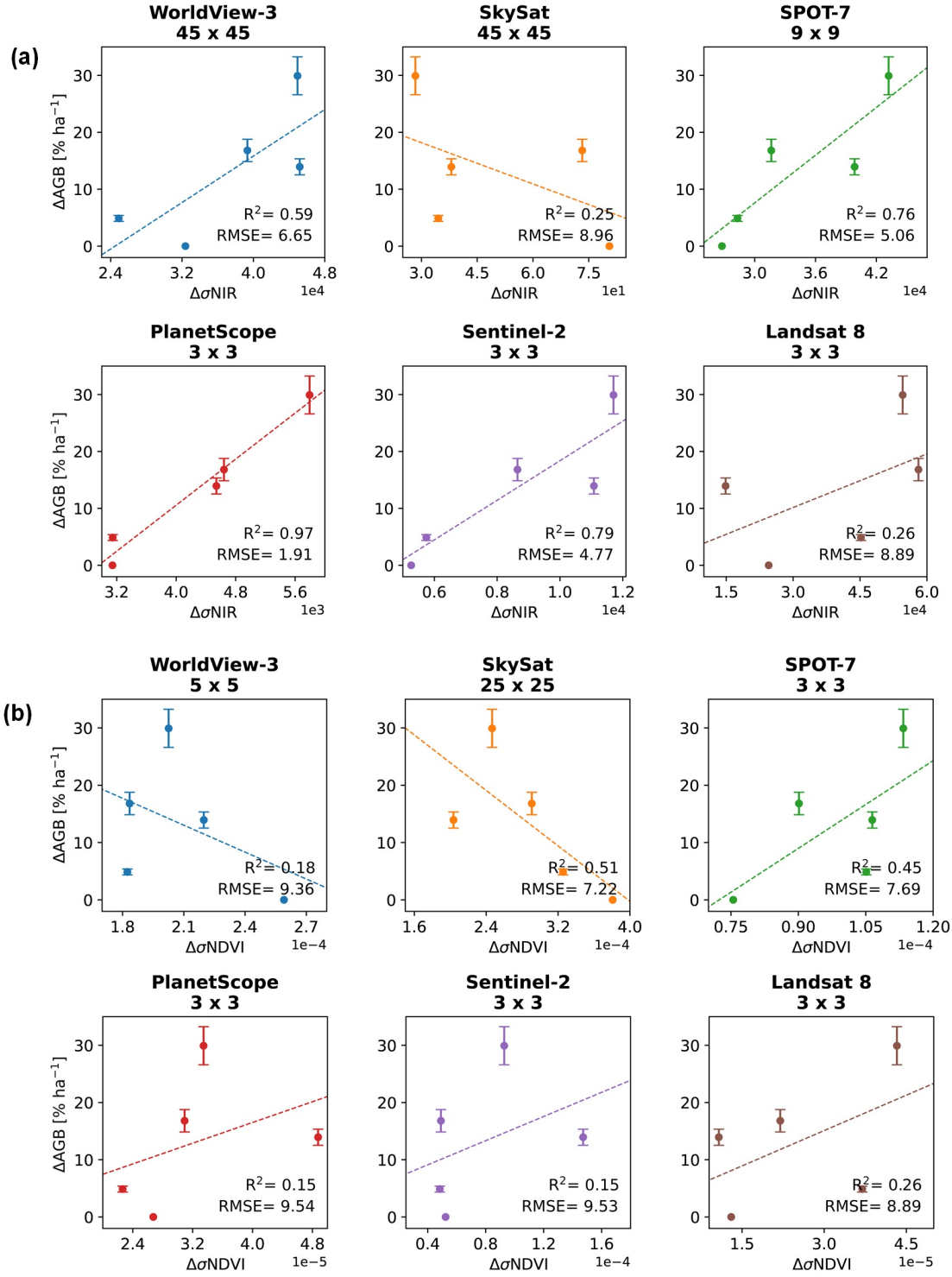

Figure 2.6: Multi-sensor comparison of the highest performing regression models for predicting biomass loss obtained from the difference in texture of (**a**) NIR and of (**b**) NDVI. The window sizes used in generating the models are reported above each subplot.

models to evaluate their performance for biomass change estimation. The best performing model is obtained from texture of PlanetScope imagery, with RMSE = 1.91 % ha^{-1}. It is followed by Sentinel-2 and SPOT-7, which have one step lower and higher resolution respectively, both showing a significant improvement in model performance when textural NIR is used (RMSE = 4.77 % ha^{-1} and RMSE = 5.06 % ha^{-1}, respectively). Biomass loss estimation with WorldView-3 is also improved when using the textural parameter (RMSE = 6.65 % ha^{-1}, as compared to RMSE = 7.97 % ha^{-1} of a model based on ΔNDVI). A small improvement is also observed in Landsat 8, but the error is still too large for justifying the use of Landsat data for small-scale degradation detection. Also SkySat appears to perform slightly better when using a textural parameter (RMSE = 7.22 % ha^{-1}, as compared to RMSE = 9.57 % ha^{-1} for simple NDVI difference). Some of these models have a p-Value < 0.05 (see Table B.3 and Table B.4 for a complete list of the results) and this proportion includes the best-fit models from PlanetScope ($p = 0.003$) and Sentinel-2 ($p = 0.045$). Finally, Figure 2.7 shows the existence of a consistent pattern across satellites that differ in sensor characteristics, acquisition times and spatial resolutions (Table 2.2).

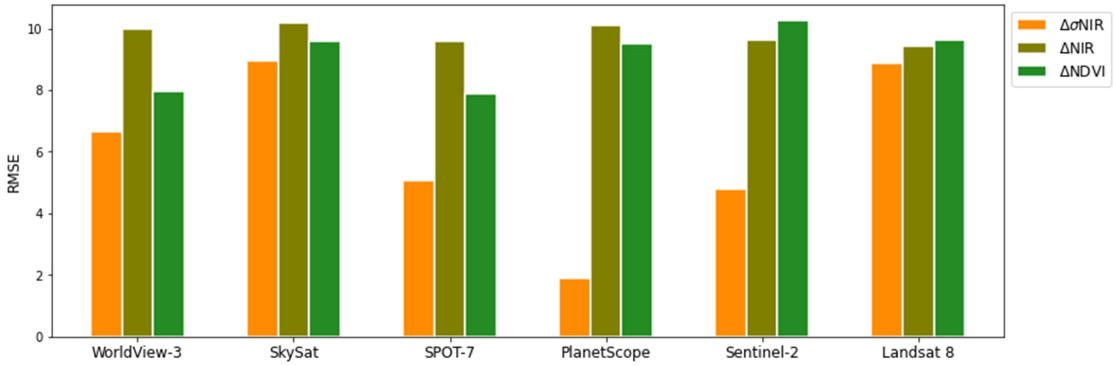

Figure 2.7: Evaluation of model performance for biomass loss estimation. The graph compares the RMSE of three models estimating biomass loss from the difference in simple NIR (ΔNIR), difference in NDVI (ΔNDVI) and difference in texture obtained from the NIR band (ΔσNIR).

2.3.3 Biomass Change Maps

Biomass change maps were produced from the best-fit models of PlanetScope, SPOT-7 and Sentinel-2 texture change data, as those were the optical sensors yielding the highest model performance (Figure 2.7). Figure 2.8 compares the three biomass change maps of the study area, at 1-ha resolution, constructed from the best fitting models, where the textural parameter was calculated from the NIR band on a window of 13.5 $\times$ 13.5 m in size for SPOT-7 (Fig. 2.8**a**), and a window of 9$\times$9 m in size for PlanetScope (Figure 2.8**b**). For Sentinel-2 a window of 3$\times$3 pixels yielded the best map, corresponding to a physical window of 30$\times$30 m in size (Figure 2.8**c**). In addition to the lowest RMSE value, the biomass change map derived from PlanetScope shows the closest qualitative agreement with the satellite observations. Areas of higher degradation, observed in proximity of the village and the river, are in agreement with the RGB imagery from 2019 and 2020 and correspond to areas of agricultural expansion into the forest concession (Figure 2.9).

2.4 Discussion

In this study we tested the ability of different high-medium resolution optical satellite datasets to detect experimentally-controlled degradation in a tropical forest in Peru. We found that sensors in the 1.5 - 10 m range showed a strong ability to detect forest degradation, particularly when analysed using a novel texture-change metric we developed using a window size approximating 10$\times$10 m. The best overall method was found for the 3 m resolution PlanetScope imagery using a texture parameter obtained from the NIR band and a window size of 9$\times$9 m. Texture-based models developed from the NIR band of SPOT-7 and Sentinel-2 data also showed good performance (Figure 2.7). A slightly weaker relationship was observed for WorldView-3, with the best model performance

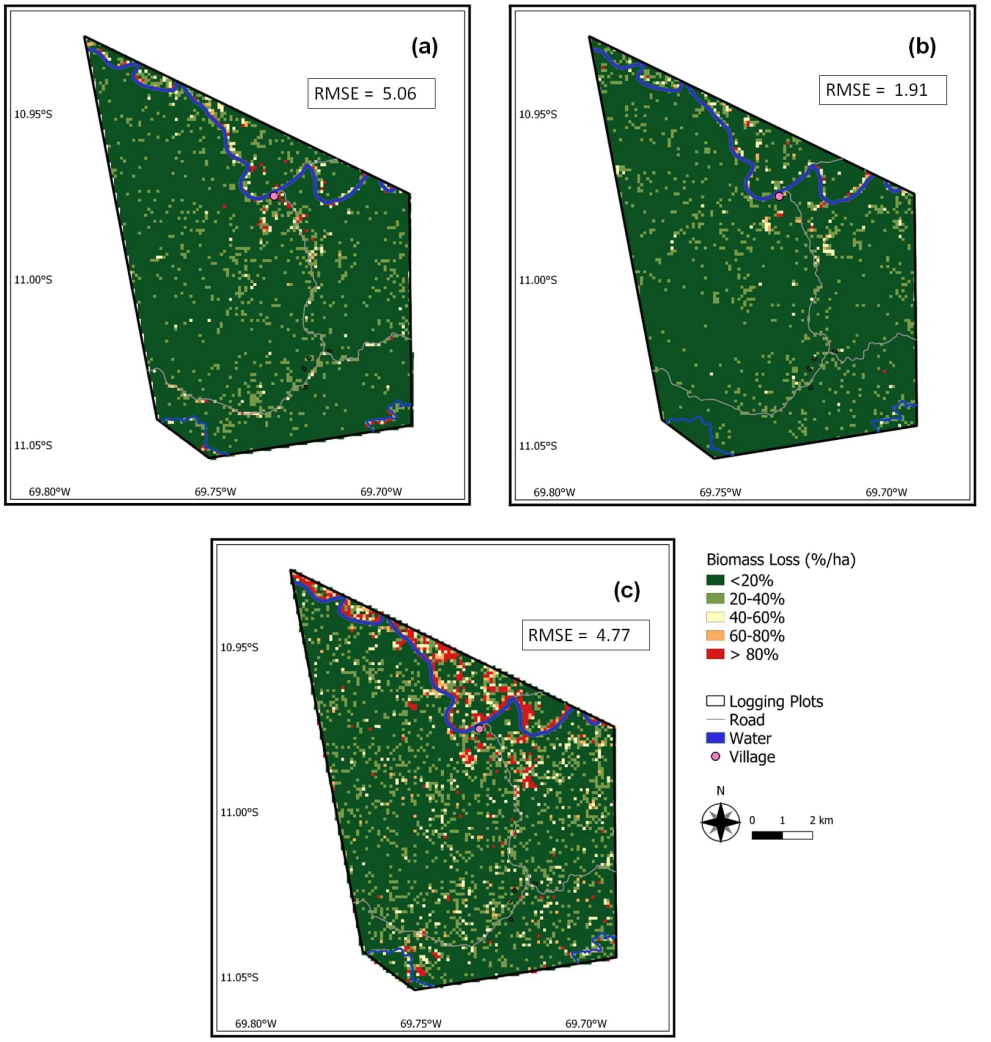

Figure 2.8: Maps of biomass change (2019-2020) over the study region derived from the texture of the NIR band for (**a**) SPOT-7, (**b**) PlanetScope and (**c**) Sentinel-2 data for a 1-ha resolution.

achieved when using a texture measure derived from the NIR band and a 14×14 m window. Overall, this approach shows great potential to transform mapping of forest degradation, though how well it transfers to other areas or types and magnitudes of forest disturbance remains to be seen.

Previous research has concluded that texture analysis improves AGB estimation performance, compared to the use of spectral parameters or vegetation indices (Nichol and Sarker, 2011; Lu, 2005; Eckert, 2012). This study confirms that texture parameters correlate more strongly with AGB change. SkySat was the only sensor where the

Figure 2.9: PlanetScope RGB data from 2019 and 2020, showing degradation of two sites undergoing conversion for pasture and agricultural use (**a**) and (**b**), both undergoing conversion for pasture and agricultural use. The right hand figures show the same location in the PlanetScope biomass loss map from Figure 2.8**b**. Visible areas of degradation and deforestation correspond to the high degradation pixels (> 40% loss per hectare) in the biomass loss map.

strongest correlation was observed for the difference in texture of the NDVI values, rather than for the difference in simple spectral bands, though it should be noted that its performance was quite poor compared to other sensors. In general, vegetation indices can improve AGB estimates, as the use of band ratios partially reduce the effects of atmospheric conditions and shadows, especially in regions of heterogeneous forest (Lu, 2005). However, vegetation indices often saturate in high biomass and multi-storied forest canopies (Lu and Batistella, 2005; Huete et al., 1997). While simple vegetation indices are computed at the pixel scale, texture is calculated from a neighbourhood of pixels that can be adjusted in size to optimise the potential of texture to measure local variability. Therefore, texture can be an effective measure to detect variations in canopy edges caused by forest fragmentation, especially in the case of close canopy forests. One important step is to identify suitable texture metrics, which requires prior knowledge on the combination of moving window sizes, image bands and texture measures that strongly correlate with changes in forest biomass. In this study, a measure of variance, derived from squaring and then differencing per-pixel standard deviation, was chosen as the texture measure to compute the variability in reflectance among neighbouring pixels,

to identify potential areas of abrupt change. We found that the best performing texture-based models were derived from the NIR band (Figure 2.6**a**). This is due to the higher 'penetration' depth of this band compared to visible light (Huete et al., 1997), which can explain the better performance of this band as compared, for example, to the ratio of the NIR and red band. As for the moving window size, this depends on the spatial resolution and extent of the observed object. A window that is too small may detect changes in pixel values that are irrelevant for forest change, whereas a window that is too large may make the relevant textural variation invisible (Lu, 2005). For purposes of detecting forest degradation, the optimal window size was selected as the window size that produced the best fitting model. We found that the the best results were given for window sizes in the range of 9-14 m. In general, the correlation between biomass change and the remote sensing observation weakens when the size of the window increases or decreases away from this optimum value, and this is true for all the sensors analysed here (Figure B.1). It is important to notice that the optimum window size reported in this study is conservative, as models computed using the next available window size still show a significant correlation. The second best-fit models for PlanetScope (15$\times$15 m window) and SPOT-7 (16.5$\times$16.5 m window) show a strong correlation (R^2 = 0.85 and R^2 = 0.72, respectively), which gradually worsen as we select larger or smaller window sizes. From the TLS models, we find that the crown widths of the logged trees in this experiment have a median value of 17.0 m (Table B.1), which is directly comparable with the window sizes of the second best-fit models. For WorldView-3 we did not test windows larger than 14.5 m in size. As for Sentinel-2, the next available window is 50 m in size, making the lower threshold the best suited for this analysis (Table B.4). Hence, this study confirms that the measurement of local variance in forest structures is enabled when crown sizes are similar to the window resolution (Nichol and Sarker, 2011).

In recent years, high resolution satellite optical data has become more abundant and available, freeing the possibility for forest monitoring to become a more democratic tool, accessed by a wider public. However, uncertainties in the remotely sensed data, especially in image preprocessing and at different levels of the processing chain, AGB calculations based on allometric models, the discrepancy between satellite acquisition date and field inventory date, can affect the accuracy of the remote sensing observations and hence the transferability of the model (Lu, 2005). As a result, individual satellite-based biomass maps over tropical areas normally have large pixel-level uncertainties (Spawn et al., 2020; Saatchi et al., 2011). Differencing such maps to produce a biomass change product means that substantial spatial errors would be indistinguishable from the physical changes in forest cover. This is the reason why differencing such maps is not recommendable, and there are currently no trusted biomass change maps over the tropics.

In this study we used field measurements of biomass change where the entity and the timescale of the disturbance events is well known, in order to reduce the uncertainty caused by the temporal mismatch between satellite and field data collection. We used change data to directly calibrate our model, deriving a map of biomass change without the need of differencing two static maps. As a result, the biomass change maps developed here are capable of producing direct estimates of forest loss, overcoming the inherent noise caused by error propagation (Figure 2.8). A visual comparison of the RGB imagery from the two study years 2019 and 2020 has identified areas of forest loss near the village, due to agricultural expansion (Figure 2.9). These areas correspond to the pixels in the PlanetScope map showing the highest amount of forest loss (> 40 % ha^{-1}). Among the three maps constructed from the best performing sensors, PlanetScope yields the highest predictive power, albeit it is not sensitive enough for detecting losses at the lower end of the degradation scale (< 20 % ha^{-1}) (Figure 2.8**b**). On the other hand, the model performs well at predicting higher levels of biomass change (red

pixels in Figure 2.9), showing that the metrics continues to rise rather than reaching a saturation point at ΔAGB = 100 % ha^{-1}. Unfortunately, the difficulty in collecting sufficient ground reference data, spanning a wider range of degradation values (currently limited to 5 - 30 % ha^{-1}), physically restricts the sample size used in this study, hampering the reproducibility of these maps. We are aware that we lack experimental data to represent higher degradation effects, which are only validated by a qualitative inspection of the remotely sensed imagery (Figure 2.9). Given the complexity and elusiveness of the subject under observation, this study has encompassed multiple methodological approaches (direct biomass change estimates, multi-band textural and spectral comparisons, TLS and forest-inventoried biomass models), which have rarely been adopted in conjunction, and certainly never on the scale of a multi-sensor analysis comprising six optical satellites.

The objective of this paper was to research into the possibility of a common road map for detecting degradation, simplifying analyses and methodologies, ultimately finding a common denominator across disparate observation platforms. The conclusion is supported by the existence of such a pattern, and anchors its logical evidence in the experimental data (ie., the size of the window is physically comparable to the tree crowns). These results need to be further validated by adding more sample data to the existing models. Furthermore, while validation is an important part of AGB estimation analyses, the lack of further ground reference data makes independent validation impossible at this stage of the research. The acquisition and successive integration of the post-logging LiDAR data will improve the prediction and accuracy of our models. We hope that the information presented here on the best combination of optical satellite and textural parameter can be used as a template for future work on biomass change estimation.

2.5 Conclusions

The objective of this study was to link experimental data of biomass change to optical remote sensing observations from six different sensors, spanning resolutions in the range of 0.3 - 30 m. Models based on spectral and textural information were developed from all the six datasets in order to find the best combination of sensor and remote sensing variable for predicting biomass change in dense tropical forests. Contrary to previous studies using satellite remote sensing data, biomass change was not estimated by subtracting two static AGB maps. Field inventory data collected before and after selective logging allowed for building models where biomass change was directly related to the change in the remote sensing variable. From this analysis we draw the following conclusions:

- Biomass change models built on image texture are more strongly correlated to ΔAGB than those built on pure spectral signatures. This is true for all the sensors analysed here;
- A comparative study showed that the best performing model was obtained for PlanetScope data, achieving a R^2 of 0.97 and RMSE of 1.91 ΔAGB % ha^{-1} ($p = 0.003$). This model consists of a texture obtained from the NIR band in a 9$\times$9 m window. In general, high correlations were observed for four out of six sensors when using the texture of the NIR band;
- The strongest relationships between field biomass change and satellite data were observed for those sensors having spatial resolutions in the middle of the 0.30 - 30m range (3 m resolution for PlanetScope, 1.5 m for SPOT-7 and 10 m for Sentinel-2). Weaker relationships were observed for the very high resolution sensors (< 1.5 m). Insignificant results were found for Landsat data at 30 m spatial resolution. This suggests that local measurements of canopy variation are possible when the data is neither too detailed (which increases the noise content) or coarse (which smooths the information content);

- We found that there is an optimal window size for detecting forest degradation when extracting textural information. This size slightly varies across the sensors; in this study, the optimal range was found between 9 - 14 m in length for a square window, suggesting that local variation in forest canopies is best measured when the window size is of comparable scale to the tree crown diameter.

Future research in the FODEX project will expand this analysis and attempt at reducing the noise content of the biomass maps by fusing multispectral optical information with the remote sensing radar measurements acquired over the study area. Local LiDAR data will also provide a larger sample size, improving the accuracy of the model. The robustness of the developed models will be tested by transferring the biomass change estimates to other regions with varying vegetation and disturbance events.

Acknowledgements

We would like to thank La Comunidad Nativa de Bélgica for allowing us to conduct this research on their land, and for offering material and moral support during our permanence in their community. We would like to specially thank the NGO AIDER - Asociación para la Investigación y Desarrollo Integral, for offering their invaluable help with the campaign preparation and for continuously supporting us with the logistics, ensuring the best outcome for our fieldwork. This research would have not been possible without the work of the field assistants. In particular, we would like to thank Roxana Sacatuma Cruz and José Sánchez Tintaya, and the field assistants from Bélgica, Arturo Aspajo López, Leoncio Aspajo Lopez, Luis López Chapiama and Kenny López Batista, for assisting us with the field inventory work, but also for their generous guidance and advice. We also acknowledge the assistance provided with customs and logistics by Prof. Eric Cosio and Dr. Norma Salinas from the Pontificia Universidad Católica del Perú. We finally thank the Regional Government of Madre de Dios for issuing the Authorisation for Scientific

Research Purposes on Local Flora outside of natural protected areas with authorisation code N° 17-MAD/AUT-IFL-2019-001. This research was funded by a European Research Council Starting Grant awarded to Edward Mitchard (The Tropical Forest Degradation Experiment - FODEX: 757526). This paper is dedicated to the memory of our colleague and friend Luis Miguel Álvarez Mayorga, who greatly contributed to the data collection for this study.

Chapter 3

Reliably mapping low-intensity forest disturbance using satellite radar data

C. Aquino[a], E. T. A. Mitchard[a], I. M. McNicol[a], H. Carstairs[a], A. Burt[b], B. L. Puma Vilca[c], M. Obiang Ebanega[d], A. Modinga Dikongo[e], C. Dassi[e], S. Mayta[f], M. Tamayo[g], P. Grijalba[g], F. Miranda[h] and M. Disney[b]

[a] *School of Geosciences, University of Edinburgh, Edinburgh, United Kingdom*

[b] *Department of Geography, University College London, London, United Kingdom*

[c] *Escuela Profesional de Biología, Universidad Nacional de San Antonio Abad del Cusco, Cusco, Perú*

[d] *Département de Géographie, Université Omar Bongo, Libreville, Gabon*

[e] *Agence Gabonaise d'Etudes et d'Observations Spatiales, Libreville, Gabon*

[f] *Asociación para la Investigación y Desarrollo Integral, Lima, Perú*

[g] *Robotic Air Systems, Lima, Perú*

[h] *Cotecmi, Lima, Perú*

Modified version of a paper published in *Frontiers in Forests and Global Change* (2022)[1]

Author contribution: C.A. conducted the analysis and wrote the manuscript under the supervision of E.T.A.M.; C.A., I.M., H.C., B.P.V, M.O.E, A.M.D, C.D, M.T., P.G. and F.M. collected the field data; A.B., M.D., S.M., B.P.,M.T., P.G. and F.M. provided project resources; E.T.A.M. obtained the funding. All authors reviewed the manuscript.

1. *Frontiers in Forests and Global Change*, vol.5, no. 1018762, doi:10.3389/ffgc.2022.1018762

Abstract

In the last decades tropical forests have experienced increased fragmentation due to a global growing demand for agricultural and forest commodities. Satellite remote sensing offers a valuable tool for monitoring forest loss, thanks to the global coverage and the temporal consistency of the acquisitions. In tropical regions, C-band Synthetic Aperture Radar (SAR) data from the Sentinel-1 mission provides cloud-free and open imagery on a 6 or 12-day repeat cycle, offering the unique opportunity to monitor forest disturbances in a timely and continuous manner. Despite recent advances, mapping subtle forest losses, such as those due to small-scale and irregular selective logging, remains problematic. A Cumulative Sum (CuSum) approach has been recently proposed for forest monitoring applications, with preliminary studies showing promising results. Unfortunately, the lack of accurate in-situ measurements of tropical forest loss has prevented a full validation of this approach, especially in the case of low-intensity logging. In this study, we used high-quality field measurements from the tropical Forest Degradation Experiment (FODEX), combining UAV LiDAR, Terrestrial Laser Scanning (TLS) and field-inventoried data of forest structural change collected in two logging concessions in Gabon and Peru. The CuSum algorithm was applied to VV-polarised Sentinel-1 ground range detected (GRD) time series to monitor a range of canopy loss events, from individual tree extraction to forest clear cuts. We developed a single change metric using the maximum of the CuSum distribution, retrieving location, time and magnitude of the disturbance events. A comparison of the CuSum algorithm with the LiDAR reference map resulted in a 78% success rate for the test site in Gabon and 65% success rate for the test site in Peru, for disturbances as small as 0.01 ha in size and for canopy height losses as fine as 10 m. A correlation between the change metric and above ground biomass (AGB) change was found with R^2 = 0.95, and R^2 = 0.83 for canopy height loss. From the regression model we directly estimated local AGB loss maps for the year 2020, at 1 ha scale and in percentages of AGB loss. Comparison with the Global Forest

Watch (GFW) Tree Cover Loss (TCL) product showed a 61% overlap between the two maps when considering only deforested pixels, with 504 ha of deforestation detected by CuSum versus 348 ha detected by GFW. Low intensity disturbances captured by the CuSum method were largely undetected by GFW and by the SAR-based RADD Alert System. The results of this study confirm this approach as a simple and reproducible change detection method for monitoring and quantifying fine-scale to high intensity forest disturbances, even in the case of multi-storied and high biomass forests.

3.1 Introduction

Forests are the major component of the terrestrial ecosystem (Pan et al., 2013), covering 31% of Earth's total land area (FAO, 2020). They play a key role in modulating the climate system (Mitchard, 2018; Nunes et al., 2020) and provide an essential source of livelihood and socio-cultural identity to local communities. The tropical biome has the largest proportion of the world's forests and the richest biodiversity, hosting 50-90% of all terrestrial species (Hoang and Kanemoto, 2021). Unfortunately, tropical forest cover has been declining annually over the last 30 years (FAO, 2020; Hansen et al., 2013), contributing to anthropogenic greenhouse gas emissions (Federici et al., 2015), biodiversity losses (Giam, 2017), disturbances in the terrestrial water cycle (D'Almeida et al., 2007) and a potential increase of infectious diseases (Castro et al., 2019; Beuchle et al., 2021). Tropical deforestation is largely driven by the expansion of agriculture and tree plantations to meet the increasing demands of global supply chains, mainly in beef and oilseeds (Pendrill et al., 2019b,a; Henders et al., 2015). Knowledge of the spatiotemporal patterns of forest disturbance can greatly contribute towards the conservation efforts; however, forest-based interventions will ultimately be effective only if framed within a critical political ecology perspective, and when the current economic model - the main driver of global deforestation - is challenged (McAfee, 2012; Nielsen, 2014; Poudel et al., 2015; Bayrak and Marafa, 2016; Asiyanbi et al., 2017).

Satellite remote sensing is the most suitable tool for estimating rates and areas of forest canopy loss at large spatial scales and in remote regions (Achard et al., 2010). In the last decade, thanks to technical advancements in remote sensing technology and the availability of satellite imagery at high spatial and temporal resolutions, yearly maps of forest loss and alert systems tracking forest disturbances in near real-time (NRT) have become operational at the national and global scale (Hansen et al., 2013, 2016; Shimabukuro et al., 2006; Vargas et al., 2019; Reiche et al., 2021). However, the extension and magnitude of finer disturbances, such as those caused by selective logging, is still

largely uncertain (Bullock et al., 2020). Recent analyses of long-term disturbances in the Brazilian Amazon have found that forest degradation affects a larger area of land than deforestation (Matricardi et al., 2020). Qin et al. (2021) have estimated that, for the period 2010-2019, 73% of the overall above ground biomass (AGB) losses in the Brazilian Amazon came from forest degradation, and only 27% from deforestation. A 30 year (1990-2019) pantropical analysis of the JRC dataset on Tropical Moist Forest (TMF) by Vancutsem et al. (2021) has shown that during the past 5 years annual deforestation has declined by 5% while forest degradation has increased by 38%, becoming the main contributing factor to forest cover loss (+2.1 million ha/year compared with the period 2005–2014). While the rate of deforestation is affected by the outcome of national territorial policies, the same is not true for the degradation rates, whose patterns are more closely interrelated with the climatic conditions (Vancutsem et al., 2021). Indeed, the JRC-TMF dataset shows that, in the Brazilian Amazon, the area of forest degradation due to selective logging and forest fires remains stable or even increases over the years of decreasing deforestation (Beuchle et al., 2021). These results stress the importance of enhancing the detection accuracy of small-scale forest disturbances, shifting the focus of national policy to monitoring and curbing this form of environmental degradation, which often precedes outright deforestation (Matricardi et al., 2020). In the tropics, monitoring systems relying on optical satellite imagery, such as the Global Forest Watch Humid Tropical Forest Alerts (Hansen et al., 2016) and the Brazilian Real-Time System for Detection of Deforestation (Shimabukuro et al., 2006), are inherently limited by cloud cover, cloud shadows, weather conditions, and rapid vegetation regrowth removing the transient signs of the disturbance events (Asner et al., 2004; Shimizu et al., 2019). For accurate monitoring of selective logging and small clearings, frequent and temporally consistent image acquisitions are needed (Herold et al., 2011). At present, Synthetic Aperture Radar (SAR) systems are the most promising tools for mapping forest disturbances in the tropics (Joshi et al., 2016; Bouvet et al., 2018a; Reiche et al., 2021; Ballère et al., 2021), thanks to the ability of the radar signal to penetrate through clouds

and to its sensitivity to forest structural parameters (Joshi et al., 2015; Mitchard et al., 2011b). The European Space Agency (ESA) Sentinel-1 mission provides free-of-charge C-band SAR images at 10 m spatial resolution and at high temporal frequencies (6 to 12 days, depending on location and data type). Sentinel-1 operates at a frequency of 5.405 GHz, corresponding to a wavelenght of ≈5 cm. Longer wavelength L-band SAR signal (≈23 cm) is considered more suitable for forest disturbance monitoring and AGB estimation than the shorter wavelength C-band SAR data (Yu and Saatchi, 2016; Mitchard et al., 2011b) because of the rapid signal saturation in high biomass forests (Le Toan et al., 1992; Imhoff, 1995; Joshi et al., 2017). However, recent work has demonstrated how the high spatial resolution combined with the frequent observations of Sentinel-1 can overcome the limitations of C-band radar, showing great potential for mapping small-scale disturbances in an accurate and timely manner (Reiche et al., 2018a; Bouvet et al., 2018b; Reiche et al., 2021; Ballère et al., 2021; Hirschmugl et al., 2020). Most approaches measured changes in SAR backscatter intensity over time, applying empirical thresholds to distinguish disturbed areas (Deutscher et al., 2017; Verhegghen et al., 2016; Lohberger et al., 2018). Bouvet et al. (2018a) introduced a novel method making use of the geometric effects of SAR shadowing to detect forest disturbances near forest edges. More recently, the first SAR-based alert system, the Radar for Detecting Deforestation (RADD) Forest Disturbance Alert, was developed for monitoring pantropical forests in near real-time (Reiche et al., 2021). The RADD system makes use of a Bayesian approach and Gaussian Mixture Models derived from historical time series metrics to calculate the probability of change in each forest pixel (Reiche et al., 2018a).

The methods mentioned above are increasingly refining the accuracy of forest disturbance detections in time and space. However, they do not provide information on changes in forest structure, for example related to biomass values or tree canopy heights. Previous research has related L-band backscatter signal to changes in AGB using a regional

empirical regression model and bi-temporal ALOS PALSAR imagery (Ryan et al., 2012). AGB was estimated at the two time points, and then the difference in AGB was calculated by subtracting the two estimates. This method is polluted by error propagation as uncertainties from each map are summed up (Hirschmugl et al., 2020).

The study presented here employs a change detection method based on the cumulative sums of Sentinel-1 time series, to retrieve information on location, time and magnitude of small-scale forest disturbance, including selective logging. The method was recently proposed for monitoring forest disturbances (Ruiz-Ramos et al., 2020) and tested on a tropical site with promising results (Ygorra et al., 2021). Here we validate this novel approach on a unique, ground-measured dataset collected by the Forest Degradation Experiment (FODEX) in Gabon and Peru, using a combination of UAV Lidar, Terrestrial Laser Scanning (TLS) and forest inventory data of small-scale disturbances caused by selective logging. In this paper we adopt the term 'forest disturbance' to describe a decrease in forest cover, which may result in the full conversion of forested land into another land type (deforestation) or in an altered ecosystem that still retains the definition of forest (Houghton, 2012). This includes natural or anthropogenic causes, such as forest fires, selective logging, forest fragmentation and edge effects. We prefer to use the term forest disturbance over forest degradation, as the former does not contain any attempt at classifying the fate and the nature of the change event, on which we may not have sufficient information (Reiche et al., 2021; Beuchle et al., 2021).As for 'low-intensity disturbance', we refer to an event that results in the removal of less than 50% of forest biomass per hectare (Houghton, 2012).In conclusion, the novelties of the present work are: (1) The validation of a SAR-based change detection algorithm on *in-situ* measurements of tropical forest loss; (2) the design of an empirically-derived, single change metric for retrieving information on location, time and magnitude of the disturbance; (3) the possibility of scaling the algorithm on larger areas, which will be addressed in the Discussion section.

3.2 Materials and Methods

3.2.1 Study Areas

To ensure the reproducibility of the change detection algorithm, we located our study areas in two distinct tropical forest ecosystems, located in the rainforests of the Amazon basin (Peru) and Central Africa (Gabon) (Figure 3.1). While having distinct forest types and ecology, we set up experimental disturbance plots and collected as far as possible identical datasets before and after logging, to act as an ideal calibration and validation site for such algorithms.

Gabon is the second most forested country in the world, with forests covering about 88% of its surface area (Poulsen et al., 2017). We established our field plots in the Ogooué-Ivindo province, in proximity of a disused airstrip (0.148 °S, 12.264 °E, Figure 3.1**A**) about 9 km North of the Ivindo village. The area is dominated by mixed lowland tropical forest, and is part of a logging concession managed by the French company Rougier Gabon, who harvests principally *Aucoumea klaineana* (Okoumé) for commercial timber. The logging concession is certified by the Forest Stewardship Council (FSC-C144419) (Carstairs et al., 2022a). The climate in the region is sub-equatorial and is characterised by the alternation of two dry seasons (June-August and December-February) and two rainy seasons (September-November and March-April). The average annual temperatures is 24 °C while the annual rainfall is around 1500 mm year^{-1}, as measured by the Tropical Rainfall Measuring Mission (TRMM 3B43) for the period going from 2009 to 2019 (Adler et al., 2003).

The second study region is located in the the southeastern Peruvian Amazon, in the Madre de Dios department. Madre de Dios is considered a biodiversity hotspot, with 40% of its territory covered by Natural Protected Areas and home to several Indigenous Communities, some of which live in voluntary isolation (Tarazona and Miyasiro-López, 2020). The presence of gold in the soil and river sediment, which is often illegally mined,

makes this area particularly vulnerable to environmental degradation (Markham and Sangermano, 2018; Diringer et al., 2020). Deforestation and forest degradation rates have been exacerbated as a result of the construction of the Interoceanic Highway (2006-2012), opening up the area for further development, agriculture, and extractivist operations (Caballero Espejo et al., 2018). We estabished the field sites in the territory of the Indigenous Bélgica Yine Community (11.02 °S, 69.72 °W, Figure 3.1**B**), about 6 km South of the Bélgica village, in an area of planned logging operations. Since 2010, the Bélgica has contracted a logging company, MADERYJA, to carry out FSC-certified timber harvesting within their forest concession (Burga Cahuana, 2013). The area is characterised by lowland tropical rainforest with a well drained forest floor (*terra firme*). The climate is warm and humid, with a dry season from May to October and a rainy season from November to April. According to the TRMM precipitation estimates, annual rainfall for this site is around 1900 mm year^{-1} for the decade 2009-2019.

Table 3.1: Forest structure characteristics of each study site. Stem densities and Aboveground Biomass (AGB) densities are derived from field inventories of all stems $>$ 10 cm Diameter at Breast Height (DBH) in eight permanent sample plots located in the two study areas. Tree heights are derived from Terrestrial Laser Scanning (TLS) measurements of the largest trees in the plots. Mortality rates for the regions are taken from Lewis *et al.* Lewis et al. (2004)

Study Area	Tree Height [m]	Stem Density [trees ha^{-1}]	AGB Density [Mg ha^{-1}]	Mortality Rate [% year^{-1}]
Ivindo, Gabon	32 - 50	300	470	1.06
Bélgica, Peru	22 - 46	650	280	2.02

3.2.2 Field Data

Four 1-ha Permanent Sample Plots were established in each logging concession and inventoried in two phases, before and after the extraction of selected trees. Standard forest inventory techniques from Phillips et al. (2001) were employed alongside Terrestrial Laser Scanning (TLS) measurements, providing three dimensional models of

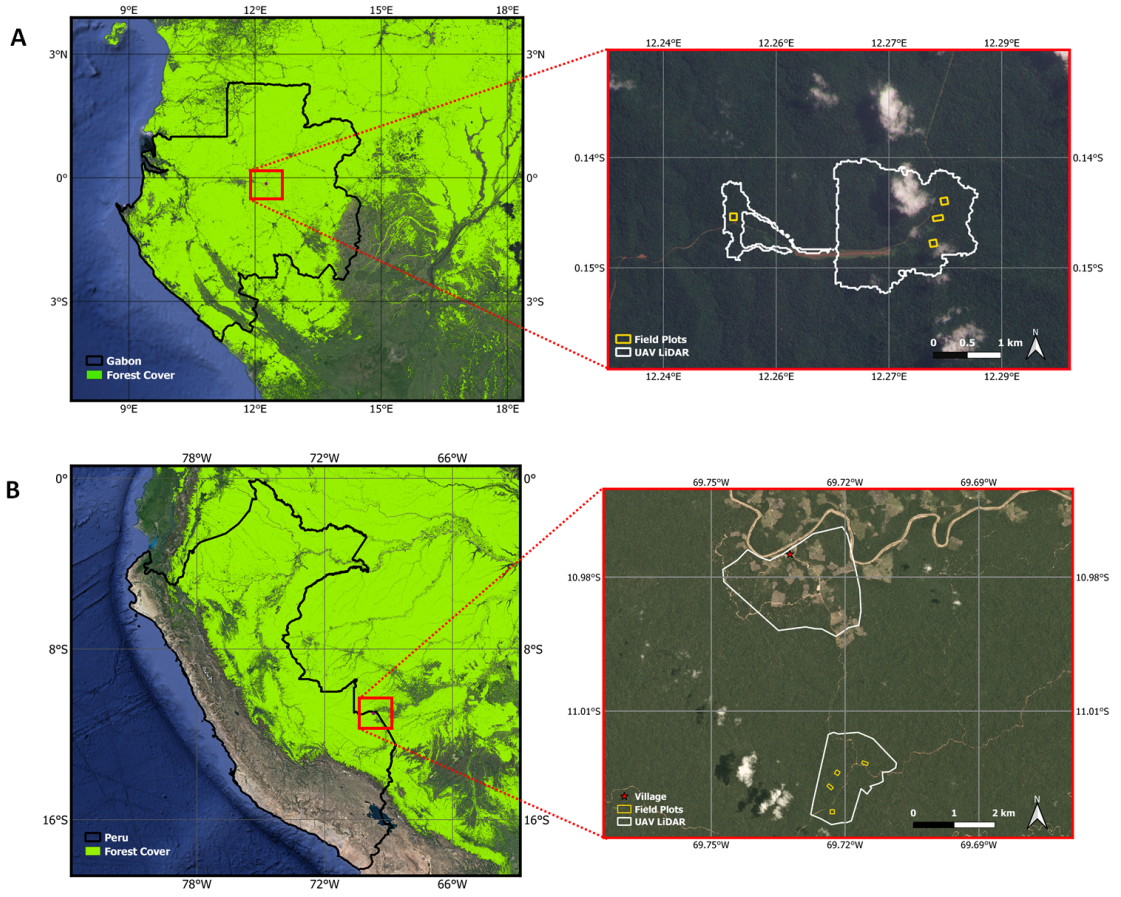

Figure 3.1: Location of the two study areas in (A) Gabon and (B) Peru. The left panels show the position of the field sites within the country boundaries. The layer in bright green is the primary humid tropical forest extent for the year 2001 from Turubanova et al. (2018). The right panels show the location of the forest plots (yellow boxes) and the area covered by the UAV LiDAR acquisitions (white). Both RGB images of the field sites date to May 2022 and are 3 m PlanetScope images acquired through Planet's Education and Research Program (Planet Team, 2017)

each tree. We also used a LiDAR sensor mounted on a unoccupied aerial vehicle (UAV) to collect change data from the wider concession. In Peru the surveyed zone includes the village surroundings, where land conversion due to agricultural expansion is taking place during the dry season, giving areas with greater forest disturbance proportions than the plots (up to 100% AGB loss) (Figure 3.1**B**).

Forest inventory

In Gabon, we established four plots in the forested area surrounding a disused airstrip, at an altitude of 500 m and on flat ground, to facilitate the UAV operations (Figure 3.1**A**). The plots had an area within 10% of 1 ha and orientations spanning 0-10°North. The position of the plot corners were measured by a differential GPS and corrected using the coordinates of the integrated GNSS receiver of the TLS. Forest inventory campaigns took place in August 2019 and then in February 2020, to account for the removal of 18 trees operated by Rougier Gabon at the end of January 2020. In Peru, we delimited four plots in the forest in proximity of the road that connects Bélgica to Iñapari, at an altitude of 300 m above sea level (Figure 3.1**B**). The plots were chosen in consultation with community members and in areas that were rich in valuable timber species, especially for use in community buildings. The plots had an area within 10% of 1 ha and orientations spanning 0-40° North. Forest inventory data was collected in May 2019 and then in October 2020, to measure biomass change resulting from the extraction of 24 trees during the second half of July 2019. In both sites, trees were selectively removed according to FSC logging protocols, in different proportions for each plot, to reproduce a range of degradation events. The Diameter at Breast Height (DBH) of the removed trees ranged between 79-131 cm in Gabon and 50-129 cm in Peru. During the pre-logging campaigns, we adopted the RAINFOR inventory protocols Phillips et al. (2001) to identify, tag and measure every living stem with DBH $>$ 10 cm. The average DBH recorded was 30 cm in Gabon and 21 cm in Peru, with DBH values ranging between 10 - 160 cm and 10 - 158 cm, respectively. We also collected X and Y coordinates ($\approx\pm$2 m) and determined tree species information with the assistance of local botanists. Each stem was visually inspected for damage and labelled according to the percentage of its remaining biomass (25, 50, 75 or 90%) as compared to an intact stem of the same size. During the post-logging inventories, as well as remeasuring all the remaining trees, we recorded the direction of tree felling and assessed the collateral damage

caused by the logging activities, according to the damage classes described above. Wood density estimates were derived from a global wood density database using tree species information Chave et al. (2009). When possible, we used species-specific wood density values. When multiple wood density values were available for the same taxon, we reported the arithmetic mean. In cases where wood density values were unavailable for a species, we used the average across the genus (29% of the stems); and, where no values were available, we applied the plot average (25% of the stems) (Medjibe et al., 2013).

A pantropical allometric model from Chave et al. (2014) was used to derive total AGB of trees in each plot from DBH (D) and wood density (ρ) values, according to a regional environmental stress factor (E) that averaged -0.096 in Gabon and 0.068 in Peru (Chave, 2014). The equation is in the following form:

$$\mathrm{AGB} = \exp[-1.803 - 0.976(E - \ln(\rho)) + 2.673\ln(D) - 0.0299 \times [\ln(D)]^2] \quad (3.1)$$

Allometric estimates of AGB at individual tree scale are found to have large uncertainties (Chave et al., 2014) which tend to increase with tree size (Burt et al., 2021; Gonzalez de Tanago et al., 2018). On the other hand, TLS measurements are found to be in better agreement with the volume data from destructive harvest experiments, with a mean tree-scale relative error of 3% (Burt et al., 2021), thus providing more accurate estimates of AGB values.

Terrestrial Laser Scanning

TLS data were collected at the same time as the pre-logging campaigns using a Riegl VZ-400 scanner. The plots were subdivided in 10 x 10 m squares and two scans were obtained at every grid intersection point, following the procedures outlined in (Wilkes et al., 2017). The point clouds of the logged trees, extracted via the treeseg package (Burt et al., 2019), were used to calculate the quantitative structural models of tree

Table 3.2: Aboveground Biomass (AGB) before and after logging and Aboveground Biomass Change (ΔAGB) figures for eight 1-ha selectively logged plots located in Gabon (G) and Peru (P), obtained by field surveys and Terrestrial Laser Scanning (TLS). Standard errors are reported in parentheses and calculated as $\sigma = \sqrt{\frac{\sum_{i=1}^{n} x_i^2}{N}}$, where x corresponds to the AGB value for each tree i

.

Plot	AGB Before Logging [Mg ha^{-1}]	AGB After Logging [Mg ha^{-1}]	Number of Trees Logged	ΔAGB [Mg ha^{-1}]	ΔAGB [% ha^{-1}]
GC1	574.2 (35.4)	443.0 (32.8)	7	131.2 (12.8)	22.8 (2.8)
GC2	399.5 (27.9)	371.1 (27.2)	2	28.3 (4.8)	7.1 (1.3)
GC3	435.3 (27.8)	380.4 (26.7)	4	55.0 (7.1)	12.6 (1.8)
GC4	473.8 (38.1)	364.9 (36.0)	5	108.9 (10.4)	23.0 (3.1)
PC1	295.6 (15.8)	245.9 (15.0)	9	49.7 (5.0)	16.8 (2.0)
PC2	266.6 (13.4)	229.5 (12.2)	6	37.1 (3.2)	13.9 (1.4)
PC3	270.7 (24.0)	189.7 (10.5)	7	81.0 (4.2)	29.9 (3.3)
PC4	261.8 (17.7)	249.1 (15.3)	2	12.8 (1.0)	4.9 (0.5)

volume (QSMs) (Calders et al., 2015; Raumonen et al., 2013). From the QSMs, the AGB of the logged trees was obtained by multiplying wood density by model volume. At the time of the analysis, processed TLS data volumes were only available for the logged trees, hence it was not possible to calculate the total AGB per plot using the TLS measurements. It is important to note that the logged trees in our experiment were, in most cases, the largest trees in the plots, with an average DBH of 102 cm (Gabon) and 79 cm (Peru). To increase accuracy and reduce allometric bias, we adopted TLS-derived biomass estimates for the logged stems. Total AGB change per plot was then calculated by summing the TLS-derived AGB of the logged trees plus the difference in allometric AGB of the remaining trees as measured by the forest inventory surveys (Table 3.2). Given their smaller sizes, we do not expect significant differences between AGB and TLS-derived estimates for the non-logged trees; on the other hand, if we use allometric equations for the logged trees, then the biomass removed per plot is overestimated by up to 29% in Peru and underestimated by up to 15% in Gabon, as compared to the values derived from the TLS measurements (Table C.1, Figure C.1).

UAV LiDAR

In Gabon, UAV LiDAR data were obtained in January 2020, prior to selective logging in the permanent plots, and then in January 2021, to measure the widespread disturbance resulting from commercial logging operations in proximity of the airstrip, which took place between November and December 2020. In Peru, the first UAV LiDAR campaign took place in May 2019 in conjunction with the pre-logging census. The post-logging LiDAR data were acquired in September 2021, accounting for changes in canopy cover due to selective logging in the study plots and agricultural encroachment in the forest fringes near the village area. For both Gabon censuses, and the first Peru census, a RIEGL miniVUX-1DL LiDAR mounted on a DELAIR DT26X fixed-wing UAV was flown at 140 m above the ground and at a speed of $\approx$17 ms^{-1}, yielding a point density of 240 pts m^{-2}. For the post-logging campaign in Peru a LiDAR RIEGL Minivux-2UAV mounted on a rotor craft was used for the UAV data collection, yielding a point density of 200 pts m^{-2}. Flight trajectories were corrected using post-processing kinematic (PPK) positioning from ground control points and a GNSS base station, resulting in a geometric accuracy of 1.8 cm (McNicol et al., 2021b). Canopy height models (CHM) for a total area of 1239 ha (354 ha in Gabon and 885 in Peru) were generated by taking the difference between the highest and lowest returns in a 25 cm cell and after noise filtering (McNicol et al., 2021b). For each site, a ΔCHM raster was obtained by taking the difference between the pre- and post-logging CHMs. Losses in canopy cover were identified as in areas where ΔCHM decreased by 10 m or more (Figure 3.2).

3.2.3 Sentinel-1 SAR Data

The European Space Agency (ESA) Sentinel-1 mission provides dual-polarisation Synthetic Aperture Radar (SAR) data at high spatial and temporal resolution. The Sentinel-1 constellation comprises two satellites: Sentinel-1A and Sentinel-1B, launched on 3rd April 2014 and 25th April 2016, respectively. Each satellite carries a SAR C-Band in-

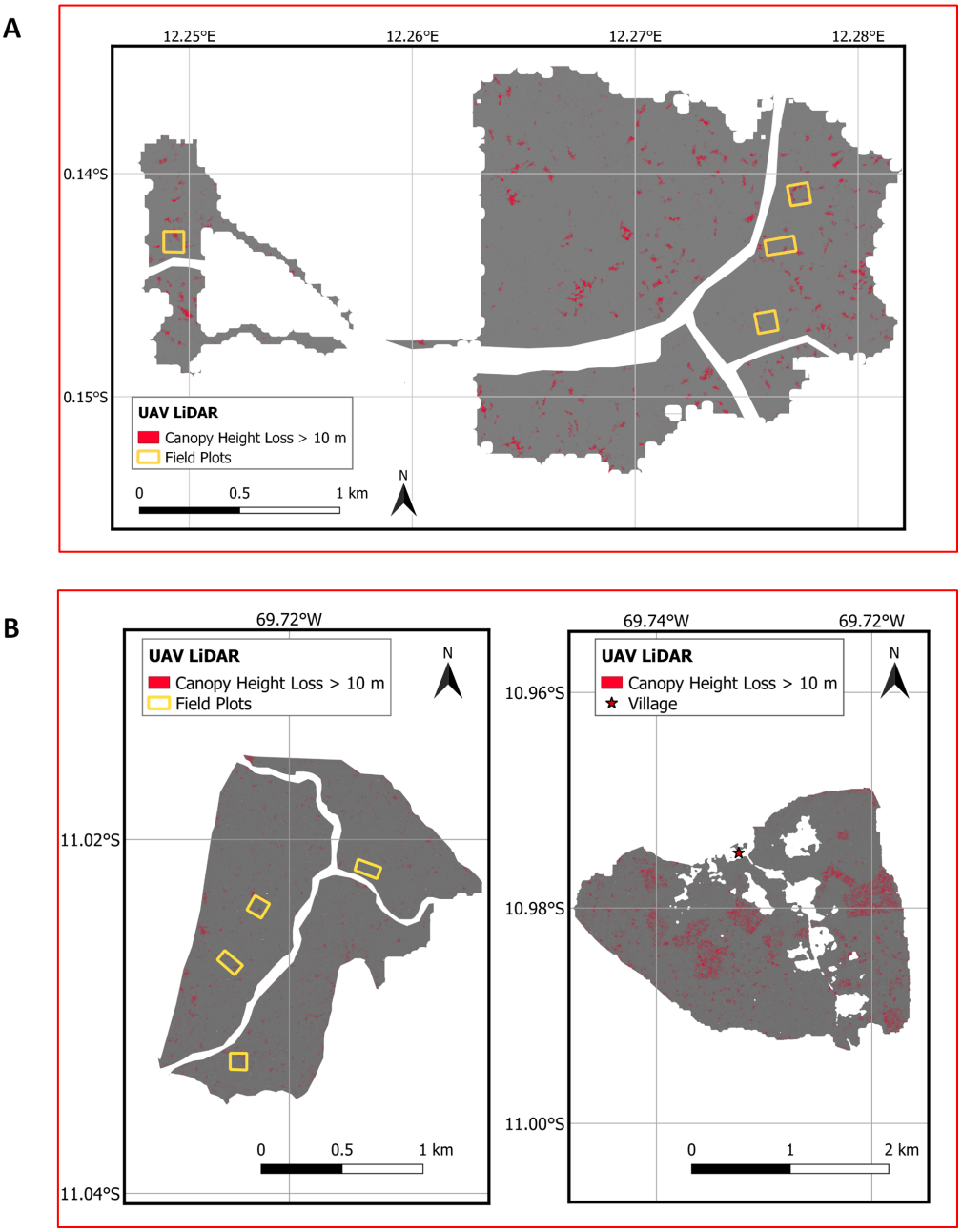

Figure 3.2: Canopy height change from UAV LiDAR measurements (gray image) showing losses in forest canopy height of more than 10 m (red). (A) Canopy height loss in Gabon from January 2020 to January 2021 indicating patches of disturbance in the study plots and in the surrounding concession; (B) Canopy height loss in Peru from May 2019 to September 2021, showing fine-scale losses in the area of the study plots (left panel) and more intensive, consistent patterns of forest to agriculture conversion in proximity of the village (right panel).

strument onboard operating at a frequency of 5.405 GHz in 4 different modes. The preferred mode for land use applications is Interferometric Wide-swath (IW) with a ground

resolution of 20 m × 5 m and a swath width of 250 km. The repeat orbit cycle of each satellite is 12 days over the field sites. The data used in this study were acquired as VV-polarised, ground range detected (GRD) products in IW mode. The provided pixel size is 10 m $\times$ 10 m. All images were retrieved in descending mode and using the same orbit for each study area (relative orbit number 80 for Gabon and 127 for Peru) to ensure a consistent radar geometry for all the scenes. All available imagery were retrieved from the geospatial cloud computing platform Google Earth Engine (GEE) (Gorelick et al., 2017) using the Python API. Sentinel-1 GRD scenes are provided by GEE already preprocessed and radiometrically calibrated to the backscatter coefficient σ^o in decibels (dB) (Google Earth Engine, 2021b).

3.2.4 Change Detection with Cumulative Sums

The cumulative sum (CuSum) algorithm is recognised as a powerful statistical method for detecting abrupt and systematic changes in time series data (Page, 1955; Taylor, 2008; Manogaran and Lopez, 2018). While being extensively used for monitoring market trends and industrial processes (Manly and Mackenzie, 2003), it has recently found applications in the environmental sciences for detecting seasonal climate changes (Manogaran and Lopez, 2018) and for monitoring deforestation and forest degradation in temperate (Ruiz-Ramos et al., 2020; Kellndorfer et al., 2019) and tropical forests (Ygorra et al., 2021). Results from Ruiz-Ramos et al. (2020) and Ygorra et al. (2021) have shown the robustness of this method for detecting cover changes in forest canopy, with overall accuracy of 77% and 91%, respectively. However, the data they used to obtain these numbers were produced by visual interpretation of optical satellite imagery, which presents many limitations. Even in 3 m resolution PlanetScope images, degradation effects preceding deforestation cannot be immediately detected, especially in the case of dense and multi-storied canopies. Moreover, and this is particularly relevant in tropical environments, canopy gaps can quickly recover in between two cloud-free images, resulting in a large

underestimation of actual forest disturbances (Ygorra et al., 2021; Asner et al., 2004; Shimizu et al., 2019). By contrast in this study we use very high resolution (25 cm) *in situ* data from UAV LiDAR to validate the CuSum method in its ability to detect subtle changes in forest canopy resulting from low-intensity logging.

CuSum implementation

Ygorra et al. (2021) found that in tropical forests the co-polarised backscatter (VV) showed best results, as compared to the cross-polarised channel (VH), and this was also confirmed by our preliminary tests. Therefore, time series data stacks were generated using the VV-polarised channel containing the spatial information (range and azimuth) and the temporal dimension for each pixel of the Sentinel-1 image over the study area and for a selected study period. The study period was set as the time of the UAV LiDAR acquisitions (January 2020 - January 2021 for Gabon and May 2019 - September 2021 for Peru). In order to capture all forest loss in the study period and build the control trend in absence of structural changes, the data cubes included all observations extending from at least one year before (reference or pre-change data) to at least six months after the UAV measurements (recovering or post-change data). For Gabon the data cube comprised a total of 89 scenes from 6th January 2019 to 21st December 2021; while for Peru a total of 127 scenes from 2nd January 2018 to 18th March 2022 were downloaded.

The cumulative sum of the residuals (CuSum) is defined as the cumulative sum of the difference between each pixel value and the mean of the timeseries:

$$R_{sum\,j} = \sum_{j=1}^{n} \sigma^{o}_{j,i} - \overline{\sigma^{o}_{i}} \tag{3.2}$$

where $\sigma^{o}_{j,i}$ is the value of each pixel i for each image j, n is the number of images and $\overline{\sigma^{o}_{i}}$ is the mean of the time series over each pixel i. Iteratively, CuSum can be written as:

$$R_{sum\,j} = (\sigma_j^o - \overline{\sigma_j^o} + R_{j-1}, j = 1,2,3,...n) \tag{3.3}$$

where the starting value for the CuSum, R_0, is equal to zero.

Figure 3.3 compares the resulting CuSum curves for disturbed and undisturbed pixels in two of our field plots, where we have precise information on the location and timing of the change event. For undisturbed pixels, seasonal variations in canopy cover (ie. phenology), or changes in the moisture content of vegetation result in small fluctuations in the CuSum curve, which, in the absence of structural changes, oscillates around a backscatter value of zero. On the other hand, the CuSum of logged pixels appear like a bell-shaped curve, steadily increasing until a sudden turn in direction. Since $\overline{\sigma_i^o}$ is the overall average, a sudden change in direction of the CuSum curve marks a shift or change in the average trend. A downward slope indicates a period of time where the values tend to be below the overall average (Taylor, 2008). Different studies have reported a decrease in the backscatter signal after forest disturbance (Joshi et al., 2015; Reiche et al., 2018a; Kellndorfer et al., 2019; Silva et al., 2022), in agreement with what is observed here. As shown by Figure 3.3, the shift from a positive to a negative trend occurs in coincidence with the time of logging. Hence, the CuSum chart not only gives an indication of change, but it also provides information on *when* the change has occurred.

Threshold Estimation and Accuracy Assessment

Figure 3.3**C** implies that it must be possible to distinguish between disturbed and undisturbed pixels by applying a threshold on the peak of the CuSum curve. *In situ* data on canopy height loss from the UAV LiDAR measurements can be used as reference data to estimate the optimum value for this threshold, instead of adopting statistical methods (Ruiz-Ramos et al., 2020) or parameterised thresholds (Ygorra et al., 2021). The LiDAR-derived ΔCHM raster (Figure 3.2) was first resampled by averaging to cells of 10 x 10 m, to allow direct comparison with Sentinel-1 data. We considered a detection as a canopy

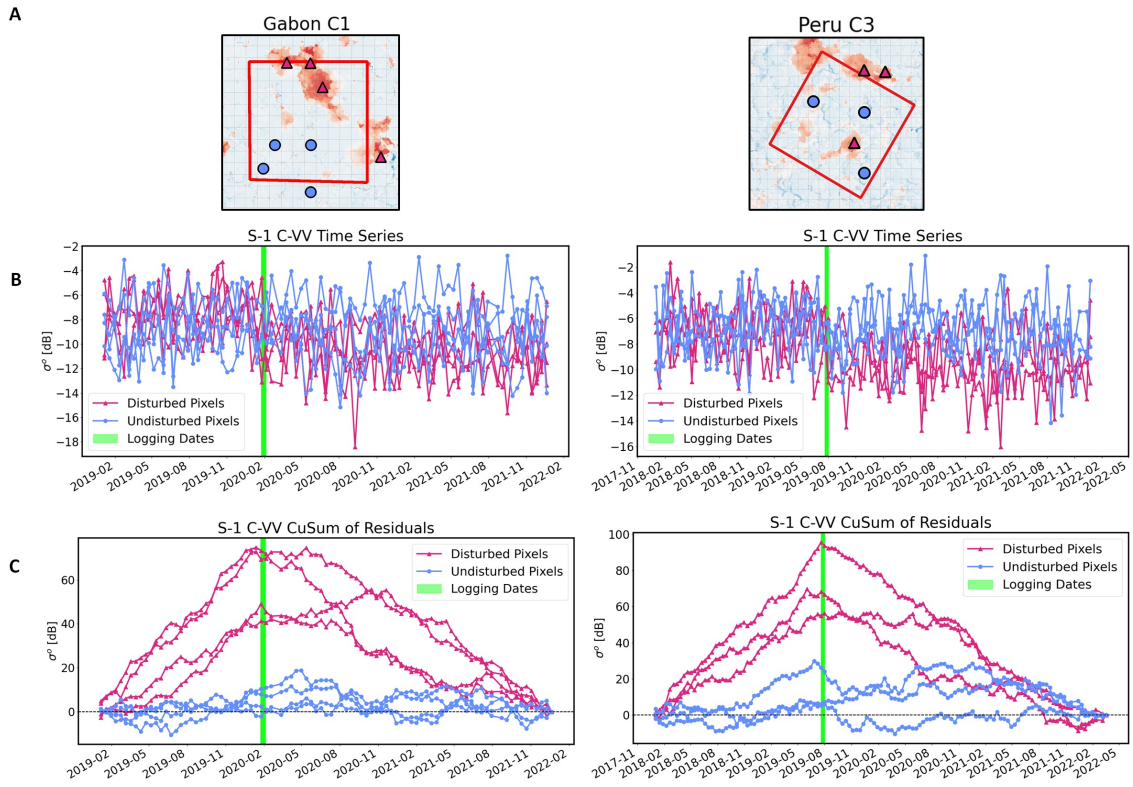

Figure 3.3: Comparison of disturbed and undisturbed pixels for selectively logged plots in (left) Gabon and (right) Peru. (A) Location of the disturbed pixels (purple triangles) and undisturbed pixels (blue circles) on the Canopy Height Change raster from the UAV LiDAR measurements. Disturbance areas on the LiDAR map are indicated in dark red. (B) Time series of Sentinel-1 (S-1) SAR backscatter values for the disturbed and undisturbed pixels. (C) CuSum curves for the disturbed and undisturbed pixels. Pixels where logging activities took place display a bell-shaped curve peaking around the time of logging (green line).

reduction of 10 m or more and determined the threshold on the value of the CuSum peak, or R_{sum_max}, by matching LiDAR canopy height loss to R_{sum_max} values within the same cell. The overall accuracy of the method is defined as the ratio between the number of real detections and the total number of pixels:

$$OverallAccuracy(OA) = \frac{TP+TN}{TP+TN+FP+FN} \tag{3.4}$$

where TP are the True Positive, ie. pixels classified as canopy loss by both the LiDAR and the CuSum algorithm; TN are the True Negative, ie. pixels classified as no change both by the LiDAR and the CuSum algorithm; FP are the False Positive, ie. pixels classified as change by the CuSum algorithm but not by the LiDAR, and FN are the False Negative, ie. pixels classified as change by the LiDAR but not by the CuSum algorithm. The threshold was determined as the value of R_{sum_max} that would minimise the False Negative and False Positive detections in the Sentinel-1 observations, in reference to the LiDAR data (Figure 3.4). Once a threshold on R_{sum_max} was applied, adjacent pixels were grouped into polygons to define the boundaries of each disturbance cluster. The same procedure was also applied to the UAV LiDAR data to extract polygons containing canopy loss values $\geq$ 10 m, which were then compared with the disturbance clusters from the CuSum algorithm. The total number of overlaps was calculated by counting the places where the geometries of the two layers intersected. Since the LiDAR data was collected at considerably higher resolution than Sentinel-1 images, small clusters in the LiDAR reference map were grouped into larger clusters by creating a 10 m buffer around each polygon. This step was necessary to avoid double counting LiDAR detections overlapping the same CuSum cluster. We used QGIS software (Polygonize plugin, QGIS version 3.10) to group raster pixels into polygons and to perform all vector operations. The overlap between the polygon datasets was performed using the `overlay()` method from the *geopandas* library implemented in Python.

So far we have described CuSum curves peaking at positive values of σ^o, with a sudden shift in the negative direction at the time of logging (Figure 3.3). Certain pixels in our study areas, however, feature a diametrically opposite trend, with CuSum curves peaking at negative σ^o and then suddenly shifting in the positive direction, meaning an increase in backscatter signal after the change event. Figure 3.5 shows our study area in Gabon with the location of pixels featuring a negative or positive CuSum, after a threshold was applied on both negative and positive peak values, as found by the processing step

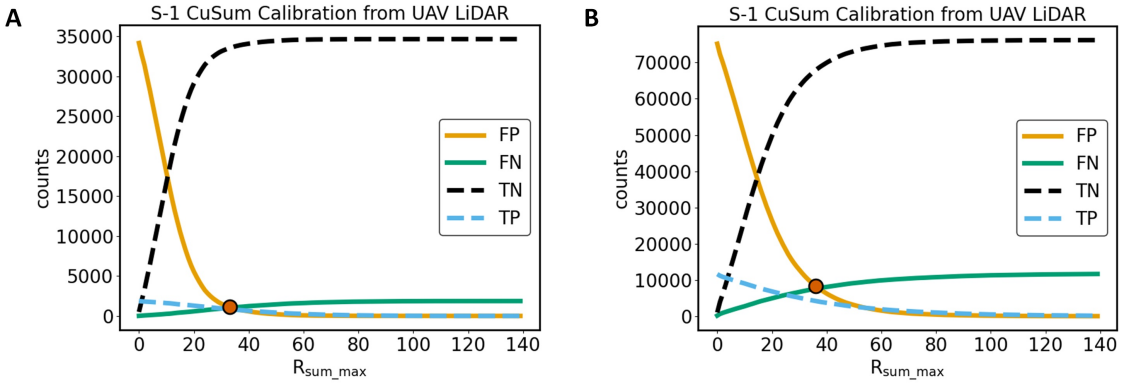

Figure 3.4: Calculating the value of the CuSum maximum (R_{sum_max}) from Sentinel-1 (S-1) time series that would minimise both False Positive (FP) and False Negative (FN) change detections in (A) Gabon and (B) Peru. The optimum value is indicated by a circle at the point of intersection between the FP and FN curves. Change is defined as a canopy height loss $\geq$ 10 m as derived from a UAV LiDAR ΔCHM raster resampled to 10 $\times$ 10 m pixels. The counts in Peru are double the size than Gabon as here the S-1 time series spans two years, consistently with the timeframe of the UAV LiDAR acquisitions. True Positive (TP) and True Negative (TN) curves are also shown in the Figure.

outlined in Figure 3.4. Figure 3.5 shows how pixels with negative CuSum peaks are spatially symmetric to pixels with positive CuSum peaks. However, by overlaying the UAV LiDAR layer, we have found that only the positive CuSum pixels correspond to areas of canopy height loss (Figure 3.5**C**). Hence for this study we have only retained pixels with positive R_{sum_max} values (decreased backscatter), interpreting the latter as canopy gaps, or areas of SAR shadow (Bouvet et al., 2018a), and negative R_{sum_max} values (increased backscatter) as the border between standing forest and the clear-cut (Villard and Borderies, 2007).

Previous studies have found that a CuSum-based change detection method performed better when filtering or smoothing the time-series (Kellndorfer et al., 2019; Ruiz-Ramos et al., 2020; Ygorra et al., 2021). We have tested the detection accuracy of the CuSum algorithm by smoothing the Sentinel-1, VV-polarised time-series with spatiotemporal filters of increasing window sizes, where a size of 1 pixel means that no smoothing was applied. The algorithm was developed using the `signal` module in Python (Virtanen

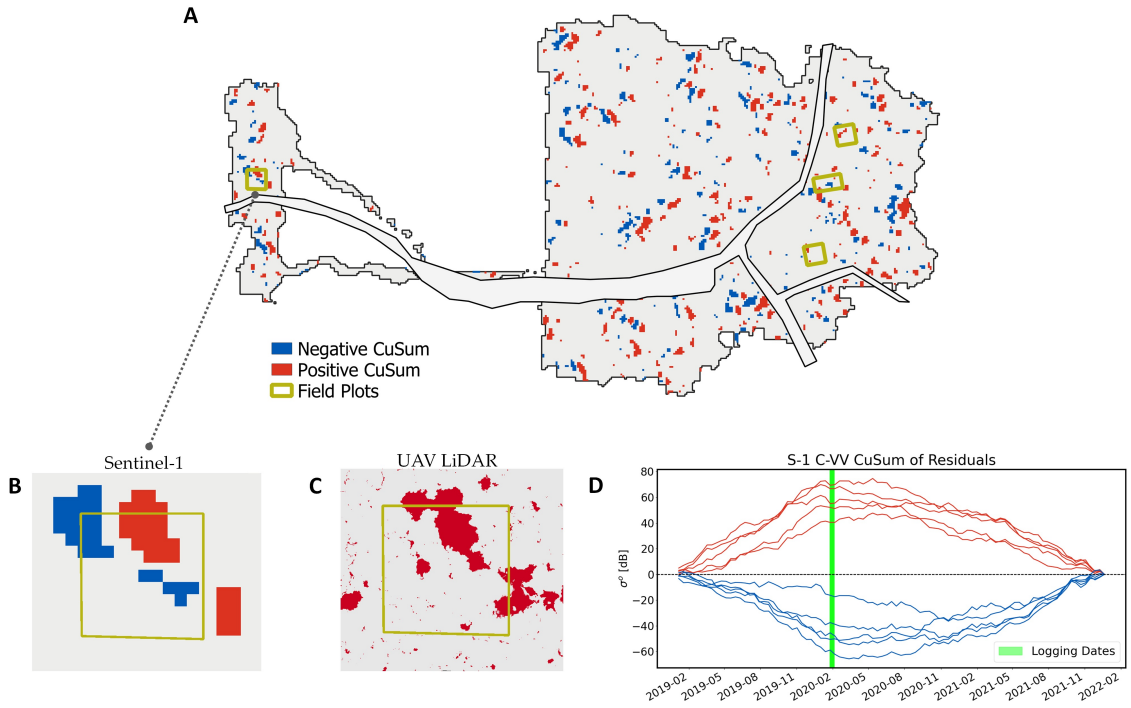

Figure 3.5: (A) Image of the study area in Gabon, showing in blue the location of pixels with negative CuSum curves and in red the location of pixels with positive CuSum curves, after applying a threshold of R_{sum_max} = 33 for the positive values and R_{sum_max} = -33 for the negative values; (B) Zoom on one of the field plots (Gabon C1), indicating how positive and negative values of R_{sum_max} are arranged symmetrically to each others; (C) The same plot, but with canopy height loss ($\geq$ 10 m) from the UAV LiDAR appearing in red; (D) CuSum curves of five pixels with negative R_{sum_max} (blue lines) and five pixels with positive R_{sum_max} (red lines) selected from the same field plot in (B). The time series of the two types of pixels feature diametrically opposite trends, expressing in the time dimension the spatial symmetry that can be seen in (A) and (B).

et al., 2020) and consists of convolving the original time series by a 3D kernel of size $w \times w \times w$, where w is the window size (in pixels). Results are shown in Table 3.3. As accuracy is found to worsen with increasing window size, we did not apply any boxcar filtering to the analysis.

Table 3.3: Comparison between the CuSum algorithm and the UAV LiDAR reference map in the study area in Gabon, when boxcar filters of increasing window sizes are applied. A detection is defined as a canopy height decrease $\geq$ 10 m in the UAV LiDAR reference map. The figures below refer to the fraction of total pixels in the study area that are assigned to each category both by the CuSum change algorithm and the LiDAR map. TP: True Positives, TN: True Negative, FP: False Positive, FN: False Negative, OA: Overall Accuracy.

Window Size (pixels)	R_{sum_max} threshold	FP	FN	TP	TN	OA
1	33	0.031	0.028	0.023	0.918	0.941
3	25	0.030	0.031	0.022	0.918	0.940
5	18	0.033	0.038	0.018	0.911	0.930
7	14	0.039	0.041	0.013	0.908	0.921

3.2.5 Biomass change estimation

Subsequently to selective logging, a reduction in forest cover amounting to a loss of 5 to 30% of initial biomass per hectare was field-measured across the eight study plots, corresponding to very low to low-intensity canopy disturbances. For this analysis we also selected four undisturbed plots (ΔAGB = 0%), two for each study site, in areas that did not experience logging activities. To encompass the full spectrum of forest disturbance, we added three plots in Peru that transitioned from forest to agricultural land (ΔAGB = 100%). The 0% and 100% biomass change plots were determined from empirical knowledge of the study area, in addition to visual inspection of the UAV LiDAR reference map and PlanetScope imagery.

Previous work had successfully correlated decreases in L-band radar backscatter to structural changes in vegetation cover (Mitchard et al., 2011a; Ryan et al., 2012; Joshi et al., 2015). However, biomass estimation in tropical forests is inherently limited by the saturation of the radar signal (Mermoz et al., 2015). Shorter wavelength C-band data is generally considered less useful because of even lower penetration depth, as compared to L-band radar (Woodhouse, 2017; Le Toan et al., 2004). On the other hand, Figure 3.3 shows CuSum curves of logged pixels peaking at different values of σ^o, possibly

indicating a variation in the intensity of the change event. For this reason, we tested the sensitivity of the maximum of the CuSum curve, R_{sum_max}, to changes in the AGB values of the study plots, ΔAGB, before and after selective logging. After taking the average value of R_{sum_max} in each plot, we analysed its relationship with ΔAGB using a linear regression model, taking ΔAGB (in units of % ha^{-1}) as the dependent variable and R_{sum_max} as the independent variable. The linear relationship between the two quantities is in the form $y = mx + c$. Substituting x with R_{sum_max} from the Sentinel-1 observations (resampled to 1 ha pixels), we obtain ΔAGB values for building a biomass change map of the two regions.

Tree Cover Loss map from Global Forest Watch

As *in-situ* biomass change data is not available for the wider regions, we evaluated the performance of the biomass change map in its ability to detect forest loss by comparing it to the Global Forest Watch (GFW) Tree Cover Loss (TCL) product from Hansen et al. (2013) for the year 2020. The comparison was performed for the test region in Peru as this area experiences more widespread forest disturbance. Since tree cover loss in the GFW dataset is defined as the complete removal of tree canopy at the Landsat pixel scale (30 m resolution) (Hansen et al., 2013) we compared this product with the ΔAGB map where we only retained values of 100% biomass loss. We resampled the GFW TCL dataset to 1 ha resolution and calculated the amount of 30 m pixels flagged as tree cover loss to retrieve the total disturbance area.

3.3 Results

3.3.1 Spatiotemporal patterns of forest disturbance

The CuSum formula from Equation 4.1 was applied to the time series of VV-polarised Sentinel-1 images acquired over two study areas in Gabon and Peru. The maximum of the CuSum curve, R_{sum_max}, was chosen as the metric for detecting change. Using the UAV LiDAR acquisitions as a reference map, we determined a detection threshold of $R_{sum\_max} > 33$ for Gabon and $R_{sum\_max} > 36$ for Peru (Figure 3.4), with OA = 94% and OA = 82%, respectively. Figure 3.6 shows pixels classified as detections after the threshold on R_{sum_max} is applied, as compared to the UAV LiDAR reference map. Change pixels are found to be spatially distributed into clusters, displaying geometrical patterns of forest disturbances. By zooming over two selectively logged plots in each study area, it is possible to observe how the clusters obtained from the CuSum algorithm consistently match patches of canopy loss from the LiDAR measurements. In Gabon, during the study period going from January 2020 to January 2021, the CuSum method detected 240 disturbance clusters covering a total of 14.4 ha (4% of the study area), while field data from the LiDAR measurements estimated 317 clusters of canopy loss $\geq$ 10 m, for a total of 18.0 ha (5% of the study area). 78% of the disturbance clusters detected with the CuSum method overlapped the location of the LiDAR detections, with both maps having a minimum mapping unit of 0.01 ha (10 $\times$ 10 m pixel size). Increasing the minimum size of the CuSum disturbance clusters improved the probability of detection: 91% of the clusters with areas $\geq$ 0.02 ha matched the LiDAR reference data, while 100% of the clusters with areas $\geq$ 0.05 ha matched the location of the LiDAR detections. However, increasing the minimum mapping unit reduces the number of detections (Table 3.4). In Peru, the CuSum time series was filtered for the study period going from May 2019 to September 2021, to match the timeframe of the LiDAR acquisitions. In total, ie. both in the village area and the field plot site, the CuSum algorithm detected 484 disturbance

clusters, with a total area of 57.7 ha (7% of the study area), while the LiDAR reference map estimated 689 disturbance patches, giving a total of 84.8 ha (10% of the study area). 65% of the CuSum detections overlapped the location of the LiDAR disturbances. This figure increased to 90% when considering CuSum clusters $\geq$ 0.05 ha, and to 99% for CuSum clusters $\geq$ 0.1 ha (Table 3.4).

The position of R_{sum_max} in the CuSum chart corresponds to the moment in time immediately before backscatter intensity drops below the historical average. As a result, the time of the disturbance event was derived by selecting the date of the image that follows the date of the inflection point in the time series. Disturbance events were filtered to retain only change pixels within a single year. This was chosen as the year when selective logging occurred in the permanent sample plots, ie. 2020 for Gabon and 2019 for Peru. Figure 3.7 shows the timing of the change detections, in units of Day of Year (DOY), in both our study areas. In Gabon, the field plots were selectively logged at the end of January 2020, while commercial logging operations in the surrounding area were carried out between November and December 2020, in coincidence with the second dry season (Figure 3.7**A**). In Peru, selected trees were extracted from the study plots during the second part of July 2019, while the rest of the area remained mostly undisturbed (Figure 3.7**B**). More significant patches of disturbance are observed near the village during a period going from June to August (Figure 3.7**C**). Indeed this time frame corresponds to the peak of the dry season, when forests fringes are cleared for agricultural fields and pasture. These observations have been further confirmed by inspection of PlanetScope imagery and conversations with the Bélgica community.

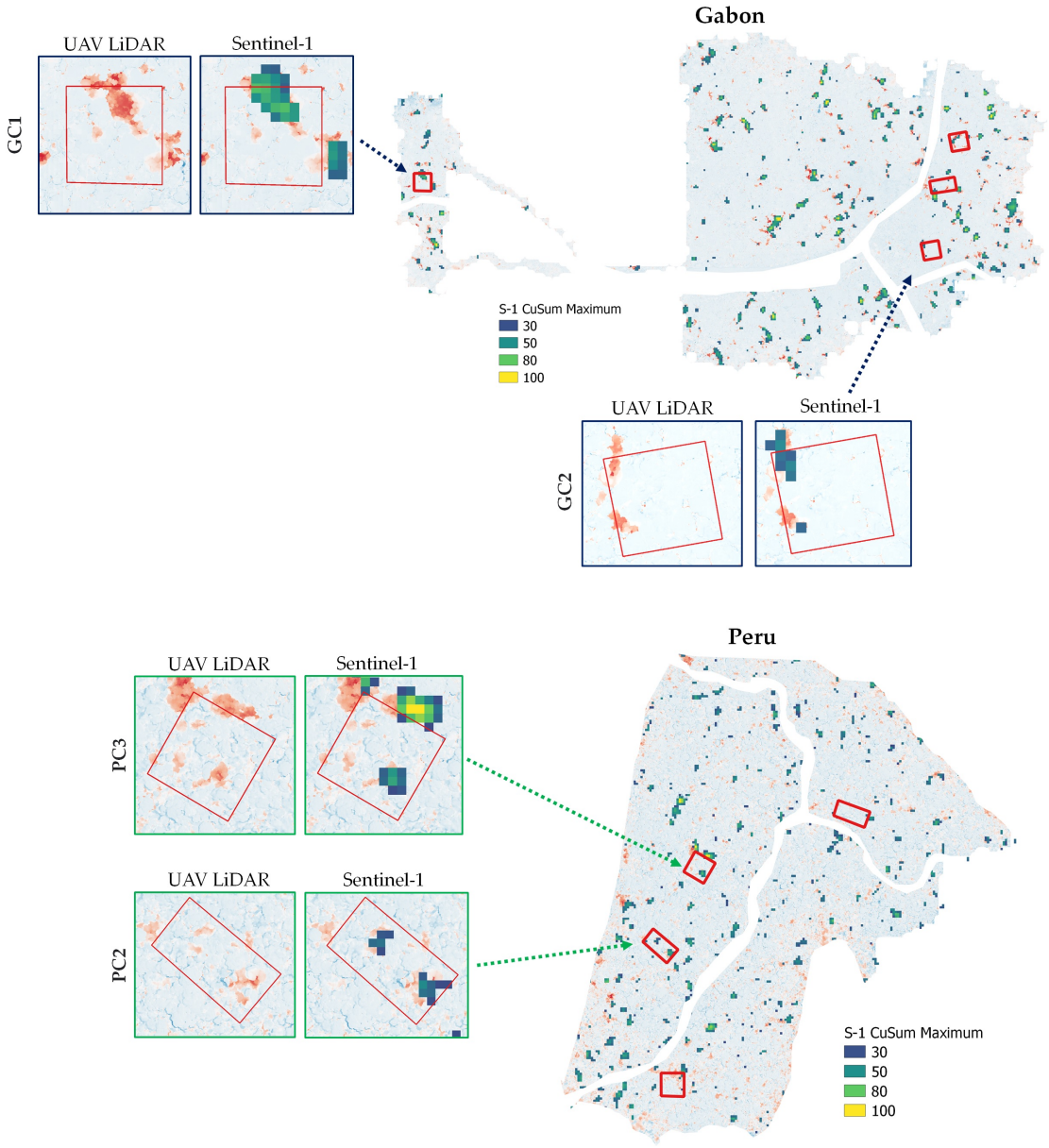

Figure 3.6: Results of the CuSum change detection algorithm showing the location of the forest disturbance pixels in the study areas in Gabon (top) and Peru (bottom). The inlets are zoomed views of two selectively logged plots for each study area. The left inlets are the UAV LiDAR reference map (25 cm resolution), with areas of canopy height loss appearing in red. The right inlets show clusters of disturbances pixels from the CuSum algorithm applied to Sentinel-1 data overlaid on the LiDAR reference map.

Table 3.4: Results from the CuSum change detection algorithm showing total number of disturbance clusters, total disturbance area and total number of overlaps with respect to the LiDAR reference map (Gabon: 317 LiDAR clusters for a total area of 18.0 ha; Peru: 689 LiDAR clusters for a total area of 84.8 ha). Results are shown for CuSum clusters of increasing minimum size (0.01, 0.02, 0.05 and 0.1 ha). CuSum clusters are classified as overlaps if they share part of their geometry with the clusters from the LiDAR reference map.

	Gabon			Peru		
Minimum cluster size (ha)	**Total Clusters**	**Total Area (ha)**	**Overlaps**	**Total Clusters**	**Total Area (ha)**	**Overlaps**
0.01	240	14.4	187	484	57.7	317
0.02	170	13.7	154	348	56.4	276
0.05	98	11.8	98	167	51.0	150
0.1	45	9.0	45	97	45.9	96

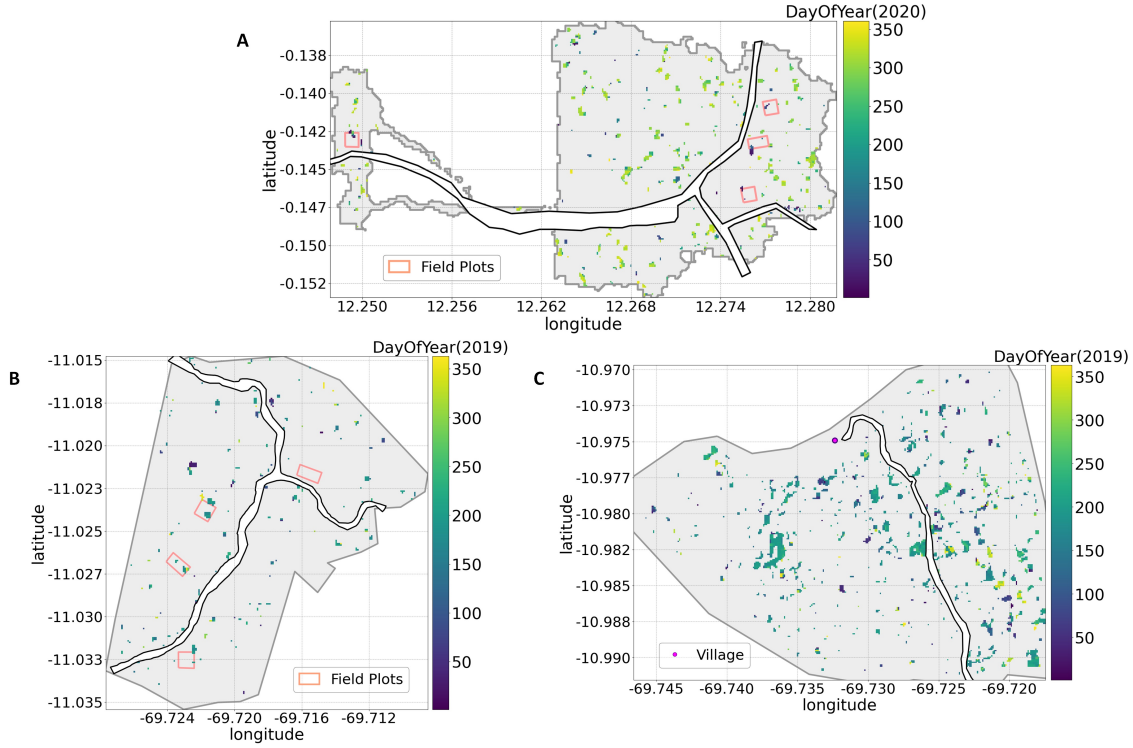

Figure 3.7: Dates of forest disturbance during the period of interest, determined as the year when the field sites were selectively logged. Dates are reported in Day of Year units (1-366); (A) Dates of forest disturbance in Gabon, for changes during the year 2020; (B) Dates of forest disturbance in Peru, showing changes occurred during the year 2019 in our study areas in proximity of the field sites and (C) near the village.

3.3.2 Retrieving the magnitude of the disturbance events

Relating the backscatter values of the CuSum maximum to the LiDAR-derived mean canopy height loss per pixel reveals an exponential decay relationship between the two quantities, implying that R_{sum_max} is sensitive to physical changes in forest canopy, from 10 m up to about 50 m in vertical drop (Figure 3.8). However, the large variations in R_{sum_max} magnitudes at pixel level makes it difficult to derive accurate values of forest canopy loss at this scale.

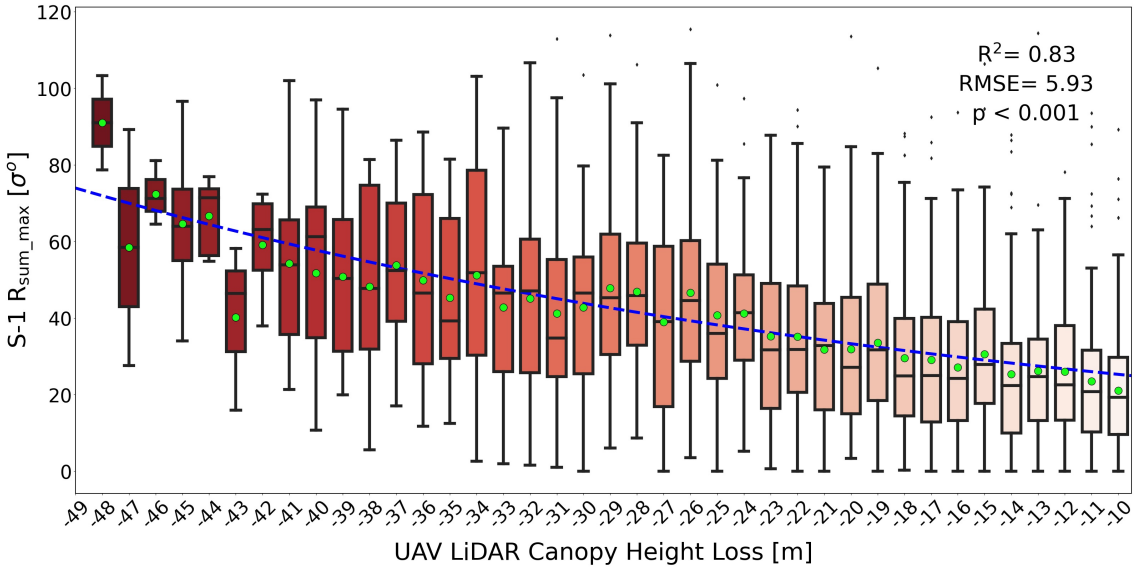

Figure 3.8: Distribution (boxplots) and means (green circles) of Sentinel-1 CuSum maximum backscatter for each UAV LiDAR measurement of canopy height loss in our study area in Gabon. Data is binned into intervals of canopy height loss of 1 m. The mean values of the distribution follow an exponential decay curve (blue dashed line) in the form $y = ae^{(-bx)}$, where $a = 18.67$ and $b = 0.03$. The coefficient of determination R^2, the Root Mean Square Error (RMSE) and the p-value are shown on the plot.

On the other hand, a strong correlation between the remotely sensed R_{sum_max} and field-measured ΔAGB was found using a linear regression model with R^2 = 0.95 and RMSE = 7.90 ($p < 0.001$) (Figure 3.9). The CuSum algorithm was applied to Sentinel-1 VV-polarised time series acquired over an area ≈250 times larger than our study site in Gabon (99,938 ha in total) and ≈150 times larger than our study site in Peru (39,559 ha in total). Maps of biomass loss for the year 2020 were produced for both locations from the coefficients of the regression model (Figure 3.10).

In Peru, where forest cut is more widespread, the GFW Tree Cover Loss map estimated a total disturbance area of 348 ha (0.9% of the total area) as compared to 504 ha (1.3% of the total area) from the CuSum-derived biomass map. 61% of the detections from the GFW map were found to overlap with the observations of 100% tree canopy loss from the CuSum map. The overlap reached 83, 73 and 90% when AGB loss values from the CuSum map were extended to ΔAGB $>$ 80%, ΔAGB $>$ 60% and ΔAGB $>$ 50%, respectively (Figure C.3).

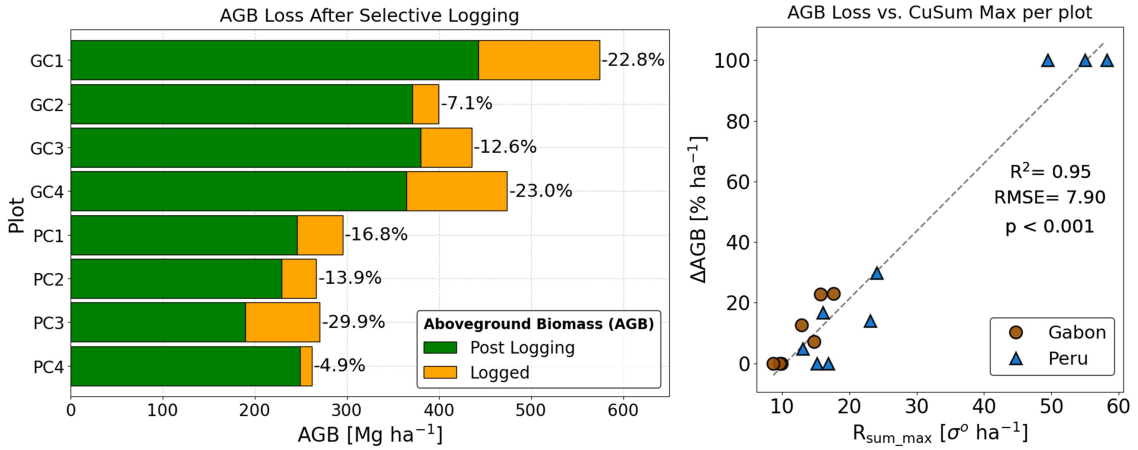

Figure 3.9: (left) AGB loss in Mg ha^{-1} in the eight 1-ha selectively logged plots in Gabon (G) and Peru (P); (right) AGB loss (ΔAGB) versus the maximum of the CuSum curve ($\mathbf{R_{sum\_max}}$) for plots in Gabon (brown circles) and Peru (blue triangles). In addition to the eight field-inventoried plots (right), four undisturbed plots (ΔAGB = 0%) and three fully deforested plots (ΔAGB = 100%) were added to the sample data.

3.3.3 Comparison to RADD Alerts

In this section we compare the CuSum change detection algorithm to the RADD disturbance alerts (Reiche et al., 2021), as both are derived from Sentinel-1 data. RADD Alerts for South America are only available from 2020, hence we chose this year for performing the comparison. As we did with the CuSum layer, RADD alert pixels were grouped into disturbance clusters to allow direct comparison with our results. In our test site in Gabon, the RADD product is able to detect only 7 disturbance clusters, as compared to 240 from the CuSum algorithm. All RADD alerts overlap the LiDAR reference map; however, none of the RADD alerts is able to detect logging in our field plots. (Figure 3.11**A**). In Peru we could not perform the comparison with our selectively logged plots, as timber was extracted during 2019. For this comparison we selected the village site, as this area normally experiences agricultural expansion during each dry season. Here RADD alerts are able to spot large and spatially continuous patches of deforestation, likely clear cuts for conversion into agriculture and pasture, omitting to detect more scattered and subtle changes (Figure 3.11**B**). In terms of total area, in our study site in Gabon, RADD is able to map 3% (0.5 ha) of the disturbance area detected by the UAV LiDAR reference map

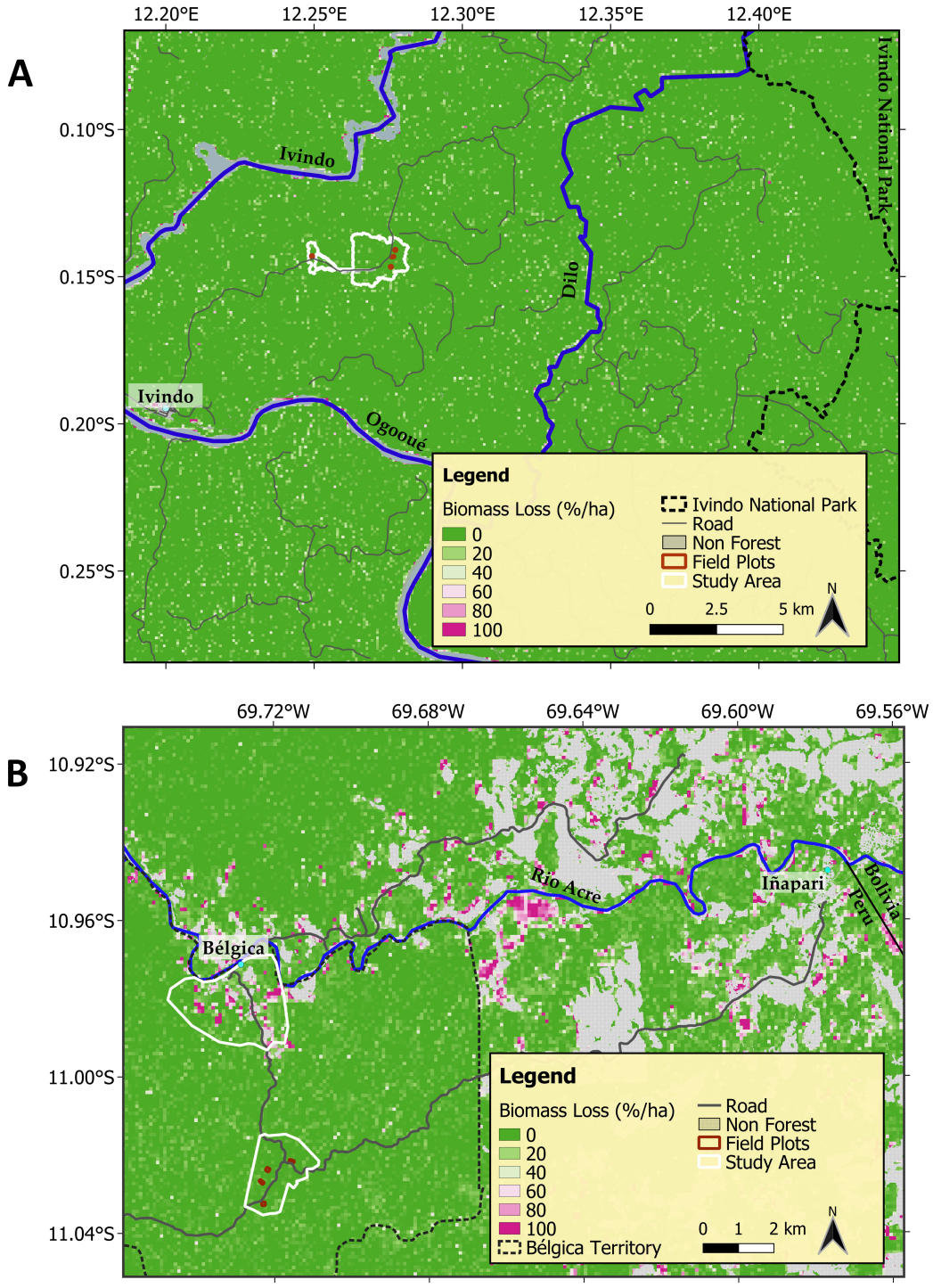

Figure 3.10: Maps of above ground biomass (AGB) loss (% per hectare) for two areas in (A) Gabon and (B) Peru, with the location of the study sites (white line) and the field plots (red boxes). Non forest areas have been masked using the primary humid tropical forest extent for the year 2001 from (Turubanova et al., 2018)

(18.0 ha), as compared to 80% coverage by CuSum (14.4 ha); in Peru, RADD is able to map 54% (42.5 ha) of the area detected by the LiDAR reference map (79.3 ha for the village site), as compared to 59% by CuSum (46.8 ha). This implies that, at least in our study sites, RADD Alerts are able to detect clear cuts, but are less sensitive to low-intensity forest disturbances.

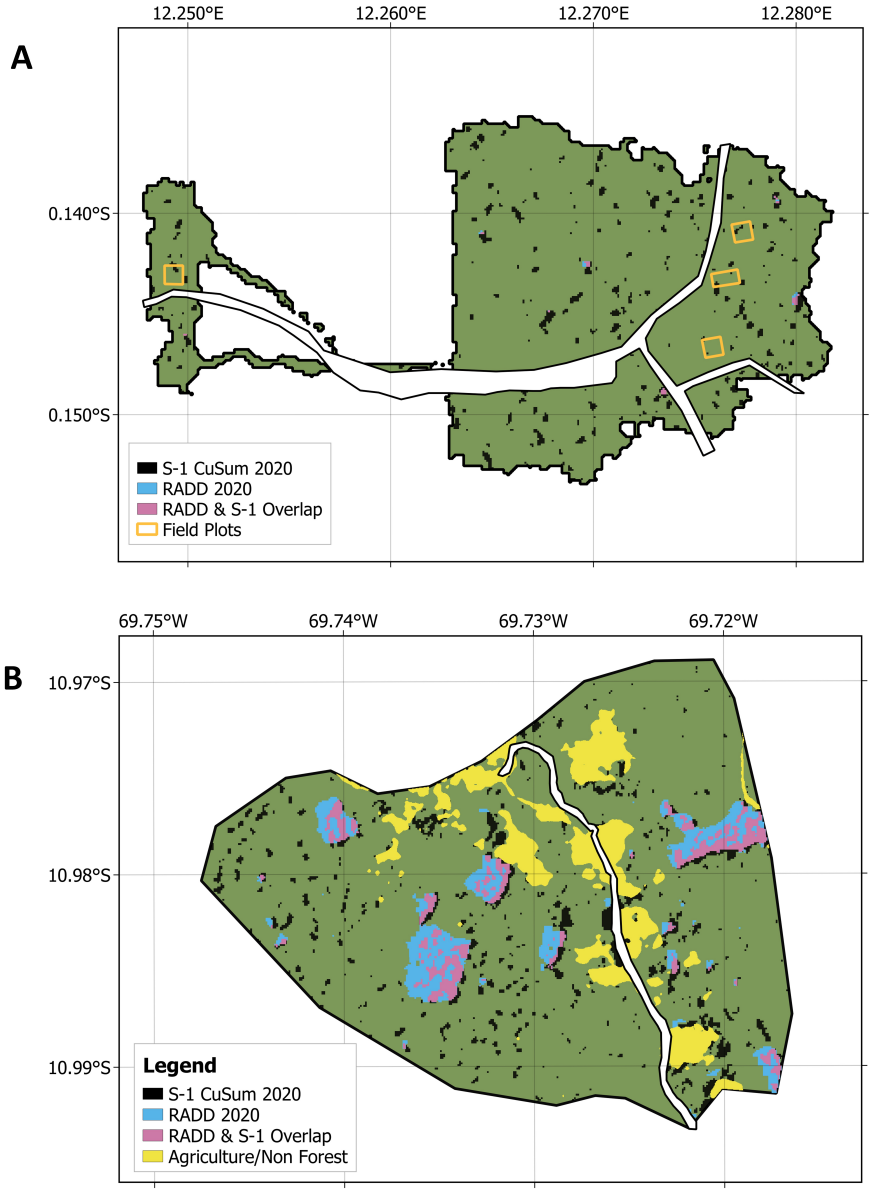

Figure 3.11: Comparison between RADD Alerts (blue) (Reiche et al., 2021) and CuSum change detection algorithm (black) for disturbances in the year 2020 in our study areas in (A) Gabon and (B) Peru. Overlapping areas between the two products are color coded in pink. The non forest mask in (B) is the product of a land cover classification produced by the authors using PlanetScope 3m resolution imagery from 16th July 2019.

3.4 Discussion

This study provides the first ground truth validation of the CuSum change detection algorithm. This was successfully tested over tropical rainforests located in the Amazon (Peru) and Central Africa (Gabon). Highly accurate information on the spatiotemporal distribution and the magnitude of forest loss was derived by a combination of field-measured UAV LiDAR, TLS and forest inventory data. We have adopted a single change metric, the maximum value of the CuSum distribution, to map the location, timing and magnitude of forest canopy loss. The sites selected for this study presented different degrees of disturbances, from individual tree removal to clear cuts and forest fragmentation in proximity of an inhabited area. The CuSum algorithm was able to detect the full spectrum of the disturbances, with a 78% probability of detection over the study site in Gabon and 65% probability of detection over the study site in Peru, for patches as small as 0.01 ha in size and canopy disturbances of 10 m and greater in vertical drop, including variations in the understory vegetation. The probability of detection increased to 100% in Gabon and 90% in Peru when considering detections equal or greater than 0.05 ha in size. Sentinel-1 data analysed with this algorithm exceeded our expectations in its ability to estimate the timing of disturbance events, such as selective logging in our study plots early in 2020 versus the more widespread selective logging in the forest concession at the end of the same year (Figure 3.7**A**).

Reproducibility and generality

The results of this study indicate that the CuSum method is an effective, simple and highly reproducible tool for monitoring forest structure dynamics, even in the case of low-intensity logging. Forest monitoring systems relying on optical imagery, such as the Global Forest Watch Alerts (Hansen et al., 2016) and DETER in Brazil (Shimabukuro et al., 2006), are inherently limited by cloud coverage, which hampers the possibility of capturing the full extent of forest loss in tropical regions. Building on the freely avail-

able, temporally dense and cloud-penetrating Sentinel-1 dataset, the CuSum method is suitable for mapping disturbances in a continuous manner and at pan-tropical scales (Hethcoat et al., 2021; Ruiz-Ramos et al., 2020). In particular, the algorithm was successfully tested in two contrasting tropical forest ecosystems, the Amazon and Central Africa rainforests, which greatly differ in species composition and stand structure. In both locations we used experimental data from UAV LiDAR to calibrate the algorithm to distinguish intact forest from disturbed forest, thus setting an empirical threshold on the change metric. Interestingly, we have found that the 95th percentile of the CuSum maximum distribution approximately corresponds to the value of this empirical threshold (Figure C.4). This opens the possibility of extending the proposed method beyond the test sites, even in the absence of *in situ* measurements of forest canopy loss. The detection accuracy of this approach needs to be further explored, and the analysis scaled to the regional level to evaluate the variability of the threshold in response to differences in forest structure and topography.

In terms of disturbance characteristics, the CuSum method was able to detect a variety of disturbance events ranging from small-scale logging for commercial timber extraction (e.g in Gabon) to large area deforestation for subsequent agricultural use (e.g near the village in Peru). This classification is only possible thanks to our detailed, first-hand knowledge of the study sites, as the CuSum method on its own does not provide any information on the underlying causes of the disturbance. For example, tree mortality, wind and other natural factors are the likely causes of canopy losses observed in the area surrounding our field plots in Peru (Figure 3.6**B**). In this case, the location and size of the disturbance clusters does not provide any information on the nature of these events, making it difficult to distinguish them from the anthropogenic disturbances that occurred within and in close proximity of the study plots. There are cases where it is possible to identify the nature of the disturbances by looking at the shape and location of the clusters. For example, new logging roads and crop fields are easily recognisable,

as they arrange themselves in geometric patterns and are usually connected to other features in the landscape. A caveat on scaling this methodology on a larger area is that automatic remote sensing approaches may not be sufficient for an accurate classification: fieldwork, knowledge of the study area and image interpretation are still crucial to fully understand the dynamics on the ground (Reams et al., 2010; Myers, 2010; Beuchle et al., 2021).

Location accuracy vs. timely event detection

The majority of fine-scale disturbances in our study areas went undetected by the RADD product, which is currently the best SAR-based system for mapping forest disturbances across the tropics (Reiche et al., 2021). In our study site in Gabon (where RADD provides data for the year of the logging activities), RADD was able to detect only 2% of the disturbances measured by our reference map (7 RADD vs. 317 LiDAR detections) - as compared to 59% from CuSum (187 CuSum vs. 317 LiDAR detections) - missing all the selective logging in our core plots. However, we have not tested the performance of the CuSum method for near real-time monitoring (NRT), which is the essential feature of the RADD Alert system. The potential of CuSum analysis for NRT has already been proposed by the literature (Ruiz-Ramos et al., 2020). As the success of the CuSum algorithm is ultimately linked to constructing an adequate picture of the pre- and post-disturbance trend, there is an intrinsic limitation on the minimum number of images required for capturing the point-wise change that we classify as a detection. In this study, we have tested the CuSum method on time series acquired using a repeat-track orbit and a descending acquisition mode, using a minimum of twelve months ($\approx$ 30 images) for building the pre-disturbance dataset and a minimum of six months ($\approx$ 15 images) for the post-disturbance trend. Enhancing NRT performance, for example by reducing the amount of images required to build the post-disturbance dataset, may also reduce the number of detections. Compared to the RADD system, the CuSum method is able to detect disturbances as small as 0.01 ha in size (as compared to 0.1 ha, the minimum

mapping unit for RADD) and can provide accurate information on time and magnitude of the disturbance events. On the other hand, the intrinsic latency of the method may not make it suitable for NRT detections. However, while future work should explore the possibility of enhancing NRT capability of the CuSum algorithm, the two systems can complement each other in terms of usage and applications. For example, while RADD may be appropriate for mapping activities that require immediate intervention (such as illegal logging), the CuSum methodology can be used for building yearly maps of forest loss, providing more accurate figures on time and magnitude of the disturbance events for long-term monitoring and reporting purposes.

Potential for Biomass Change Estimates

In this study we explored for the first time the relationship between the CuSum method and forest physical parameters, using the same metric that was adopted for mapping location and time of the disturbances. A statistically significant relationship (R^2 = 0.95 and $p < 0.001$) was found between the CuSum maximum and field-measured AGB loss percentages at a 1 ha scale (Figure 3.9). The spread of R_{sum_max} values for the assumed 0% and 100% ΔAGB plots in Figure 3.9 is evidence that the plots were not field-inventoried, and hence the associated value of ΔAGB may be inaccurate. For example, plots that are not selectively logged will still experience small variations in forest biomass due to natural tree mortality. Despite the underlying noise, these plots adds evidence to the assumption that the magnitude of R_{sum_max} is directly correlated to the amount of biomass removed. Hence, a pan-tropical linear model was used for directly deriving maps of forest biomass change with values ranging from 0% (intact forest) to 100% change (deforestation). The maps show different levels of disturbance compared to each other, which can be explained by the distinctive characteristics of the two sites. In Gabon, this region is scarcely populated, the main human settlement being the village of Ivindo in the western corner, which is also the site of Rougier's logging camp. The rest of the area is dominated by a dense canopy cover and is largely part of Rougier's forest

concession, bordered east by Ivindo National Park and south by the Ogooué River. Here, timber is logged on a rotational basis and at low-intensities, according to FSC-certified protocols. Limited patches of deforestation are observed in proximity of the village, likely caused by the logging camp activities, as it was observed during the field campaigns. The area in Peru, on the other hand, is characterised by a higher human presence, especially concentrated in and the around the town of Iñapari and the Bélgica village, with small, isolated households scattered along the Acre River, which marks the border between Peru and Brazil. Consistent patterns of forest disturbance are visible in proximity of human settlements and bordering grasslands and agricultural fields, indicating agricultural expansion into the forest fringes. Most of these patterns are concentrated along transport infrastructures, namely the Acre River and the road connecting Iñapari to Bélgica. However, land use in Bélgica's territory (dashed black line) is regulated and, with the exception of the area around the village which is allocated to agricultural/urban use, it is mainly divided between a protected area and a forest concession for low-intensity timber extraction. Indeed, the biomass change map shows a clear demarcation in land use as soon as the road from Iñapari enters Bélgica's territory (Figure 3.10**B**). These observations are in line with findings from previous studies (Hirschmugl et al., 2020), which report similar patterns of forest disturbances in test sites located in the forests of Peru and Gabon.

A lack of ground measurements of forest biomass change in these areas combined with the absence of remote sensing products on AGB loss figures makes it difficult to validate these maps; however, at least for deforestation rates (AGB Loss = 100%), we can compare our findings with the GFW dataset (Hansen et al., 2016). In Peru, where forest disturbance is more widespread, we found a 61% overlap between the two maps, for detections covering $\approx$1% of the overall study area. The overlap increased to 90% when the CuSum map included pixels containing at least 50% biomass loss (Figure C.3). Different spatial resolutions - 30 x 30 m for the original GFW dataset, resampled to 100

x 100 m for comparing purposes - and the geometric incongruency of the two sensors (Landsat for GFW vs. Sentinel-1 for our study) are limiting factors for this analysis, where we may be excluding pixels that are very close but not intersecting. The final result still shows the ability of the CuSum algorithm to correctly locate the deforestation areas, presenting itself as a complementary tool to optical datasets for monitoring forest loss.

Limitations and future work

This study presents a first empirical application of the CuSum method, showing the potential of this technique for future forest disturbance mapping. On the other hand, this work opens up further trajectories of research, which can refine the methodology presented here, or even translate the analysis to other areas of investigation where change detection methods are required.

In this work we have only considered the co-polarised backscatter (VV), which is generally sensitive to surface or double-bounce scattering mechanisms between radar signal and measured target. On the other hand, the cross-polarised channel (VH) is useful to describe variations in the presence of multiple-bounce or volume scattering. A combination of co- and cross-polarized backscatter, such as the ratio of VH and VV backscatter, should be more sensitive to vegetation dynamics (Veloso et al., 2017). Ygorra et al. (2021) has concluded that the best detection of vegetation cover change is achieved when combining both VV and VH; hence, future work should look at adding information from the VH channel, and possibly testing the detection ability of the combined ratio (VH/VV). The number of detections may be further increased by combining both the positive and negative CuSum curves that were shown in Figure 3.5. Such analysis may also improve our understanding of the scattering mechanisms at play in the presence of the change event. In this study we have focused on the detection of a single change event over the entire period of observation. Nonetheless, a pixel may experience multiple disturbances, especially over the course of a multi-year analysis. For example, different

waves of selective logging may occur within the same pixel, leading to a clearing event or to conversion into another land use. A complete analysis of the disturbance trends should include the detection of these secondary change points. This can be achieved by dividing the time series before and after R_{sum_max} and repeating the analysis until the value of R_{sum_max} falls below the selected threshold.

Another direction of work should then focus on generalising the algorithm beyond the availability of *in-situ* measurements, by improving the thresholding procedure and decoupling it from the empirical data, for example by using statistical inference as proposed here, or more advanced time series techniques. Furthermore, the ability to retrieve biomass loss estimates directly from the change metric should be refined by adding more ground measurements to the regression model covering the entire spectrum of forest disturbance rates; and by using ground measurements, including the low-magnitude AGB loss, to validate the final product. The output should be validated in different areas and for different magnitudes of biomass change, especially for the low-intensity variations. Adding calibration data at finer resolutions ($<$ 1 ha), for example using the LiDAR metrics, would allow to retrieve estimates of biomass change potentially even at the original 10 m scale, providing better results for local and regional assessments of forest health.

Since the CuSum technique is essentially a change detection method, it can be exploited for monitoring other types of abrupt or sustained changes in land use, such as crop dynamics, floods and soil cover changes (Ruiz-Ramos et al., 2020; Ygorra et al., 2021). It can be similarly implemented on other SAR-based datasets at different wavelengths, such as the upcoming ESA's Biomass P-band mission, NASA's NISAR L/S-band and JAXA's ALOS-4 L-band, all planned for launch in 2023. Due to the nature of the field measurements, the analysis in this paper was limited to measures of forest loss; however, this does not exclude the possibility of using the same method for mapping forest

regrowth. A very interesting line of research would be to observe the behaviour of the CuSum distribution in the case of positive changes in stand volume or in canopy height, expanding the analysis to include estimates of forest gain, which are still excluded from current SAR-based monitoring systems.

3.5 Conclusions

This study presents a simple and effective methodology for detecting fine-scale disturbances in dense and multistoried tropical forests. A single metric based on the cumulative sums of VV-polarised Sentinel-1 time series was used to retrieve location, time and magnitude of the disturbances. The results of the change detection algorithm were tested on highly detailed, *in situ* measurements of forest canopy loss retrieved with a combination of UAV LiDAR, TLS and field inventory surveys, in the two distinct tropical forests located in Gabon and Peru. The probability of detection for this new method was 78% in the test site in Gabon and 65% in the test site in Peru, for disturbances as small as 0.01 ha in size and for drops in tree height as low as 10 m, including changes in understory vegetation. The timing of the detections matched the time when selective logging was carried out the field plots; in the wider concessions, it was consistent with the patterns of disturbances of the two test sites. The algorithm presented here was able to capture different intensities of forest degradation and deforestation, outdoing other forest monitoring tools such as the SAR-based RADD system and the Landsat-based GFW tool in capturing finer and more widespread tropical forest disturbances. In addition to other forest monitoring systems, the methodology outlined in this paper has the potential of retrieving the magnitude of the disturbance. A correlation between the change metric and biomass change was found with R^2 = 0.95, and R^2 = 0.83 for canopy height loss. Given the global coverage and free availability of Sentinel-1 data, the approach can be generalised to the regional scale and potentially used to quantify other types of forest dynamics, such as forest regrowth.

Acknowledgments

We wish to thank La Comunidad Nativa de Bélgica for allowing us to conduct this research on their land and for their generous hospitality; the NGO AIDER for offering their invaluable help with preparation and field logistics with the Peruvian campaigns; Prof. Eric Cosio and Dr. Norma Salinas from the Pontificia Universidad Católica del Perú for their assistance with customs and logistics. We would like to thank the staff of Rougier Gabon, including Evanillho Téodoro Muaño Bondjale and Aimé Manfoumbi, for hosting us in Ivindo and supporting us with our fieldwork. We are very grateful to Alfred Ngomanda from the Centre National de la Recherche Scientifique et Technologique (CENAREST); to the Agence Nationale des Parcs Nationaux (ANPN); to Le Ministère des Eaux, des Forets, de la Mer, de l'Environnement du Gabon, and to the Institut de Recherche en Ecologie Tropicale (IRET) for their invaluable support to our research in Gabon. This research would have not been possible without the work of the field assistants. In particular, we would like to thank Luis Miguel Álvarez Mayorga, Roxana Sacatuma Cruz, José Sánchez Tintaya, Arturo Aspajo López, Leoncio Aspajo Lopez, Luis López Chapiama and Kenny López Batista for the assistance in Peru; Joseph Amelim Boukandja and the community of Ivindo for assisting us with the fieldwork in Gabon.

Chapter 4

2020 Forest Disturbance Maps for Gabon and Peru at 10 m Resolution

C. Aquino[a], *E. T. A. Mitchard*[a], *K. Nomura*[b], *I. M. McNicol*[a], *H. Carstairs*[a], *A. Burt*[c] *and M. Disney*[c,d]

[a] *School of Geosciences, University of Edinburgh, Edinburgh, United Kingdom*

[b] *Climate Engine, Carson City, Nevada, United States*

[c] *Department of Geography, University College London, London, United Kingdom*

[d] *NERC National Centre for Earth Observation, London, United Kingdom*

Modified version of a paper in preparation for *Nature Scientific Data*, September 2022

Author contribution: C.A. conducted the analysis and wrote the manuscript under the supervision of E.T.A.M.; C.A developed the software with support from K.N.; C.A., I.M., H.C. and A.B collected the field data; M.D. provided the resources; E.T.A.M. obtained the funding.

Abstract

It is thought that tropical forests are experiencing high and increasing rates of human disturbance every year, with devastating consequences for the global climate, biodiversity, and the local communities that rely on these ecosystems. Complete deforestation is currently well-mapped with free and open satellite products being used to set and enforce policy. Forest degradation however, despite likely covering a far larger area than deforestation, has no equivalent reliable data products, with policy as a result often set based largely on anecdotal information. Accurate maps capturing small-scale forest disturbances, such as selective logging and mining, are urgently needed. Here we present forest disturbance maps at high spatial resolution (10 m) for the large, high forest cover countries Peru and Gabon for the year 2020, derived from Sentinel-1 Synthetic Aperture Radar satellite data, validated using a field experiment in both countries. We describe the analysis workflow and provide the change detection algorithm allowing the generation of maps for other regions and monitoring periods. The dataset provides critical information on the size, time and magnitude of the disturbances, supporting countries and local communities in identifying, assessing and tackling the drivers of forest loss.

4.1 Background & Summary

Tropical forests harbour the highest levels of biodiversity among all land ecosystems (Hill and Hill, 2001), support local community livelihoods and influence the global climate through evaporative cooling and their dominant role in the carbon cycle (Bonan, 2008). Yet, an international demand for agricultural and wood products is accelerating the destruction of these forests (Pendrill et al., 2019a,b; Henders et al., 2015; Hoang and Kanemoto, 2021), threatening their ability to sequester carbon and mitigate the effects of a warming climate (Mitchard, 2018). Given the importance of forests to human well-being, understanding the status, trends and underlying causes of deforestation and forest degradation is essential. In the last decade, open access satellite imagery at high spatial and temporal resolutions has enabled researchers to gain unprecedented knowledge on forest disturbance regimes. Annual maps of forest loss at the national and pantropical scale have been produced by different studies (Gao et al., 2020; Hirschmugl et al., 2017). The Global Forest Change (GFC) dataset on annual forest loss (Hansen et al., 2013) is derived from 30 m resolution Landsat imagery and is widely used for estimating national deforestation rates (Nomura et al., 2019; Harris et al., 2018). However, forest degradation events, such as those caused by selective logging and understory fires, are largely underestimated (Milodowski et al., 2017; Pearson et al., 2017). This is problematic, as forest degradation is now thought to affect larger areas of land than deforestation (Qin et al., 2021; Matricardi et al., 2020).

The JRC dataset on Tropical Moist Forest (TMF) change, also derived from Landsat imagery, is currently the only product providing explicit estimates of forest degradation at the pantropical scale, in addition to deforestation data (Vancutsem et al., 2021). Similarly to the GFC maps, its accuracy varies regionally depending on change dynamics and image availability: as it is based on optical satellite data (Landsat) it obtains few images in frequently cloudy regions, which include many tropical forest areas, and is insensitive to sub-canopy or low-intensity degradation (Hansen et al., 2016; Shimizu et al., 2019).

Moreover, it is impossible to detect small-scale events, like the extraction of a single tree, within a 30×30 m pixel. Currently, Synthetic Aperture Radar (SAR) systems are emerging as the most promising tool for continuous forest monitoring (Reiche et al., 2021; Ballère et al., 2021; Joshi et al., 2016; Bouvet et al., 2018a). Unlike optical sensors, the SAR signal is unaffected by most clouds and atmospheric effects and can be operated day and night (Joshi et al., 2015; Lu et al., 2014).

Since the launch of the Copernicus Sentinel-1 mission in 2014, high-resolution C-band SAR data are now available free-of-charge and at the global scale. Sentinel-1 provides systematic acquisitions provided at a 10 m spatial resolution on a 6- or 12-day revisit time, making it suitable for consistent and timely monitoring of forest disturbances. Recent work has shown how the dense time series of Sentinel-1 allow to overcome the environmental limitations of C-band radar, obtaining accurate detections of forest loss at the local and regional level (Carstairs et al., 2022b; Bouvet et al., 2018a; Reiche et al., 2018b; Ballère et al., 2021; Hirschmugl et al., 2020; Hethcoat et al., 2021; Hoekman et al., 2020). On the other hand, large-scale forest disturbance maps have started to emerge only very recently (Reiche et al., 2021; Silva et al., 2022; Doblas et al., 2020), partly because of the scarce availability of globally consistent data until the Sentinel-1 mission. At present, the only SAR-based pantropical maps of forest disturbance are provided by the Radar for Detecting Deforestation (RADD) Forest Disturbance Alert. The product has a minimum mapping unit of 0.2 ha and is designed for near real-time detection of tropical forest loss (Reiche et al., 2021).

Widening access to high-resolution satellite imagery as well as advances in change detection techniques are increasingly refining the accuracy of forest monitoring systems (Bullock et al., 2022). However, the majority of these products lack information on the magnitude of forest structural change, for example related to biomass or canopy height changes. Even in the case of pure deforestation, where there is an assumption that all trees are lost, the degree of biomass change is hard to quantify due to a spatial

mis-match between forest loss and biomass products, which are typically produced at a coarser resolution (Dubayah et al., 2022; Avitabile et al., 2016; Santoro and Cartus, 2021). Comparing biomass maps from different points in time does not give good estimates of biomass change: the high uncertainties, and signal saturation at high biomass values, makes differencing such maps effectively just noise (Mitchard et al., 2013a; Réjou-Méchain et al., 2019). Furthermore, there is an increasing need of calibrating wall-to-wall disturbance maps on local measurements of forest degradation, to reflect the complexity and regional variation of the different tropical ecosystems (Næsset et al., 2020).

In this paper, we use Sentinel-1 SAR data to produce the first 10 m resolution forest disturbance maps for Peru and Gabon for the year 2020, with information on area, date and magnitude of the disturbance events. The two countries are home to important tropical forest ecosystems, the Amazon in Peru and the Central African rainforests in Gabon, which differ in forest structure and ecology. The maps are generated using a change detection algorithm implemented in Python, which can be adapted by the user to generate disturbance maps for regions and monitoring periods of their choice. Both maps have been calibrated using unique ground measurements before and after selective logging, collected by the Forest Degradation Experiment (FODEX) in Peru and Gabon using a combination of UAV LiDAR, Terrestrial Laser Scanning and forest inventory data (Aquino et al., 2022). We find that the FODEX maps, presented in this study, compare well with other state-of-the-art global or pantropical products, achieving comparable or better results in the detection of small-scale disturbance events, thus improving estimates of national rates of forest loss.

Methods

Overview

To retrieve forest disturbance maps at the national scale, each country was subdivided into grid squares of 30 $\times$ 30 km in size. The pre-processing workflow shown in Fig.4.1 was developed in Python and applied to each grid cell. The approach has the advantage of parallelising the computation and avoiding hitting memory limits when downloading large tiles of satellite data. For each grid cell we produced forest disturbance maps showing date, size and magnitude of the change event. The core of the analysis is built on the cumulative sum (CuSum) change detection algorithm, a powerful yet simple statistical method to detect abrupt changes in time series data (Page, 1955; Taylor, 2008; Manogaran and Lopez, 2018). The algorithm has been recently proposed for forest monitoring applications (Ygorra et al., 2021; Ruiz-Ramos et al., 2020) and was calibrated by Aquino et al. (2022) on ground-truth measurements of selective logging from experimental sites in Gabon and Peru. Here, we developed methods to enable CuSum to be run at a very large scale on Sentinel-1 data, producing the first country-level application of the CuSum, and thus the first high-resolution high-accuracy maps of forest disturbance and its magnitude at the national level.

Image Pre-processing

Sentinel-1 images were acquired through the geospatial cloud computing platform Google Earth Engine (Gorelick et al., 2017) (`https://earthengine.google.com/`). All images were retrieved as VV-polarised, ground range detected (GRD) products in Interferometric Wide (IW) mode. Sentinel-1 data is provided by Google Earth Engine already preprocessed and radiometrically calibrated to the backscatter coefficient σ_0 in decibels (dB).

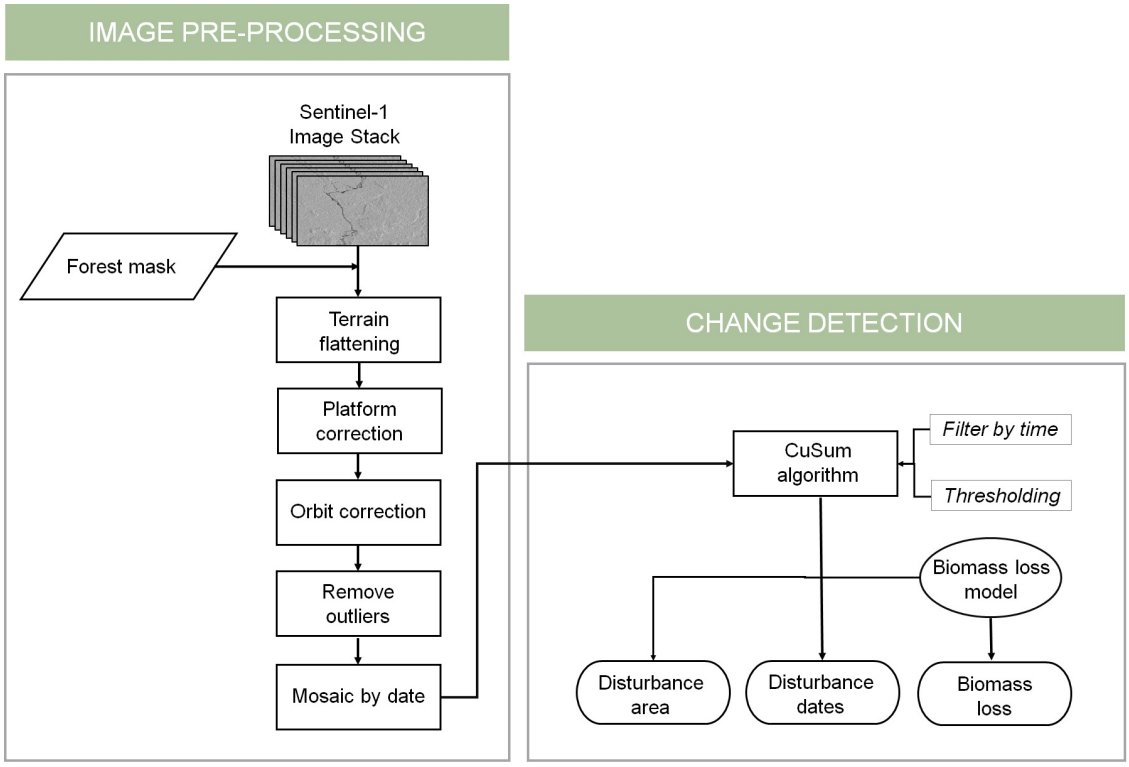

Figure 4.1: Flowchart of the forest disturbance detection method for national-scale mapping.

In order to capture all forest disturbances that occurred during the calendar year 2020, we built a time series stack including images ranging from six months before to six months after that year, namely from 1 July 2019 to 30 June 2021. Selecting a longer timeframe is necessary for distinguishing the change event from the background noise, especially in the case of disturbances occurred at beginning or at the end of 2020 (Aquino et al., 2022). We restricted the analysis to disturbances of primary forest by masking each image with the primary humid tropical forest layer for the year 2001 from Turubanova et al. (2018) with annual forest loss from 2001-2019 (Hansen et al., 2013) removed.

Naively applying the algorithm from Aquino et al. (2022) to a stack of Sentinel-1 images downloaded directly from Google Earth Engine would give a poor result, with artefacts dominating the degradation and deforestation signal. Consistent and clean time series data are necessary for monitoring forest change (Qiu et al., 2019), so the

following pre-processing steps were applied to the image stack (Fig. 4.1). First, to minimise the geometrical distortions produced by different incidence angles, we normalised backscatter intensities to terrain-flattened γ_0 (Small, 2011). While γ_0 is suitable for multi-temporal analysis with different viewing geometries, it is found that incidence angle effects persist after terrain flattening when VV-polarised backscatter is used (Arias et al., 2022; Carstairs et al., 2022a). To ensure that the observed changes are caused by real physical processes, we used images from the same sensor, either Sentinel-1A or Sentinel-1B, each time choosing the platform that provided the largest number of observations. Likewise, we maintained a stable radar geometry by choosing images acquired from the same orbit track. Sentinel-1 satellites cover Peru in both ascending and descending flight direction, while only descending passes are available for Gabon (European Space Agency, 2022b). To ensure a fair comparison between the two sites for this initial study, we chose to acquire data in the descending mode only for both sites. We then inspected the time series stack to remove corrupted or empty images, which can affect the result of the change detection analysis when calculating the mean of the time series. Land cover types such as forest, bare ground and water have backscatter values above -26 dB (Arellano et al., 2019). Therefore, images with radar intensities well below this threshold ($<$ -40 dB) were considered corrupted, and we removed them from the analysis. Finally, it is important to note that Sentinel-1 imagery in IW mode is cut into slices of $\sim$185 km (Google Earth Engine, 2021c; European Space Agency, 2022a). As a final step, slices are assembled to the size of the grid cell by mosaicking images that were acquired on the same date.

Change detection

After pre-processing, satellite imagery was imported in Python using the `xarray` module, an efficient and streamlined approach to manipulate multi-dimensional time series data (Hoyer and Hamman, 2017). For each pixel, we calculated the cumulative sum (CuSum) of the difference between the pixel value and the mean of the time series, according to the formula (Ygorra et al., 2021):

$$R_{sum\,j} = \sum_{i=1}^{n} \sigma^{o}_{i,j} - \overline{\sigma^{o}_{j}} \tag{4.1}$$

where $\sigma^{o}_{i,j}$ is the value of each pixel j for each image i, n is the number of images and $\overline{\sigma^{o}_{j}}$ is the mean of the time series over each pixel j.

The maximum value, or peak, of the CuSum distribution is used as a change indicator containing information on location, time and magnitude of the disturbance:

$$R_{sum\_max\,j} = max(R_{sum\,j}) \tag{4.2}$$

where $R_{sum\_max\,j}$ is the maximum of the CuSum distribution $R_{sum\,j}$ for each pixel j. To distinguish disturbed from undisturbed pixels we adopted the empirical thresholds derived from the calibration of the CuSum algorithm with in-situ UAV LiDAR measurements of canopy loss (R_{sum_max} > 33 for Gabon and R_{sum_max} > 36 for Peru) (Aquino et al., 2022). The disturbance date is set as the date of the peak of the CuSum distribution, which corresponds to the inflection point of the backscatter trend (Taylor, 2008). After applying the threshold, the CuSum distribution is filtered to select only data from 2020. The peak of the resulting CuSum curves and the dates corresponding to the peaks are extracted to generate maps containing location and date of the disturbance. Fig.4.2 and Fig.4.3 show the resulting maps for Gabon and Peru with the date of the forest disturbance in units of Day of Year (DOY, 1-366). We grouped adjacent pixels using the object-based algorithms

from Google Earth Engine (Google Earth Engine, 2021a), retrieving the area of each disturbance cluster. Experimental data from selectively logged plots in Gabon and Peru suggests that the peak of the CuSum curve also provides an estimate of the intensity of the disturbance (Aquino et al., 2022). Biomass loss maps in units of percentage loss per hectare were derived from the biomass loss model developed by Aquino et al. (2022), correlating R_{sum_max} to field-measured biomass loss from these selectively logged plots in Gabon and Peru (Fig. 4.3).

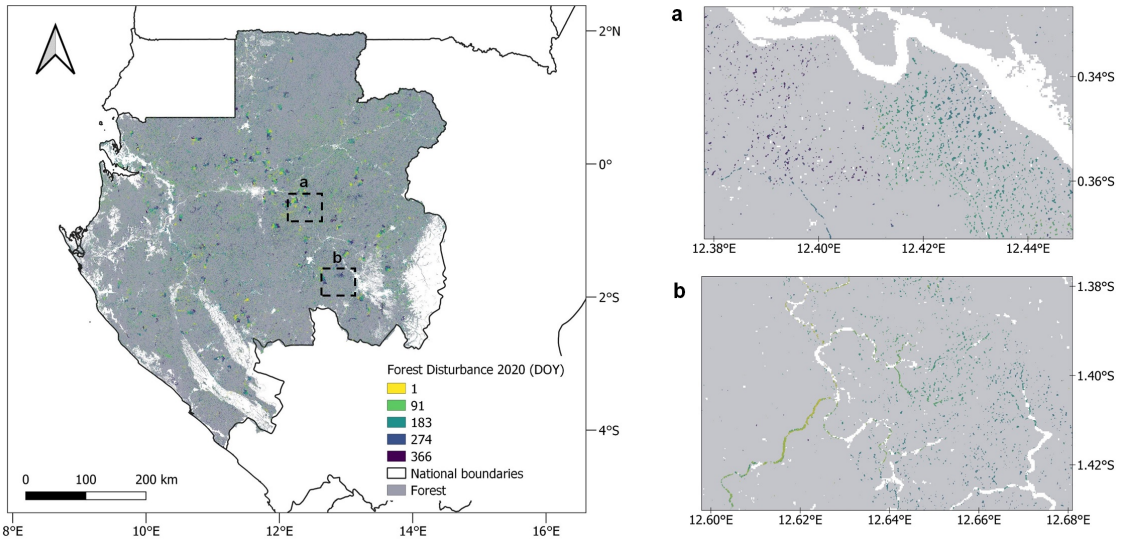

Figure 4.2: (left) Forest disturbance map for Gabon with the date of the disturbance in 2020 in units of Day of Year (DOY, 1-366). **a**) Enlargement on the Ogooué-Ivindo province showing systematic logging of a forest block in the the Cora Wood Gabon concession; **b**) Enlargement on the Ogooué-Lolo province showing the construction of a road earlier in 2020 and widespread logging following road expansion later in the year. The maps are produced at 10 m resolution. For visualisation purposes, the country-scale map on the left is rendered using the mode of the DOY values in a 250 m pixel.

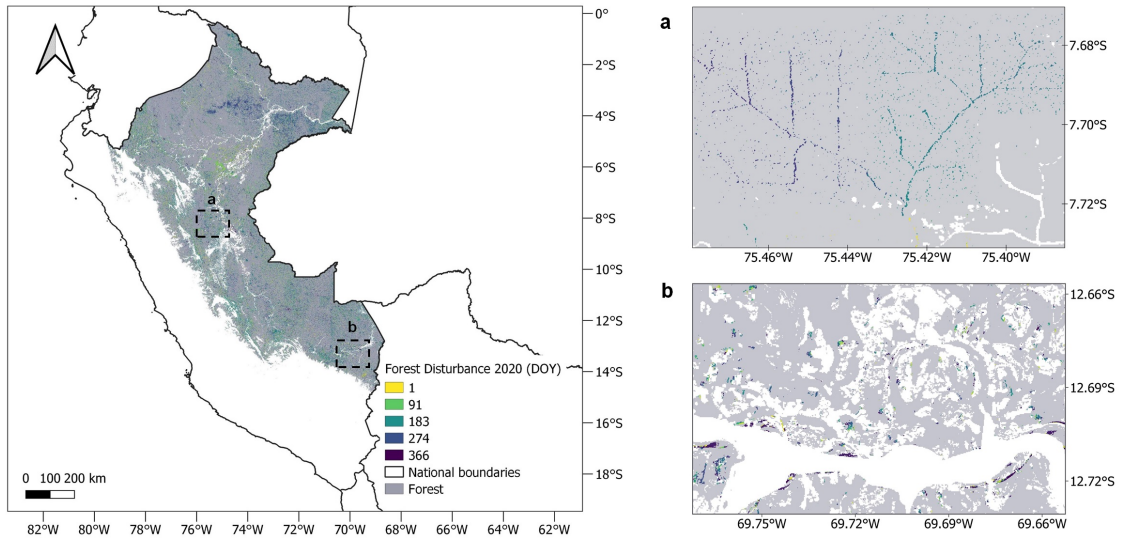

Figure 4.3: (left) Forest disturbance map for Peru with the date of the disturbance in 2020 in units of Day of Year (DOY, 1-366). **a**) Enlargement on the Loreto region showing the construction of logging roads and ensuing selective logging in two moments of the year. **b**) Enlargement on the Madre de Dios region showing deforestation likely caused by gold mining. The maps are produced at 10 m resolution. For visualisation purposes, the country-scale map on the left is rendered using the mode of the DOY values in a 250 m pixel.

4.2 Data Records

High-resolution forest disturbance maps for Gabon and Peru for the year 2020 can be accessed in Google Earth Engine as `ee.Image()` objects using the Asset IDs provided in Table 4.1. In addition, data can be interactively visualised and compared to other forest disturbance products using the Google Earth Engine app: `https://chiara-aquino.users.earthengine.app/view/fodex-disturbances-gabon-peru`. All source maps, supporting data sets and tables are also available to download from the Edinburgh Data Share: `https://datashare.ed.ac.uk/handle/10283/4116`.

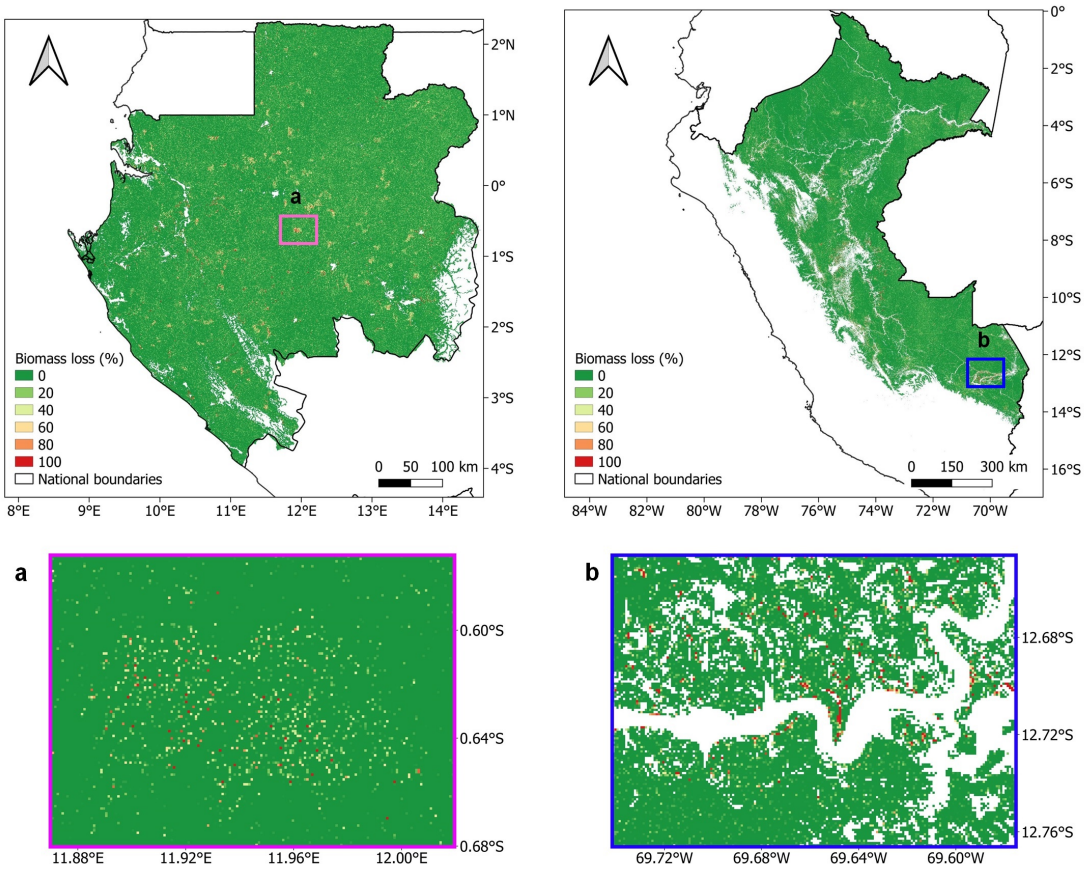

Figure 4.4: Forest disturbance maps for Gabon (left) and Peru (right) showing aboveground biomass loss percentages in 2020. **a**), Enlargement on the Ogooué-Lolo/Ogooué-Ivindo provinces in Gabon, showing the presence of both deforested and degraded forest in the concession owned by Leroy Gabon. **b**) Enlargement on the Madre de Dios region in Peru, showing complete forest loss likely due to gold mining activities near the Madre de Dios river. The maps are produced at 100 m resolution. For visualisation purposes, the country-scale maps at the top are rendered using the mode of the biomass loss values in a 250 m pixel.

4.3 Technical Validation

The outputs of the CuSum change detection algorithm have been previously validated in two study areas in Gabon and Peru using in-situ LiDAR measurements of forest canopy loss. This yielded a 78% success rate for the test site in Gabon and a 65% success rate for the test site in Peru, showing disturbances as small as 0.01 ha in size and canopy height losses as fine as 10 m (Aquino et al., 2022). In the absence of reference data on forest degradation, the country-level maps generated in this study were compared to

Table 4.1: Lists of available layers and Assets ID for accessing the forest disturbance maps on Google Earth Engine.

Country	Asset Description	Asset ID
Gabon	Date of Disturbance (DOY)*	projects/fodex/assets/GabonDate2020
Gabon	Area of Disturbance (m^2 $cluster^{-1}$)	projects/fodex/assets/GabonArea2020
Gabon	Biomass Loss (% ha^{-1})	projects/fodex/assets/GabonAGBLoss2020
Peru	Date of Disturbance (DOY)*	projects/fodex/assets/PeruDate2020
Peru	Area of Disturbance (m^2 $cluster^{-1}$)	projects/fodex/assets/PeruArea2020
Peru	Biomass Loss (% ha^{-1})	projects/fodex/assets/PeruAGBLoss2020

* DOY = Day of Year in 2020

other state-of-the-art products providing measurements of forest loss in the two regions: Sentinel-1 based RADD alerts (Reiche et al., 2021), and two different Landsat-based products, the JRC Tropical Moist Forest (TMF) (Vancutsem et al., 2021) and the Global Forest Change (GFC) data on primary forest loss (Hansen et al., 2013).

A visual comparison of the different products is shown in Fig.4.5 over a small area in Gabon. The most prominent features, detected by all maps with varying levels of detail, appear to be a road going from North to South-West and a larger, deforested patch approximately halfway along the road. Finer but widespread disturbances visible in the FODEX map are undetected by JRC and GFC, while only the largest clusters are visible in the RADD alerts. Furthermore, the FODEX map indicates the existence of another road, going from South to North East, suggesting that those disturbances are likely due to multiple logging activities spreading in an area opened up by new roads. This is also evidence that small-scale forest disturbances affect a much larger area than outright deforestation, with 171 ha and 146 ha of disturbed forest measured by FODEX and RADD respectively, as compared to only 45 ha reported by the GFC (Fig. 4.5).

Table 4.2 shows total estimates of disturbed primary forest at the country scale, as measured by each product. For JRC, the layers containing degradation and deforestation data (named ‘Degradation year’ and ‘Deforestation year’ and filtered for 2020) are first analysed separately and then as a single product. In Gabon, FODEX estimates an

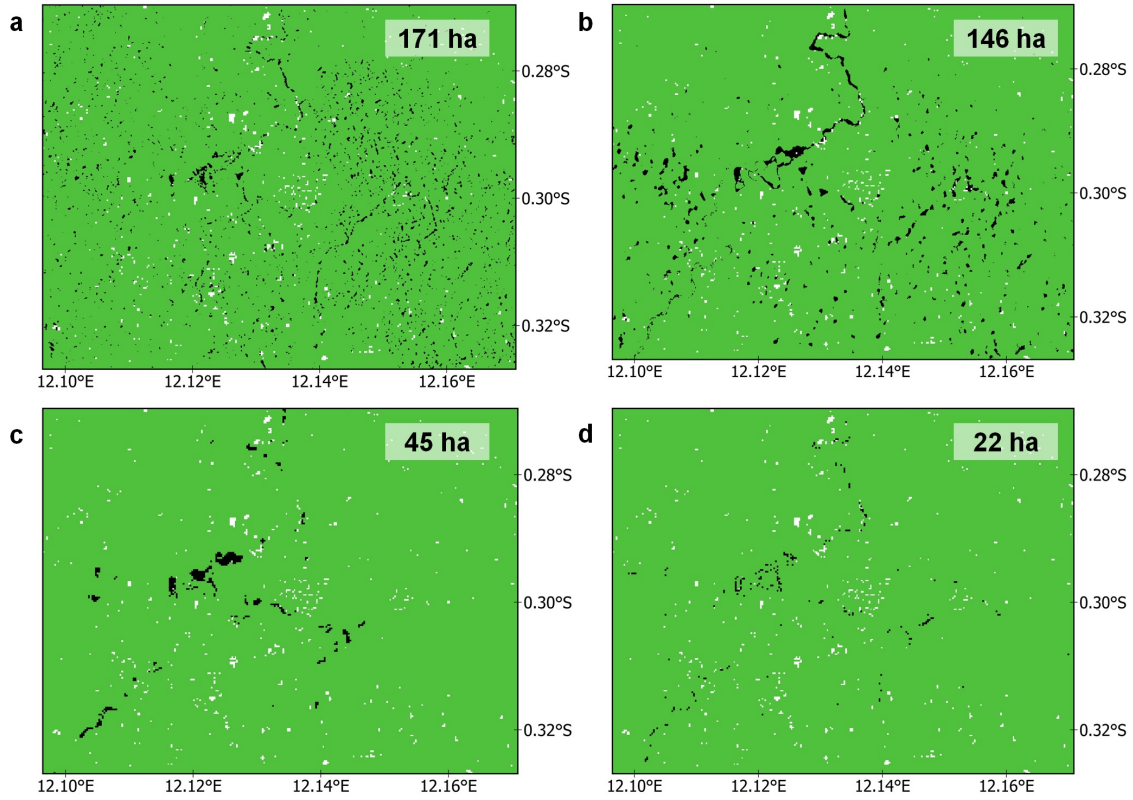

Figure 4.5: Comparison of mapped forest disturbances in 2020 for an area of ∼100 km^2 in the Ogooué-Ivindo province of Gabon for **a**) FODEX; **b**) RADD; **c**) the Global Forest Change (GFC) dataset on primary forest loss and **d**) the JRC Tropical Moist Forest (TMF) product showing both the degradation and deforestation data. The total area of forest disturbance is reported with each map.

annual forest disturbance rate of 0.17%, which is comparable to RADD (0.15%) but is more than double the rates estimated by GFC and JRC (0.05% and 0.07%, respectively). In Peru, the forest disturbance rate estimated by FODEX is slightly below that of other products (0.22% for FODEX, as compared to 0.28% for RADD and GFC). In Gabon, deforestation rates have been generally low, with single-tree extraction for the timber industry as the main cause of forest disturbance (Minnemeyer et al., 2000). In Peru, commercial gold mining, road construction and agricultural expansion affect larger portions of forest, causing its conversion into a different land use (Caballero Espejo et al., 2018). This trend also emerges from the JRC dataset, when comparing areas of deforestation with forest degradation in the two regions (Table 4.2). The FODEX product has a minimum mapping unit of 0.01 ha (compared to ≈0.1-0.2 ha for the other datasets),

making it suitable for the detection of small-scale disturbance events. This explains the higher proportion of disturbances detected by FODEX in Gabon, where subtle forest disturbances are more common. As for Peru, large areas of deforestation are generally mapped by FODEX as clusters of smaller detections, resulting in a fragmentation of the deforested area and therefore in an underestimation of total forest loss. This may be due to a lack of tuning of thresholds of the algorithm for detecting large areas of clearance, that disturbance in some of these areas started at an earlier time point, or due to the higher resolution of our product.

While the JRC TMF product offers degradation and deforestation maps for a long-term period (30 years), we found that in some regions these products underestimate forest loss as compared to other SAR-derived maps, likely due to the limitations in the use of optical data (Figure 4.5). In conclusion, the FODEX maps add valuable information on subtle disturbance processes (such as fire, selective logging and natural forest dynamics), complementing the data provided by other forest monitoring systems and contributing to derive more accurate estimates of carbon fluxes from land-cover change.

4.4 Usage Notes

The product does not distinguish human-induced from natural forest disturbances, such as windthrow, wildfires or flooding. However, the spatial distribution of pixels can give an indication of the underlying causes of the disturbance. Large clusters, often observed in recognisable geometrical patterns, are typically a sign of anthropogenic activities. The disturbance date information aids the visual interpretation as it shows the expansion of logging roads or systematic logging of a forest concession over the course of the year (Fig. 4.2a, Fig 4.3b). On the other hand, isolated, single-pixel disturbances, especially those found randomly scattered in remote regions, are likely an indication of natural forest dynamics.

Table 4.2: Total forest disturbed area and disturbance rates in Gabon and Peru for the year 2020, showing results from the FODEX maps, the RADD Alerts, the Global Forest Change (GFC) data on primary forest loss and the JRC Tropical Moist Forest (TMF) product on deforestation, degradation, and deforestation and degradation combined. The disturbance rate is calculated by considering the amount of primary forest that is affected by the disturbance. The extent of primary humid tropical forest is 22,452 kha in Gabon and 68,224 kha in Peru Turubanova et al. (2018).

	Gabon		**Peru**	
Product	**Disturbed Area (ha)**	**Disturbance Rate**	**Disturbed Area (ha)**	**Disturbance Rate**
FODEX	39,250	0.17%	147,267	0.22%
RADD	34,234	0.15%	191,698	0.28%
GFC	10,645	0.05%	193,785	0.28%
JRC TMF (Deforestation)	1,678	0.01%	103,442	0.15%
JRC TMF (Degradation)	13,254	0.06%	146,552	0.21%
JRC TMF (Total)	14,931	0.07%	249,994	0.37%

We expect the maps to give further insights into forest disturbance activities in Peru and Gabon, especially when used in conjunction with other datasets. The Open Data Portal of the Global Forest Watch provides freely downloadable spatial data layers, ranging from maps of forest concessions and oil palm plantations to mining permits (Giam, 2017). One example application of the FODEX maps in combination with the GFW dataset is shown in Table D.1, providing areas of disturbed forest in logging concessions in Gabon for the year 2020. Comparing these results with the country-level estimates in Table 4.2 indicates that more than half (58%) of the disturbed forest area in Gabon is located within licensed logging concessions, the majority of which are owned by foreign capital.

The maps provided with this study are not the only output that can be generated with the CuSum change detection script. With minimal input from the user, the code can be adapted to produce forest disturbance maps for any other region or time periods, provided that there are at least 6 months of available data following the period of observation. The script is written in Python and is provided free and open source. All source data are derived from freely available datasets. For convenience, we have used Google Earth Engine for downloading Sentinel-1 imagery. However, since Google Earth Engine is not an open source software, the script is designed to import data acquired from other sources. Sentinel-1 images can be freely downloaded from the Copernicus Open Access Hub (Copernicus, 2020) or the VisioTerra platform (VisioTerra, 2015). Data need to be pre-processed as calibrated, terrain-corrected, analysis-ready imagery at 10 m pixel spacing following the steps described by Google Earth Engine (Google Earth Engine, 2021b) and in the Methods section of this paper. This includes the application of orbit files, GRD border noise and thermal noise removal and terrain correction to σ_0. The European Space Agency's Sentinel-1 Toolbox can be used for these purposes (European Space Agency, 2021). In addition, we have used the object-based algorithms from Google Earth Engine to cluster adjacent pixels (Google Earth Engine, 2021a). The operation can be equally performed using the Polygonizer plugin available in the free and open source

software QGIS (https://plugins.qgis.org/plugins/Polygonizer/). The plugin is based on the polygonize utility of the Geospatial Data Abstraction Library (GDAL) (GDAL/OGR contributors, 2022) (https://gdal.org/programs/gdal_polygonize.html). The operation can be implemented for command-line execution in Python, which is suitable if processing large datasets.

4.5 Code availability

The Python script for producing forest disturbance maps using the CuSum change detection algorithm is available in the GitHub repository: https://github.com/chiaquino/S1_CuSum

Acknowledgements

We thank La Comunidad Nativa de Bélgica in Peru and Rougier Gabon for allowing us to collect the field data that was used to calibrate the maps in their forest concessions. We also thank everyone that supported us in the data collections campaigns: the field assistants, the local organisations, in particular the NGO AIDER, Robotic Air Systems and COTECMI in Peru; IRET, CENAREST, ANPN, Le Ministère des Eaux, des Forets, de la Mer, de l'Environnement, and the community of Ivindo in Gabon. This study was funded by a European Research Council Starting Grant awarded to Edward Mitchard (The Tropical Forest Degradation Experiment - FODEX: 757526).

Chapter 5

Conclusions

5.1 Summary

The main objective of this study was to collect new field, UAV and satellite remote sensing datasets to enable the testing and development of algorithms to detect small-scale disturbances in tropical forests using satellite remote sensing imagery, including both optical and SAR sensors. This topic was investigated in the previous three chapters by answering the following research questions:

1. Can we detect small-scale forest disturbances in dense, multi-storied tropical forests using optical remote sensing data?
2. To overcome the limitations of optical imagery and improve detection accuracy, can we measure disturbances in high-biomass forest with Sentinel-1 C-band SAR data?
3. Can we generalise change detection methods from the local to the country scale, to derive accurate forest disturbance maps for monitoring AGB change?

In the following section, I discuss the contribution of this thesis to the development of these research areas, based on the findings in Chapter 2-4. I also examine the limitations as well as further research directions suggested by these findings. Finally, I provide a brief contextualisation of the results and discuss their implications using a political ecology perspective.

Chapter 2

In this chapter, I compared the performance of six multispectral optical satellite sensors at 0.3 – 30 m spatial resolution in their ability to predict forest degradation in selectively logged plots in the Peruvian Amazon. The differences in spectral reflectance, NDVI and texture before and after logging were correlated to field-measured AGB loss, when tested using linear regression models.

- What is the best combination of optical sensor and remote sensing parameter to detect biomass change?

The best-performing model was found for PlanetScope (3 m data), with R^2 = 0.97, RMSE = 1.91 (in units of ΔAGB % ha^{-1}) and $p < 0.005$. This model is obtained from the texture of the NIR band using a square window of 9 m $\times$9 m. In general, high correlations were observed for four out of six sensors when using the texture of the NIR band, higher than for any other metric and band. From the best-performing models, we directly derived AGB change maps from the difference in NIR texture, without the need of subtracting two one-time AGB maps (which would likely not have been possible using optical data).

- How do optical sensors at different resolutions compare in their ability to detect biomass change?

The highest correlations between field-measured AGB change and satellite data were observed for those sensors with spatial resolutions in the middle of the studied range (0.30 - 30 m): 1.5 m SPOT-7, 3 m PlanetScope and 10 m Sentinel-2. Weaker relationships were observed for the very high resolution sensors ($<$ 1.5 m) WorldView-3 and SkySat. Insignificant results were found for Landsat data at 30 m spatial resolution. These findings suggest that optically-based measurements of forest loss are possible when the data is neither too detailed (which increases the noise content) or coarse (which smooths the information content), at least in areas with a similar tree crown size to these forests in Peru.

- When using image texture as a change detection method, what are the optimum characteristics to detect forest degradation?

This study indicates that a change in image texture is more strongly correlated to ΔAGB than simple changes in spectral reflectance values or NDVI. This result confirms the findings of previous research investigating the use of texture for estimating AGB (but never applied to AGB change). Hence, texture provides a valid solution for overcoming signal saturation in mapping change in biomass in dense tropical forests. Ultimately, choosing texture as a change detection method requires the selection of a suitable texture parameter, moving window size and spectral band from which to calculate it. In this study, the best performing textural models were obtained from the NIR band and using a variance parameter. As for the optimum window size, it slightly varies across the sensors, ranging between 9 m and 14 m for a square window. This implies that changes in forest canopies are best measured when the window size is of comparable scale to the tree crown diameter ($\sim$17 m for the logged trees in the study plots).

Chapter 3

To address the challenge of monitoring forest cover in tropical regions affected by persistent cloud cover, as is the case with our field site in Gabon, Sentinel-1 SAR data was tested using a novel statistical method, based on the Cumulative Sum (CuSum) of continuous time series. Satellite data were validated on ground measurements of forest loss in Peru and Gabon collected with a combination of UAV LiDAR, TLS and field inventory surveys, covering a total area of 1239 ha.

- Temporally dense and high-resolution data from C-band SAR can accurately map small-scale forest disturbances when using a CuSum change detection method.

A comparison of the CuSum algorithm with the LiDAR reference map resulted in a 78% success rate for the test site in Gabon and 65% success rate for the test site in Peru, for disturbance patches as small as 0.01 ha in size and for canopy height losses as fine as 10 m, including changes in understory vegetation. The probability of detection increased to 100% in Gabon and 90% in Peru when considering detections equal or greater than 0.05 ha in size. This suggests that the high spatial resolution combined with the frequent observations of Sentinel-1 can overcome the limitations of short-wavelength C-band radar, with great potential for mapping forest degradation in an accurate manner.

- A single change metric can be developed from the CuSum algorithm providing information on location, timing and magnitude of the disturbance events.

By calibrating the CuSum algorithm on field measurements of selective logging, it was possible to apply an empirical threshold on the peak of the CuSum distribution to distinguish between disturbed and undisturbed pixels. The value and position of this peak in the CuSum distribution contain information on location, time and magnitude of the disturbances and thus can be adopted as a single metric for change detection. Sentinel-1 data analysed with this method exceeded our expectations in its ability to estimate the timing of the disturbance events: the timing of the detections matched the time of selective logging in the field plots; in the wider concessions, it was consistent with the patterns of disturbances of the two test sites. Finally, a statistically significant relationship (R^2 = 0.95 and $p < 0.001$) was found between the CuSum maximum and field-measured AGB loss (in units of % ha^{-1}). This allowed the generation of AGB change maps of the wider area, which are found to be in agreement with land use patterns in the two study regions.

- Compared to other forest monitoring products, the CuSum method maps small-scale forest disturbances with higher spatial accuracy.

A comparison of the CuSum method with the Landsat-based Global Forest Watch (GFW) Tree Cover Loss (TCL) product showed a 61% overlap between the two maps when considering only deforested pixels, with 504 ha of deforestation detected by CuSum versus 348 ha detected by GFW for the study area in Peru. Low intensity disturbances captured by CuSum were largely undetected by GFW and by the RADD Alert System, which is currently the best SAR-based product for mapping forest disturbances in the tropics. In Gabon, RADD was able to detect only 2% of the disturbances measured by the LiDAR reference map, missing all selective logging in our field plots.

Chapter 4

I applied the method described in Chapter 3 over the whole of Peru and Gabon, with the aim of producing forest disturbance maps for the year 2020, showing location, date and magnitude of the disturbance events.

- Is it possible to develop a processing workflow for Sentinel-1 data to scale up results from the local to the national scale, using free/open software and datasets?

To retrieve forest disturbance maps at the national scale, each country was subdivided into grid squares of 30 $\times$ 30 km in size. The change detection workflow was developed in Python and applied to each grid cell. Parallelising the computation means that data processing can be performed on local servers, without recurring to cloud-computing (non-open source) platforms such as Google Earth Engine. Input satellite data can be freely downloaded, either from Google Earth Engine or from the Copernicus Open Access Hub. All the processing steps in the analysis can be performed in Python and using QGIS/GDAL. The algorithm can be adapted to produce maps for different period of times and regions, depending on the user's choice.

- When small-scale disturbances are included, what is the total area of forest loss for Peru and Gabon?

In Gabon, total disturbed area for 2020 was 39,250 ha, corresponding to 0.17% of primary intact forest. In Peru, total disturbed area for 2020 was 147,267 ha, corresponding to 0.22% of primary intact forest.

- How do results compare with other available deforestation and degradation maps?

Our maps were compared to other state-of-the-art products providing measurements of forest loss in the two regions: the SAR-based RADD alerts and two different Landsat-based products, the JRC TMF and the GFC data on primary forest loss. In Gabon, we estimated an annual forest disturbance rate of 0.17%, which is comparable to RADD (0.15%) but is more than double the rates estimated by GFC and JRC TMF (0.05% and 0.07%, respectively). In Peru, our estimate is slightly below that of other products (0.22% for our method, as compared to 0.28% for RADD and GFC, and 0.37% for JRC TMF). This is due to change detection method, which maps large areas of deforestation as clusters of smaller detections. In Peru, where deforestation is more diffuse than in Gabon, the fragmentation of deforested areas results in an underestimation of total forest loss.

5.2 Limitations and future research

The main limitations and areas of improvement in this thesis are related to: 1) data availability, and 2) change detection methods.

5.2.1 Data availability

The study suffers from the scarce availability of ground-truth measurements of forest degradation, which are essential for calibrating the statistical models and for validating the results of the AGB change maps. Research studies on tropical ecology typically use networks of permanent sample plots (PSPs) to monitor changes in forest dynamics, and for calibrating and validating remote sensing products. The most extensive project

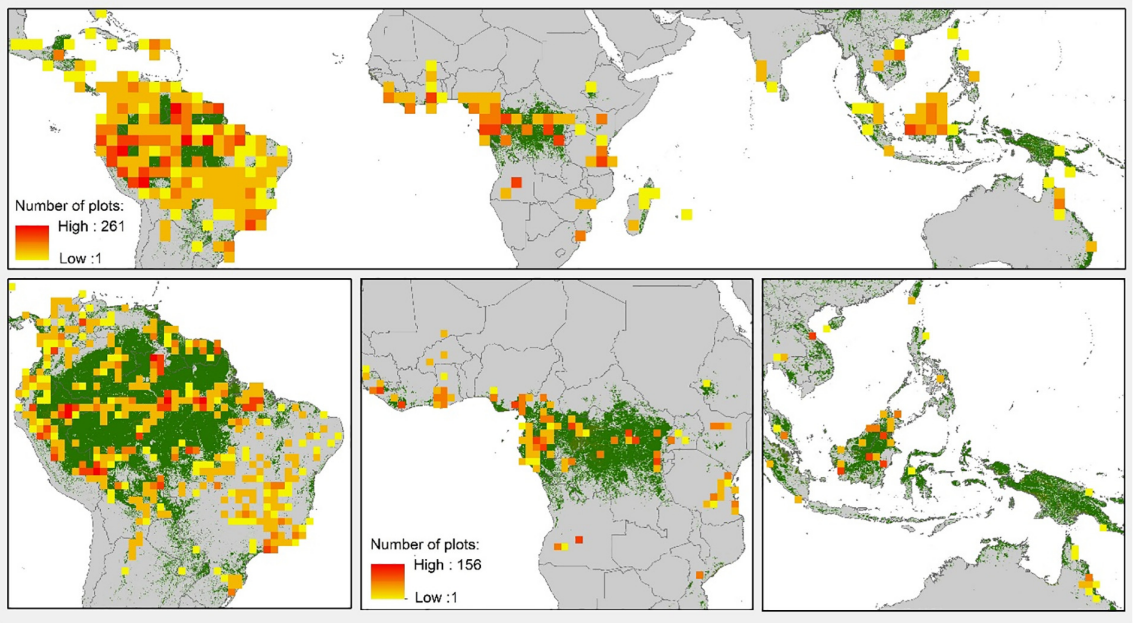

Figure 5.1: Current extent of ForestPlots.net, showing the sample density of the 4062 multiple- and single-inventory plots hosted at ForestPlots.net in a 2.5° pixel resolution. Taken from Figure 1 in ForestPlots.net et al. (2021)

of this kind, ForestPlots.net (`https://forestplots.net/`), links researchers from 54 countries across 24 plot networks for long-term monitoring of pan-tropical forests (ForestPlots.net et al., 2021) (Figure 5.1). Despite the invaluable contribution of these networks to our understanding of tropical ecosystems, the vast majority of the existing PSPs focus on intact or protected forest rather than on disturbed areas, and they are by their nature very rarely disturbed between censuses, meaning that they are not suited for measuring forest degradation (Wheeler et al., 2021).

The experimental data collected by the FODEX team (including me) and presented in this thesis constitute a unique dataset of forest degradation, both for the quality of the measurements (as a combination of UAV LiDAR, TLS and forest inventory surveys) and for the nature of the experimental setup, which allowed to measure different intensities of forest structural change. While the global networks of ForestPlots.net tend to focus on long-term processes, such as changes in tree biomass as a result of increasing temperatures and atmospheric carbon concentrations, it is also important to

quantify shorter term impacts on forest biomass as a result of selective logging and fires, which are increasingly threatening the integrity of primary and old-growth forests. In this thesis, having established and measured PSPs of forest biomass change, I was able to build statistical models to predict AGB loss directly from the remote sensing metrics, without the need of subtracting two one-time AGB maps. Unfortunately, due to the cost, legal/ethical and logistical challenges of the experiment, the sample size was restricted to the low part of the forest disturbance spectrum (5 - 30 % AGB loss ha^{-1}). To generate more comprehensive AGB change maps and improve their predictive validity, the statistical models should be refined by adding more degradation PSPs covering the entire forest disturbance spectrum, from 0% (no loss) to 100% (complete deforestation). Such plots would be ideally located in existing forest concessions or close to possible sources of disturbance, such as villages, roads or agricultural fields (Wheeler et al., 2021). The output maps should be validated in different areas and for different magnitudes of biomass change, especially for the low-intensity variations.

A critical lack of ground-truth measurements of forest degradation meant that accuracy assessment could only be performed using other remote sensing products. However, such products are in turn validated using optical remote sensing data, e.g. PlanetScope and Sentinel-2 imagery for the RADD Alerts (Reiche et al., 2021), or are only capable of measuring total or near-total tree cover loss, as it is the case with the GFC maps (Hansen et al., 2013). Therefore, it is essential to include degradation data in the existing pantropical plot networks, for example following the field protocols suggested by Wheeler et al. (2021).

5.2.2 Change detection

In this thesis I presented two change detection methods, one based on textural analysis of satellite optical data, and another built on the cumulative sums (CuSum) of C-band SAR time series. While the selection of either method should depend on considerations such as data availability over a specific region and time period, it is important to highlight that previous research has also focused on multi-sensor approaches combining data from SAR and optical sensors (Hoan et al., 2013; Vaglio Laurin et al., 2013; Reiche, 2015; Hirschmugl et al., 2020). To improve estimation of forest biomass change, future research could integrate the optical texture parameters proposed in this study with SAR-derived texture metrics (Pierce et al., 2003). Likewise, the CuSum algorithm can be applied to time series data from optical imagery (e.g. Sentinel-2) using NDVI or other suitable vegetation indices (Li et al., 2022), and combined with the Sentinel-1, CuSum-derived dataset described in this study.

The CuSum change detection method proved to be highly effective at detecting small-scale forest disturbances in our study areas, outdoing forest monitoring tools such as the RADD Alert system and the GFC maps. On the other hand, the CuSum algorithm was not optimised for real-time monitoring, which is the fundamental feature of the RADD Alert system. While the two products are derived from the same datasets, they differ in purpose and methodology. The RADD detection method is designed for near real-time detection (NRT) and therefore timeliness is the major consideration. For RADD, the probability of forest cover loss is iteratively updated with each new observation, and filtered according to a set threshold, which determines the confidence level of the forest loss event (Reiche et al., 2018a). In our study, the highest priority is given to spatial accuracy. The CuSum algorithm has been calibrated locally, using an empirically-derived threshold, and developed for a specific location and mechanism of disturbance. The calibration with in-situ LiDAR data is what determines the confidence level of the observations, and this is the reason why spatial accuracy is significantly higher than in

RADD. This does not exclude the possibility of using both systems to meet different uses and applications: for example, while RADD may be suited for mapping urgent intervention (such as illegal logging), the CuSum method can be used for generating yearly maps of forest disturbance, providing more accurate figures on annual rates of forest loss. It is possible to optimise the CuSum algorithm for NRT and reduce the latency of the detection, but this will likely imply a trade-off between timeliness and accuracy.

Another limitation of the CuSum algorithm in its current implementation is that it only allows for the detection of a maximum one change event over the entire period of observation. However, it is possible for an area to experience multiple disturbances, especially when conducting a multi-year analysis. For forest degradation or deforestation detection, for example, this could happen when multiple instances of selective logging precede a clearing event, resulting in different time series profiles of radar backscatter. Thus, a comprehensive analysis of the disturbance trends should include the detection of these secondary change points.

Finally, in the national-scale disturbance maps generated using the CuSum method, human-induced disturbances (such as selective logging, clearance for agricultural production and mining) are not separated from natural forest dynamics (e.g. windthrow, wildfires, flooding, or simple mortality of large trees). There are cases where it is possible to identify the nature of the disturbances by looking at the shape and location of the clusters. For example, new logging roads and crop fields are easily recognisable, as they arrange themselves in geometric patterns and are usually connected to other features in the landscape. However, automatic remote sensing approaches are not always sufficient for an accurate classification: fieldwork, knowledge of the study area and image interpretation are still crucial to fully understand the dynamics on the ground (Reams et al., 2010; Myers, 2010; Beuchle et al., 2021). More research is desired to understand and classify the causes of the disturbance events as detected by these maps, and separate natural from anthropogenic drivers, following the research directions of Carstairs et al. (2022b).

5.3 Implications and concluding remarks

In May 2022, I attended ESA's Living Planet Symposium in Bonn to present the work described in Chapter 3. During one of the Forest Biomass sessions, after a crowded room was introduced to the latest advances in global forest monitoring, a member of the audience asked: 'Why, if our maps are getting better and better, are deforestation rates getting worse?'. The silence that followed this apparently straightforward question, and the decision of the session chair to quickly move on to the next presenter, is symptomatic of the disconnection between the scientific community and the political context in which this research is taking place. The urgency of the climate crisis and the drastic decisions that need to be taken in this decade - if we wish to mitigate the worst effects of global warming (IPCC, 2022) - require scientists to expand their attention beyond the technical aspects of their research. My motivation for conducting this PhD work was compelled by this sense of urgency and the need to take action to halt environmental degradation. However, throughout my research years, I developed awareness of the limitations of the standard approach in the physical sciences, which often overlooks the interconnection of environmental change with the broader economic and political context. The analysis of these relationships is the perspective adopted by political ecology (Biersack, 2006; Perreault et al., 2015).

In recent decades a trend has emerged in conservation, which supports the idea of 'selling nature to save it' (McAfee, 1999). Offering market solutions to environmental problems is at the core of Payments for Ecosystem Services (PES) and Reducing Emissions from Deforestation and Degradation (REDD) programmes, where financial institutions disburse payments to countries from the Global South to conserve forests and peatlands as sites of carbon sequestration. Previous literature has contested the premises of these schemes, which can exacerbate existing inequalities (McAfee, 2012; Nielsen, 2014; Poudel et al., 2015; Bayrak and Marafa, 2016; Chomba et al., 2016; Asiyanbi et al., 2017). In particular, by making avoided deforestation commensurable, forests are

reduced to mere carbon stocks, with the risk of focusing conservation on a single aspect of forest ecosystem functioning (Stephan, 2012). The language of the financial markets, through the use of expressions like ‘natural asset’, ‘natural capital’ and ‘carbon stocks’ has pervaded the scientific literature, shaping research priorities of ecologists and environmental scientists by demanding increasingly standardized measures of ecosystem service commodities (Robertson, 2006).

Maps can be powerful tools of knowledge, but by no means do they offer a neutral and objective vision of the world. Maps do not exist outside of power structures: they can shape spatial relations through the lenses of the dominant actors, determining ownership, access to resources and social norms (Harley, 1989; Nietschmann, 1995; Wood, 2010). The drivers of tropical forest loss are now well-known and are directly linked to international supply chains and unsustainable demands of agricultural and forest commodities (Pendrill et al., 2019b; Hoang and Kanemoto, 2021). While the maps and the mapping techniques presented in this thesis can offer further insights into the patterns of tropical forest disturbances, my hope is that they will not be destined to reinforce inequalities and exclusivity in resource use. The wealth of knowledge that these maps can offer could instead be catalysed to challenge current resource allocation and the fundamental drivers of forest loss, empowering actors and communities whose survival is often threatened by extractivist industries, and who directly depend on the forests for their livelihoods. Hence why, in this thesis, I deliberately avoid mentioning PES, REDD and carbon sequestering schemes, in the effort to direct the scientific discourse away from the commodification of nature and towards the protection of forests for their intrinsic worth. As we know, time is critical: we have to act now, to avoid the catastrophic consequences that are already unfolding for millions of people living on our planet, and for the future generations.

Appendix A

Supplementary Materials for Chapter 1

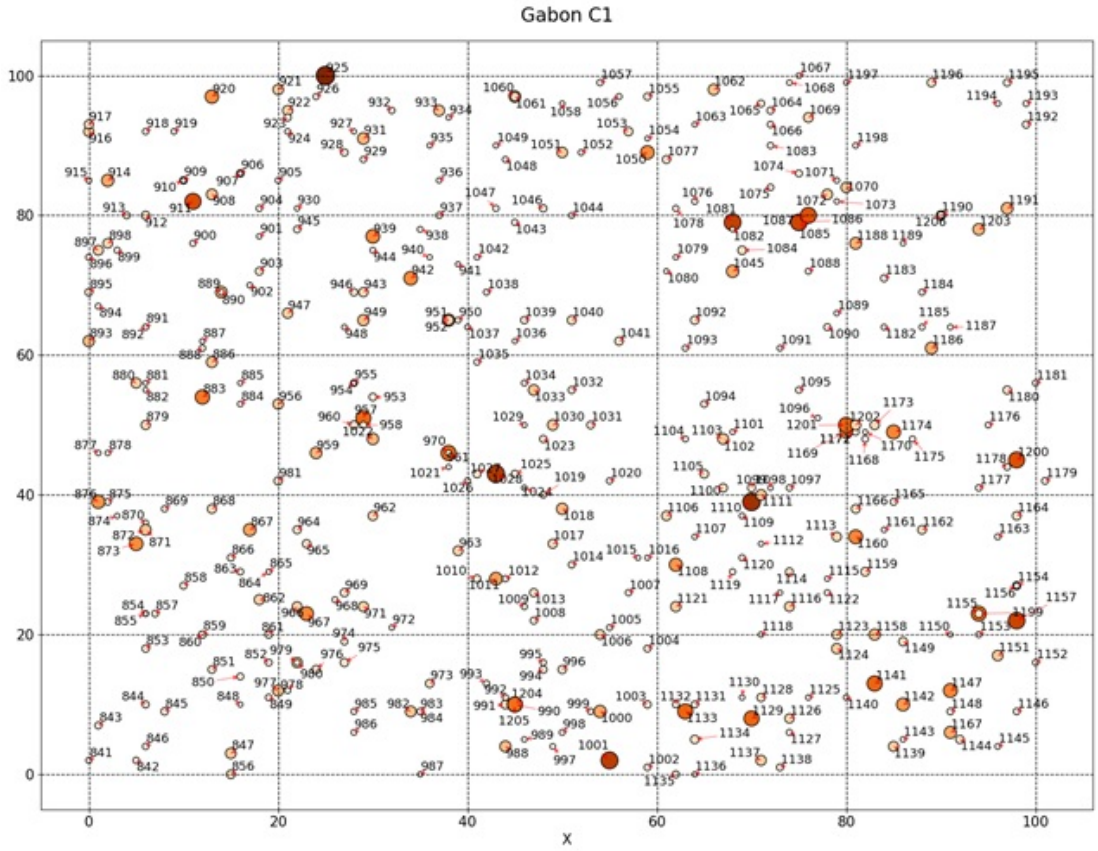

Figure A.1: Stem map for 1 ha plot

A. Remeasurement sheet

Forest Reinventory (FODEX) Date (dd /mm /yyy) _____ Notes:

Plot number __ Sheet # __ Name of recorder _____

Sub-plot	Tag No.	Species	DBH (cm)	Base tag	POM (m)	X (m)	Y (m)	Dead	Fallen	Broken	Damage	Log	Comments (Stumps = height of stump) / (old DBH = DBH @ old POM)
			.										
			.										
			.										
			.										
			.										
			.										
			.										
			.										
			.										
			.										
			.										
			.										
			.										
			.										
			.										

Figure A.2: Re-measurement sheet for forest inventory plots

New Recruits (FODEX)

Plot number ___ Sheet # ___

Date (dd /mm /yyy) _____

Name of recorder _____

Notes:

Sub-plot	Tag No.	Species	DBH (cm)	Base tag	POM (m)	X (m)	Y (m)	Dead	Fallen	Broken	Damage	Comments
			.									
			.									
			.									
			.									
			.									
			.									
			.									
			.									
			.									
			.									
			.									
			.									
			.									
			.									
			.									
			.									
			.									
			.									
			.									
			.									
			.									
			.									
			.									
			.									
			.									
			.									
			.									

Figure A.3: New recruits sheet for forest inventory plots

Appendix B

Supplementary Materials for Chapter 2

Table B.1: Diameter at Breast Height (DBH), height and crown width of the logged trees from the Terrestrial Laser Scanning (TLS) measurements.

Plot	Tree Tag	DBH [cm]	Height [m]	Crown Width [m]
C1	2571	73.8	34.7	24.3
C1	2452	69.7	35.9	16.7
C1	1906	75.0	46.1	16.4
C1	2550	87.9	35.4	22.2
C1	2562	71.9	34.6	16.9
C1	2049	46.2	30.2	10.6
C1	2076	64.8	29.4	20.2
C1	2301	84.2	35.1	21.1
C1	2538	48.6	28.5	10.8
C2	1720	65.6	28.2	17.1
C2	1551	81.9	25.0	16.7
C2	1326	82.9	39.7	22.4
C2	1254	57.0	31.7	11.7
C2	1692	54.2	28.6	13.4
C2	1849	95.0	31.3	24.7

Continued on next page

Table B.1 – *Continued from previous page*

Plot	Tree Tag	DBH [cm]	Height [m]	Crown Width [m]
C3	459	92.3	30.5	15.9
C3	296	127.1	40.4	33.8
C3	680	51.2	30.9	11.4
C3	577	85.0	45.3	19.1
C3	623	61.1	36.5	13.3
C3	115	78.1	40.5	19.7
C3	132	53.1	22.8	22.1
C4	760	57.8	28.8	17.9
C4	793	56.5	29.5	15.9

Table B.2: Comparison between Aboveground Biomass change (ΔAGB) figures of four 1-ha selectively logged plots, where the AGB of the logged trees is calculated either using an allometric equation (Allometric ΔAGB) or Terrestrial Laser Scanning data (TLS ΔAGB). Allometric ΔAGB is calculated as the difference in AGB between the first and second inventory, while TLS ΔAGB is the sum of the TLS volumes for the logged trees and the difference in AGB between the first and second inventory for the unlogged trees, derived from the allometric models. Standard errors are reported in parentheses.

Plot	Allometric ΔAGB [Mg ha^{-1}]	TLS ΔAGB [Mg ha^{-1}]	Percentage Difference
C1	60.9(5.9)	49.7(5.0)	20%
C2	49.6(5.1)	37.1(3.2)	29%
C3	99.7(6.4)	81.0(4.2)	21%
C4	14.6(1.4)	12.8(1.0)	13%

Table B.3: Statistically significant Pearson's correlation coefficients r, R^2, p-Value and Root Mean Square Error (RMSE) for linear relationships between biomass change and the derived spectral parameters, including NDVI. For each sensor, spectral parameters are listed in the order of decreasing correlations.

Sensor	Parameter	Pearson's r	R^2	p-Value	RMSE [% ha^{-1}]
WorldView-3	NDVI	-0.639	0.408	0.246	7.970
	red	0.584	0.341	0.301	8.411
	green	0.336	0.113	0.581	9.759
	blue	0.536	0.287	0.352	8.747
	NIR	-0.270	0.073	0.661	9.976
SkySat	NDVI	-0.383	0.146	0.525	9.571
	red	-0.133	0.018	0.832	10.269
	green	-0.345	0.119	0.570	9.726
	blue	-0.583	0.339	0.303	8.420
	NIR	-0.186	0.035	0.764	10.179
SPOT-7	NDVI	-0.651	0.424	0.234	7.866
	red	0.511	0.261	0.379	8.906
	green	0.218	0.048	0.724	10.110
	blue	0.585	0.343	0.300	8.399
	NIR	-0.376	0.142	0.532	9.598
PlanetScope	NDVI	-0.396	0.157	0.509	9.511
	red	0.287	0.082	0.640	9.925
	green	0.053	0.003	0.932	10.345
	blue	0.169	0.028	0.786	10.212
	NIR	-0.226	0.051	0.715	10.093
Sentinel-2	NDVI	-0.138	0.019	0.825	10.262
	red	-0.020	0.000	0.975	10.358

Continued on next page

Table B.3 – *Continued from previous page*

Sensor	Parameter	Pearson's r	R^2	p-Value	RMSE [% ha^{-1}]
	green	-0.674	0.454	0.213	7.657
	blue	-0.135	0.018	0.829	10.266
	NIR	-0.368	0.135	0.542	9.633
Landsat 8	NDVI	-0.366	0.134	0.545	9.642
	red	-0.341	0.116	0.574	9.738
	green	-0.645	0.416	0.240	7.918
	blue	-0.572	0.327	0.314	8.498
	NIR	-0.416	0.173	0.486	9.421

Table B.4: Statistically significant Pearson's correlation coefficients r, R^2, p-Value and Root Mean Square Error (RMSE) for linear relationships between biomass change and the derived textural parameters. For each sensor, textural parameters are listed in the order of increasing window size (in pixels). Large windows are ignored for sensors with spatial resolutions $\geq$10 m.

Sensor	Parameter	Window Size	Pearson's r	R^2	p-Value	RMSE [% ha^{-1}]
WorldView-3	Blue	3×3	0.288	0.083	0.639	9.922
		5×5	0.294	0.086	0.631	9.903
		7×7	0.293	0.086	0.632	9.905
		9×9	0.290	0.084	0.636	9.915
		11×11	0.286	0.082	0.641	9.928
		15×15	0.276	0.076	0.653	9.957
		19×19	0.265	0.070	0.666	9.989
		25×25	0.251	0.063	0.684	10.029
		45×45	0.197	0.039	0.751	10.158
	Green	3×3	0.629	0.396	0.255	8.051

Continued on next page

Table B.4 – *Continued from previous page*

Sensor	Parameter	Window Size	Pearson's r	R^2	p-Value	RMSE [% ha^{-1}]
		5×5	0.652	0.425	0.233	7.857
		7×7	0.646	0.417	0.239	7.907
		9×9	0.625	0.390	0.260	8.089
		11×11	0.595	0.355	0.289	8.323
		15×15	0.516	0.267	0.373	8.871
		19×19	0.409	0.167	0.495	9.456
		25×25	0.217	0.047	0.726	10.114
		45×45	-0.271	0.074	0.659	9.971
	Red	3×3	-0.126	0.016	0.840	10.277
		5×5	-0.150	0.023	0.810	10.243
		7×7	-0.164	0.027	0.792	10.219
		9×9	-0.176	0.031	0.777	10.199
		11×11	-0.187	0.035	0.764	10.178
		15×15	-0.210	0.044	0.734	10.129
		19×19	-0.238	0.057	0.700	10.062
		25×25	-0.280	0.078	0.649	9.947
		45×45	-0.344	0.119	0.570	9.726
	NIR	3×3	0.240	0.058	0.697	10.057
		5×5	0.251	0.063	0.684	10.029
		7×7	0.254	0.065	0.680	10.019
		9×9	0.256	0.066	0.677	10.014
		11×11	0.262	0.069	0.670	9.997
		15×15	0.303	0.092	0.620	9.874
		19×19	0.371	0.137	0.539	9.623
		25×25	0.479	0.229	0.415	9.096

Continued on next page

Table B.4 – *Continued from previous page*

Sensor	Parameter	Window Size	Pearson's r	R^2	p-Value	RMSE [% ha^{-1}]
		45×45	0.767	0.588	0.131	6.652
	NDVI	3×3	-0.423	0.179	0.478	9.387
		5×5	-0.429	0.184	0.471	9.359
		7×7	-0.396	0.157	0.510	9.515
		9×9	-0.348	0.121	0.566	9.713
		11×11	-0.293	0.086	0.632	9.905
		15×15	-0.187	0.035	0.763	10.176
		19×19	-0.106	0.011	0.866	10.302
		25×25	-0.042	0.002	0.946	10.351
		45×45	-0.129	0.017	0.837	10.274
SkySat	Blue	3×3	0.534	0.285	0.354	8.757
		5×5	0.095	0.009	0.880	10.314
		7×7	-0.133	0.018	0.831	10.268
		9×9	-0.259	0.067	0.674	10.008
		11×11	-0.338	0.114	0.579	9.752
		15×15	-0.443	0.197	0.454	9.286
		19×19	-0.499	0.249	0.392	8.975
		25×25	-0.540	0.292	0.347	8.718
		45×45	-0.584	0.341	0.301	8.408
	Green	3×3	0.600	0.360	0.284	8.286
		5×5	0.522	0.272	0.367	8.838
		7×7	0.435	0.189	0.464	9.329
		9×9	0.290	0.084	0.636	9.916
		11×11	0.165	0.027	0.791	10.218
		15×15	0.028	0.001	0.964	10.356

Continued on next page

Table B.4 – *Continued from previous page*

Sensor	Parameter	Window Size	Pearson's r	R^2	p-Value	RMSE [% ha^{-1}]
		19×19	-0.020	0.000	0.975	10.358
		25×25	-0.024	0.001	0.970	10.357
		45×45	-0.025	0.001	0.968	10.357
	Red	3×3	0.538	0.289	0.350	8.736
		5×5	0.335	0.113	0.581	9.760
		7×7	0.195	0.038	0.754	10.162
		9×9	0.087	0.007	0.890	10.321
		11×11	0.000	0.000	0.999	10.360
		15×15	-0.119	0.014	0.849	10.286
		19×19	-0.173	0.030	0.780	10.203
		25×25	-0.198	0.039	0.749	10.155
		45×45	-0.287	0.082	0.639	9.924
	NIR	3×3	0.271	0.073	0.659	9.973
		5×5	0.225	0.051	0.716	10.094
		7×7	0.179	0.032	0.773	10.192
		9×9	-0.035	0.001	0.955	10.354
		11×11	-0.286	0.082	0.641	9.929
		15×15	-0.362	0.131	0.549	9.657
		19×19	-0.394	0.155	0.512	9.522
		25×25	-0.427	0.182	0.474	9.370
		45×45	-0.502	0.252	0.388	8.958
	NDVI	3×3	0.095	0.009	0.879	10.313
		5×5	-0.335	0.112	0.582	9.763
		7×7	-0.466	0.217	0.429	9.166
		9×9	-0.522	0.273	0.366	8.834

Continued on next page

Table B.4 – *Continued from previous page*

Sensor	Parameter	Window Size	Pearson's r	R^2	p-Value	RMSE [% ha^{-1}]
		11×11	-0.543	0.294	0.345	8.702
		15×15	-0.593	0.352	0.292	8.343
		19×19	-0.663	0.440	0.223	7.756
		25×25	-0.717	0.514	0.173	7.220
		45×45	-0.377	0.142	0.531	9.594
SPOT-7	Blue	3×3	0.083	0.007	0.894	10.324
		5×5	0.005	0.000	0.993	10.360
		7×7	-0.127	0.016	0.839	10.276
		9×9	-0.329	0.109	0.588	9.782
		11×11	-0.795	0.632	0.108	6.289
		15×15	-0.914	0.836	0.030	4.194
		19×19	-0.809	0.654	0.097	6.093
		25×25	-0.624	0.389	0.261	8.098
		45×45	-0.066	0.004	0.916	10.337
	Green	3×3	0.117	0.014	0.851	10.289
		5×5	0.105	0.011	0.867	10.303
		7×7	0.159	0.025	0.799	10.229
		9×9	0.288	0.083	0.638	9.921
		11×11	-0.195	0.038	0.753	10.161
		15×15	-0.394	0.156	0.511	9.520
		19×19	-0.339	0.115	0.577	9.746
		25×25	-0.185	0.034	0.765	10.181
		45×45	0.139	0.019	0.823	10.259
	Red	3×3	-0.542	0.294	0.346	8.708
		5×5	-0.662	0.439	0.223	7.761

Continued on next page

Table B.4 – *Continued from previous page*

Sensor	Parameter	Window Size	Pearson's r	R^2	p-Value	RMSE [% ha^{-1}]
		7×7	-0.639	0.408	0.246	7.972
		9×9	-0.556	0.309	0.330	8.609
		11×11	-0.488	0.238	0.404	9.043
		15×15	-0.400	0.160	0.504	9.494
		19×19	-0.319	0.102	0.600	9.818
		25×25	-0.220	0.048	0.722	10.107
		45×45	-0.246	0.061	0.689	10.041
	NIR	3×3	0.371	0.137	0.539	9.622
		5×5	0.645	0.415	0.240	7.921
		7×7	0.839	0.704	0.075	5.633
		9×9	0.873	0.762	0.053	5.058
		11×11	0.848	0.719	0.070	5.493
		15×15	0.757	0.573	0.138	6.769
		19×19	0.689	0.475	0.198	7.510
		25×25	0.618	0.382	0.267	8.145
		45×45	0.273	0.075	0.656	9.966
	NDVI	3×3	0.670	0.449	0.216	7.691
		5×5	0.173	0.030	0.781	10.204
		7×7	-0.150	0.023	0.809	10.243
		9×9	-0.304	0.092	0.619	9.871
		11×11	-0.384	0.147	0.524	9.567
		15×15	-0.448	0.201	0.449	9.260
		19×19	-0.450	0.202	0.447	9.253
		25×25	-0.417	0.174	0.485	9.416

Continued on next page

Table B.4 – *Continued from previous page*

Sensor	Parameter	Window Size	Pearson's r	R^2	p-Value	RMSE [% ha^{-1}]
		45×45	-0.363	0.132	0.548	9.653
PlanetScope	Blue	3×3	-0.657	0.431	0.229	7.813
		5×5	-0.683	0.466	0.204	7.568
		7×7	-0.711	0.505	0.178	7.287
		9×9	-0.755	0.571	0.140	6.788
		11×11	-0.777	0.604	0.122	6.519
		15×15	-0.773	0.598	0.125	6.572
		19×19	-0.810	0.657	0.096	6.069
		25×25	-0.880	0.774	0.049	4.929
		45×45	0.312	0.097	0.609	9.843
	Green	3×3	0.632	0.399	0.253	8.030
		5×5	0.189	0.036	0.761	10.174
		7×7	-0.170	0.029	0.785	10.210
		9×9	-0.386	0.149	0.521	9.555
		11×11	-0.525	0.276	0.363	8.814
		15×15	-0.638	0.407	0.247	7.980
		19×19	-0.634	0.402	0.251	8.011
		25×25	-0.676	0.458	0.210	7.630
		45×45	-0.802	0.644	0.102	6.185
	Red	3×3	0.516	0.267	0.373	8.872
		5×5	0.258	0.067	0.675	10.008
		7×7	0.067	0.005	0.914	10.337
		9×9	-0.094	0.009	0.880	10.314
		11×11	-0.274	0.075	0.656	9.964
		15×15	-0.372	0.139	0.537	9.615

Continued on next page

Table B.4 – *Continued from previous page*

Sensor	Parameter	Window Size	Pearson's r	R^2	p-Value	RMSE [% ha^{-1}]
		19×19	-0.427	0.183	0.473	9.367
		25×25	-0.463	0.214	0.432	9.183
		45×45	-0.695	0.483	0.193	7.449
	NIR	3×3	0.983	0.966	0.003	1.910
		5×5	0.921	0.849	0.026	4.029
		7×7	0.861	0.741	0.061	5.271
		9×9	0.770	0.593	0.128	6.611
		11×11	0.635	0.404	0.249	8.001
		15×15	0.511	0.262	0.379	8.903
		19×19	0.562	0.315	0.325	8.572
		25×25	0.381	0.145	0.527	9.581
		45×45	0.380	0.144	0.529	9.585
	NDVI	3×3	0.390	0.152	0.516	9.540
		5×5	0.249	0.062	0.687	10.034
		7×7	0.216	0.047	0.728	10.116
		9×9	0.188	0.035	0.762	10.175
		11×11	0.165	0.027	0.791	10.219
		15×15	0.133	0.018	0.831	10.268
		19×19	0.113	0.013	0.857	10.294
		25×25	0.134	0.018	0.830	10.267
		45×45	0.409	0.167	0.494	9.454
Sentinel-2	Blue	3×3	0.343	0.118	0.571	9.730
		5×5	0.016	0.000	0.980	10.359
	Green	3×3	0.867	0.751	0.057	5.165
		5×5	0.005	0.000	0.993	10.360

Continued on next page

Table B.4 – *Continued from previous page*

Sensor	Parameter	Window Size	Pearson's r	R^2	p-Value	RMSE [% ha^{-1}]
	Red	3×3	0.493	0.243	0.399	9.014
		5×5	0.153	0.023	0.806	10.238
	NIR	3×3	0.887	0.788	0.045	4.774
		5×5	0.752	0.566	0.142	6.825
	NDVI	3×3	0.392	0.153	0.514	9.533
		5×5	0.401	0.161	0.503	9.490
Landsat 8	Blue	3×3	0.842	0.710	0.073	5.582
	Green	3×3	0.563	0.317	0.323	8.565
	Red	3×3	0.618	0.381	0.267	8.148
	NIR	3×3	0.514	0.264	0.376	8.889
	NDVI	3×3	0.513	0.263	0.376	8.892

(a)

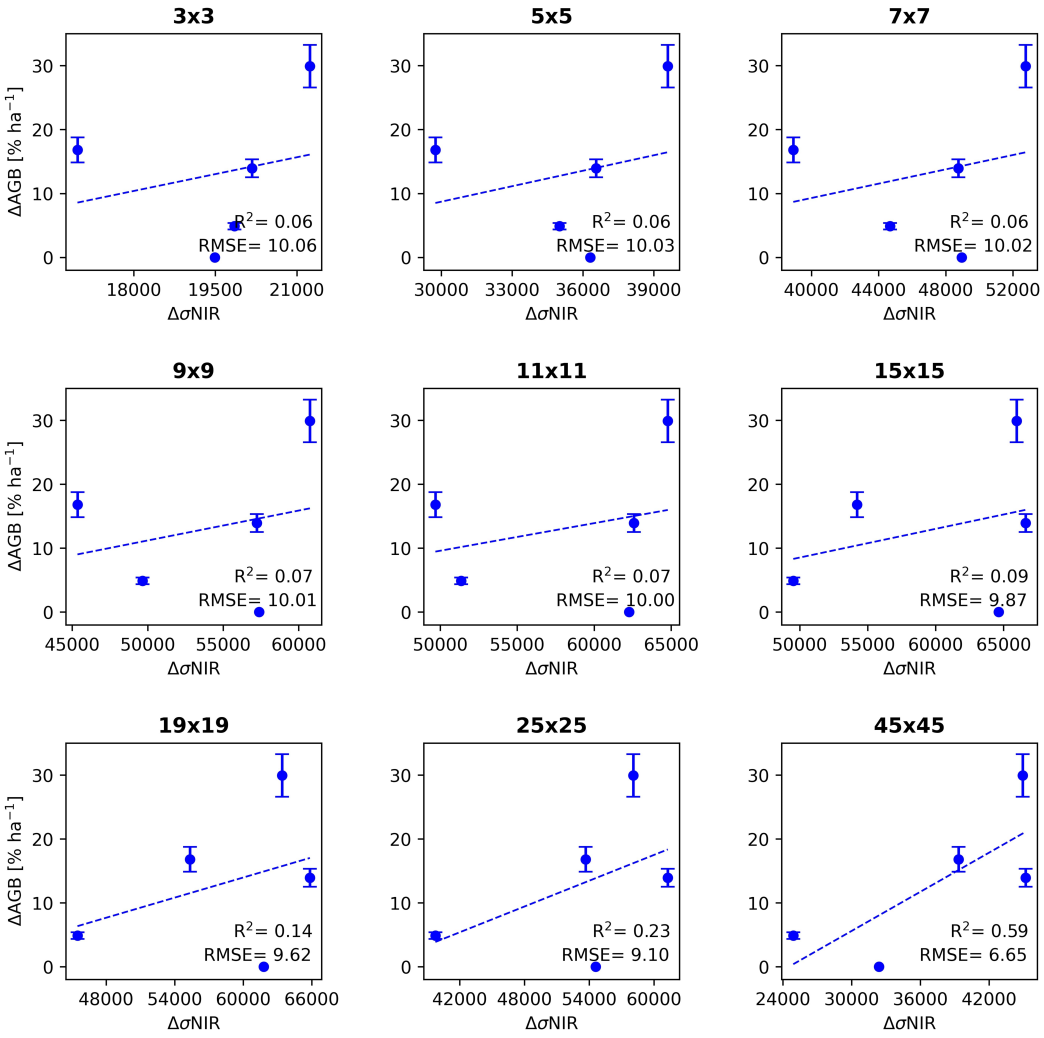
3x3
5x5
7x7
9x9
11x11
15x15
19x19
25x25
45x45
ΔAGB [% ha^{-1}]
ΔσNIR
R^2= 0.06
RMSE= 10.06
R^2= 0.06
RMSE= 10.03
R^2= 0.06
RMSE= 10.02
R^2= 0.07
RMSE= 10.01
R^2= 0.07
RMSE= 10.00
R^2= 0.09
RMSE= 9.87
R^2= 0.14
RMSE= 9.62
R^2= 0.23
RMSE= 9.10
R^2= 0.59
RMSE= 6.65

(b)

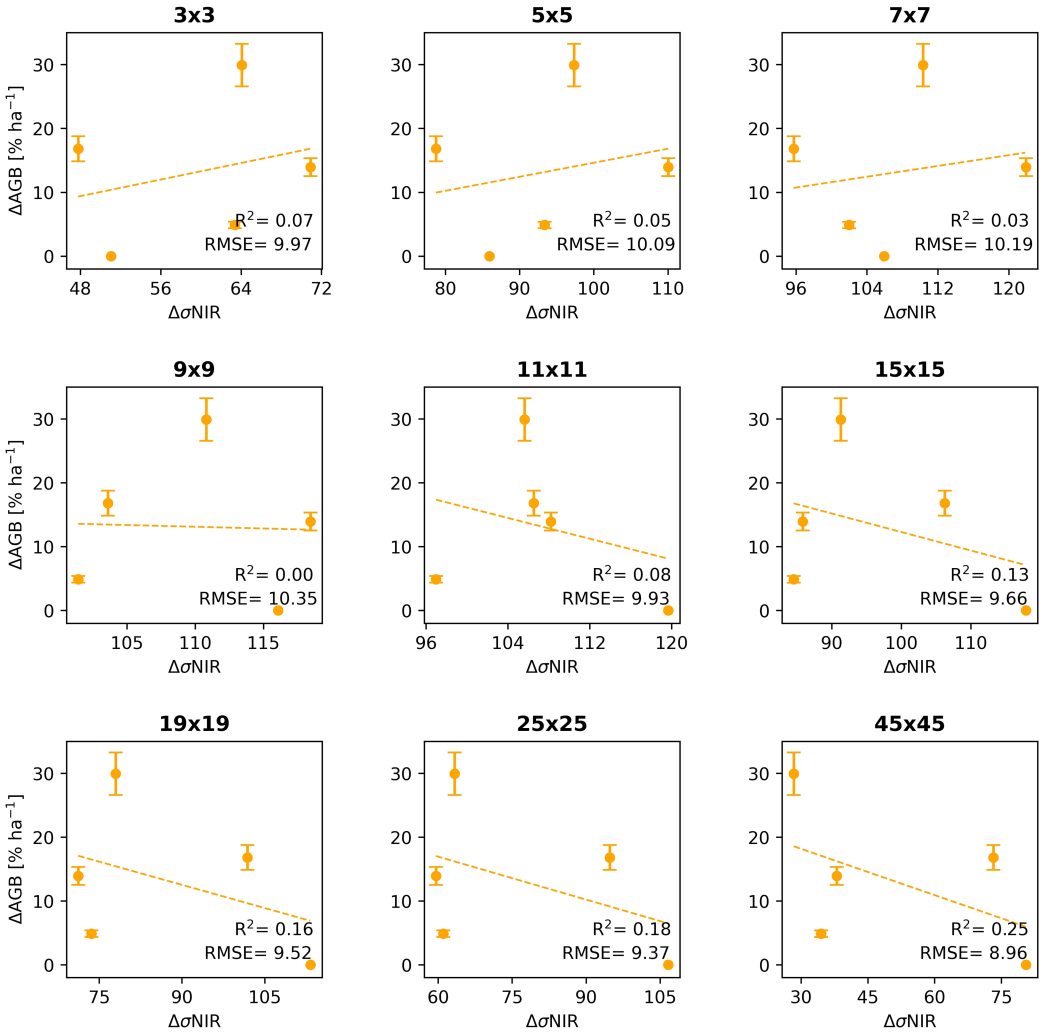
3x3
5x5
7x7
9x9
11x11
15x15
19x19
25x25
45x45
ΔAGB [% ha^{-1}]
ΔσNIR
R^2= 0.07
RMSE= 9.97
R^2= 0.05
RMSE= 10.09
R^2= 0.03
RMSE= 10.19
R^2= 0.00
RMSE= 10.35
R^2= 0.08
RMSE= 9.93
R^2= 0.13
RMSE= 9.66
R^2= 0.16
RMSE= 9.52
R^2= 0.18
RMSE= 9.37
R^2= 0.25
RMSE= 8.96

(c)

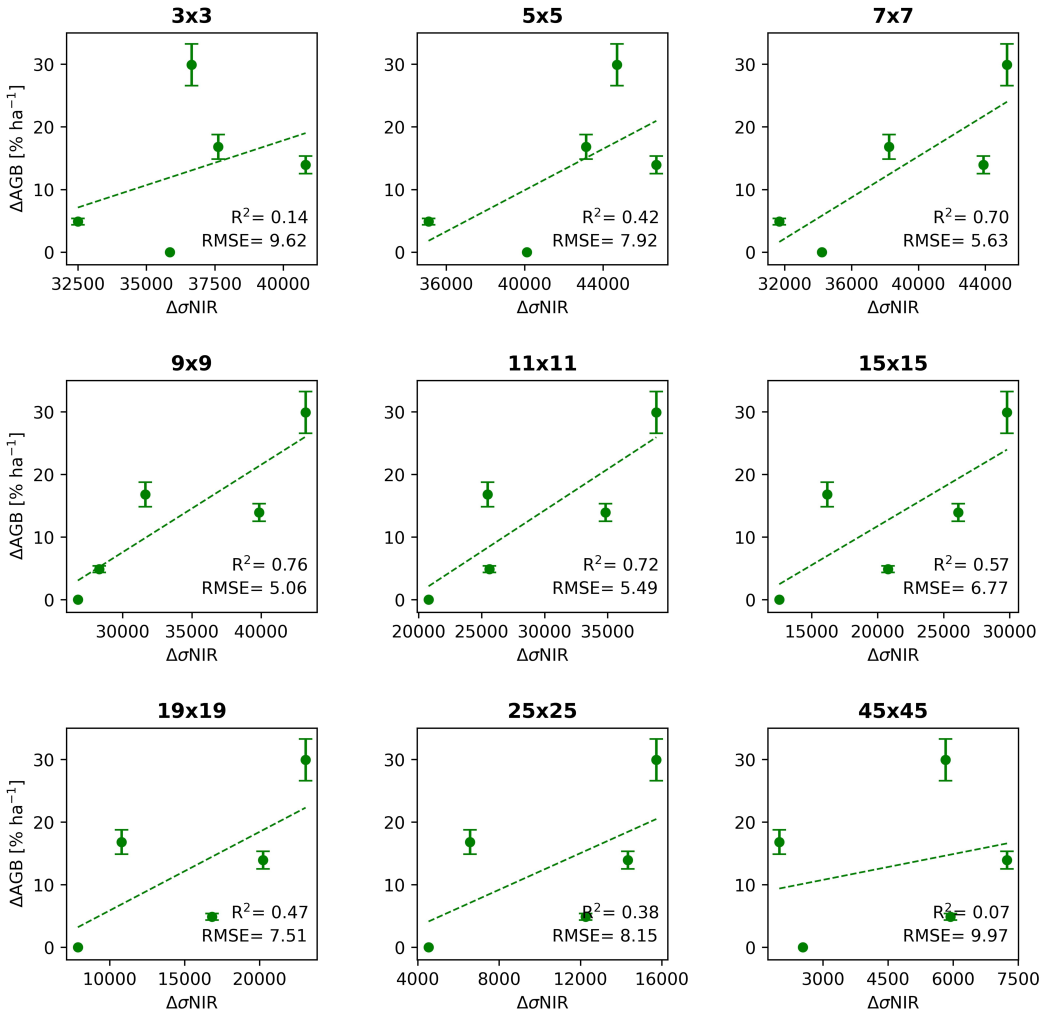
3x3
5x5
7x7
9x9
11x11
15x15
19x19
25x25
45x45
ΔAGB [% ha^{-1}]
ΔσNIR
R^2= 0.14
RMSE= 9.62
R^2= 0.42
RMSE= 7.92
R^2= 0.70
RMSE= 5.63
R^2= 0.76
RMSE= 5.06
R^2= 0.72
RMSE= 5.49
R^2= 0.57
RMSE= 6.77
R^2= 0.47
RMSE= 7.51
R^2= 0.38
RMSE= 8.15
R^2= 0.07
RMSE= 9.97

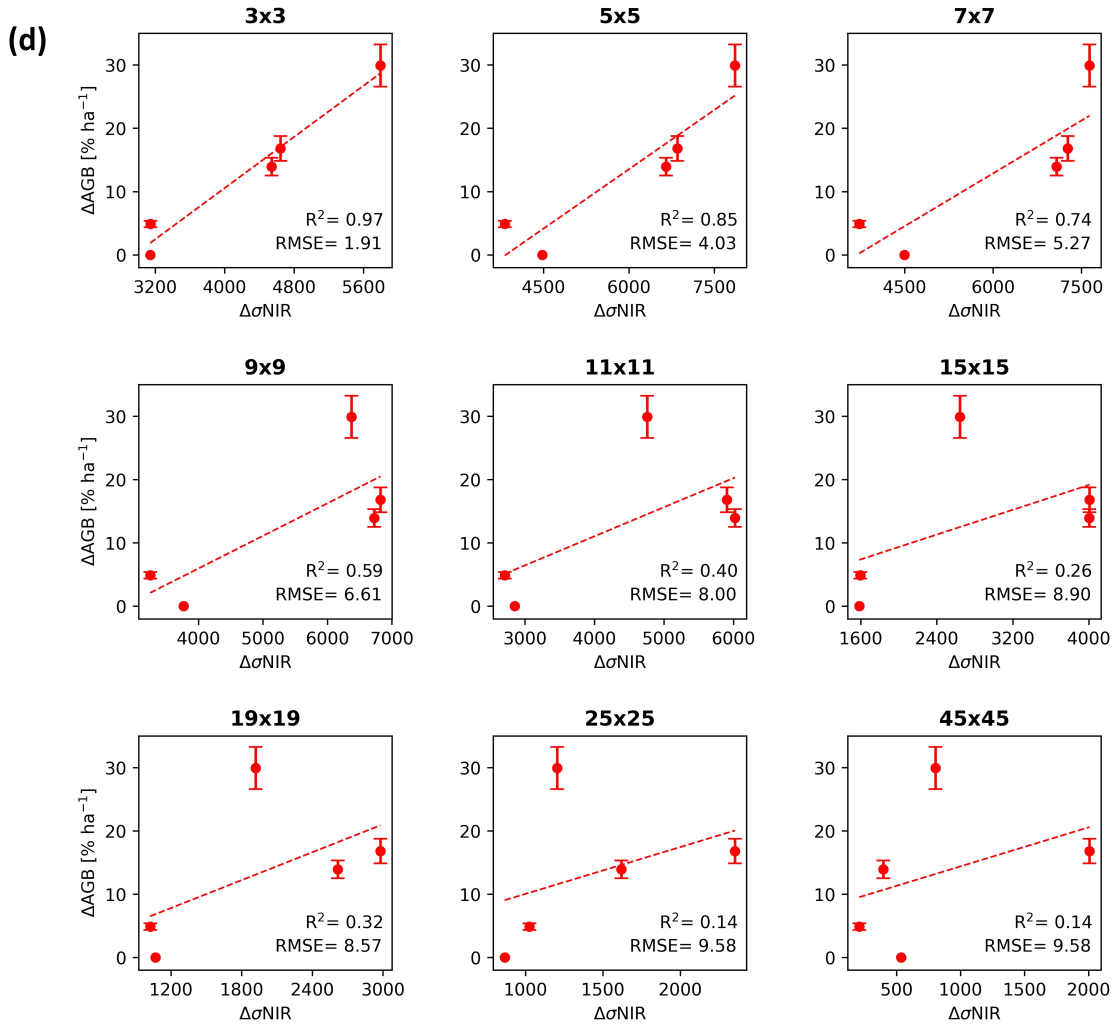

Figure B.1: Regression models for predicting biomass change from the difference in texture of the NIR bands (Δ-σNIR), at increasing window sizes, for the highest resolution sensors (0.3 - 3 m resolution): (**a**) WorldView-3; (**b**) SkySat; (**c**) SPOT-7 and (**d**) PlanetScope.

Appendix C

Supplementary Materials for Chapter 3

Table C.1: Comparison between Aboveground Biomass change (ΔAGB) figures of eight 1-ha selectively logged plots located in Gabon (G) and Peru (P), where the AGB of the logged trees is calculated either using an allometric equation (Allometric ΔAGB) or Terrestrial Laser Scanning data (TLS ΔAGB). Allometric ΔAGB is calculated as the difference in AGB between the first and second inventory. TLS ΔAGB is the sum of the TLS volumes for the logged trees and the difference in AGB between the first and second inventory for the unlogged trees. Standard errors are reported in parentheses.

Plot	Allometric ΔAGB [Mg ha^{-1}]	TLS ΔAGB [Mg ha^{-1}]	Percentage Difference
GC1	131.2 (12.7)	131.2 (12.8)	0.1%
GC2	26.9 (4.8)	28.3 (4.8)	-5.3%
GC3	56.1 (7.8)	55.0 (7.1)	2.1%
GC4	93.4 (8.3)	108.9 (10.4)	-15.3%
PC1	60.9 (5.9)	49.7 (5.0)	20.3%
PC2	49.6 (5.1)	37.1 (3.2)	28.8%
PC3	99.7 (6.4)	81.0 (4.2)	20.7%
PC4	14.6 (1.4)	12.8 (1.0)	13.1%

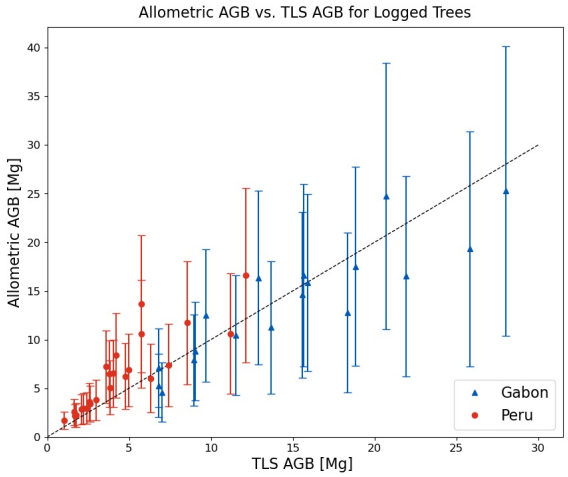

Figure C.1: Comparison between Aboveground Biomass (AGB) values derived using allometric equations and AGB values derived from Terrestrial Laser Scanning (TLS) measurements for the logged trees in Gabon (blue triangles) and Peru (red circles).

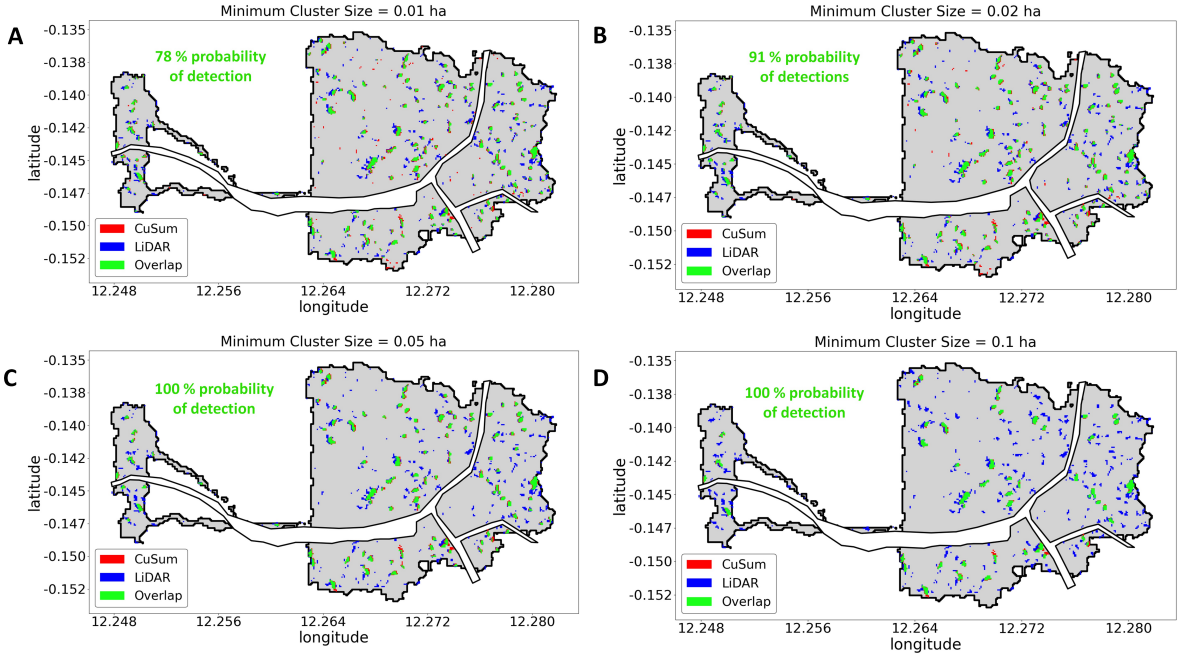

Figure C.2: Maps of the CuSum spatial results for the study in area in Gabon, showing the location of the detections from the CuSum method (red), the results from the LiDAR reference map (blue) and the overlaps between CuSum and LiDAR detections, for CuSum clusters of increasing size: (A) CuSum clusters $\geq$ 0.01 ha; (B) CuSum clusters $\geq$ 0.02 ha; (C) CuSum clusters $\geq$ 0.05 ha; (D) CuSum clusters $\geq$ 0.1 ha.

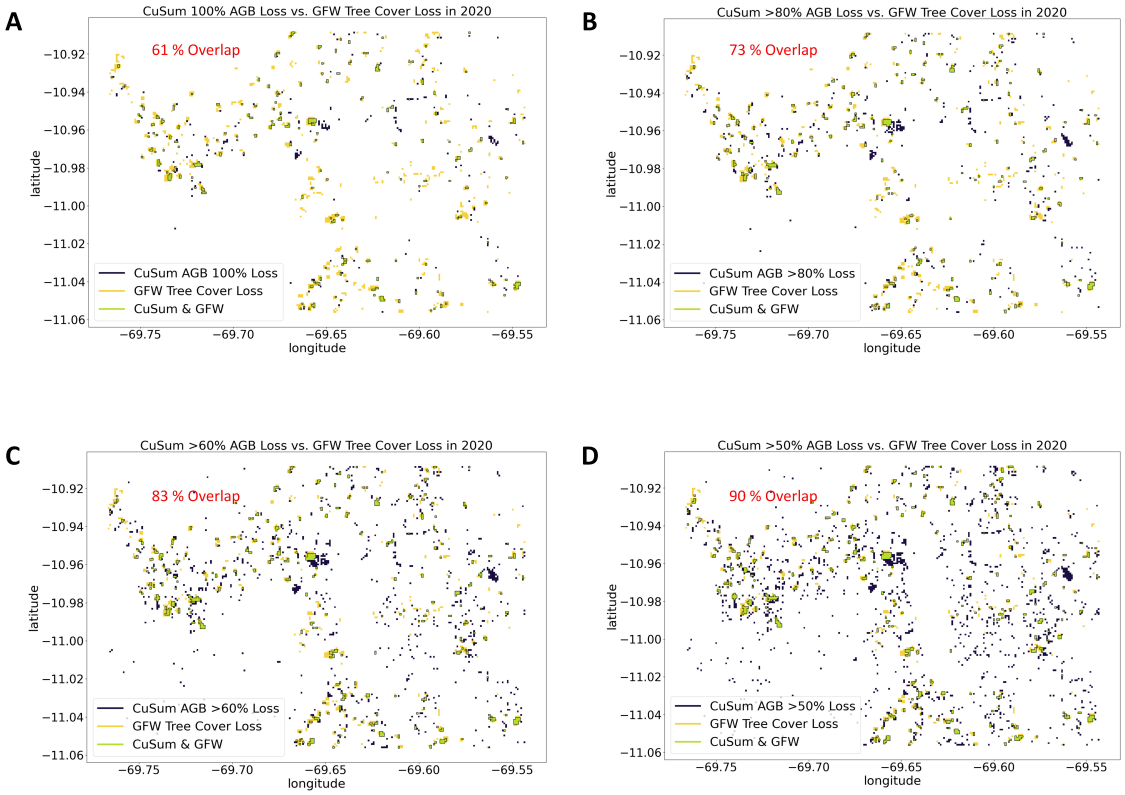

Figure C.3: Comparing the GFW Tree Cover Loss product and the CuSum-derived aboveground biomass (AGB) loss map for the Peru test site, at different threshold of AGB loss: (A) AGB Loss = 100%, (B) CuSum AGB Loss $>$ 80 %; (C) CuSum AGB Loss $>$ 60 %; (D) CuSum AGB Loss $>$ 50 %.

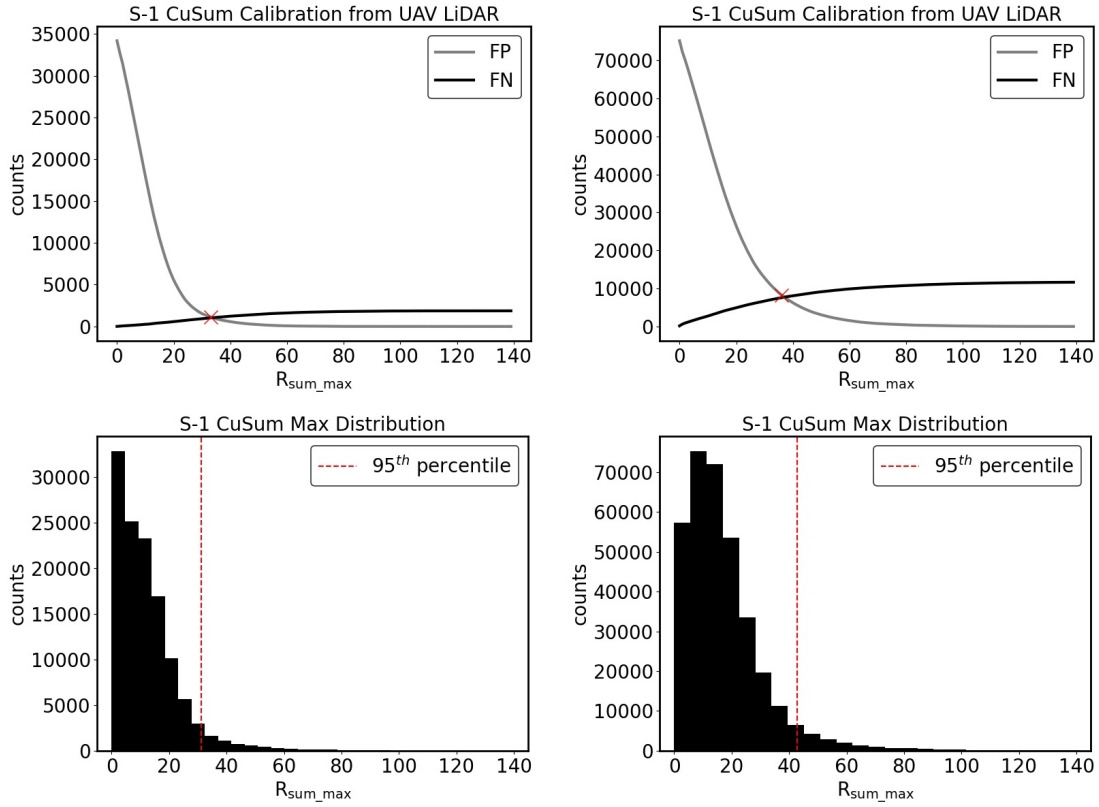

Figure C.4: Comparison of thresholding procedures for change detection. 1) Thresholding using UAV LiDAR data to calculate the value minimising both False Positive (FP) and False Negative (FN) detections yields R_{sum_max} = 33 for Gabon (top left) and R_{sum_max} = 36 for Peru (top right). 2) Thresholding using the 95th percentile of the R_{sum_max} distribution gives a value of R_{sum_max} = 31 for Gabon (bottom left) and R_{sum_max} = 42 for Peru (bottom right).

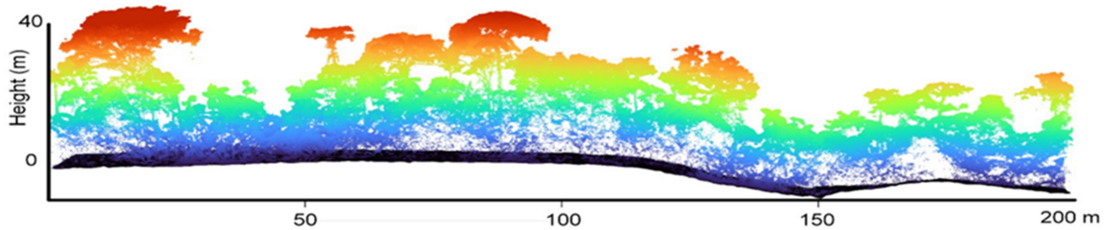

Figure C.5: LiDAR vertical profile of the field site in Gabon, showing the presence of multi-storied forest canopies.

Appendix D

Supplementary Materials for Chapter 4

Table D.1: Area of disturbed forest in logging concessions in Gabon for 2020.

Origin of Capital	Logging Company	Disturbed Area (ha)
Gabon	Bayonne	321
France	Bois et Scierie de l'Ogooué (BSO)	969
Gabon	Bokoue Lobé	96
Malaysia	Bonus Harvest/CIPLAC	500
Malaysia	Bordamur/Toujours Vert	361
Lebanon	Compagnie Africaine d'Exploitation du Bois	35
France	Compagnie Forestière du Haut Ogooué (CIFHO)	677
France	Companie des Bois du Gabon (CBG)	940
India	Companie Forestière des Abeilles (CFA/DLH)	767
Italy	CORA WOOD	1,270
China	Exploitation Forestière de Moanda (EFM-SSMO)	443
France	Exploitation Gabonaise de Grumes (EGG)	335
China	Export Négoce du Bois (ENB)	136
France	FOREEX	130
Gabon	Forestry Development Gabon (FDG)	276
China	Gabon ALONG SARL	71
China	Gabon Export Bois-ASSALA-Compagnie Bois Kota	184

Continued on next page

Table D.1 – *Continued from previous page*

Origin of Capital	Logging Company	Disturbance Area (ha)
India	GAW/GSEZW-HO/OI	511
India	GAW-Ngounié	562
China	GIB-Tale	33
Gabon	GIE OKANO	169
India	GIW/GSEZW-Oyem	214
India	GIW-Estuaire	148
India	GIW-Minvoul	87
Lebanon	Grand Bois	271
South Africa	Grande Mayumba	218
India	GSEZ/GSEZW-Sud Ngounié	478
India	GSEZ-Olam Zolendé	486
India	GSEZW-Lambaréné Lacs	599
China	HUA JIA	289
Gabon	IBNG Lambaréné	85
Gabon	IMENOU Plateau	31
China	Industrie Forestière de Lambaréné (IFL)	178
Lebanon	LEROY GABON	1,205
China	Mitzic Exploitation Forestière (MEF)	128
China	Mont Pele Bois (MPB)	236
China	New Oriental International Investiment (NOII)	309
Gabon	Obangué	135
India	OLAM Gabon	492
China	OSSIE Industrie	270
China	PENG XIN SARL (PXS)	485
Switzerland	Precious Wood/ex CEB	1,259

Continued on next page

Table D.1 – *Continued from previous page*

Origin of Capital	Logging Company	Disturbance Area (ha)
China	Rain Forest Management (RFM)	242
France	Regroupement FOREEX OKANO/TCBG	160
Malaysia	Rimbunan Hijau Gabon	181
France	Rougier Gabon	914
Gabon	SNBG-OVG	114
France	Société des Bois de Lastourville/ Transbois	706
Gabon	SEEF	840
Malaysia	SFIK	389
France	Société Import Export Bois (SIEB)	76
Gabon	Société Nationale des Bois du Gabon (SNBG)	182
Gabon	TAURIAN	86
Lebanon	STIBG	21
China	SUNLY	1,260
China	TALIBOIS	109
China	Transport Bois Negoce International (TBNI)	714
China	Tropical Logs Production (TLP)	70
Lebanon	Tropical Timber Industry Board (TTIB)	110
China	WAN CHUAN Timber SARL (WCTS)	116
Total		**22,679**

Bibliography

F. Achard, H.-J. Stibig, H. D. Eva, E. J. Lindquist, A. Bouvet, O. Arino, and P. Mayaux. Estimating tropical deforestation from Earth observation data. *Carbon Management*, 1 (2):271–287, Dec. 2010. URL http://www.tandfonline.com/doi/abs/10.4155/cmt.10.30.

F. Achard, R. Beuchle, P. Mayaux, H.-J. Stibig, C. Bodart, A. Brink, S. Carboni, B. Desclée, F. Donnay, H. D. Eva, A. Lupi, R. Raši, R. Seliger, and D. Simonetti. Determination of tropical deforestation rates and related carbon losses from 1990 to 2010. *Global Change Biology*, 20(8):2540–2554, 2014. URL https://onlinelibrary.wiley.com/doi/abs/10.1111/gcb.12605. _eprint: https://onlinelibrary.wiley.com/doi/pdf/10.1111/gcb.12605.

R. F. Adler, G. J. Huffman, A. Chang, R. Ferraro, P.-P. Xie, J. Janowiak, B. Rudolf, U. Schneider, S. Curtis, D. Bolvin, A. Gruber, J. Susskind, P. Arkin, and E. Nelkin. The Version-2 Global Precipitation Climatology Project (GPCP) Monthly Precipitation Analysis (1979–Present). *Journal of Hydrometeorology*, 4(6):1147–1167, Dec. 2003. URL http://journals.ametsoc.org/doi/10.1175/1525-7541(2003)004<1147:TVGPCP>2.0.CO;2.

C. T. Almeida, J. F. Oliveira-Júnior, R. C. Delgado, P. Cubo, and M. C. Ramos. Spatiotemporal rainfall and temperature trends throughout the Brazilian Legal Amazon, 1973–2013. *International Journal of Climatology*, 37(4):2013–2026, 2017. doi: 10.1002/joc.4831. URL https://onlinelibrary.wiley.com/doi/abs/10.1002/joc.4831.

G. Amarnath, S. Babar, and M. S. R. Murthy. Evaluating MODIS-vegetation continuous field products to assess tree cover change and forest fragmentation in India – A multi-scale satellite remote sensing approach. *The Egyptian Journal of Remote Sensing and Space Science*, 20(2):157–168, Dec. 2017. URL https://www.sciencedirect.com/science/article/pii/S1110982317302132.

C. Aquino, E. T. A. Mitchard, I. M. McNicol, H. Carstairs, A. Burt, B. L. Puma Vilca, M. Obiang Ebanéga, A. Modinga Dikongo, C. Dassi, S. Mayta, M. Tamayo, P. Grijalba, F. Miranda, and M. Disney. Reliably mapping low-intensity forest disturbance using satellite radar data. *Frontiers in Forests and Global Change*, 5, 2022. URL https://www.frontiersin.org/articles/10.3389/ffgc.2022.1018762.

C. M. Arellano, A. A. Maralit, E. C. Paringit, C. J. Sarmiento, R. A. Faelga, F. A. Tandoc, C. Vidad, R. Lopez, and F. J. Pamittan. Multi-temporal Analysis of Dense and Sparse Forests' Radar Backscatter Using Sentinel-1A Collection In Google Earth Engine. *The International Archives of the Photogrammetry, Remote Sensing and Spatial Information Sciences*, XLII-4/W19:23–30, Dec. 2019. URL https://www.int-arch-photogramm-remote-sens-spatial-inf-sci.net/XLII-4-W19/23/2019/.

M. Arias, M. Campo-Bescós, and J. Álvarez Mozos. On the influence of acquisition geometry in backscatter time series over wheat. *International Journal of Applied Earth Observation and Geoinformation*, 106:102671, Feb. 2022. URL https://www.sciencedirect.com/science/article/pii/S0303243421003780.

A. P. Asiyanbi, A. A. Arhin, and U. Isyaku. REDD+ in West Africa: Politics of Design and Implementation in Ghana and Nigeria. *Forests*, 8(3):78, Mar. 2017. URL https://www.mdpi.com/1999-4907/8/3/78.

G. P. Asner. Cloud cover in Landsat observations of the Brazilian Amazon. *International Journal of Remote Sensing*, 22(18):3855–3862, Jan. 2001. URL https://doi.org/10.1080/01431160010006926.

G. P. Asner, M. Keller, R. Pereira, Jr, J. C. Zweede, and J. N. M. Silva. Canopy Damage and Recovery After Selective Logging in Amazonia: Field and Satellite Studies. *Ecological Applications*, 14(sp4):280–298, 2004. URL https://onlinelibrary.wiley.com/doi/abs/10.1890/01-6019.

K. G. Austin, M. González-Roglich, D. Schaffer-Smith, A. M. Schwantes, and J. J. Swenson. Trends in size of tropical deforestation events signal increasing dominance of industrial-scale drivers. *Environmental Research Letters*, 12(5):054009, May 2017. URL https://doi.org/10.1088/1748-9326/aa6a88.

V. Avitabile, M. Herold, G. B. M. Heuvelink, S. L. Lewis, O. L. Phillips, G. P. Asner, J. Armston, P. S. Ashton, L. Banin, N. Bayol, N. J. Berry, P. Boeckx, B. H. J. de Jong, B. DeVries, C. A. J. Girardin, E. Kearsley, J. A. Lindsell, G. Lopez-Gonzalez, R. Lucas, Y. Malhi, A. Morel, E. T. A. Mitchard, L. Nagy, L. Qie, M. J. Quinones, C. M. Ryan, S. J. W. Ferry, T. Sunderland, G. V. Laurin, R. C. Gatti, R. Valentini, H. Verbeeck, A. Wijaya, and S. Willcock. An integrated pan-tropical biomass map using multiple reference datasets. *Global Change Biology*, 22(4):1406–1420, 2016. URL https://onlinelibrary.wiley.com/doi/abs/10.1111/gcb.13139.

A. Baccini, S. J. Goetz, W. S. Walker, N. T. Laporte, M. Sun, D. Sulla-Menashe, J. Hackler, P. S. A. Beck, R. Dubayah, M. A. Friedl, S. Samanta, and R. A. Houghton. Estimated carbon dioxide emissions from tropical deforestation improved by carbon-density maps. *Nature Climate Change*, 2(3):182–185, Mar. 2012. URL https://www.nature.com/articles/nclimate1354.

A. Baccini, W. Walker, L. Carvalho, M. Farina, D. Sulla-Menashe, and R. A. Houghton. Tropical forests are a net carbon source based on aboveground measurements of gain and loss. *Science*, Oct. 2017. URL https://www.science.org/doi/abs/10.1126/science.aam5962.

M. Ballère, A. Bouvet, S. Mermoz, T. Le Toan, T. Koleck, C. Bedeau, M. André, E. Forestier, P.-L. Frison, and C. Lardeux. SAR data for tropical forest disturbance alerts in French Guiana: Benefit over optical imagery. *Remote Sensing of Environment*, 252:112159, Jan. 2021. URL https://www.sciencedirect.com/science/article/pii/S0034425720305320.

N. Bassey. Stop the Continent Grab and the REDD-ification of Africa. No REDD in Africa Network, 2015.

M. M. Bayrak and L. M. Marafa. Ten Years of REDD+: A Critical Review of the Impact of REDD+ on Forest-Dependent Communities. *Sustainability*, 8(7):620, July 2016. URL https://www.mdpi.com/2071-1050/8/7/620.

C. Beer, M. Reichstein, E. Tomelleri, P. Ciais, M. Jung, N. Carvalhais, C. Rödenbeck, M. A. Arain, D. Baldocchi, G. B. Bonan, A. Bondeau, A. Cescatti, G. Lasslop, A. Lindroth, M. Lomas, S. Luyssaert, H. Margolis, K. W. Oleson, O. Roupsard, E. Veenendaal, N. Viovy, C. Williams, F. I. Woodward, and D. Papale. Terrestrial Gross Carbon Dioxide Uptake: Global Distribution and Covariation with Climate. *Science*, 329(5993):834–838, Aug. 2010. URL https://www.science.org/doi/10.1126/science.1184984. Publisher: American Association for the Advancement of Science.

R. Beuchle, F. Achard, C. Bourgoin, C. Vancutsem, H. Eva, and M. Follador. Deforestation and forest degradation in the Amazon - Status and trends up to year 2020. *JRC Publications Repository*, June 2021. URL https://publications.jrc.ec.europa.eu/repository/handle/JRC124955.

A. Biersack. Reimagining Political Ecology: Culture/Power/History/Nature. Nov. 2006. URL https://read.dukeupress.edu/books/book/1070/chapter/151907/Reimagining-Political-EcologyCulture-Power-History.

O. M. Bollandsås, T. G. Gregoire, E. Næsset, and B.-H. Øyen. Detection of biomass change in a Norwegian mountain forest area using small footprint airborne laser scanner data. *Statistical Methods & Applications*, 22(1):113–129, Mar. 2013.

G. B. Bonan. Forests and Climate Change: Forcings, Feedbacks, and the Climate Benefits of Forests. *Science*, 320(5882):1444–1449, June 2008. URL https://www.science.org/doi/full/10.1126/science.1155121.

A. Bouvet, S. Mermoz, M. Ballère, T. Koleck, and T. Le Toan. Use of the SAR Shadowing Effect for Deforestation Detection with Sentinel-1 Time Series. *Remote Sensing*, 10 (8):1250, Aug. 2018a. URL https://www.mdpi.com/2072-4292/10/8/1250.

A. Bouvet, S. Mermoz, T. Le Toan, L. Villard, R. Mathieu, L. Naidoo, and G. P. Asner. An above-ground biomass map of African savannahs and woodlands at 25m resolution derived from ALOS PALSAR. *Remote Sensing of Environment*, 206:156–173, Mar. 2018b. URL https://www.sciencedirect.com/science/article/pii/S0034425717306053.

D. S. Boyd and F. M. Danson. Satellite remote sensing of forest resources: three decades of research development. *Progress in Physical Geography: Earth and Environment*, 29(1):1–26, Mar. 2005.

A. Braun. Radar satellite imagery for humanitarian response. Bridging the gap between technology and application, Aug. 2019. URL https://publikationen.uni-tuebingen.de/xmlui/handle/10900/91317.

B. Brede, K. Calders, A. Lau, P. Raumonen, H. M. Bartholomeus, M. Herold, and L. Kooistra. Non-destructive tree volume estimation through quantitative structure modelling: Comparing UAV laser scanning with terrestrial LIDAR. *Remote Sensing of Environment*, 233:111355, Nov. 2019. URL https://www.sciencedirect.com/science/article/pii/S0034425719303748.

S. Brown and F. a. A. O. o. t. U. Nations. *Estimating Biomass and Biomass Change of Tropical Forests: A Primer*. Food & Agriculture Org., 1997.

E. L. Bullock, C. E. Woodcock, and P. Olofsson. Monitoring tropical forest degradation using spectral unmixing and Landsat time series analysis. *Remote Sensing of Environment*, 238:110968, Mar. 2020. URL https://www.sciencedirect.com/science/article/pii/S0034425718305200.

E. L. Bullock, S. P. Healey, Z. Yang, R. Houborg, N. Gorelick, X. Tang, and C. Andrianirina. Timeliness in forest change monitoring: A new assessment framework demonstrated using Sentinel-1 and a continuous change detection algorithm. *Remote Sensing of Environment*, 276:113043, July 2022. URL https://www.sciencedirect.com/science/article/pii/S0034425722001572.

C. Burga Cahuana. Participation and Representation: REDD+ in the Native Communities of Belgica and Infierno in the Peruvian Amazon. Master's thesis, University of Illinois at Urbana-Champaign, 2013.

A. Burt, M. Disney, and K. Calders. Extracting individual trees from lidar point clouds using treeseg. *Methods in Ecology and Evolution*, 10(3):438–445, 2019. ISSN 2041-210X. URL https://onlinelibrary.wiley.com/doi/abs/10.1111/2041-210X.13121.

A. Burt, M. Boni Vicari, A. C. L. da Costa, I. Coughlin, P. Meir, L. Rowland, and M. Disney. New insights into large tropical tree mass and structure from direct harvest and terrestrial lidar. *Royal Society Open Science*, 8(2):201458, 2021. URL https://royalsocietypublishing.org/doi/10.1098/rsos.201458.

J. Caballero Espejo, M. Messinger, F. Román-Dañobeytia, C. Ascorra, L. E. Fernandez, and M. Silman. Deforestation and Forest Degradation Due to Gold Mining in the Peruvian Amazon: A 34-Year Perspective. *Remote Sensing*, Dec. 2018. URL https://www.mdpi.com/2072-4292/10/12/1903.

K. Calders, G. Newnham, A. Burt, S. Murphy, P. Raumonen, M. Herold, D. Culvenor, V. Avitabile, M. Disney, J. Armston, and M. Kaasalainen. Nondestructive estimates of above-ground biomass using terrestrial laser scanning. *Methods in Ecology and Evolution*, 6(2):198–208, 2015. URL https://onlinelibrary.wiley.com/doi/abs/10.1111/2041-210X.12301.

H. Carstairs, E. T. A. Mitchard, I. McNicol, C. Aquino, A. Burt, M. O. Ebanega, A. M. Dikongo, J.-L. Bueso-Bello, and M. Disney. An Effective Method for InSAR Mapping of Tropical Forest Degradation in Hilly Areas. *Remote Sensing*, 14(3):452, Jan. 2022a. URL https://www.mdpi.com/2072-4292/14/3/452.

H. Carstairs, E. T. A. Mitchard, I. McNicol, C. Aquino, E. Chezeaux, M. O. Ebanega, A. M. Dikongo, and M. Disney. Sentinel-1 Shadows Used to Quantify Canopy Loss from Selective Logging in Gabon. *Remote Sensing*, 14(17):4233, Jan. 2022b. URL https://www.mdpi.com/2072-4292/14/17/4233.

M. C. Castro, A. Baeza, C. T. Codeço, Z. M. Cucunubá, A. P. Dal'Asta, G. A. D. Leo, A. P. Dobson, G. Carrasco-Escobar, R. M. Lana, R. Lowe, A. M. V. Monteiro, M. Pascual, and M. Santos-Vega. Development, environmental degradation, and disease spread in the Brazilian Amazon. *PLOS Biology*, 17(11):e3000526, Nov. 2019. URL https://journals.plos.org/plosbiology/article?id=10.1371/journal.pbio.3000526.

J. Chave. Generic tree allometric models. 2014. URL https://chave.ups-tlse.fr/pantropical_allometry.htm. (Last accessed on 13/01/2021).

J. Chave, R. Condit, S. Aguilar, A. Hernandez, S. Lao, and R. Perez. Error propagation and scaling for tropical forest biomass estimates. *Philosophical Transactions of the Royal Society B: Biological Sciences*, 359(1443):409–420, Mar. 2004. URL https://www.ncbi.nlm.nih.gov/pmc/articles/PMC1693335/.

J. Chave, D. Coomes, S. Jansen, S. L. Lewis, N. G. Swenson, and A. E. Zanne. Towards a worldwide wood economics spectrum. *Ecology Letters*, 12(4), 2009. URL https://www.readcube.com/articles/10.1111%2Fj.1461-0248.2009.01285.x.

J. Chave, M. Réjou-Méchain, A. Búrquez, E. Chidumayo, M. S. Colgan, W. B. C. Delitti, A. Duque, T. Eid, P. M. Fearnside, R. C. Goodman, M. Henry, A. Martínez-Yrízar, W. A. Mugasha, H. C. Muller-Landau, M. Mencuccini, B. W. Nelson, A. Ngomanda, E. M. Nogueira, E. Ortiz-Malavassi, R. Pélissier, P. Ploton, C. M. Ryan, J. G. Saldarriaga, and G. Vieilledent. Improved allometric models to estimate the aboveground biomass of tropical trees. *Global Change Biology*, 20(10):3177–3190, 2014. URL https://onlinelibrary.wiley.com/doi/abs/10.1111/gcb.12629.

A. Chhatre and A. Agrawal. Trade-offs and synergies between carbon storage and livelihood benefits from forest commons. *Proceedings of the National Academy of Sciences*, 106(42):17667–17670, Oct. 2009. URL https://www.pnas.org/content/106/42/17667.

S. Chomba, J. Kariuki, J. F. Lund, and F. Sinclair. Roots of inequity: How the implementation of REDD+ reinforces past injustices. *Land Use Policy*, 50:202–213, Jan. 2016. URL https://www.sciencedirect.com/science/article/pii/S0264837715002926.

Copernicus. Copernicus Open Access Hub, 2020. URL https://scihub.copernicus.eu/dhus/#/home. (Last accessed on 23/08/2022).

P. G. Curtis, C. M. Slay, N. L. Harris, A. Tyukavina, and M. C. Hansen. Classifying drivers of global forest loss. *Science*, 361(6407):1108–1111, Sept. 2018. URL https://www.science.org/doi/10.1126/science.aau3445.

M. E. J. Cutler, D. S. Boyd, G. M. Foody, and A. Vetrivel. Estimating tropical forest biomass with a combination of SAR image texture and Landsat TM data: An assessment of predictions between regions. *ISPRS Journal of Photogrammetry and Remote Sensing*, 70:66–77, June 2012. URL https://www.sciencedirect.com/science/article/pii/S0924271612000652.

C. D'Almeida, C. J. Vörösmarty, G. C. Hurtt, J. A. Marengo, S. L. Dingman, and B. D. Keim. The effects of deforestation on the hydrological cycle in Amazonia: a review on scale and resolution. *International Journal of Climatology*, 27(5):633–647, 2007. URL https://onlinelibrary.wiley.com/doi/abs/10.1002/joc.1475.

R. B. de Andrade, J. K. Balch, A. L. Parsons, D. Armenteras, R. M. Roman-Cuesta, and J. Bulkan. Scenarios in tropical forest degradation: carbon stock trajectories for REDD+. *Carbon Balance and Management*, 12(1):6, Mar. 2017. URL https://doi.org/10.1186/s13021-017-0074-0.

G. De Grandi, R. Lucas, and J. Kropacek. Analysis by Wavelet Frames of Spatial Statistics in SAR Data for Characterizing Structural Properties of Forests. *IEEE Transactions on Geoscience and Remote Sensing*, 47(2):494–507, Feb. 2009. URL http://ieeexplore.ieee.org/document/4695998/.

F. de Souza Mendes, D. Baron, G. Gerold, V. Liesenberg, and S. Erasmi. Optical and SAR Remote Sensing Synergism for Mapping Vegetation Types in the Endangered Cerrado/Amazon Ecotone of Nova Mutum—Mato Grosso. *Remote Sensing*, 11(10):1161, Jan. 2019. URL https://www.mdpi.com/2072-4292/11/10/1161.

J. Deutscher, K. Gutjahr, R. Perko, H. Raggam, M. Hirschmugl, and M. Schardt. Humid tropical forest monitoring with multi-temporal L-, C- and X-band SAR data. In *2017 9th International Workshop on the Analysis of Multitemporal Remote Sensing Images (MultiTemp)*, pages 1–4, June 2017.

DigitalGlobe. Radiometric Use of WorldView-3 Imagery. 2016. URL https://dg-cms-uploads-production.s3.amazonaws.com/uploads/document/file/207/Radiometric_Use_of_WorldView-3_v2.pdf. (Last accessed on 17/04/2021).

S. E. Diringer, A. J. Berky, M. Marani, E. J. Ortiz, O. Karatum, D. L. Plata, W. K. Pan, and H. Hsu-Kim. Deforestation Due to Artisanal and Small-Scale Gold Mining Exacerbates Soil and Mercury Mobilization in Madre de Dios, Peru. *Environmental Science & Technology*, 54(1):286–296, Jan. 2020. URL https://doi.org/10.1021/acs.est.9b06620.

M. I. Disney, M. Boni Vicari, A. Burt, K. Calders, S. L. Lewis, P. Raumonen, and P. Wilkes. Weighing trees with lasers: advances, challenges and opportunities. *Interface Focus*, 8(2):20170048, Apr. 2018. URL https://royalsocietypublishing.org/doi/full/10.1098/rsfs.2017.0048.

J. Doblas, Y. Shimabukuro, S. Sant'Anna, A. Carneiro, L. Aragão, and C. Almeida. Optimizing Near Real-Time Detection of Deforestation on Tropical Rainforests Using Sentinel-1 Data. *Remote Sensing*, 12(23):3922, Jan. 2020. URL https://www.mdpi.com/2072-4292/12/23/3922.

I. Douglas. Ecosystems and Human Well-Being. In D. A. Dellasala and M. I. Goldstein, editors, *Encyclopedia of the Anthropocene*, pages 185–197. Elsevier, Oxford, Jan. 2018. URL https://www.sciencedirect.com/science/article/pii/B9780128096659092065.

R. Dubayah, J. B. Blair, S. Goetz, L. Fatoyinbo, M. Hansen, S. Healey, M. Hofton, G. Hurtt, J. Kellner, S. Luthcke, J. Armston, H. Tang, L. Duncanson, S. Hancock, P. Jantz, S. Marselis, P. L. Patterson, W. Qi, and C. Silva. The Global Ecosystem Dynamics Investigation: High-resolution laser ranging of the Earth's forests and topography. *Science of Remote Sensing*, 1:100002, June 2020. URL https://www.sciencedirect.com/science/article/pii/S2666017220300018.

R. Dubayah, J. Armston, S. P. Healey, J. M. Bruening, P. L. Patterson, J. R. Kellner, L. Duncanson, S. Saarela, G. Ståhl, Z. Yang, H. Tang, J. B. Blair, L. Fatoyinbo, S. Goetz, S. Hancock, M. Hansen, M. Hofton, G. Hurtt, and S. Luthcke. GEDI launches a new era of biomass inference from space. *Environmental Research Letters*, 17(9): 095001, Aug. 2022. URL https://doi.org/10.1088/1748-9326/ac8694.

R. O. Dubayah, S. L. Sheldon, D. B. Clark, M. A. Hofton, J. B. Blair, G. C. Hurtt, and R. L. Chazdon. Estimation of tropical forest height and biomass dynamics using lidar remote sensing at La Selva, Costa Rica. *Journal of Geophysical Research: Biogeosciences*, 115(G2), 2010. URL https://onlinelibrary.wiley.com/doi/abs/10.1029/2009JG000933.

L. A. Duguma, P. A. Minang, B. E. Aynekulu, S. Carsan, J. Nzyoka, A. Bah, and R. H. Jamnadass. From Tree Planting to Tree Growing: Rethinking Ecosystem Restoration Through Tree. Working Paper, World Agroforestry, Dec. 2020. URL https://cgspace.cgiar.org/handle/10568/111525.

G. Duveiller, J. Hooker, and A. Cescatti. The mark of vegetation change on Earth's surface energy balance. *Nature Communications*, 9(1):679, Feb. 2018. URL https://www.nature.com/articles/s41467-017-02810-8.

S. Eckert. Improved Forest Biomass and Carbon Estimations Using Texture Measures from WorldView-2 Satellite Data. *Remote Sensing*, 4(4):810–829, Apr. 2012. URL https://www.mdpi.com/2072-4292/4/4/810.

A. Esquivel-Muelbert, O. L. Phillips, R. J. W. Brienen, S. Fauset, M. J. P. Sullivan, T. R. Baker, K.-J. Chao, T. R. Feldpausch, E. Gloor, N. Higuchi, J. Houwing-Duistermaat, J. Lloyd, H. Liu, Y. Malhi, B. Marimon, B. H. Marimon Junior, A. Monteagudo-Mendoza, L. Poorter, M. Silveira, E. V. Torre, E. A. Dávila, J. del Aguila Pasquel, E. Almeida, P. A. Loayza, A. Andrade, L. E. O. C. Aragão, A. Araujo-Murakami, E. Arets, L. Arroyo, G. A. Aymard C., M. Baisie, C. Baraloto, P. B. Camargo, J. Barroso, L. Blanc, D. Bonal,

F. Bongers, R. Boot, F. Brown, B. Burban, J. L. Camargo, W. Castro, V. C. Moscoso, J. Chave, J. Comiskey, F. C. Valverde, A. L. da Costa, N. D. Cardozo, A. Di Fiore, A. Dourdain, T. Erwin, G. F. Llampazo, I. C. G. Vieira, R. Herrera, E. Honorio Coronado, I. Huamantupa-Chuquimaco, E. Jimenez-Rojas, T. Killeen, S. Laurance, W. Laurance, A. Levesley, S. L. Lewis, K. L. L. M. Ladvocat, G. Lopez-Gonzalez, T. Lovejoy, P. Meir, C. Mendoza, P. Morandi, D. Neill, A. J. Nogueira Lima, P. N. Vargas, E. A. de Oliveira, N. P. Camacho, G. Pardo, J. Peacock, M. Peña-Claros, M. C. Peñuela-Mora, G. Pickavance, J. Pipoly, N. Pitman, A. Prieto, T. A. M. Pugh, C. Quesada, H. Ramirez-Angulo, S. M. de Almeida Reis, M. Rejou-Machain, Z. R. Correa, L. R. Bayona, A. Rudas, R. Salomão, J. Serrano, J. S. Espejo, N. Silva, J. Singh, C. Stahl, J. Stropp, V. Swamy, J. Talbot, H. ter Steege, J. Terborgh, R. Thomas, M. Toledo, A. Torres-Lezama, L. V. Gamarra, G. van der Heijden, P. van der Meer, P. van der Hout, R. V. Martinez, S. A. Vieira, J. V. Cayo, V. Vos, R. Zagt, P. Zuidema, and D. Galbraith. Tree mode of death and mortality risk factors across Amazon forests. *Nature Communications*, 11(1):5515, Nov. 2020. URL `https://www.nature.com/articles/s41467-020-18996-3`.

European Space Agency. Sentinel-1 Toolbox - Sentinel Online, 2021. URL `https://sentinel.esa.int/web/sentinel/toolboxes/sentinel-1`. (Last accessed 24/08/2022).

European Space Agency. Product Slices, 2022a. URL `https://sentinels.copernicus.eu/web/sentinel/user-guides/sentinel-1-sar/data-formats/product-slices`. (Last accessed 14/09/2022).

European Space Agency. Sentinel-1- Observation Scenario - Planned Acquisitions - ESA - Sentinel Online, 2022b. URL `https://sentinels.copernicus.eu/web/sentinel/missions/sentinel-1/observation-scenario`. (Last accessed 6/09/2022).

FAO. *Global Forest Resources Assessment 2020: Key findings*. FAO, Rome, Italy, 2020. URL https://www.fao.org/documents/card/en/c/ca8753en.

S. Federici, F. N. Tubiello, M. Salvatore, H. Jacobs, and J. Schmidhuber. New estimates of CO2 forest emissions and removals: 1990–2015. *Forest Ecology and Management*, 352:89–98, Sept. 2015. URL https://www.sciencedirect.com/science/article/pii/S0378112715002443.

T. R. Feldpausch, J. Lloyd, S. L. Lewis, R. J. W. Brienen, M. Gloor, A. Monteagudo Mendoza, G. Lopez-Gonzalez, L. Banin, K. Abu Salim, K. Affum-Baffoe, M. Alexiades, S. Almeida, I. Amaral, A. Andrade, L. E. O. C. Aragão, A. Araujo Murakami, E. J. M. M. Arets, L. Arroyo, G. A. Aymard C., T. R. Baker, O. S. Bánki, N. J. Berry, N. Cardozo, J. Chave, J. A. Comiskey, E. Alvarez, A. d. Oliveira, A. D. Fiore, G. Djagbletey, T. F. Domingues, T. L. Erwin, P. M. Fearnside, M. B. França, M. A. Freitas, N. Higuchi, E. H. C, Y. Iida, E. Jiménez, A. R. Kassim, T. J. Killeen, W. F. Laurance, J. C. Lovett, Y. Malhi, B. S. Marimon, B. H. Marimon-Junior, E. Lenza, A. R. Marshall, C. Mendoza, D. J. Metcalfe, E. T. A. Mitchard, D. A. Neill, B. W. Nelson, R. Nilus, E. M. Nogueira, A. Parada, K. S.-H. Peh, A. Pena Cruz, M. C. Peñuela, N. C. A. Pitman, A. Prieto, C. A. Quesada, F. Ramírez, H. Ramírez-Angulo, J. M. Reitsma, A. Rudas, G. Saiz, R. P. Salomão, M. Schwarz, N. Silva, J. E. Silva-Espejo, M. Silveira, B. Sonké, J. Stropp, H. E. Taedoumg, S. Tan, H. t. Steege, J. Terborgh, M. Torello-Raventos, G. M. F. v. d. Heijden, R. Vásquez, E. Vilanova, V. A. Vos, L. White, S. Willcock, H. Woell, and O. L. Phillips. Tree height integrated into pantropical forest biomass estimates. *Biogeosciences*, 9(8):3381–3403, Aug. 2012. URL https://www.biogeosciences.net/9/3381/2012/.

S. K. Filippelli, M. A. Lefsky, and M. E. Rocca. Comparison and integration of lidar and photogrammetric point clouds for mapping pre-fire forest structure. *Remote Sensing of Environment*, 224:154–166, Apr. 2019. URL https://www.sciencedirect.com/science/article/pii/S0034425719300355.

F. Fleischman, S. Basant, A. Chhatre, E. A. Coleman, H. W. Fischer, D. Gupta, B. Güneralp, P. Kashwan, D. Khatri, R. Muscarella, J. S. Powers, V. Ramprasad, P. Rana, C. R. Solorzano, and J. W. Veldman. Pitfalls of Tree Planting Show Why We Need People-Centered Natural Climate Solutions. *BioScience*, 70(11):947–950, Nov. 2020. URL https://doi.org/10.1093/biosci/biaa094.

ForestPlots.net, C. Blundo, J. Carilla, R. Grau, A. Malizia, L. Malizia, O. Osinaga-Acosta, M. Bird, M. Bradford, D. Catchpole, A. Ford, A. Graham, D. Hilbert, J. Kemp, S. Laurance, W. Laurance, F. Y. Ishida, A. Marshall, C. Waite, H. Woell, J.-F. Bastin, M. Bauters, H. Beeckman, P. Boeckx, J. Bogaert, C. De Canniere, T. de Haulleville, J.-L. Doucet, O. Hardy, W. Hubau, E. Kearsley, H. Verbeeck, J. Vleminckx, S. W. Brewer, A. Alarcón, A. Araujo-Murakami, E. Arets, L. Arroyo, E. Chavez, T. Fredericksen, R. G. Villaroel, G. G. Sibauty, T. Killeen, J. C. Licona, J. Lleigue, C. Mendoza, S. Murakami, A. P. Gutierrez, G. Pardo, M. Peña-Claros, L. Poorter, M. Toledo, J. V. Cayo, L. J. Viscarra, V. Vos, J. Ahumada, E. Almeida, J. Almeida, E. A. de Oliveira, W. A. da Cruz, A. A. de Oliveira, F. A. Carvalho, F. A. Obermuller, A. Andrade, F. A. Carvalho, S. A. Vieira, A. C. Aquino, L. Aragão, A. C. Araújo, M. A. Assis, J. A. M. A. Gomes, F. Baccaro, P. B. de Camargo, P. Barni, J. Barroso, L. C. Bernacci, K. Bordin, M. B. de Medeiros, I. Broggio, J. L. Camargo, D. Cardoso, M. A. Carniello, A. L. C. Rochelle, C. Castilho, A. A. J. F. Castro, W. Castro, S. C. Ribeiro, F. Costa, R. C. de Oliveira, I. Coutinho, J. Cunha, L. da Costa, L. da Costa Ferreira, R. da Costa Silva, M. da Graça Zacarias Simbine, V. de Andrade Kamimura, H. C. de Lima, L. de Oliveira Melo, L. de Queiroz, J. R. de Sousa Lima, M. do Espírito Santo, T. Domingues, N. C. dos Santos Prestes, S. E. S. Carneiro, F. Elias, G. Eliseu, T. Emilio, C. L. Farrapo, L. Fernandes, G. Ferreira, J. Ferreira, L. Ferreira, S. Ferreira, M. F. Simon, M. A. Freitas, Q. S. García, A. G. Manzatto, P. Graça, F. Guilherme, E. Hase, N. Higuchi, M. Iguatemy, R. I. Barbosa, M. Jaramillo, C. Joly, J. Klipel, I. L. do Amaral, C. Levis, A. S. Lima, M. L. Dan, A. Lopes, H. Madeiros, W. E. Magnusson,

R. M. dos Santos, B. Marimon, B. H. M. Junior, R. M. M. Grillo, L. Martinelli, S. M. Reis, S. Medeiros, M. Meira-Junior, T. Metzker, P. Morandi, N. M. do Nascimento, M. Moura, S. C. Müller, L. Nagy, H. Nascimento, M. Nascimento, A. N. Lima, R. O. de Araújo, J. O. Silva, M. Pansonato, G. P. Sabino, K. M. P. de Abreu, P. J. F. P. Rodrigues, M. Piedade, D. Rodrigues, J. R. Rodrigues Pinto, C. Quesada, E. Ramos, R. Ramos, P. Rodrigues, T. R. de Sousa, R. Salomão, F. Santana, M. Scaranello, R. S. Bergamin, J. Schietti, J. Schöngart, G. Schwartz, N. Silva, M. Silveira, C. S. Seixas, M. Simbine, A. C. Souza, P. Souza, R. Souza, T. Sposito, E. S. Junior, J. D. do Vale, I. C. G. Vieira, D. Villela, M. Vital, H. Xaud, K. Zanini, C. E. Zartman, N. K. H. Ideris, F. b. H. Metali, K. A. Salim, M. S. Saparudin, R. M. Serudin, R. S. Sukri, S. Begne, G. Chuyong, M. N. Djuikouo, C. Gonmadje, M. Simo-Droissart, B. Sonké, H. Taedoumg, L. Zemagho, S. Thomas, F. Baya, G. Saiz, J. S. Espejo, D. Chen, A. Hamilton, Y. Li, T. Luo, S. Niu, H. Xu, Z. Zhou, E. Álvarez Dávila, J. C. A. Escobar, H. Arellano-Peña, J. C. Duarte, J. Calderón, L. M. C. Bravo, B. Cuadrado, H. Cuadros, A. Duque, L. F. Duque, S. M. Espinosa, R. Franke-Ante, H. García, A. Gómez, R. González-M., Idárraga-Piedrahíta, E. Jimenez, R. Jurado, W. L. Oviedo, R. López-Camacho, O. A. M. Cruz, I. M. Polo, E. Paky, K. Pérez, A. Pijachi, C. Pizano, A. Prieto, L. Ramos, Z. R. Correa, J. Richardson, E. Rodríguez, G. M. Rodriguez M., A. Rudas, P. Stevenson, M. Chudomelová, M. Dancak, R. Hédl, S. Lhota, M. Svatek, J. Mukinzi, C. Ewango, T. Hart, E. K. Yakusu, J. Lisingo, J.-R. Makana, F. Mbayu, B. Toirambe, J. T. Mukendi, L. Kvist, G. Nebel, S. Báez, C. Céron, D. M. Griffith, J. E. G. Andino, D. Neill, W. Palacios, M. C. Peñuela-Mora, G. Rivas-Torres, G. Villa, S. Demissie, T. Gole, T. Gonfa, K. Ruokolainen, M. Baisie, F. Bénédet, W. Betian, V. Bezard, D. Bonal, J. Chave, V. Droissart, S. Gourlet-Fleury, A. Hladik, N. Labrière, P. Naisso, M. Réjou-Méchain, P. Sist, L. Blanc, B. Burban, G. Derroire, A. Dourdain, C. Stahl, N. N. Bengone, E. Chezeaux, F. E. Ondo, V. Medjibe, V. Mihindou, L. White, H. Culmsee, C. D. Rangel, V. Horna, F. Wittmann, S. Adu-Bredu, K. Affum-Baffoe, E. Foli, M. Balinga, A. Roopsind, J. Singh, R. Thomas, R. Zagt, I. K. Murthy,

K. Kartawinata, E. Mirmanto, H. Priyadi, I. Samsoedin, T. Sunderland, I. Yassir, F. Rovero, B. Vinceti, B. Hérault, S.-I. Aiba, K. Kitayama, A. Daniels, D. Tuagben, J. T. Woods, M. Fitriadi, A. Karolus, K. L. Khoon, N. Majalap, C. Maycock, R. Nilus, S. Tan, A. Sitoe, I. Coronado G., L. Ojo, R. de Assis, A. D. Poulsen, D. Sheil, K. A. Pezo, H. B. Verde, V. C. Moscoso, J. C. C. Oroche, F. C. Valverde, M. C. Medina, N. D. Cardozo, J. de Rutte Corzo, J. del Aguila Pasquel, G. F. Llampazo, L. Freitas, D. G. Cabrera, R. G. Villacorta, K. G. Cabrera, D. G. Soria, L. G. Saboya, J. M. G. Rios, G. H. Pizango, E. H. Coronado, I. Huamantupa-Chuquimaco, W. H. Huasco, Y. T. H. Aedo, J. L. M. Peña, A. M. Mendoza, V. M. Rodriguez, P. N. Vargas, S. C. P. Ramos, N. P. Camacho, A. P. Cruz, F. R. Arevalo, J. R. Huaymacari, C. R. Rodriguez, M. A. R. Paredes, L. R. Bayona, R. del Pilar Rojas Gonzales, M. E. R. Peña, N. S. Revilla, Y. C. S. Shareva, R. T. Trujillo, L. V. Gamarra, R. V. Martinez, J. V. Arenas, C. Amani, S. A. Ifo, Y. Bocko, P. Boundja, R. Ekoungoulou, M. Hockemba, D. Nzala, A. Fofanah, D. Taylor, G. Bañares-de Dios, L. Cayuela, G.-d. la Cerda, M. Macía, J. Stropp, M. Playfair, V. Wortel, T. Gardner, R. Muscarella, H. Priyadi, E. Rutishauser, K.-J. Chao, P. Munishi, O. Bánki, F. Bongers, R. Boot, G. Fredriksson, J. Reitsma, H. ter Steege, T. van Andel, P. van de Meer, P. van der Hout, M. van Nieuwstadt, B. van Ulft, E. Veenendaal, R. Vernimmen, P. Zuidema, J. Zwerts, P. Akite, R. Bitariho, C. Chapman, E. Gerald, M. Leal, P. Mucunguzi, K. Abernethy, M. Alexiades, T. R. Baker, K. Banda, L. Banin, J. Barlow, A. Bennett, E. Berenguer, N. Berry, N. M. Bird, G. A. Blackburn, F. Brearley, R. Brienen, D. Burslem, L. Carvalho, P. Cho, F. Coelho, M. Collins, D. Coomes, A. Cuni-Sanchez, G. Dargie, K. Dexter, M. Disney, F. Draper, M. Duan, A. Esquivel-Muelbert, R. Ewers, B. Fadrique, S. Fauset, T. R. Feldpausch, F. França, D. Galbraith, M. Gilpin, E. Gloor, J. Grace, K. Hamer, D. Harris, K. Jeffery, T. Jucker, M. Kalamandeen, B. Klitgaard, A. Levesley, S. L. Lewis, J. Lindsell, G. Lopez-Gonzalez, J. Lovett, Y. Malhi, T. Marthews, E. McIntosh, K. Melgaço, W. Milliken, E. Mitchard, P. Moonlight, S. Moore, A. Morel, J. Peacock, K. S. H. Peh, C. Pendry, R. T. Pennington, L. de Oliveira Pereira, C. Peres, O. L. Phillips,

G. Pickavance, T. Pugh, L. Qie, T. Riutta, K. Roucoux, C. Ryan, T. Sarkinen, C. S. Valeria, D. Spracklen, S. Stas, M. Sullivan, M. Swaine, J. Talbot, J. Taplin, G. van der Heijden, L. Vedovato, S. Willcock, M. Williams, L. Alves, P. A. Loayza, G. Arellano, C. Asa, P. Ashton, G. Asner, T. Brncic, F. Brown, R. Burnham, C. Clark, J. Comiskey, G. Damasco, S. Davies, T. Di Fiore, T. Erwin, W. Farfan-Rios, J. Hall, D. Kenfack, T. Lovejoy, R. Martin, O. M. Montiel, J. Pipoly, N. Pitman, J. Poulsen, R. Primack, M. Silman, M. Steininger, V. Swamy, J. Terborgh, D. Thomas, P. Umunay, M. Uriarte, E. V. Torre, O. Wang, K. Young, G. A. Aymard C., L. Hernández, R. H. Fernández, H. Ramírez-Angulo, P. Salcedo, E. Sanoja, J. Serrano, A. Torres-Lezama, T. C. Le, T. T. Le, and H. D. Tran. Taking the pulse of Earth's tropical forests using networks of highly distributed plots. *Biological Conservation*, 260:108849, Aug. 2021. URL https://www.sciencedirect.com/science/article/pii/S0006320720309071.

S. Francini, G. D'Amico, E. Vangi, C. Borghi, and G. Chirici. Integrating GEDI and Landsat: Spaceborne Lidar and Four Decades of Optical Imagery for the Analysis of Forest Disturbances and Biomass Changes in Italy. *Sensors*, 22(5):2015, Jan. 2022. URL https://www.mdpi.com/1424-8220/22/5/2015.

S. E. Franklin, R. J. Hall, L. M. Moskal, A. J. Maudie, and M. B. Lavigne. Incorporating texture into classification of forest species composition from airborne multispectral images. *International Journal of Remote Sensing*, 21(1):61–79, Jan. 2000. URL https://doi.org/10.1080/014311600210993.

H. Fuchs, P. Magdon, C. Kleinn, and H. Flessa. Estimating aboveground carbon in a catchment of the Siberian forest tundra: Combining satellite imagery and field inventory. *Remote Sensing of Environment*, 113(3):518–531, Mar. 2009. URL https://www.sciencedirect.com/science/article/pii/S0034425708003064.

Y. Gao, M. Skutsch, J. Paneque-Gálvez, and A. Ghilardi. Remote sensing of forest degradation: a review. *Environmental Research Letters*, 15(10):103001, Sept. 2020. URL https://doi.org/10.1088/1748-9326/abaad7.

L. V. Gatti, L. S. Basso, J. B. Miller, M. Gloor, L. Gatti Domingues, H. L. G. Cassol, G. Tejada, L. E. O. C. Aragão, C. Nobre, W. Peters, L. Marani, E. Arai, A. H. Sanches, S. M. Corrêa, L. Anderson, C. Von Randow, C. S. C. Correia, S. P. Crispim, and R. A. L. Neves. Amazonia as a carbon source linked to deforestation and climate change. *Nature*, 595(7867):388–393, July 2021. URL https://www.nature.com/articles/s41586-021-03629-6.

GDAL/OGR contributors. *GDAL/OGR Geospatial Data Abstraction software Library*. 2022. doi: 10.5281/zenodo.5884351. URL https://gdal.org.

J. Ghazoul, Z. Burivalova, J. Garcia-Ulloa, and L. A. King. Conceptualizing Forest Degradation. *Trends in Ecology & Evolution*, 30(10):622–632, Oct. 2015. URL https://www.sciencedirect.com/science/article/pii/S0169534715001913.

X. Giam. Global biodiversity loss from tropical deforestation. *Proceedings of the National Academy of Sciences*, 114(23):5775–5777, June 2017. URL https://www.pnas.org/doi/10.1073/pnas.1706264114.

J. Gonzalez de Tanago, A. Lau, H. Bartholomeus, M. Herold, V. Avitabile, P. Raumonen, C. Martius, R. C. Goodman, M. Disney, S. Manuri, A. Burt, and K. Calders. Estimation of above-ground biomass of large tropical trees with terrestrial LiDAR. *Methods in Ecology and Evolution*, 9(2):223–234, 2018. URL https://onlinelibrary.wiley.com/doi/abs/10.1111/2041-210X.12904.

Google Earth Engine. Object-based methods. 2021a. URL https://developers.google.com/earth-engine/guides/image_objects. (Last accessed on 15/09/22).

Google Earth Engine. Sentinel-1 Algorithms. Dec. 2021b. URL https://developers.google.com/earth-engine/guides/sentinel1. (Last accessed on 06/09/22).

Google Earth Engine. Synthetic Aperture Radar (SAR) Basics, Apr. 2021c. URL https://developers.google.com/earth-engine/tutorials/community/sar-basics. (Last accessed on 06/09/22).

N. Gorelick, M. Hancher, M. Dixon, S. Ilyushchenko, D. Thau, and R. Moore. Google Earth Engine: Planetary-scale geospatial analysis for everyone. *Remote Sensing of Environment*, 202:18–27, Dec. 2017. URL https://www.sciencedirect.com/science/article/pii/S0034425717302900.

J. Grace, E. Mitchard, and E. Gloor. Perturbations in the carbon budget of the tropics. *Global Change Biology*, 20(10):3238–3255, 2014. URL https://onlinelibrary.wiley.com/doi/abs/10.1111/gcb.12600.

N. Gregorio, J. Herbohn, R. Tripoli, and A. Pasa. A Local Initiative to Achieve Global Forest and Landscape Restoration Challenge—Lessons Learned from a Community-Based Forest Restoration Project in Biliran Province, Philippines. *Forests*, 11(4):475, Apr. 2020. URL https://www.mdpi.com/1999-4907/11/4/475.

S. Hancock, J. Armston, M. Hofton, X. Sun, H. Tang, L. I. Duncanson, J. R. Kellner, and R. Dubayah. The GEDI Simulator: A Large-Footprint Waveform Lidar Simulator for Calibration and Validation of Spaceborne Missions. *Earth and Space Science*, 6(2):294–310, 2019. URL https://onlinelibrary.wiley.com/doi/abs/10.1029/2018EA000506.

M. C. Hansen, P. V. Potapov, R. Moore, M. Hancher, S. A. Turubanova, A. Tyukavina, D. Thau, S. V. Stehman, S. J. Goetz, T. R. Loveland, A. Kommareddy, A. Egorov, L. Chini, C. O. Justice, and J. R. G. Townshend. High-Resolution Global Maps of 21st-Century Forest Cover Change. *Science*, 342(6160):850–853, Nov. 2013. URL https://science.sciencemag.org/content/342/6160/850.

M. C. Hansen, A. Krylov, A. Tyukavina, P. V. Potapov, S. Turubanova, B. Zutta, S. Ifo, B. Margono, F. Stolle, and R. Moore. Humid tropical forest disturbance alerts using Landsat data. *Environmental Research Letters*, 11(3):034008, Mar. 2016. URL https://doi.org/10.1088/1748-9326/11/3/034008.

J. B. Harley. Deconstructing the map. *Cartographica: The International Journal for Geographic Information and Geovisualization*, 26(2):1–20, June 1989. URL https://www.utpjournals.press/doi/abs/10.3138/E635-7827-1757-9T53. Publisher: University of Toronto Press.

N. Harris, C. Davis, E. D. Goldman, R. Petersen, and S. Gibbes. Comparing Global and National Approaches to Estimating Deforestation Rates in REDD+ Countries, June 2018. URL https://www.wri.org/research/comparing-global-and-national-approaches-estimating-deforestation-rates-redd-countries.

N. L. Harris, D. A. Gibbs, A. Baccini, R. A. Birdsey, S. de Bruin, M. Farina, L. Fatoyinbo, M. C. Hansen, M. Herold, R. A. Houghton, P. V. Potapov, D. R. Suarez, R. M. Roman-Cuesta, S. S. Saatchi, C. M. Slay, S. A. Turubanova, and A. Tyukavina. Global maps of twenty-first century forest carbon fluxes. *Nature Climate Change*, 11(3):234–240, Mar. 2021. URL https://www.nature.com/articles/s41558-020-00976-6.

S. Henders, U. M. Persson, and T. Kastner. Trading forests: land-use change and carbon emissions embodied in production and exports of forest-risk commodities. *Environmental Research Letters*, 10(12):125012, Dec. 2015. URL https://doi.org/10.1088/1748-9326/10/12/125012.

M. Herold, R. M. Román-Cuesta, D. Mollicone, Y. Hirata, P. Van Laake, G. P. Asner, C. Souza, M. Skutsch, V. Avitabile, and K. MacDicken. Options for monitoring and estimating historical carbon emissions from forest degradation in the context of REDD+. *Carbon Balance and Management*, 6(1):13, Nov. 2011. URL https://doi.org/10.1186/1750-0680-6-13.

M. G. Hethcoat, J. M. B. Carreiras, D. P. Edwards, R. G. Bryant, and S. Quegan. Detecting tropical selective logging with C-band SAR data may require a time series approach. *Remote Sensing of Environment*, 259:112411, June 2021. URL https://www.sciencedirect.com/science/article/pii/S0034425721001292.

J. L. Hill and R. A. Hill. Why are tropical rain forests so species rich? Classifying, reviewing and evaluating theories. *Progress in Physical Geography: Earth and Environment*, 25(3):326–354, Sept. 2001. URL https://doi.org/10.1177/030913330102500302.

T. C. Hill, M. Williams, A. A. Bloom, E. T. A. Mitchard, and C. M. Ryan. Are Inventory Based and Remotely Sensed Above-Ground Biomass Estimates Consistent? *PLOS ONE*, 8(9):e74170, Sept. 2013. URL https://journals.plos.org/plosone/article?id=10.1371/journal.pone.0074170.

M. Hirschmugl, H. Gallaun, M. Dees, P. Datta, J. Deutscher, N. Koutsias, and M. Schardt. Methods for Mapping Forest Disturbance and Degradation from Optical Earth Observation Data: a Review. *Current Forestry Reports*, 3(1):32–45, Mar. 2017. URL https://doi.org/10.1007/s40725-017-0047-2.

M. Hirschmugl, J. Deutscher, C. Sobe, A. Bouvet, S. Mermoz, and M. Schardt. Use of SAR and Optical Time Series for Tropical Forest Disturbance Mapping. *Remote Sensing*, 12(4):727, Jan. 2020. URL https://www.mdpi.com/2072-4292/12/4/727.

N. T. Hoan, R. Tateishi, B. Alsaaideh, T. Ngigi, I. Alimuddin, and B. Johnson. Tropical forest mapping using a combination of optical and microwave data of ALOS. *International Journal of Remote Sensing*, 34(1):139–153, Jan. 2013. ISSN 0143-1161. doi: 10.1080/01431161.2012.709329. URL https://doi.org/10.1080/01431161.2012.709329. Publisher: Taylor & Francis _eprint: https://doi.org/10.1080/01431161.2012.709329.

N. T. Hoang and K. Kanemoto. Mapping the deforestation footprint of nations reveals growing threat to tropical forests. *Nature Ecology & Evolution*, 5(6):845–853, June 2021. URL https://www.nature.com/articles/s41559-021-01417-z.

D. Hoekman, B. Kooij, M. Quiñones, S. Vellekoop, I. Carolita, S. Budhiman, R. Arief, and O. Roswintiarti. Wide-Area Near-Real-Time Monitoring of Tropical Forest Degradation and Deforestation Using Sentinel-1. *Remote Sensing*, 12(19):3263, Jan. 2020. URL https://www.mdpi.com/2072-4292/12/19/3263.

N. Hosonuma, M. Herold, V. D. Sy, R. S. D. Fries, M. Brockhaus, L. Verchot, A. Angelsen, and E. Romijn. An assessment of deforestation and forest degradation drivers in developing countries. *Environmental Research Letters*, 7(4):044009, Oct. 2012. URL https://doi.org/10.1088/1748-9326/7/4/044009.

R. A. Houghton. Carbon emissions and the drivers of deforestation and forest degradation in the tropics. *Current Opinion in Environmental Sustainability*, 4(6):597–603, Dec. 2012. URL http://www.sciencedirect.com/science/article/pii/S1877343512000723.

R. A. Houghton and A. A. Nassikas. Global and regional fluxes of carbon from land use and land cover change 1850–2015. *Global Biogeochemical Cycles*, 31(3):456–472, 2017. URL https://agupubs.onlinelibrary.wiley.com/doi/abs/10.1002/2016GB005546.

S. Hoyer and J. Hamman. xarray: ND labeled arrays and datasets in Python. *Journal of Open Research Software*, 5(1), 2017. Publisher: Ubiquity Press.

A. Huete, H. Liu, and W. van Leeuwen. The use of vegetation indices in forested regions: issues of linearity and saturation. In *IGARSS'97. 1997 IEEE International Geoscience and Remote Sensing Symposium Proceedings. Remote Sensing - A Scientific Vision for Sustainable Development*, volume 4, pages 1966–1968 vol.4, Aug. 1997.

M. L. Imhoff. Radar backscatter and biomass saturation: ramifications for global biomass inventory. *IEEE Transactions on Geoscience and Remote Sensing*, 33(2):511–518, Mar. 1995.

IPCC. IPCC special report on climate change, desertification, land degradation, sustainable land management, food security, and greenhouse gas fluxes in terrestrial ecosystems. *Summary for Policy Makers. Geneva: Intergovernmental Panel on Climate Change (IPCC)*, 2019.

IPCC. *Climate Change 2022: Impacts, Adaptation, and Vulnerability. Contribution of Working Group II to the Sixth Assessment Report of the Intergovernmental Panel on Climate Change*. Cambridge University Press. In Press., 2022.

S. Johnson. Discourse and Practice of REDD+ in Ghana and the Expansion of State Power. *Sustainability*, 13(20):11358, Jan. 2021. URL https://www.mdpi.com/2071-1050/13/20/11358.

N. Joshi, E. T. Mitchard, N. Woo, J. Torres, J. Moll-Rocek, A. Ehammer, M. Collins, M. R. Jepsen, and R. Fensholt. Mapping dynamics of deforestation and forest degradation in tropical forests using radar satellite data. *Environmental Research Letters*, 10(3): 034014, Mar. 2015. URL https://doi.org/10.1088/1748-9326/10/3/034014.

N. Joshi, M. Baumann, A. Ehammer, R. Fensholt, K. Grogan, P. Hostert, M. R. Jepsen, T. Kuemmerle, P. Meyfroidt, E. T. A. Mitchard, J. Reiche, C. M. Ryan, and B. Waske. A Review of the Application of Optical and Radar Remote Sensing Data Fusion to Land Use Mapping and Monitoring. *Remote Sensing*, 8(1):70, Jan. 2016. URL https://www.mdpi.com/2072-4292/8/1/70.

N. Joshi, E. T. A. Mitchard, M. Brolly, J. Schumacher, A. Fernández-Landa, V. K. Johannsen, M. Marchamalo, and R. Fensholt. Understanding 'saturation' of radar signals over forests. *Scientific Reports*, 7(1):3505, June 2017. URL https://www.nature.com/articles/s41598-017-03469-3.

J. Kellndorfer, A. Flores-Anderson, K. Herndon, and R. Thapa. Using SAR data for mapping deforestation and forest degradation. *The SAR Handbook. Comprehensive Methodologies for Forest Monitoring and Biomass Estimation; ServirGlobal: Hunstville, AL, USA*, pages 65–79, 2019.

J. R. Kellner, J. Armston, M. Birrer, K. C. Cushman, L. Duncanson, C. Eck, C. Falleger, B. Imbach, K. Král, M. Krůček, J. Trochta, T. Vrška, and C. Zgraggen. New Opportunities for Forest Remote Sensing Through Ultra-High-Density Drone Lidar. *Surveys in Geophysics*, 40(4):959–977, July 2019. URL https://doi.org/10.1007/s10712-019-09529-9.

K. C. Kelsey and J. C. Neff. Estimates of Aboveground Biomass from Texture Analysis of Landsat Imagery. *Remote Sensing*, 6(7):6407–6422, July 2014. URL https://www.mdpi.com/2072-4292/6/7/6407.

S. Y. Kotchenova, E. F. Vermote, R. Matarrese, and J. Frank J. Klemm. Validation of a vector version of the 6S radiative transfer code for atmospheric correction of satellite data. Part I: Path radiance. *Applied Optics*, 45(26):6762–6774, Sept. 2006. URL https://www.osapublishing.org/ao/abstract.cfm?uri=ao-45-26-6762.

T. M. Kuplich, P. J. Curran, and P. M. Atkinson. Relating SAR image texture to the biomass of regenerating tropical forests. *International Journal of Remote Sensing*, 26(21):4829–4854, Nov. 2005. URL https://doi.org/10.1080/01431160500239107.

T. Le Toan, A. Beaudoin, J. Riom, and D. Guyon. Relating forest biomass to SAR data. *IEEE Transactions on Geoscience and Remote Sensing*, 30(2):403–411, Mar. 1992.

T. Le Toan, S. Quegan, I. Woodward, M. Lomas, N. Delbart, and G. Picard. Relating Radar Remote Sensing of Biomass to Modelling of Forest Carbon Budgets. *Climatic Change*, 67(2-3):379–402, Dec. 2004. URL http://link.springer.com/10.1007/s10584-004-3155-5.

M. A. Lefsky, D. J. Harding, M. Keller, W. B. Cohen, C. C. Carabajal, F. D. B. Espirito-Santo, M. O. Hunter, and R. d. Oliveira. Estimates of forest canopy height and aboveground biomass using ICESat. *Geophysical Research Letters*, 32(22), 2005. URL https://agupubs.onlinelibrary.wiley.com/doi/abs/10.1029/2005GL023971.

A. T. Leite-Filho, V. Y. de Sousa Pontes, and M. H. Costa. Effects of Deforestation on the Onset of the Rainy Season and the Duration of Dry Spells in Southern Amazonia. *Journal of Geophysical Research: Atmospheres*, 124(10):5268–5281, 2019. URL https://onlinelibrary.wiley.com/doi/abs/10.1029/2018JD029537.

S. L. Lewis. Tropical forests and the changing earth system. *Philosophical Transactions of the Royal Society B: Biological Sciences*, 361(1465):195–210, Jan. 2006. URL https://www.ncbi.nlm.nih.gov/pmc/articles/PMC1626535/.

S. L. Lewis, O. L. Phillips, D. Sheil, B. Vinceti, T. R. Baker, S. Brown, A. W. Graham, N. Higuchi, D. W. Hilbert, W. F. Laurance, J. Lejoly, Y. Malhi, A. Monteagudo, P. Nunez Vargas, B. Sonke, NUR SUPARDI, J. W. Terborgh, and R. Vasquez Martinez. Tropical forest tree mortality, recruitment and turnover rates: calculation, interpretation and comparison when census intervals vary. *Journal of Ecology*, 92(6):929–944, Dec. 2004. URL https://onlinelibrary.wiley.com/doi/10.1111/j.0022-0477.2004.00923.x.

S. L. Lewis, C. E. Wheeler, E. T. A. Mitchard, and A. Koch. Restoring natural forests is the best way to remove atmospheric carbon. *Nature*, 568(7750):25–28, Apr. 2019. URL https://www.nature.com/articles/d41586-019-01026-8.

J. Li, C. Li, W. Xu, H. Feng, F. Zhao, H. Long, Y. Meng, W. Chen, H. Yang, and G. Yang. Fusion of optical and SAR images based on deep learning to reconstruct vegetation NDVI time series in cloud-prone regions. *International Journal of Applied Earth Observation and Geoinformation*, 112:102818, Aug. 2022. URL https://www.sciencedirect.com/science/article/pii/S1569843222000206.

Y. Li, M. Li, C. Li, and Z. Liu. Forest aboveground biomass estimation using Landsat 8 and Sentinel-1A data with machine learning algorithms. *Scientific Reports*, 10(1): 9952, June 2020. URL https://www.nature.com/articles/s41598-020-67024-3.

M. Lin, Q. Ling, H. Pei, Y. Song, Z. Qiu, C. Wang, T. Liu, and W. Gong. Remote Sensing of Tropical Rainforest Biomass Changes in Hainan Island, China from 2003 to 2018. *Remote Sensing*, 13(9):1696, Jan. 2021. URL https://www.mdpi.com/2072-4292/13/9/1696.

S. Lohberger, M. Stängel, E. C. Atwood, and F. Siegert. Spatial evaluation of Indonesia's 2015 fire-affected area and estimated carbon emissions using Sentinel-1. *Global Change Biology*, 24(2):644–654, 2018. URL https://onlinelibrary.wiley.com/doi/abs/10.1111/gcb.13841.

D. Lu. Aboveground biomass estimation using Landsat TM data in the Brazilian Amazon. *International Journal of Remote Sensing*, 26(12):2509–2525, June 2005. URL https://doi.org/10.1080/01431160500142145.

D. Lu. The potential and challenge of remote sensing-based biomass estimation. *International Journal of Remote Sensing*, 27(7):1297–1328, Apr. 2006.

D. Lu and M. Batistella. Exploring TM image texture and its relationships with biomass estimation in Rondônia, Brazilian Amazon. *Acta Amazonica*, 35:249–257, June 2005.

D. Lu, G. Li, and E. Moran. Current situation and needs of change detection techniques. *International Journal of Image and Data Fusion*, 5(1):13–38, Jan. 2014. URL https://doi.org/10.1080/19479832.2013.868372.

D. Lu, Q. Chen, G. Wang, L. Liu, G. Li, and E. Moran. A survey of remote sensing-based aboveground biomass estimation methods in forest ecosystems. *International Journal of Digital Earth*, 9(1):63–105, Jan. 2016. URL https://doi.org/10.1080/17538947.2014.990526.

A. J. Luckman, A. C. Frery, C. C. F. Yanasse, and G. B. Groom. Texture in airborne SAR imagery of tropical forest and its relationship to forest regeneration stage. *International Journal of Remote Sensing*, 18(6):1333–1349, Apr. 1997. URL https://doi.org/10.1080/014311697218458.

J. G. Lyon, D. Yuan, R. S. Lunetta, and C. D. Elvidge. A change detection experiment using vegetation indices. *Photogramm. Eng. Remote Sens*, pages 143–150, 1998.

K. Magessa, S. Wynne-Jones, and N. Hockley. Are policies for decentralised forest governance designed to achieve full devolution? Evidence from Eastern Africa. *International Forestry Review*, 22(1):83–101, Mar. 2020. URL https://go.gale.com/ps/i.do?p=AONE&sw=w&issn=14655489&v=2.1&it=r&id=GALE%7CA618134987&sid=googleScholar&linkaccess=abs.

B. F. Manly and D. I. Mackenzie. CUSUM environmental monitoring in time and space. *Environmental and Ecological Statistics*, 10(2):231–247, June 2003. URL https://doi.org/10.1023/A:1023682426285.

G. Manogaran and D. Lopez. Spatial cumulative sum algorithm with big data analytics for climate change detection. *Computers & Electrical Engineering*, 65:207–221, Jan. 2018. URL https://www.sciencedirect.com/science/article/pii/S004579061730811X.

D. Marceau, P. Howarth, J. Dubois, and D. Gratton. Evaluation Of The Grey-level Co-occurrence Matrix Method For Land-cover Classification Using Spot Imagery. *IEEE Transactions on Geoscience and Remote Sensing*, 28(4):513–519, July 1990. ISSN 1558-0644.

J. A. Marengo, C. M. Souza, K. Thonicke, C. Burton, K. Halladay, R. A. Betts, L. M. Alves, and W. R. Soares. Changes in Climate and Land Use Over the Amazon Region: Current and Future Variability and Trends. *Frontiers in Earth Science*, 6, 2018. URL https://www.frontiersin.org/articles/10.3389/feart.2018.00228.

B. A. Margono, S. Turubanova, I. Zhuravleva, P. Potapov, A. Tyukavina, A. Baccini, S. Goetz, and M. C. Hansen. Mapping and monitoring deforestation and forest degradation in Sumatra (Indonesia) using Landsat time series data sets from 1990 to 2010. *Environmental Research Letters*, 7(3):034010, July 2012. URL https://doi.org/10.1088/1748-9326/7/3/034010.

K. E. Markham and F. Sangermano. Evaluating Wildlife Vulnerability to Mercury Pollution From Artisanal and Small-Scale Gold Mining in Madre de Dios, Peru. *Tropical Conservation Science*, 11:1940082918794320, Jan. 2018. URL https://doi.org/10.1177/1940082918794320.

E. A. T. Matricardi, D. L. Skole, O. B. Costa, M. A. Pedlowski, J. H. Samek, and E. P. Miguel. Long-term forest degradation surpasses deforestation in the Brazilian Amazon. *Science*, 369(6509):1378–1382, Sept. 2020. URL https://science.sciencemag.org/content/369/6509/1378.

K. McAfee. Selling Nature to save It? Biodiversity and Green Developmentalism. *Environment and Planning D: Society and Space*, 17(2):133–154, Apr. 1999. URL https://doi.org/10.1068/d170133. Publisher: SAGE Publications Ltd STM.

K. McAfee. The Contradictory Logic of Global Ecosystem Services Markets. *Development and Change*, 43(1):105–131, 2012. URL https://onlinelibrary.wiley.com/doi/abs/10.1111/j.1467-7660.2011.01745.x.

I. McNicol. FODEX - Field Manual for Plot Establishment and Tree Measurement. 2018.

I. McNicol, C. Aquino, A. Burt, H. Carstairs, M. Disney, and E. Mitchard. The Forest Degradation Experiment (FODEX). page 3, 2021a.

I. M. McNicol, C. M. Ryan, and E. T. A. Mitchard. Carbon losses from deforestation and widespread degradation offset by extensive growth in African woodlands. *Nature Communications*, 9(1):3045, Aug. 2018. URL https://www.nature.com/articles/s41467-018-05386-z.

I. M. McNicol, E. T. A. Mitchard, C. Aquino, A. Burt, H. Carstairs, C. Dassi, A. Modinga Dikongo, and M. I. Disney. To What Extent Can UAV Photogrammetry Replicate UAV LiDAR to Determine Forest Structure? A Test in Two Contrasting Tropical Forests. *Journal of Geophysical Research: Biogeosciences*, 126(12), 2021b.

R. E. McRoberts, E. Naesset, T. Gobakken, and O.-M. Bollandsas. Indirect and direct estimation of forest biomass change using forest inventory and airborne laser scanning data. *Remote Sensing of Environment. 164: 36-42.*, 164:36–42, 2015. URL http://www.fs.usda.gov/treesearch/pubs/56463.

V. P. Medjibe, F. E. Putz, and C. Romero. Certified and Uncertified Logging Concessions Compared in Gabon: Changes in Stand Structure, Tree Species, and Biomass. *Environmental Management*, 51(3):524–540, Mar. 2013. URL https://doi.org/10.1007/s00267-012-0006-4.

S. Mermoz, M. Réjou-Méchain, L. Villard, T. Le Toan, V. Rossi, and S. Gourlet-Fleury. Decrease of L-band SAR backscatter with biomass of dense forests. *Remote Sensing of Environment*, 159:307–317, Mar. 2015. URL https://www.sciencedirect.com/science/article/pii/S0034425714005112.

V. Meyer, S. S. Saatchi, J. Chave, J. W. Dalling, S. Bohlman, G. A. Fricker, C. Robinson, M. Neumann, and S. Hubbell. Detecting tropical forest biomass dynamics from repeated airborne lidar measurements. *Biogeosciences*, 10(8):5421–5438, Aug. 2013. URL https://bg.copernicus.org/articles/10/5421/2013/.

D. T. Milodowski, E. T. A. Mitchard, and M. Williams. Forest loss maps from regional satellite monitoring systematically underestimate deforestation in two rapidly changing parts of the Amazon. *Environmental Research Letters*, 12(9):094003, Sept. 2017. URL https://iopscience.iop.org/article/10.1088/1748-9326/aa7e1e.

S. Minnemeyer, J.-G. Collomb, J.-B. Mikissa, S. Mundunga, H. N. Nzao, J. Madouma, J. d. D. Mapaga, C. Mikolo, N. Rabenkogo, S. Akagah, E. Bayani-Ngoye, and A. Mofouma. A First Look at Logging in Gabon. Feb. 2000. URL https://policycommons.net/artifacts/1360940/a-first-look-at-logging-in-gabon/1975039/.

E. T. Mitchard, S. S. Saatchi, A. Baccini, G. P. Asner, S. J. Goetz, N. L. Harris, and S. Brown. Uncertainty in the spatial distribution of tropical forest biomass: a comparison of pan-tropical maps. *Carbon Balance and Management*, 8(1):10, Oct. 2013a. URL https://doi.org/10.1186/1750-0680-8-10.

E. T. A. Mitchard. The tropical forest carbon cycle and climate change. *Nature*, 559 (7715):527, July 2018. URL https://www.nature.com/articles/s41586-018-0300-2.

E. T. A. Mitchard, S. S. Saatchi, S. L. Lewis, T. R. Feldpausch, F. F. Gerard, I. H. Woodhouse, and P. Meir. Comment on 'A first map of tropical Africa's above-ground biomass derived from satellite imagery'. *Environmental Research Letters*, 6 (4):049001, Oct. 2011a. URL https://doi.org/10.1088%2F1748-9326%2F6%2F4%2F049001.

E. T. A. Mitchard, S. S. Saatchi, S. L. Lewis, T. R. Feldpausch, I. H. Woodhouse, B. Sonké, C. Rowland, and P. Meir. Measuring biomass changes due to woody encroachment and deforestation/degradation in a forest–savanna boundary region of central Africa using multi-temporal L-band radar backscatter. *Remote Sensing of Environment*, 115(11):2861–2873, Nov. 2011b. URL http://www.sciencedirect.com/science/article/pii/S0034425711001337.

E. T. A. Mitchard, P. Meir, C. M. Ryan, E. S. Woollen, M. Williams, L. E. Goodman, J. A. Mucavele, P. Watts, I. H. Woodhouse, and S. S. Saatchi. A novel application of satellite radar data: measuring carbon sequestration and detecting degradation in a community forestry project in Mozambique. *Plant Ecology & Diversity*, 6(1):159–170, Mar. 2013b. URL https://doi.org/10.1080/17550874.2012.695814.

E. T. A. Mitchard, T. R. Feldpausch, R. J. W. Brienen, G. Lopez-Gonzalez, A. Monteagudo, T. R. Baker, S. L. Lewis, J. Lloyd, C. A. Quesada, M. Gloor, H. t. Steege, P. Meir, E. Alvarez, A. Araujo-Murakami, L. E. O. C. Aragão, L. Arroyo, G. Aymard, O. Banki, D. Bonal, S. Brown, F. I. Brown, C. E. Cerón, V. C. Moscoso, J. Chave, J. A. Comiskey, F. Cornejo, M. C. Medina, L. D. Costa, F. R. C. Costa, A. D. Fiore, T. F. Domingues, T. L. Erwin, T. Frederickson, N. Higuchi, E. N. H. Coronado, T. J. Killeen, W. F. Laurance, C. Levis, W. E. Magnusson, B. S. Marimon, B. H. M. Junior, I. M. Polo, P. Mishra, M. T. Nascimento, D. Neill, M. P. N. Vargas, W. A. Palacios, A. Parada, G. P. Molina, M. Peña-Claros, N. Pitman, C. A. Peres, L. Poorter, A. Prieto, H. Ramirez-Angulo, Z. R. Correa, A. Roopsind, K. H. Roucoux, A. Rudas, R. P. Salomão, J. Schietti, M. Silveira, P. F. d. Souza, M. K. Steininger, J. Stropp, J. Terborgh, R. Thomas, M. Toledo, A. Torres-Lezama, T. R. v. Andel, G. M. F. v. d. Heijden, I. C. G. Vieira, S. Vieira, E. Vilanova-Torre, V. A. Vos, O. Wang, C. E. Zartman, Y. Malhi, and O. L. Phillips. Markedly divergent estimates of Amazon forest carbon density from ground plots and satellites. *Global Ecology and Biogeography*, 23(8):935–946, 2014. URL `https://onlinelibrary.wiley.com/doi/abs/10.1111/geb.12168`.

R. Mlambo, I. H. Woodhouse, F. Gerard, and K. Anderson. Structure from Motion (SfM) photogrammetry with drone data: a low cost method for monitoring greenhouse gas emissions from forests in developing countries. *Forests*, 8(3), Mar. 2017.

D. Moreno-Mateos, E. B. Barbier, P. C. Jones, H. P. Jones, J. Aronson, J. A. López-López, M. L. McCrackin, P. Meli, D. Montoya, and J. M. Rey Benayas. Anthropogenic ecosystem disturbance and the recovery debt. *Nature Communications*, 8(1):14163, Jan. 2017. URL `https://www.nature.com/articles/ncomms14163`.

A. Myers. Camp Delta, Google Earth and the ethics of remote sensing in archaeology. *World Archaeology*, 42(3):455–467, Sept. 2010. URL `https://doi.org/10.1080/00438243.2010.498640`.

G.-J. Nabuurs, N. H. Ravindranath, K. Paustian, A. Freibauer, W. Hohenstein, W. Makundi, H. Aalde, A. Y. Abdelgadir, A. S. A. Khalil, J. Barton, K. Bickel, S. Bin-Musa, D. Blain, R. Boer, K. Byrne, C. Cerri, L. Ciccarese, D.-C. Choque, E. Duchemin, L. Dja, J. Ford-Robertson, W. Galinski, J.-C. Germon, H. Ginzo, M. Gytarsky, L. Heath, and D. Loustau. LUCF sector good practice guidance. 2003. URL https://publications.csiro.au/rpr/pub?list=BRO&pid=changeme:1968&sb=RECENT&n=1&rpp=10&page=476&tr=4842&dr=all&dc4.browseYear=2003https://www.tripadvisor.co.uk/ShowTopic-g1-i10702-k13648750-Multiple_addresses_on_UK_passenger_locator_form-Air_Travel.html.

J. E. Nichol and M. L. R. Sarker. Improved Biomass Estimation Using the Texture Parameters of Two High-Resolution Optical Sensors. *IEEE Transactions on Geoscience and Remote Sensing*, 49(3):930–948, Mar. 2011.

T. D. Nielsen. The role of discourses in governing forests to combat climate change. *International Environmental Agreements: Politics, Law and Economics*, 14(3):265–280, Sept. 2014. URL http://link.springer.com/10.1007/s10784-013-9223-4.

B. Nietschmann. Defending the Miskito reefs with maps and GPS: mapping with sail, scuba, and satellite. *Cultural survival quarterly*, 18(4):34–37, 1995.

K. Nomura, E. T. Mitchard, S. J. Bowers, and G. Patenaude. Missed carbon emissions from forests: comparing countries' estimates submitted to UNFCCC to biophysical estimates. *Environmental Research Letters*, 14(2):024015, Feb. 2019. URL https://doi.org/10.1088/1748-9326/aafc6b.

Norway. Norway's International Climate and Forest Initiative (NICFI), 2021. URL https://www.nicfi.no/. https://www.nicfi.no/ (Last accessed on 29/04/2021).

L. J. R. Nunes, C. I. R. Meireles, C. J. Pinto Gomes, and N. M. C. Almeida Ribeiro. Forest Contribution to Climate Change Mitigation: Management Oriented to Carbon Capture and Storage. *Climate*, 8(2):21, Feb. 2020. URL https://www.mdpi.com/2225-1154/8/2/21.

E. Næsset, R. E. McRoberts, A. Pekkarinen, S. Saatchi, M. Santoro, D. Trier, E. Zahabu, and T. Gobakken. Use of local and global maps of forest canopy height and aboveground biomass to enhance local estimates of biomass in miombo woodlands in Tanzania. *International Journal of Applied Earth Observation and Geoinformation*, 89: 102109, July 2020. URL https://www.sciencedirect.com/science/article/pii/S0303243419312103.

M. A. Othman, Z. H. Ash'aari, A. Z. Aris, and M. F. Ramli. Tropical deforestation monitoring using NDVI from MODIS satellite: a case study in Pahang, Malaysia. *IOP Conference Series: Earth and Environmental Science*, 169:012047, July 2018. URL https://doi.org/10.1088/1755-1315/169/1/012047.

A. M. Pacheco-Pascagaza, Y. Gou, V. Louis, J. F. Roberts, P. Rodríguez-Veiga, P. da Conceição Bispo, F. D. B. Espírito-Santo, C. Robb, C. Upton, G. Galindo, E. Cabrera, I. P. Pachón Cendales, M. A. Castillo Santiago, O. Carrillo Negrete, C. Meneses, M. Iñiguez, and H. Balzter. Near Real-Time Change Detection System Using Sentinel-2 and Machine Learning: A Test for Mexican and Colombian Forests. *Remote Sensing*, 14(3):707, Feb. 2022. URL https://www.mdpi.com/2072-4292/14/3/707.

E. S. Page. A test for a change in a parameter occurring at an unknown point. *Biometrika*, 42(3-4):523–527, Dec. 1955. URL https://doi.org/10.1093/biomet/42.3-4.523.

Y. Pan, R. A. Birdsey, J. Fang, R. Houghton, P. E. Kauppi, W. A. Kurz, O. L. Phillips, A. Shvidenko, S. L. Lewis, J. G. Canadell, P. Ciais, R. B. Jackson, S. W. Pacala, A. D. McGuire, S. Piao, A. Rautiainen, S. Sitch, and D. Hayes. A Large and Persistent Carbon Sink in the World's Forests. *Science*, 333(6045):988–993, Aug. 2011. URL http://science.sciencemag.org/content/333/6045/988.

Y. Pan, R. A. Birdsey, O. L. Phillips, and R. B. Jackson. The Structure, Distribution, and Biomass of the World's Forests. *Annual Review of Ecology, Evolution, and Systematics*, 44(1):593–622, 2013. URL https://doi.org/10.1146/annurev-ecolsys-110512-135914.

T. R. H. Pearson, S. Brown, L. Murray, and G. Sidman. Greenhouse gas emissions from tropical forest degradation: an underestimated source. *Carbon Balance and Management*, 12(1):3, Feb. 2017. URL https://doi.org/10.1186/s13021-017-0072-2.

F. Pendrill, U. M. Persson, J. Godar, and T. Kastner. Deforestation displaced: trade in forest-risk commodities and the prospects for a global forest transition. *Environmental Research Letters*, 14(5):055003, May 2019a. URL https://doi.org/10.1088/1748-9326/ab0d41.

F. Pendrill, U. M. Persson, J. Godar, T. Kastner, D. Moran, S. Schmidt, and R. Wood. Agricultural and forestry trade drives large share of tropical deforestation emissions. *Global Environmental Change*, 56:1–10, May 2019b. URL https://www.sciencedirect.com/science/article/pii/S0959378018314365.

T. A. Perreault, G. Bridge, and J. McCarthy. *The Routledge handbook of political ecology*. Routledge London, 2015.

O. Phillips, T. Baker, T. Feldpausch, and R. Brienen. RAINFOR Field Manual for Plot Establishment and Remeasurement. page 27, 2001.

L. Pierce, P. Liang, and M. Dobson. Texture estimation in SAR images of forests. In *IGARSS 2003. 2003 IEEE International Geoscience and Remote Sensing Symposium. Proceedings (IEEE Cat. No.03CH37477)*, volume 6, pages 4010–4012 vol.6, July 2003.

Planet. Planet Imagery Product Specifications. URL `https://earth.esa.int/eogateway/documents/20142/37627/Planet-combined-imagery-product-specs-2020.pdf`. (Last accessed on 04/04/2021).

Planet Labs. Education and Research Program. 2021. URL `https://www.planet.com/markets/education-and-research/`. (Last accessed on 04/06/2021).

Planet Team. Planet Application Program Interface: In Space for Life on Earth. San Francisco, CA, 2017. URL `https://api.planet.com`. (Last accessed on 25/04/2021).

S. T. Plumb, E. A. Nielsen, and Y.-S. Kim. Challenges of Opportunity Cost Analysis in Planning REDD+: A Honduran Case Study of Social and Cultural Values Associated with Indigenous Forest Uses. *Forests*, 3(2):244–264, June 2012. URL `https://www.mdpi.com/1999-4907/3/2/244`.

P. V. Potapov, S. A. Turubanova, M. C. Hansen, B. Adusei, M. Broich, A. Altstatt, L. Mane, and C. O. Justice. Quantifying forest cover loss in Democratic Republic of the Congo, 2000–2010, with Landsat ETM+ data. *Remote Sensing of Environment*, 122:106–116, July 2012. URL `https://www.sciencedirect.com/science/article/pii/S0034425712000430`.

K. P. Poudel, J. W. Flewelling, and H. Temesgen. Predicting Volume and Biomass Change from Multi-Temporal Lidar Sampling and Remeasured Field Inventory Data in Panther Creek Watershed, Oregon, USA. *Forests*, 9(1):28, Jan. 2018. URL `https://www.mdpi.com/1999-4907/9/1/28`. Number: 1 Publisher: Multidisciplinary Digital Publishing Institute.

M. Poudel, R. Thwaites, D. Race, and G. R. Dahal. Social equity and livelihood implications of REDD+ in rural communities – a case study from Nepal. *International Journal of the Commons*, 9(1):177–208, Mar. 2015. URL http://www.thecommonsjournal.org/articles/10.18352/ijc.444/. Number: 1.

J. R. Poulsen, S. E. Koerner, Z. Miao, V. P. Medjibe, L. N. Banak, and L. J. T. White. Forest structure determines the abundance and distribution of large lianas in Gabon. *Global Ecology and Biogeography*, 26(4):472–485, 2017. URL https://onlinelibrary.wiley.com/doi/abs/10.1111/geb.12554.

A. Puissant, J. Hirsch, and C. Weber. The utility of texture analysis to improve per-pixel classification for high to very high spatial resolution imagery. *International Journal of Remote Sensing*, 26(4):733–745, Feb. 2005. URL https://doi.org/10.1080/01431160512331316838.

S. Puliti, J. Breidenbach, J. Schumacher, M. Hauglin, T. F. Klingenberg, and R. Astrup. Above-ground biomass change estimation using national forest inventory data with Sentinel-2 and Landsat. *Remote Sensing of Environment*, 265: 112644, Nov. 2021. URL https://www.sciencedirect.com/science/article/pii/S0034425721003643.

Y. Qin, X. Xiao, J.-P. Wigneron, P. Ciais, M. Brandt, L. Fan, X. Li, S. Crowell, X. Wu, R. Doughty, Y. Zhang, F. Liu, S. Sitch, and B. Moore. Carbon loss from forest degradation exceeds that from deforestation in the Brazilian Amazon. *Nature Climate Change*, 11(5):442–448, May 2021. URL https://www.nature.com/articles/s41558-021-01026-5.

S. Qiu, Y. Lin, R. Shang, J. Zhang, L. Ma, and Z. Zhu. Making Landsat Time Series Consistent: Evaluating and Improving Landsat Analysis Ready Data. *Remote Sensing*, 11(1):51, Jan. 2019. URL https://www.mdpi.com/2072-4292/11/1/51.

S. Quegan, T. Le Toan, J. Chave, J. Dall, J.-F. Exbrayat, D. H. T. Minh, M. Lomas, M. M. D'Alessandro, P. Paillou, K. Papathanassiou, F. Rocca, S. Saatchi, K. Scipal, H. Shugart, T. L. Smallman, M. J. Soja, S. Tebaldini, L. Ulander, L. Villard, and M. Williams. The European Space Agency BIOMASS mission: Measuring forest above-ground biomass from space. *Remote Sensing of Environment*, 227:44–60, June 2019. URL https://www.sciencedirect.com/science/article/pii/S0034425719301233.

P. Raumonen, M. Kaasalainen, M. Åkerblom, S. Kaasalainen, H. Kaartinen, M. Vastaranta, M. Holopainen, M. Disney, and P. Lewis. Fast Automatic Precision Tree Models from Terrestrial Laser Scanner Data. *Remote Sensing*, 5(2):491–520, Feb. 2013.

G. A. Reams, C. K. Brewer, and R. W. Guldin. Remote sensing alone is insufficient for quantifying changes in forest cover. *Proceedings of the National Academy of Sciences*, 107(38):E145–E145, Sept. 2010. URL https://www.pnas.org/doi/10.1073/pnas.1008665107.

J. Reiche. *Combining SAR and optical satellite image time series for tropical forest monitoring*. Wageningen University, Wageningen, 2015. ISBN 978-94-6257-313-0.

J. Reiche, E. Hamunyela, J. Verbesselt, D. Hoekman, and M. Herold. Improving near-real time deforestation monitoring in tropical dry forests by combining dense Sentinel-1 time series with Landsat and ALOS-2 PALSAR-2. *Remote Sensing of Environment*, 204:147–161, Jan. 2018a. URL https://www.sciencedirect.com/science/article/pii/S0034425717304959.

J. Reiche, R. Verhoeven, J. Verbesselt, E. Hamunyela, N. Wielaard, and M. Herold. Characterizing Tropical Forest Cover Loss Using Dense Sentinel-1 Data and Active Fire Alerts. *Remote Sensing*, 10(5):777, May 2018b. URL https://www.mdpi.com/2072-4292/10/5/777.

J. Reiche, A. Mullissa, B. Slagter, Y. Gou, N.-E. Tsendbazar, C. Odongo-Braun, A. Vollrath, M. J. Weisse, F. Stolle, A. Pickens, G. Donchyts, N. Clinton, N. Gorelick, and M. Herold. Forest disturbance alerts for the Congo Basin using Sentinel-1. *Environmental Research Letters*, 16(2):024005, Jan. 2021. URL https://iopscience.iop.org/article/10.1088/1748-9326/abd0a8.

Rights and Resources Initiative. A Global Baseline of Carbon Storage in Collective Lands, 2018. URL https://rightsandresources.org/wp-content/uploads/2016/10/Toward-a-Global-Baseline-of-Carbon-Storage-in-Collective-Lands-November-2016-RRI-WHRC-WRI-report.pdf. (Accessed on 07/03/2020).

M. M. Robertson. The nature that capital can see: science, state, and market in the commodification of ecosystem services. *Environment and Planning D: society and space*, 24(3):367–387, 2006.

P. Rodríguez-Veiga, S. Saatchi, K. Tansey, and H. Balzter. Magnitude, spatial distribution and uncertainty of forest biomass stocks in Mexico. *Remote Sensing of Environment*, 183:265–281, Sept. 2016. URL https://www.sciencedirect.com/science/article/pii/S0034425716302425.

P. Rodríguez-Veiga, J. Wheeler, V. Louis, K. Tansey, and H. Balzter. Quantifying Forest Biomass Carbon Stocks From Space. *Current Forestry Reports*, 3(1):1–18, Mar. 2017. URL https://doi.org/10.1007/s40725-017-0052-5.

J. Ruiz-Ramos, A. Marino, C. Boardman, and J. Suarez. Continuous Forest Monitoring Using Cumulative Sums of Sentinel-1 Timeseries. *Remote Sensing*, 12(18):3061, Jan. 2020. URL https://www.mdpi.com/2072-4292/12/18/3061.

C. M. Ryan, T. Hill, E. Woollen, C. Ghee, E. Mitchard, G. Cassells, J. Grace, I. H. Woodhouse, and M. Williams. Quantifying small-scale deforestation and forest degradation in African woodlands using radar imagery. *Global Change Biology*, 18(1): 243–257, 2012. URL https://onlinelibrary.wiley.com/doi/abs/10.1111/j.1365-2486.2011.02551.x.

M. Réjou-Méchain, B. Tymen, L. Blanc, S. Fauset, T. R. Feldpausch, A. Monteagudo, O. L. Phillips, H. Richard, and J. Chave. Using repeated small-footprint LiDAR acquisitions to infer spatial and temporal variations of a high-biomass Neotropical forest. *Remote Sensing of Environment*, 169:93–101, Nov. 2015. URL https://www.sciencedirect.com/science/article/pii/S0034425715300894.

M. Réjou-Méchain, N. Barbier, P. Couteron, P. Ploton, G. Vincent, M. Herold, S. Mermoz, S. Saatchi, J. Chave, F. de Boissieu, J.-B. Féret, S. M. Takoudjou, and R. Pélissier. Upscaling Forest Biomass from Field to Satellite Measurements: Sources of Errors and Ways to Reduce Them. *Surveys in Geophysics*, 40(4):881–911, July 2019. URL https://doi.org/10.1007/s10712-019-09532-0.

S. S. Saatchi, N. L. Harris, S. Brown, M. Lefsky, E. T. A. Mitchard, W. Salas, B. R. Zutta, W. Buermann, S. L. Lewis, S. Hagen, S. Petrova, L. White, M. Silman, and A. Morel. Benchmark map of forest carbon stocks in tropical regions across three continents. *Proceedings of the National Academy of Sciences*, 108(24):9899–9904, June 2011. URL https://www.pnas.org/content/108/24/9899.

S. A. Sader, R. B. Waide, W. T. Lawrence, and A. T. Joyce. Tropical forest biomass and successional age class relationships to a vegetation index derived from landsat TM data. *Remote Sensing of Environment*, 28:143–198, Apr. 1989. URL https://www.sciencedirect.com/science/article/pii/0034425789901120.

T. Santika, E. Meijaard, S. Budiharta, E. A. Law, A. Kusworo, J. A. Hutabarat, T. P. Indrawan, M. J. Struebig, S. Raharjo, I. Huda, Sulhani, A. D. Ekaputri, S. Trison, M. Stigner, and K. A. Wilson. Community forest management in Indonesia: Avoided deforestation in the context of anthropogenic and climate complexities. *Global Environmental Change*, 46:60–71, Aug. 2017. URL http://dx.doi.org/10.1016/j.gloenvcha.2017.08.002.

M. Santoro and O. Cartus. ESA Biomass Climate Change Initiative (Biomass_cci): Global datasets of forest above-ground biomass for the years 2010, 2017 and 2018, v2, 2021. URL https://catalogue.ceda.ac.uk/uuid/84403d09cef3485883158f4df2989b0c.

P. Sarabandi, F. Yamazaki, M. Matsuoka, and A. Kiremidjian. Shadow detection and radiometric restoration in satellite high resolution images. In *IGARSS 2004. 2004 IEEE International Geoscience and Remote Sensing Symposium*, volume 6, pages 3744–3747 vol.6, Sept. 2004.

N. Sasaki and F. E. Putz. Critical need for new definitions of “forest” and “forest degradation” in global climate change agreements. *Conservation Letters*, 2(5): 226–232, 2009. URL https://onlinelibrary.wiley.com/doi/abs/10.1111/j.1755-263X.2009.00067.x.

D. Schimel, B. B. Stephens, and J. B. Fisher. Effect of increasing CO2 on the terrestrial carbon cycle. *Proceedings of the National Academy of Sciences of the United States of America*, 112(2):436–441, Jan. 2015. URL https://www.ncbi.nlm.nih.gov/pmc/articles/PMC4299228/.

Y. Shimabukuro, V. Duarte, L. Anderson, D. Valeriano, E. Arai, R. Freitas, B. F. Rudorff, and M. Moreira. Near real time detection of deforestation in the Brazilian Amazon using MODIS imagery. *Ambiente e Agua - An Interdisciplinary Journal of Applied Science*, 1(1):37–47, 2006. URL http://www.ambi-agua.net/seer/index.php/ambi-agua/article/view/13. Number: 1.

K. Shimizu, T. Ota, and N. Mizoue. Detecting Forest Changes Using Dense Landsat 8 and Sentinel-1 Time Series Data in Tropical Seasonal Forests. *Remote Sensing*, 11 (16):1899, Jan. 2019. URL https://www.mdpi.com/2072-4292/11/16/1899.

C. A. Silva, L. Duncanson, S. Hancock, A. Neuenschwander, N. Thomas, M. Hofton, L. Fatoyinbo, M. Simard, C. Z. Marshak, J. Armston, S. Lutchke, and R. Dubayah. Fusing simulated GEDI, ICESat-2 and NISAR data for regional aboveground biomass mapping. *Remote Sensing of Environment*, 253:112234, Feb. 2021. URL https://www.sciencedirect.com/science/article/pii/S0034425720306076.

C. A. Silva, G. Guerrisi, F. Del Frate, and E. E. Sano. Near-real time deforestation detection in the Brazilian Amazon with Sentinel-1 and neural networks. *European Journal of Remote Sensing*, 55(1):129–149, Dec. 2022. URL https://doi.org/10.1080/22797254.2021.2025154.

D. Small. Flattening Gamma: Radiometric Terrain Correction for SAR Imagery. *IEEE Transactions on Geoscience and Remote Sensing*, 49(8):3081–3093, Aug. 2011.

S. S. Somvanshi and M. Kumari. Comparative analysis of different vegetation indices with respect to atmospheric particulate pollution using sentinel data. *Applied Computing and Geosciences*, 7:100032, Sept. 2020. URL https://www.sciencedirect.com/science/article/pii/S2590197420300148.

J. Souza, J. V. Siqueira, M. H. Sales, A. V. Fonseca, J. G. Ribeiro, I. Numata, M. A. Cochrane, C. P. Barber, D. A. Roberts, and J. Barlow. Ten-Year Landsat Classification of Deforestation and Forest Degradation in the Brazilian Amazon. *Remote Sensing*, 5 (11):5493–5513, Nov. 2013. URL https://www.mdpi.com/2072-4292/5/11/5493.

S. A. Spawn, C. C. Sullivan, T. J. Lark, and H. K. Gibbs. Harmonized global maps of above and belowground biomass carbon density in the year 2010. *Scientific Data*, 7 (1):112, Apr. 2020. URL https://www.nature.com/articles/s41597-020-0444-4.

B. Stephan. Bringing discourse to the market: the commodification of avoided deforestation. *Environmental Politics*, 21(4):621–639, July 2012. URL http://www.tandfonline.com/doi/abs/10.1080/09644016.2012.688357.

J. S. Sze, L. R. Carrasco, D. Childs, and D. P. Edwards. Reduced deforestation and degradation in Indigenous Lands pan-tropically. *Nature Sustainability*, pages 1–8, Nov. 2021. URL https://www.nature.com/articles/s41893-021-00815-2.

Y. Tarazona and M. Miyasiro-López. Monitoring tropical forest degradation using remote sensing. Challenges and opportunities in the Madre de Dios region, Peru. *Remote Sensing Applications: Society and Environment*, 19:100337, Aug. 2020. URL https://www.sciencedirect.com/science/article/pii/S2352938519304124.

W. Taylor. Change-Point Analysis: A Powerful New Tool For Detecting Changes. 2008.

J. R. G. Townshend and C. O. Justice. Analysis of the dynamics of African vegetation using the normalized difference vegetation index. *International Journal of Remote Sensing*, 7(11):1435–1445, Nov. 1986. URL https://doi.org/10.1080/01431168608948946.

S. Tuominen and A. Pekkarinen. Performance of different spectral and textural aerial photograph features in multi-source forest inventory. *Remote Sensing of Environment*, 94(2):256–268, Jan. 2005. URL https://www.sciencedirect.com/science/article/pii/S0034425704003244.

S. Turubanova, P. V. Potapov, A. Tyukavina, and M. C. Hansen. Ongoing primary forest loss in Brazil, Democratic Republic of the Congo, and Indonesia. *Environmental Research Letters*, 13(7):074028, July 2018. URL https://doi.org/10.1088/1748-9326/aacd1c.

U Mueller-Wilm, O Devignot, and L Pessiot. S2 MPC Sen2Cor configuration and user manual., 2017. URL https://step.esa.int/thirdparties/sen2cor/2.4.0/Sen2Cor_240_Documenation_PDF/S2-PDGS-MPC-L2A-SUM-V2.4.0.pdf. (Last accessed on 14/05/2020).

UNFCCC. Report of the Conference of the Parties on its seventh session, held at Marrakesh from 29 October to 10 November 2001 (FCCC/CP/2001/13/Add. 1, UNFCCC, Marrakesh, Morocco, 2001). 2002.

G. Vaglio Laurin, V. Liesenberg, Q. Chen, L. Guerriero, F. Del Frate, A. Bartolini, D. Coomes, B. Wilebore, J. Lindsell, and R. Valentini. Optical and SAR sensor synergies for forest and land cover mapping in a tropical site in West Africa. *International Journal of Applied Earth Observation and Geoinformation*, 21:7–16, Apr. 2013. URL https://www.sciencedirect.com/science/article/pii/S0303243412001651.

S. van der Walt, J. L. Schönberger, J. Nunez-Iglesias, F. Boulogne, J. D. Warner, N. Yager, E. Gouillart, T. Yu, and scikit-image contributors. scikit-image: image processing in Python. *PeerJ*, 2:e453, 2014.

G. R. van der Werf, D. C. Morton, R. S. DeFries, J. G. J. Olivier, P. S. Kasibhatla, R. B. Jackson, G. J. Collatz, and J. T. Randerson. CO2 emissions from forest loss. *Nature Geoscience*, 2(11):737–738, Nov. 2009. URL https://www.nature.com/articles/ngeo671.

C. Vancutsem, F. Achard, J.-F. Pekel, G. Vieilledent, S. Carboni, D. Simonetti, J. Gallego, L. E. O. C. Aragão, and R. Nasi. Long-term (1990–2019) monitoring of forest cover changes in the humid tropics. *Science Advances*, 7(10):eabe1603, Mar. 2021. URL https://www.science.org/doi/10.1126/sciadv.abe1603.

C. Vargas, J. Montalban, and A. A. Leon. Early warning tropical forest loss alerts in Peru using Landsat. *Environmental Research Communications*, 1(12):121002, Oct. 2019. URL https://doi.org/10.1088/2515-7620/ab4ec3.

A. Veloso, S. Mermoz, A. Bouvet, T. Le Toan, M. Planells, J.-F. Dejoux, and E. Ceschia. Understanding the temporal behavior of crops using Sentinel-1 and Sentinel-2-like data for agricultural applications. *Remote Sensing of Environment*, 199:415–426, Sept. 2017. URL https://www.sciencedirect.com/science/article/pii/S0034425717303309.

A. Verhegghen, H. Eva, G. Ceccherini, F. Achard, V. Gond, S. Gourlet-Fleury, and P. O. Cerutti. The Potential of Sentinel Satellites for Burnt Area Mapping and Monitoring in the Congo Basin Forests. *Remote Sensing*, 8(12):986, Dec. 2016. URL https://www.mdpi.com/2072-4292/8/12/986.

E. Vermote, J. Roger, B. Franch, and S. Skakun. LaSRC (Land Surface Reflectance Code): Overview, application and validation using MODIS, VIIRS, LANDSAT and Sentinel 2 data's. In *IGARSS 2018 - 2018 IEEE International Geoscience and Remote Sensing Symposium*, pages 8173–8176, July 2018.

S. M. Vicente-Serrano, F. Pérez-Cabello, and T. Lasanta. Assessment of radiometric correction techniques in analyzing vegetation variability and change using time series of Landsat images. *Remote Sensing of Environment*, 112(10):3916–3934, Oct. 2008. URL https://www.sciencedirect.com/science/article/pii/S0034425708002186.

L. Villard and P. Borderies. Backscattering Border Effects for Forests at C-band. *PIERS Online*, 3(5):731–735, 2007. URL http://piers.mit.edu/piersonline/piers.php?year=2007&volume=3&number=5&page=731.

B. Vira, C. Wildburger, and S. Mansourian. Forests, trees and landscapes for food security and nutrition: a global assessment report. *IUFRO World Series*, 33, 2015. URL https://www.cabdirect.org/globalhealth/abstract/20153184716.

P. Virtanen, R. Gommers, T. E. Oliphant, M. Haberland, T. Reddy, D. Cournapeau, E. Burovski, P. Peterson, W. Weckesser, J. Bright, S. J. van der Walt, M. Brett, J. Wilson, K. J. Millman, N. Mayorov, A. R. J. Nelson, E. Jones, R. Kern, E. Larson, C. J. Carey, Polat, Y. Feng, E. W. Moore, J. VanderPlas, D. Laxalde, J. Perktold, R. Cimrman, I. Henriksen, E. A. Quintero, C. R. Harris, A. M. Archibald, A. H. Ribeiro, F. Pedregosa, P. van Mulbregt, and SciPy 1.0 Contributors. SciPy 1.0: Fundamental Algorithms for Scientific Computing in Python. *Nature Methods*, 17:261–272, 2020.

VisioTerra. VtWeb. 2015. https://visioterra.org/VtWeb/ (Last accessed on 03/09/2022).

F. Warmerdam. The Geospatial Data Abstraction Library. In G. B. Hall and M. G. Leahy, editors, *Open Source Approaches in Spatial Data Handling*, Advances in Geographic Information Science, pages 87–104. Springer, Berlin, Heidelberg, 2008. URL https://doi.org/10.1007/978-3-540-74831-1_5.

C. E. Wheeler, E. T. A. Mitchard, H. E. Nalasco Reyes, G. Iñiguez Herrera, J. I. Marquez Rubio, H. Carstairs, and M. Williams. A New Field Protocol for Monitoring Forest Degradation. *Frontiers in Forests and Global Change*, 4, 2021. URL https://www.frontiersin.org/articles/10.3389/ffgc.2021.655280.

D. Wheeler, B. Guzder-Williams, R. Petersen, and D. Thau. Rapid MODIS-based detection of tree cover loss. *International Journal of Applied Earth Observation and Geoinformation*, 69:78–87, July 2018. URL https://ui.adsabs.harvard.edu/abs/2018IJAEO..69...78W.

P. Wilkes, A. Lau, M. Disney, K. Calders, A. Burt, J. Gonzalez de Tanago, H. Bartholomeus, B. Brede, and M. Herold. Data acquisition considerations for Terrestrial Laser Scanning of forest plots. *Remote Sensing of Environment*, 196:140–153, July 2017. URL https://www.sciencedirect.com/science/article/pii/S003442571730189X.

M. G. Windisch, E. L. Davin, and S. I. Seneviratne. Prioritizing forestation based on biogeochemical and local biogeophysical impacts. *Nature Climate Change*, 11 (10):867–871, Oct. 2021. URL https://www.nature.com/articles/s41558-021-01161-z.

D. Wood. *Rethinking the Power of Maps*. Guilford Press, Apr. 2010. Google-Books-ID: WjGGRJwGIaAC.

I. H. Woodhouse. *Introduction to Microwave Remote Sensing*. CRC Press, July 2017. URL https://www.taylorfrancis.com/books/mono/10.1201/9781315272573/introduction-microwave-remote-sensing-iain-woodhouse.

I. H. Woodhouse, E. T. A. Mitchard, M. Brolly, D. Maniatis, and C. M. Ryan. Radar backscatter is not a 'direct measure' of forest biomass. *Nature Climate Change*, 2 (8):556–557, Aug. 2012. ISSN 1758-6798. doi: 10.1038/nclimate1601. URL https://www.nature.com/articles/nclimate1601.

B. Ygorra, F. Frappart, J. P. Wigneron, C. Moisy, T. Catry, F. Baup, E. Hamunyela, and S. Riazanoff. Monitoring loss of tropical forest cover from Sentinel-1 time-series: A CuSum-based approach. *International Journal of Applied Earth Observation and Geoinformation*, 103:102532, Dec. 2021. URL https://www.sciencedirect.com/science/article/pii/S0303243421002397.

Y. Yu and S. Saatchi. Sensitivity of L-Band SAR Backscatter to Aboveground Biomass of Global Forests. *Remote Sensing*, 8(6):522, June 2016. URL https://www.mdpi.com/2072-4292/8/6/522.

D. C. Zemp, C.-F. Schleussner, H. M. J. Barbosa, M. Hirota, V. Montade, G. Sampaio, A. Staal, L. Wang-Erlandsson, and A. Rammig. Self-amplified Amazon forest loss due to vegetation-atmosphere feedbacks. *Nature Communications*, 8(1):1–10, Mar. 2017. URL `https://www.nature.com/articles/ncomms14681`.

L. R. V. Zeppetello, L. A. Parsons, J. T. Spector, R. L. Naylor, D. S. Battisti, Y. J. Masuda, and N. H. Wolff. Large scale tropical deforestation drives extreme warming. *Environmental Research Letters*, 15(8):084012, July 2020. URL `https://doi.org/10.1088/1748-9326/ab96d2`.